# Bridging the Gap: From Metal-Rich to Pnicogen-Rich Quaternary Phosphides and Arsenides

by

Krishna Kumar Ramachandran

A thesis submitted in partial fulfillment of the requirements for the degree of

Doctor of Philosophy

Department of Chemistry
University of Alberta

# Abstract

Several series of rare-earth and transition-metal-containing pnictides such as $RE_2Mn_3Cu_9Pn_7$, $REMnCu_4P_3$, $REMM'Pn_2$ ($M$ = Mn, Cu, Ag; $M'$ = Cu, Zn, Cd; $Pn$ = P, As) and $REAg_{1-x}Zn_yAs_2$ were synthesized, and their crystal structures were determined using X-ray diffraction methods. The electronic properties and bonding interactions were examined using TB-LMTO computational calculations. The electrical and magnetic properties of the samples were measured using QD-PPMS and the optical properties were measured by diffuse reflectance spectroscopy.

The flexibility of metal positions is examined in different ternary systems to evaluate how the physical properties such as magnetism, electrical resistivity, and optical band gaps are affected. Both metal-rich and pnicogen-rich (P, As) compounds were synthesized to examine the applicability of the Zintl-Klemm concept and under what conditions it fails. Detailed crystal structure determinations have been carried out for these phases. The bonding in these compounds was evaluated using band structure calculations. As a secondary objective, the thesis discusses the structural relationship with physical properties such as electrical conductivity, magnetism, and optical band gap of these new quaternary phosphides and arsenides. Combining these two ideas, it is possible to successfully tune the physical properties of new materials.

# Preface

असतो मा सद्गमय ।
तमसो मा ज्योतिर्गमय ।
मृत्योर्मा अमृतं गमय ।

Asato Ma Sat Gamaya

Tamaso Ma Jyotir Gamaya

Mrityor Ma Amritam Gamaya

(*Brihadaranyaka Upanishad*)

Oh Lord, lead me from Asat (deception) to Sat (truthfulness), enlighten me from the ignorance to the world of knowledge, enrich my deeds immortal that I could leave behind for the future generations, and bridge this gap in me to make me a better human being.

The thesis titled "Bridging the Gap: From Metal-Rich to Pnicogen-Rich Quaternary Phosphides and Arsenides" is a summary of the research work I have performed during my graduate studies in Dr. Mar's laboratory. Most of the chapters included in this thesis are published in different journals, which have collaborations and co-authors. The nature and extent of my contribution to the work has been included in this thesis and is summarized below.

Chapter 2 of this thesis has been published as S. S. Stoyko, K. K. Ramachandran, C. S. Mullen, and A. Mar, "Rare-Earth Manganese Copper Pnictides $RE_2Mn_3Cu_9Pn_7$ (*Pn* = P, As): Quaternary Ordered Variant of the $Zr_2Fe_{12}P_7$-Type Structure," *Inorg. Chem.* **2013**, *52*, 1040-1046. I was responsible for synthesizing, assisting in characterization, and

writing the first draft of the manuscript. S. S. Stoyko proposed the project, assisted in synthesis, characterization along with C. S. Mullen. A. Mar was involved in preparing and submitting the manuscript to the journal.

Chapter 3 of this thesis has been published as K. K. Ramachandran, S. S. Stoyko, C. S. Mullen, and A. Mar, "Rare-earth Manganese Copper Phosphides *RE*$MnCu_4P_3$ (*RE* = GdHo): The first Quaternary Ordered Variants of the $YCo_5P_3$-Type Structure," *Inorg Chem.* **2015**, *54*, 860-866. My contribution to the work was synthesis, assisted in crystal structure determination and all other characterization including band structure calculations and writing the initial drafts of the manuscript. S. S. Stoyko proposed the project, assisted in synthesis and characterization along with S. C. Mullen. A. Mar was involved in manuscript preparation and submission process.

Chapter 4 of this thesis has been published as K. K. Ramachandran, C. Genet, and A. Mar, "Quaternary Rare-Earth Arsenides *RE*$Ag_{1-x}Zn_yAs_2$ (*RE* = La-Nd, Sm, Gd-Dy) with Tetragonal $SrZnBi_2$- and $HfCuSi_2$-type structures," *J. Solid State Chem.* **2015**, *231*, 204-211. This project was entirely proposed and characterized by me. I prepared the preliminary drafts of the manuscript. C. Genet assisted me in synthesis and characterization. A. Mar, the supervisory author, involved in preparing and submitting the manuscript to the journal.

Chapter 5 of this thesis has been published as S. S. Stoyko, K. K. Ramachandran, P. E. R. Blanchard, K. A. Rosmus, J. A. Aitken, and A. Mar, "Three Series of Quaternary Rare-Earth Transition-Metal Pnictides with $CaAl_2Si_2$-type structures: *RE*$CuZnP_2$, *RE*$AgZnP_2$, and *RE*$AgZnAs_2$," *J. Solid State Chem.* **2014**, *213*, 275-286. My contribution

to the work was synthesis, characterization (excluding diffuse reflectance study) of *RE*$AgCdP_2$, and initial draft of the manuscript. P. E. R. Blanchard contributed to XPS measurements, assisted S. S. Stoyko in synthesizing and characterizing *RE*$CuZnP_2$ and *RE*$AgZnAs_2$. We collaborated with K. A. Rosmus and J. A. Aitken for diffuse reflectance study. A. Mar, the supervisory author, involved in preparing and submitting the manuscript to the journal.

Chapter 6 of this thesis is not a published work but this will be co-authored by B. Ruellan, S. S. Stoyko, P. E. R. Blanchard, J. R. Glenn, J. A. Aitken, A. Mar. My contribution was synthesizing and characterizing the new series of *RE*$AgCdP_2$ and $TbMnCuP_2$. I have done band structure calculations of *REMM'*$P_2$ and magnetic studies of $TbMnCuP_2$. I also contributed in the preparation of initial drafts of the manuscript. B. Ruellen assisted me in *RE*$AgCdP_2$ Ruellen. P. E. R. Blanchard initially made the *RE*$MnCuP_2$ along with S. S. Stoyko. J. R. Glenn and J. A. Aitken assisted in collecting and analyzing optical band gap of the materials using diffuse reflectance spectroscopy. A. Mar, the supervisory author, involved in preparing and submitting the manuscript to the journal.

# Acknowledgements

I would like to express my sincere gratitude to Dr. Arthur Mar, he is an inspiring supervisor, an excellent mentor, and a good friend. He is a very approachable person and always appreciate the work you do, whether it is big or small. Rather than giving instructions and solutions, Dr. Mar would always like to give hints and let me think by myself, which has benefited in developing my knowledge and enthusiasm towards Chemistry. He has not only helped me in the research, but also assisted in improving my personality as well as my networking skills. Dr. Mar has taught me how to face and defend myself in difficult and challenging situation. I am extremely thankful to University of Alberta for giving me a great opportunity to work with an eminent scientist like Dr. Mar.

I would like to thank the University of Alberta, Department of Chemistry for all the facilities provided for fulfilling my graduate degree. I would like to extend my gratitude to Dr. Norman Gee for his huge support and help in teaching assistantship. I am so grateful to have such a supportive supervisory committee, Dr. Jon Veinot and Dr. Gabrial Hanna, with whom I can discuss any issues. I would like to thank Jon and Leah for giving me an opportunity to work with ATUMS and providing me with international travel fellowship to Germany, which was almost like a dream come true. I would also like to thank Dr. Martin Cowie, Dr. Jillian Buriak for their inspiring coursework. I am glad to have Dr. Michael Serpe and Dr. Moritz Heimpel in my candidacy exam. It was impossible to finish my work with out the help of collaboration and I would like to express my sincere gratitude to Dr. Jennifer Aitken and Dr. Tom Nilges.

I am extremely grateful to Bob and Mike for their support in XRD, Dirk, Paul and all those who work in machine shop, Anita, Tyler, Kim and Allen from electronic shop, and Kyle and Ernesto for their tremendous help in fixing and troubleshooting QD-PPMS.

I have several people in my life who has given me the importance and inspiration, the strength and courage and the love and care I needed and I would like to thank each of them for their support throughout my life including my family, teachers and friends. I would like to thank my caring parents Ramachandran and Indira, my loving brother Vishnu, sister Sumitra, nephew Aditye, grandmother Sarojini and my best friend Sandeep for always being there for me. I don't have words to thank my Canadian grandmother, Silvia Heimpel for providing me the best and comfortable boarding in Canada and also for her unconditional love and support. It is impossible to include my entire friends list here but I would like to name a few of them including my old and current lab mates Stan, Brent, Brianna, Scott, Mansura, Anton, Xinsong, Abishek, Danissa, and Wenlong for giving me the best time in laboratory. I would like to extend my sincere gratitude to my friends in University Javix, Sindhu, Jerry, Neha, Santu, Arpan for giving me enjoyable moments to cherish. I would like to thank all the members in the social group AHIMSA, CKCA, Let's Talk Science and INDSA for giving me a memorable experience in Edmonton. It is important to mention my pervious mentors Dr. Joy Joseph, Dr. T. N. Guru Row, Dr. Tapas Maji for their support; my closest friends Sajesh, Sunil, Seetha, Reshmi, Anju, Adarsh, Jerry Jospeph and many others for all their support and prayers.

The research was funded by the University of Alberta, the Natural Sciences and Engineering Research Council of Canada, NSERC CREATE-IRTG ATUMS. My sincere

gratitude to all my undergraduate students, internship students I supervised, and all those who are missing in the list. Thanks to one and all including the readers!!!

# Table of Contents

# List of Tables

# List of Figures

# List of Symbols and Abbreviations

| | |
|---|---|
| $\alpha$ | Absorption co-efficient |
| $\theta$ | Angle of reflection |
| $\theta_P$ | Weiss constant |
| $\lambda$ | Wavelength; Inelastic mean free path |
| $\rho$ | Density |
| $\chi$ | Magnetic susceptibility |
| $\mu_{eff}$ | Effective magnetic moment |
| 1D | One dimensional |
| 2D | Two dimensional |
| 3D | Three dimensional |
| $a\ b\ c\ \alpha\ \beta\ \gamma$ | Unit cell parameters |
| AFM | Antiferromagnetism |
| APS | Advanced photon source |
| BVS | Bond valence sum |
| ASA | Atomic sphere approximation |
| COHP | Crystal orbital Hamilton population |
| COOP | Crystal orbital overlap population |
| $C$ | Curie constant |
| $d_{hkl}$ | d-spacing |
| DFT | Density functional theory |

| | |
|---|---|
| DOS | Density of states |
| $e^-$ | Electron |
| $E_F$ | Fermi level |
| $E_g$ | Band gap |
| $E_u$ | Urbach energy |
| EDX | Energy dispersive X-ray analysis |
| FC | Field-cooled |
| FM | Ferromagnetism |
| $F(R_\infty)$ | Kubelka-Munk (K-M) function |
| $g$ | Total number of valence electrons |
| $g_j$ | Landé factor |
| $H$ | Magnetic field |
| $hkl$ | Miller indices |
| IR | Infrared |
| $j$ | Angular momentum |
| $k$ | Wave vector |
| $l$ | Orbital angular momentum |
| LDA | Local density approximation |
| LMTO | Linear muffin-tin orbital |
| $M$ | Magnetization; Transition metal |
| $n$ | Number of valence electrons |
| $Pn$ | Pnicogen (phosphides and arsenides) |

| | |
|---|---|
| PM | Paramagnetism |
| PPMS | Physical property measurement system |
| $R$ | Reflectance, Reliability factor |
| *RE* | Rare-earth |
| $S$ | Goodness of fit, scattering coefficient |
| SEM | Scanning electron microscope |
| $T$ | Temperature |
| $T_c$ | Critical temperature; Curie temperature |
| $T_N$ | Néel temperature |
| TB | Tight-binding |
| $V$ | Cell volume; applied voltage |
| VEC | Valence electron concentration |
| XRD | X-ray diffraction |
| $Z$ | Atomic number; nuclear charge |
| $Z_{eff}$ | Effective nuclear charge |
| ZFC | Zero-field cooled |

# Chapter 1

# Introduction

## 1.1 Solid State Compounds

Chemical substances can be broadly classified into those that are molecular and those that are non-molecular, which have extended structures and are usually solids. Solid-state chemistry deals with the synthesis, structures, properties, and applications of non-molecular substances, typically inorganic and crystalline. Inorganic extended solids can undergo transformations that molecules cannot; for example, they can be doped (in which a fraction of a specific component is substituted with another element) to modify properties such as electrical conductivity or band gap in a gradual manner.[1] The study of solid-state compounds can be conveniently divided into (i) oxides and halides, which are usually highly ionic and electrically insulating, and (ii) non-oxides, which encompass chalcogenides, pnictides, and intermetallic compounds. Solid-state chemists are interested in exploring the reactivity of different elements, determining and designing structures, and measuring and improving physical properties. The focus of this thesis is on phosphides and arsenides, which exhibit diverse bonding character and interesting physical properties such as ferromagnetism and semiconductivity.

## 1.2 Metal Phosphides and Arsenides

Perhaps the most well-known pnictides are the so-called III-V semiconductors which are the foundation of modern electronic and optical devices (e.g., GaAs, $Al_xGa_{1-x}As$, GaP).[2] There are many other binary, ternary, and quaternary pnictides exhibiting diverse

compositions, structures, and properties. Depending on the relative proportions of metal and pnicogen, these compounds can be considered to be metal-rich or pnicogen-rich. It is useful to present an overview of previously known transition-metal phosphides and arsenides.

Early investigations revealed the existence of various transition-metal phosphides and arsenides (*M* = transition metals; *Pn* = P, As), the most common compositions being $M_3Pn$, $M_2Pn$, $M_4Pn_3$, $M_3Pn_2$, $MPn$, $M_2Pn_3$, $MPn_2$ , $MPn_3$, and $MP_4$. Measurements of their physical properties were relatively sparse. Although the magnetic behaviour of $M_2Pn$ and $MPn$ phases was mostly unremarkable, a few were ferromagnetic with quite high Curie temperatures (217 K for $Fe_2P$, 317 K for MnAs).[3,4] The compounds $M_3Pn_2$ (*M*= Cd, Zn) were initially identified to be potential thermoelectric materials because they exhibit quite low thermal conductivities and high electrical conductivities (~1 W/m·K and ~$10^3$ $\Omega^{-1}$.cm$^{-1}$).[5] Promising applications as catalysts have been found for $M_3P$ (*M* = Ni, Pd), $M_2P$ (*M*= Rh, Fe, Ni, Co), and $MP$ (*M*= Mo, Co, W) in hydrodesulfurization,[6,7] hydrodenitrogenation,[8] hydrodechlorination,[9] and hydrodeoxygenation[10,11] processes. $Ni_3P$ is also used as an industrial coating.[12] Recently, $Ni_2P$ has been found to be a catalyst for water splitting which can help in storing solar energy.[13] $Cu_3P$ and FeP are possible anode material for Li-ion batteries.[14,15] Mixed-metal phosphides and arsenides (especially $MnFeP_{0.45}As_{0.55}$) have found a particularly interesting application as magnetocaloric materials for magnetic refrigeration.[16]

Among ternary pnictides, $BaFe_2As_2$ and related phases (including pnictide oxides like LaFeAsO) have attracted enormous attention for their superconducting properties; the

transition temperature can be raised to as high as 55 K through appropriate doping (in $SmFeAsO_xF_{1-x}$).[17] These superconducting compounds adopt the $ThCr_2Si_2$-type structure, which is a prevalent one in solid-state chemistry. An equally interesting class of ternary pnictides that also contain many $ThCr_2Si_2$-type phases are those containing a rare-earth and a transition metal. Many *RE*–*M*–(P, As) phases are known, but they are largely limited to a late transition metal for the *M* component, and more remains to be done (**Table 1-1**).[18] Among $ThCr_2Si_2$-type phases in these systems, $LaRu_2P_2$ has long been known to be superconducting at rather low temperature (4.1 K) but $LaRu_2As_2$ was recently found to have a higher transition temperature (7.8 K).[19,20] An exciting discovery was that $EuFe_2As_2$ becomes superconducting at 35 K when doped with Na.[21] A potential new application for *RE*–*M*–(P, As) phases is as thermoelectric materials, given that the corresponding antimonides have been heavily investigated (e.g., $LaFe_4Sb_{12}$, Yb$M_2Sb_2$ (*M* = Mn, Zn, Cd) doped with Ca).[22-24] In particular, phases with the $CaAl_2Si_2$-type structure, which is closely related to the $ThCr_2Si_2$-type structure, may also be good candidates for this application. Among these, $YbZn_2P_2$ is a good starting point because its thermoelectric figure of merit can probably be improved (*ZT* of ~0.1).[25]

To date, there are far fewer quaternary phosphides and arsenides. If one considers all possible combinations of rare-earth metals (14), transition metals (30), and the two pnicogens, P and As, there are over 10,000 quaternary systems *RE*–*M*–*M′*–(P, As) to be investigated, where *M* and *M′* are two different transition metals. Assuming that each system contains several quaternary phases, the number of potential new compounds is enormous. Yet, only a tiny fraction of these have been reported: $RE_5Ni_{16}Zr_3As_{12}$ (*RE*= Ce-

Nd, Sm, Gd-Lu, Yb), $YbMnCuP_2$, *RE*$AgZnP_2$ (La, Sm), $(La, Ce)_{12}Rh_{30}P_{21}$, $La_{0.5}Ce_{0.5}Ru_4P_{12}$, $RE_2Co_9M_3Pn_7$ (*RE*= Ce, Gd, Er; *M*= W, Cr, Fe; *Pn*= P, As), $Eu_2MPt_7P_3$ (*M*= Fe, Mn, Zn), $Eu_2CuZn_2P_3$, $Eu_3Cu_2Zn_2P_4$, $EuAg_2ZnAs_3$, $EuRh_{2-x}Co_xP_2$ (x=0 - 0.2), *RE*$CuZnP_2$ (*RE*= Ce, Sm, Yb), $EuPd_{1-x}M_xAs$ (*M*= Ag, Au), $EuFe_{2-x}Co_xAs_2$, $Ce_4Mn_{0.4}Zn_{1.3}As_7$, $Ce_4Mn_{0.6}Zn_{1.2}As_5$.[18] Introducing more components in these multinary phases permits greater control of properties. For example, $YbCuZnP_2$ is derived from $YbZn_2P_2$ but has improved thermoelectric properties ($ZT$ = 0.6 at 1000K).[25]

One of the main goals in my research was to synthesize, to understand the structure, and properties of the unknown quaternary arsenides and phosphides.

**Table 1-1.** Reported rare-earth- transition metal arsenides and phosphides.[18]

| **Ti** | **V** | **Cr** | **Mn** | **Fe** | **Co** | **Ni** | **Cu** | **Zn** |
|---|---|---|---|---|---|---|---|---|
| | | | $RE_2Mn_{12}P_7$<br>*RE*$Mn_2Pn_2$<br>$Eu_{14}MnPn_{11}$ | *RE*$Fe_2P_2$<br>*RE*$Fe_5P_3$<br>$RE_2Fe_{12}P_7$<br>*RE*$Fe_4Pn_{12}$<br>$RE_5Fe_{19}P_{12}$<br>$RE_{12}Fe_{57.5}As_{41}$ | *RE*$Co_2Pn_2$<br>*RE*$Co_5Pn_3$<br>*RE*$Co_3P_2$<br>$RE_2Co_{12}Pn_7$<br>$RE_5Co_{19}P_{12}$<br>$RE_{0.2}Co_4P_{12}$<br>$GdCo_4P_3$ | *RE*$Ni_2Pn_2$<br>$RE_2Ni_{12}Pn_7$<br>$RE_6Ni_{20}Pn_{13}$<br>$RE_7Ni_{19}Pn_3$<br>*RE*$Ni_7As_5$<br>*RE*Ni*Pn*<br>$RE_5Ni_{19}P_{12}$ | *RE*$CuPn_2$<br>$RE_5Cu_{19}P_{12}$<br>$EuCu_{1.75}As_2$<br>$EuCu_4As_2$<br>$Yb_2Cu_4As_3$ | *RE*$Zn_2As_3$<br>*RE*$Zn_{0.67}As_2$<br>$RE_{0.67}Zn_2As_2$<br>*RE*$Zn_3P_3$<br>*RE*$Zn_{2-x}As_2$•*n*(*RE*As)<br>*RE*$Zn_{2-x}As_2$<br>$RE_{2-y}Zn_4As_4$•*n*(*RE*As)<br>*RE*$Zn_2P_2$ (Eu, Yb) |
| **Zr** | **Nb** | **Mo** | **Tc** | **Ru** | **Rh** | **Pd** | **Ag** | **Cd** |
| | $Eu_{13}NbAs_{11}$ | | | $EuRuAs_2$<br>*RE*$Ru_4Pn_{12}$<br>$La_5Ru_{19}P_{12}$<br>$RE_6Ru_{20}P_{13}$ | *RE*$Rh_2P_2$<br>$EuRhPn_2$<br>$RE_{12}Rh_{30}P_{21}$<br>(*RE* =La+Ce) | *RE*$Pd_2Pn_2$<br>*RE*$Pd_3As_2$<br>*RE*Pd*Pn* | *RE*$AgAs_2$<br>$EuAgPn$<br>$EuAg_4As_2$ | *RE*$Cd_3As_3$<br>*RE*$Cd_2P_3$ (Eu, Yb) |
| **Hf** | **Ta** | **W** | **Re** | **Os** | **Ir** | **Pt** | **Au** | **Hg** |
| | | | | *RE*$Os_4Pn_{12}$ | *RE*$Ir_2Pn_2$<br>$RE_5Ir_{19}P_{12}$ | EuPtP | *RE*$AuAs_2$<br>*RE*Au*Pn* | |

*n*= 3, 4, 5, 6 . *Pn*- P, As, *RE* = rare-earth element

## 1.3 Electron Counting Schemes

In contrast to molecular substances, the bonding in extended inorganic solids is not often easy to rationalize. The difference in electronegativities of the components in metal phosphides and arsenides is intermediate: the bonding is neither strongly ionic (as would occur in oxides or halides) nor strongly metallic (as would occur in genuine intermetallics composed of similar metals). Depending on the relative proportions of metal and pnicogen, it may be possible to explain the bonding through simple electron counting rules.

### 1.3.1 Intermetallics and Metal-rich Phases

Compounds consisting of two or more metals in a definite proportion and adopting a definite structure are called intermetallics. Generally, because metallic elements do not differ much in their electronegativities, electron transfer is assumed to be minimal and the valence electrons are completely delocalized within the solid. As a consequence, there are no simple rules to relate the bonding in intermetallics to the electron count. This is not to say that the electronic structure is not important; rather, the crystal structures of intermetallics depend in a complicated way on the electronic structure of the entire solid which must be evaluated through band structure calculations. For a small subset of intermetallics composed of Cu or Zn in combination with Al, Sn, or Ag, called Hume-Rothery phases,[26] there does exist a correlation between the valence electron count and the crystal structure adopted. Although metal phosphides and arsenides would not normally considered to be intermetallics, if the proportion of metal is high, their structures would resemble those of intermetallics and the bonding would show essentially metallic character.[27]

Many binary pnictides of first-row transition metals have the formulas $M_3Pn$, $M_2Pn$, and $MPn$. As can be anticipated, there structures show extensive networks of $M$–$M$ bonds ranging from 2.6–3.1 Å, similar to those found in the elemental metals.[18] Both $M_3Pn$ and $M_2Pn$ have structures containing $Pn$-centred trigonal prisms, which are quite common motifs in many metal-rich pnictides. These trigonal prisms can be connected in many different ways, as shown for $Fe_2P$ (**Figure 1-2**).[28] The monophosphides $MP$ ($M$ = Cr, Mn, Fe, Co) are interesting in that they show not only $M$–$P$ bonds but also zigzag chains of $M$–$M$ bonds (**Figure 1-1**).[29,30]

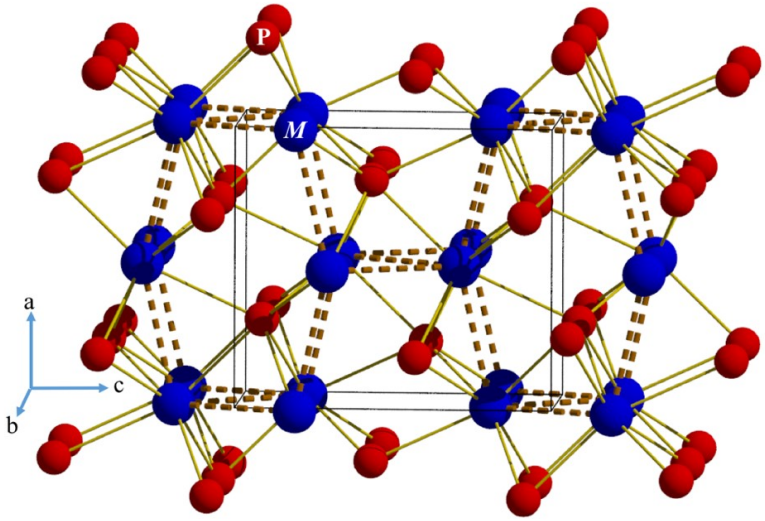


**Figure 1-1.** Crystal structure of $MP$ (MnP-type) showing $M$–$M$ bonds, $M$–P bonds viewing along $b$ axis.

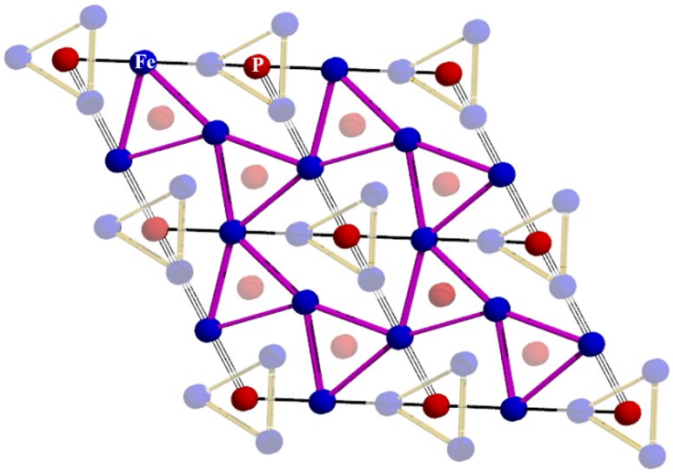


**Figure 1-2.** A view of $Fe_2P$ crystal structure along *c* direction showing the phosphorous centred trigonal prisms of Fe–Fe bonds. The shaded atoms and bonds are at one half of the *c* axis of the unit cell.

### 1.3.2 Normal Valence Compounds

A guiding principle in bonding is that atoms attain an octet of valence electrons, either through transfer or sharing of electrons. Compounds that satisfy this rule are termed *normal valence*; simple ionic compounds and most molecular substances fall in this category. The Zintl-Klemm concept extends this idea to situations where electronegativity differences are smaller but the assumption of full electron transfer is still applied even if this is not quite valid. Intermetallics consisting of an electropositive metal (alkali or alkaline-earth metals) and a more electronegative *metametal* or *semimetal* (in group 13, 14, or 15) that exhibit normal valence are called Zintl phases (e.g., NaTl, $CaSi_2$, $SrAs_3$, LiAgAs, $Li_2AgSb$).[26,27] As shown in **Figure 1-3**, the boundary separating electronegative metals that form Zintl phases is not clear-cut. Similarly, compounds containing rare-earth metals as the electropositive component can sometimes be considered Zintl phases (e.g., $CeP_5$, $LaAs_2$, $NdP_2$),[26] and it is up to debate whether transition metals can be included. Thus, an

important question is whether phosphides and arsenides containing rare-earth and transition metals satisfy normal valence.

Although the Zintl concept does not predict structure, it is helpful in rationalizing the bonding. If the number of electrons transferred to the electronegative metal is insufficient to attain an octet, homoatomic bonds have to form between two or more of these electronegative atoms, resulting in polyanionic networks. Conversely, if there is an excess of electrons remaining on the electropositive metal after enough have been transferred to the electronegative metal, then homoatomic bonds have to form between two or more of these electropositive atoms, resulting in polycationic networks. To apply the Zintl concept in a binary compound $M_mX_x$, the *valence electron concentration per anion*,[26] VEC($X$) is evaluated by counting the total number of valence electrons and dividing by the number of $X$ atoms in the chemical formula:

$$\mathrm{VEC}(X) = (me_M + xe_X)/x. \qquad (1\text{-}1)$$

If VEC($X$) = 8, no homoatomic bonds form and only simple ions are present in *simple ionic compounds*. If VEC($X$) < 8, the $X$ atoms are short of an octet but can attain one by sharing electrons to form $X$–$X$ bonds, the number of which is 8 – VEC($X$), in *polyanionic compounds*. For metal pnictides, this electron counting rule agrees with expectations based on formal charge: a $Pn^0$ species forms three $Pn$–$Pn$ bonds, as found in the elemental structures; a $Pn^{1-}$ species forms two $Pn$–$Pn$ bonds, as found in NaP-type compounds;[31] a $Pn^{2-}$ species froms one $Pn$–$Pn$ bond, as found in $Sr_2P_2$-type compounds;[32] and a $Pn^{3-}$ species is an isolated ion, as found in $Na_3P$.[33] If VEC($X$) > 8, there is an excess of electrons

not needed to satisfy the octet on the *X* atoms, and this excess remaining on the *M* atoms can be used to form *M*–*M* bonds, the number of which is $(x/m)\cdot(\mathrm{VEC}(X) - 8)$, in *polycationic compounds* like GaS, where it forms one Ga–Ga bond. Although simple ionic and polyanionic compounds are common and relatively well understood, polycationic compounds are not and they often do not follow simple rules for bonding.

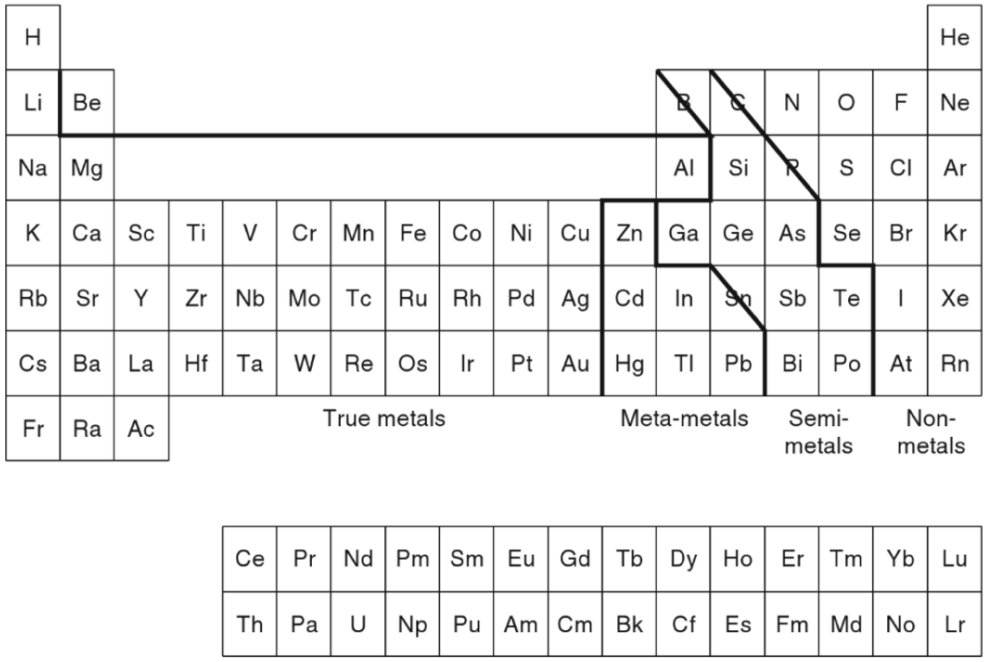


**Figure 1-3.** The periodic table division suggested by Klemm (1950).

### 1.3.3 Polyanionic Compounds

There is much emerging evidence that binary phosphides and arsenides containing rare-earth and transition metals can be considered as Zintl phases. Many of them are polyanionic compounds, displaying interesting networks with *Pn*–*Pn* bonds in the form of discrete units, 1D chains, and 2D nets. Perhaps the most famous example is skutterudite,

$Co^{3+}As_3^{3-}$, in which each $As^{1-}$ species having six electrons must form homoatomic bonds to two other As atoms (we say that As is "two-bonded"), resulting in discrete square $As_4$ units.[53] In the $NdAs_2$-type structure, adopted by several *REPn*$_2$ phases (*RE* = Ce, Pr, Nd; *Pn* = P, As), the formulation $Nd^{3+}As_2^{3-}$ agrees with the presence of finite units $As_4^{6-}$ with $As^{2-}$ at the terminal sites and $As^{1-}$ at the interior sites.[54] High-temperature $La^{3+}As_2^{3-}$ consists of discrete units of $As_3^{5-}$ (V-shaped) and $As_5^{7-}$ (5-membered fragment).[55] Infinite chains are found in $Zn^{2+}As_2^{2-}$, where each $As^{1-}$ is two-bonded, and in $Au_2^{2+}P_3^{2-}$, where cyclohexane-like $P_6^{4-}$ units are linked together.[56,57] $Zr^{2+}As_2^{2-}$ contains infinite four-atom-wide ribbons of As atoms.[58] Among examples of 2D nets, $Nb^{5+}(As^{3-})(As^{2-})$ contains distorted graphene-like layers with long and short bonds formed by the $As^{2-}$ atoms, and $Ce^{3+}P_5^{3-}$ contains corrugated 2D sheets of $P_5^{3-}$ outlining large 12-membered rings.[59,60] The *Pn*–*Pn* bonds in above described compounds are shown in **Figure 1-4**.

Ternary and quaternary pnictides can also exhibit complex polyanionic networks. Infinite square nets are quite common, as found in $Sm^{3+}Cu^{1+}(P^{1-})(P^{3-})$, which has the prevalent $HfCuSi_2$-type structure; however, 2*c*-1$e^-$ bonds must be invoked between the $P^{1-}$ atoms.[61] In fact, the most numerous ternary rare-earth transition-metal pnictides are *REMPn*$_2$ phases, which adopt various tetragonal structures containing *Pn* square nets.

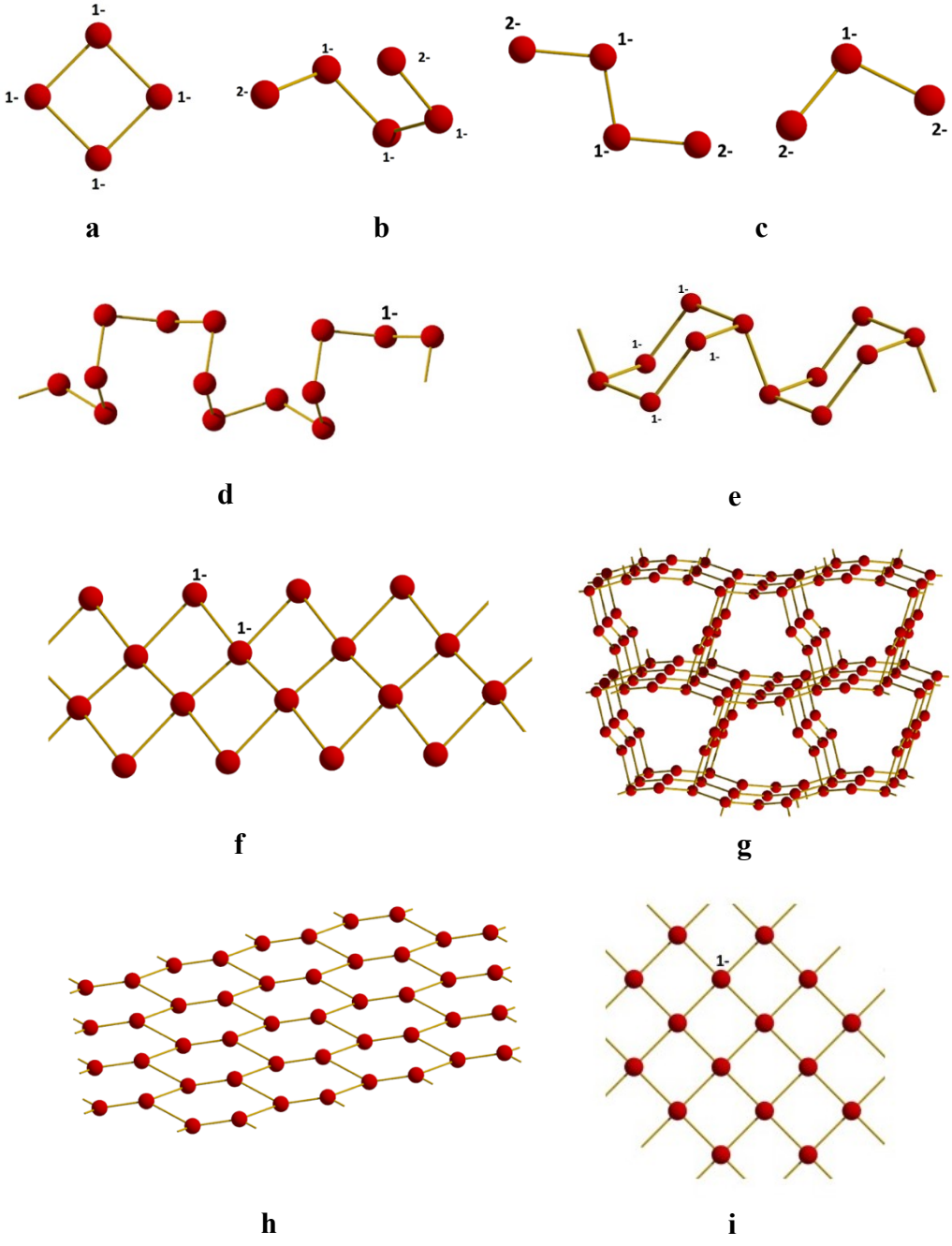


**Figure 1-4.** (a) discrete square $As_4$ units in $CoAs_3$, (b) $As_4^{6-}$ in $NdAs_2$, (c) $As_3^{5-}$ and $As_5^{7-}$ in $LaAs_2$, (d) infinite chains of As atoms in $ZnAs_2$, (e) linked cyclohexane-like $P_6^{4-}$ units in $Au_3P_2$, (f) four-atom-wide ribbons of As atoms in $ZrAs_2$, (g) corrugated 2D sheets of $P_5^{3-}$ in $CeP_5$, (h) distorted graphene-like layers in $NbAs_2$, (i) infinite P square nets in $SmCuP_2$.

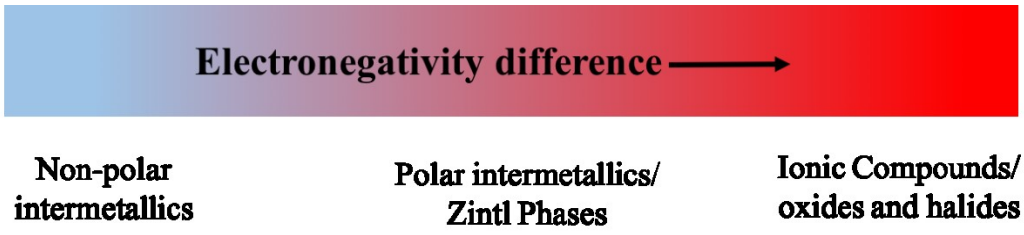


**Figure 1-5.** Graphical representation showing different intermetallic phases in terms of electronegativity difference.

### 1.3.4 Polycationic Bonding

Unlike polyanionic compounds, which are now quite numerous, polycationic compounds are relatively few and are poorly understood. Since by definition, metallic bonding is delocalized, it is highly unusual to find metal-rich phases that exhibit localized *M*–*M* bonds and satisfying normal valence rules. In compounds with the SiAs-type (adopted by SiAs, GeP, GeAs, and GaTe)[18] and GaS-type structures (adopted by GaS, GaSe, and InSe),[18] the electron counting rules describe earlier give VEC(*X*) = 9, implying that *M*–*M* bonds must be present, the number of which is (*x*/*m*)·(VEC(*X*) – 8) = 1. In agreement with this prediction, these structures contain *M*–*M* dumbbells in which each *M* atom is one-bonded (**Figure 1-6**). In the ternary arsenide $BaGe_2As_2$, an extension to the electron counting rules gives VEC(*X*) = ½·(2 + 2(4) + 2(5)) = 10. If *M*–*M* bonds are assumed to be formed by the Ge and not the Ba atoms, there should be (*x*/*m*)·(VEC(*X*) – 8) = (2/2) (10 – 8) = 2; that is, each Ge atom should be two-bonded. Accordingly, the structure of $BaGe_2As_2$ contains zigzag chains of Ge atoms (**Figure 1-7**). With further modification of these electron counting rules, it may be possible to rationalize the structures

of polycationic compounds containing clusters of metal atoms in which fractional bonding is assumed.

Metal clusters are well-known in organometallic compounds such as $Os_3(CO)_{12}$ and $Ir_4(CO)_{12}$,[26] in which the number of *M*–*M* bonds can be predicted by rules based on electron count: $b_{(M-M)} = ½\cdot(18n - g)$, where $n$ is the number of metal atoms and $g$ is the total number of valence electrons. In these instances, the *M*–*M* bonds are 2*c*–2e bonds and these clusters are said to be electron-precise. Analogous metal clusters can also be found in extended solids but sometimes delocalized bonding must be invoked. For example, $MoCl_2$ contains octahedral $Mo_6Cl_8$ clusters with bridging Cl atoms, and is electron-precise.[26] However, $Nb_6Cl_{14}$ contains $Nb_6Cl_{18}$ clusters with both bridging and terminal Cl atoms, and is not electron-precise; the electron counting rule fails here and delocalized multicentre bonding is believed to take place.[26]

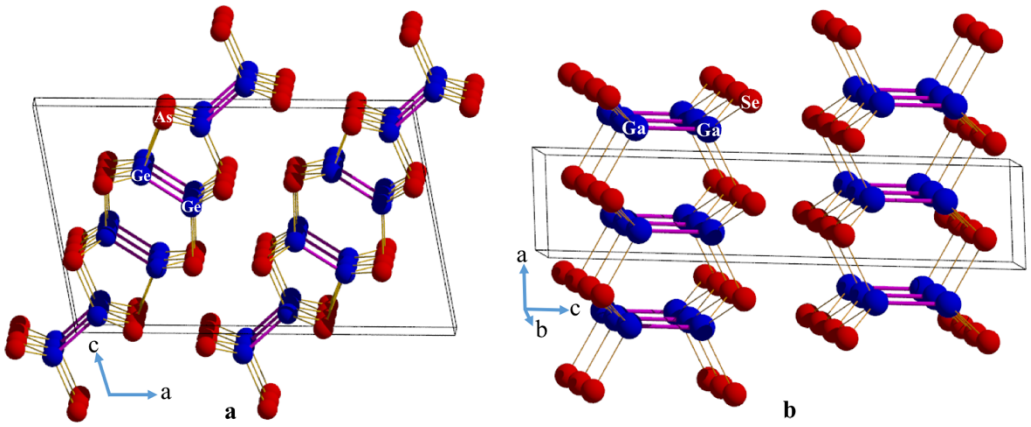


**Figure 1-6.** (a) Ge–Ge bonds in GeAs, a view along *b* axis; (b) Ga–Ga bonds in GaSe, a view along *b* axis

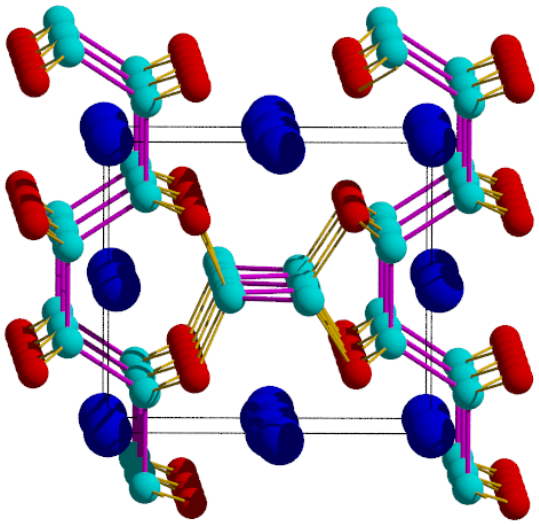

**Figure 1-7.** View of $BaGe_2As_2$ along a direction with alternating zigzag chains of Ge along *a* and *b* axis.

The bonding in intermetallic compounds is quite diverse. When the combination of metals differs little in electronegativity, there are no simple rules relating electron count to structures and bonding (other than in special cases such as the Hume-Rothery phases). At the other extreme, when there is a large difference in electronegativity in an intermetallic compound, the Zintl concept may work well to rationalize structures and bonding. There is no clear boundary between these extremes. Thus, it is of interest to determine under what circumstances metal phosphides and arsenides can be considered to be Zintl phases, and when they cannot.

## 1.4 Synthesis

As is typical for solid-state reactions, high temperatures are generally required to overcome diffusion barriers. The fate of solid-state reactions is difficult to predict because their mechanisms remain poorly understood, although recent efforts have been made to

address this problem.[34] For the preparation of rare-earth-containing pnictides in this thesis, direct reactions of high-purity elements at intermediate to high temperatures (usually above 800 °C) were used. Excessively high temperatures and fast heating rates were avoided to prevent loss of volatile components, especially P, As, and Zn. To ensure complete reaction, multiple regrinding and reheating procedures were applied.

Some precautions have to be taken for certain starting materials. The preferred form for the rare-earth metals is not powders, which are usually already partially oxidized when purchased, but rather ingots. Appropriate amounts of the rare-earth metals are freshly filed as needed and quickly loaded into the reaction container. Red phosphorus, which is slightly hygroscopic, as well as arsenic, which is highly toxic, are both handled within a glove box. It goes without saying that protective wear is necessary when handling these materials. The mixture of starting materials is pressed into pellets to improve contact. Fused silica tubes are a good choice of container for the preparation of pnictides (**Figure 1-8**); the rare-earth metals tend to react faster with the other starting materials and do not pose any serious problems in reacting with the container. The tubes are then evacuated and sealed, and placed within computer-controlled furnaces.

Good quality single crystals can often be obtained simply upon slow cooling of the sample, assuming that the melting temperature of a desired compound has been exceeded. In the literature, many phosphides have been crystallized with aid of a Sn flux. In this thesis, a small amount of $I_2$ (~30 mg) added to a sample has been found to be effective in growing large crystals of both phosphides and arsenides. The role of $I_2$ is not exactly clear,

but it acts as a mineralizer probably involving a chemical vapour transport mechanism in which gas-phase species are reversibly deposited to promote crystal growth (**Figure 1-9**).

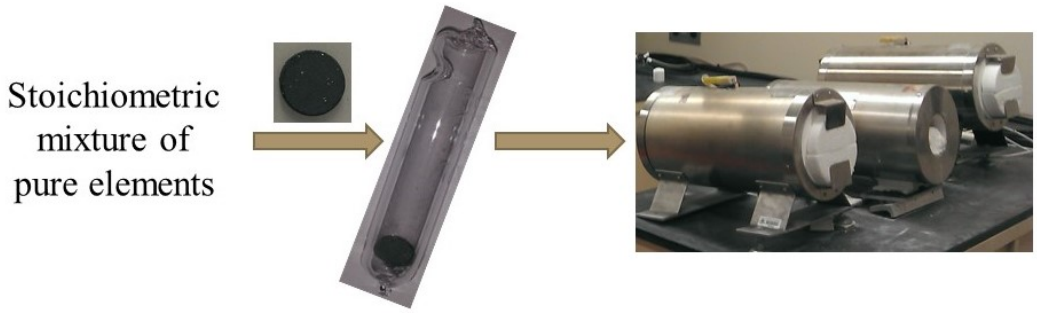


**Figure 1-8.** Sequence of quaternary pnictide synthesis starting with a pressed pellet of a stoichiometric mixture of the elements placed in an evacuated fused-silica tube and then heated in a high temperature furnace.

## 1.5 Characterization

### 1.5.1 X-ray Diffraction

By far the most important technique for characterizing solid-state compounds is X-ray diffraction (XRD). This is in contrast to molecular substances, which are more commonly characterized by spectroscopic methods such as NMR and IR spectroscopy. X-ray diffraction can be used for phase identification and quantitative phase analysis of a powder sample. With more detailed analysis, full crystal structures can be determined. Other applications include detecting phase transitions and estimating particle sizes.

When X-rays strike a crystal, they are scattered by periodic arrangement of atoms. In a simple treatment of X-ray diffraction, the incident X-rays strike sets of parallel lattice

planes separated by a constant spacing $d_{hkl}$, defined by the unit cell parameters. To satisfy the condition for constructive interference, the path length travelled by X-rays striking adjacent lattice planes must differ by an integral number of wavelengths (Bragg's law):

$$n\lambda = 2d_{hkl}sin\,\theta \qquad (1\text{-}2)$$

Here, $\lambda$ is the wavelength (typically Cu $K_\alpha$ or Mo $K_\alpha$), $d_{hkl}$ is the interplanar distance, $n$ is the order of reflection, and $\theta$ is the diffraction angle. (In practice, the angle between diffracted and transmitted radiation, $2\theta$, is more conveniently measured.) Because diffraction of higher order $n$ by lattice planes ($hkl$) is equivalent to first-order diffraction by lattice planes ($nh, nk, nl$), Bragg's law is simplified to:

$$sin\,\theta = \frac{\lambda}{2d_{hkl}} \qquad (1\text{-}3)$$

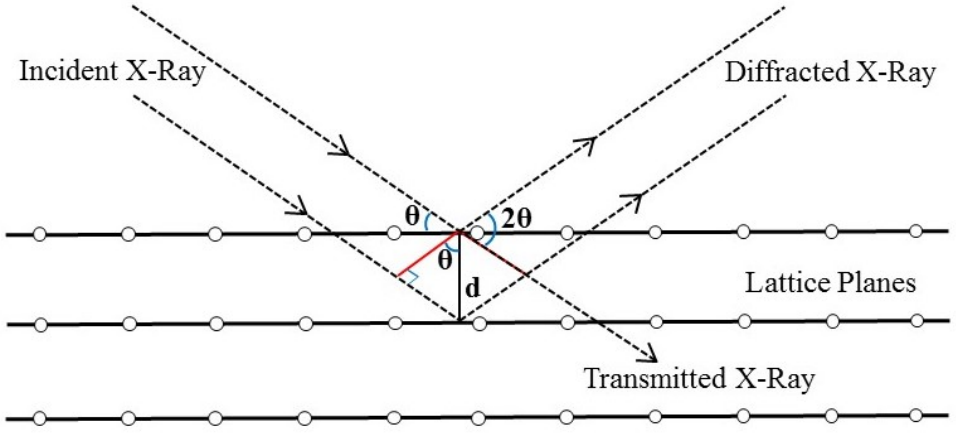


**Figure 1-9.** Diffraction of X-ray diffraction from the lattice plane

#### 1.5.1.1 Powder X-ray Diffraction

Powder XRD is a nondestructive method for qualitative and quantitative analysis of solid-state samples. It is also possible to determine crystal structures from powder XRD, usually when good models are known, but in general this is more easily done with single-crystal XRD. In this thesis, the powder diffractometer used is equipped with a curved position-sensitive (CPS) detector, which provides the advantage of collecting the entire XRD pattern at once rather than having to scan through an angular range. The sample is ground to fine powder and placed on a rotating holder to randomize particle orientations. The XRD pattern is a plot of the intensities of diffraction peaks (in counts per second) as a function of angle $2\theta$ (usually between 10 and 90°). For phase identifications, the experimental patterns are compared with simulated patterns of known phases, created using crystallographic data available in Pearson's Crystal Data[18] and plotted using PowderCell 2.4.[35] A sample XRD pattern is shown in **Figure 1-10**. If new phases are identified, their unit cell parameters are refined using Unit Cell.[36]

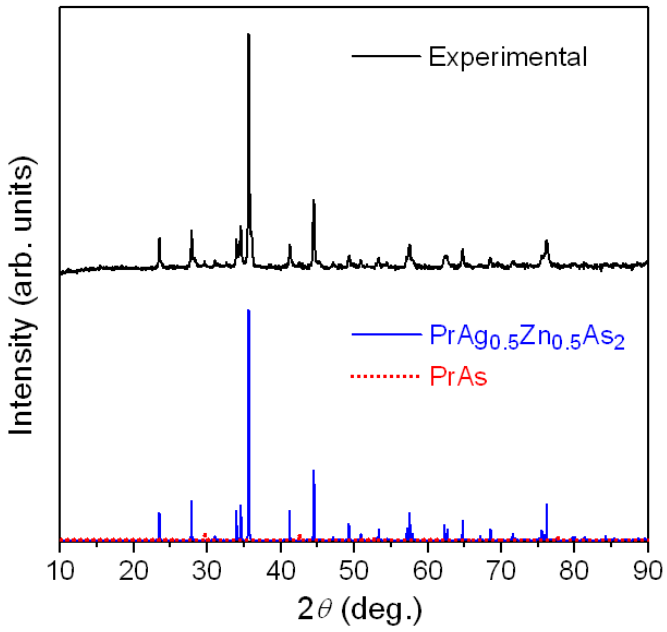


**Figure 1-10.** Experimental (top) and simulated powder patterns (bottom) of $PrAg_{0.5}Zn_{0.5}As_2$ along with PrAs impurity.

#### 1.5.1.2 Single-crystal X-ray Diffraction

Single-crystal XRD is invaluable for determining crystal structures. Only a brief overview is provided here; full details are available in many resources and textbooks.[38-40]

Prior to collecting single-crystal XRD data, it is advisable to confirm the chemical composition of the crystal (through EDX analysis) to avoid duplicating known structures. Ideally, the same crystal examined by EDX analysis is selected, cut into an appropriate size (<0.5 mm) if necessary, and then mounted on a glass fiber attached to a brass pin. The crystal is placed on a goniometer on a Bruker PLATFORM diffractometer equipped with a SMART APEX II CCD area detector and a Mo $K_\alpha$ radiation source. Typically, a full dataset is collected with $\omega$ scans at 4–8 different $\phi$ angles with a frame width of 0.3° and an

exposure time of 10–20 s per frame depending on the quality of the crystal. Because the compounds examined in this thesis contain many heavy elements, it is important to measure the faces and dimensions of the crystal to apply absorption corrections later.

Data reduction and integration were performed using the program SAINT. A numerical face-indexed absorption correction was applied with the use of SADABS. Solving a crystal structure used to be the most challenging step, but modern programs, such as those in the SHELXTL program package,[41] have now made this relatively routine. Nevertheless, solid-state compounds can still offer many pitfalls. In particular, care must be taken to select the correct space group, through inspection of systematic absences and intensity symmetry. If a compound is suspected to adopt a known structure type, a model is available as a starting point. Otherwise, for unknown structures, direct methods work well to locate initial atomic positions.

Through least-squares refinements, the model is improved to give more accurate positions and displacement parameters. Occupancies of atomic sites may also need to be refined. The objective of refinement is to minimize the sum of the squares of the deviations between the observed and calculated intensities. A structure refinement is generally considered to be acceptable when the residual (*R*-value) is less than 0.10 and the goodness-of-fit (*S*) is close to 1.[39,40] For ease of comparison to other structures, it is useful to standardize the atomic coordinates, with the use of STRUCTURE TIDY.[42]

### 1.5.2 Energy Dispersive X-ray (EDX) Analysis

EDX analysis is a non-destructive technique for determining chemical composition. A sample is examined within a JEOL JSM-6010 LA scanning electron microscope. A high-energy electron beam is directed toward a smooth, clean surface of the sample, several processes can happen. The relevant process in EDX is that core-shell electrons of atoms are ionized, leaving a hole, which is subsequently filled by electrons in higher levels. In the course of this relaxation, X-rays are emitted with a wavelength and energy characteristic of the element (**Figure 1-11**). An EDX spectrum is a plot of intensity as a function of energy. Identifying the energy of characteristic X-rays provides a means of qualitative analysis, and measuring the relative intensities of X-ray peaks provides a means of quantitative analysis.

The relative amount of a given element is typically measured to an accuracy of ~5 mole %. The uncertainties in EDX analysis arise from how X-rays are detected and how intensities are processed. Besides emission peaks, the X-ray spectrum may contain internal fluorescence peaks, escape peaks, and sum peaks. The main problem is that the interaction of the electron beam with the sample depends on the composition. These matrix effects require correction for atomic number $Z$, absorption $A$, and fluorescence $F$.[43]

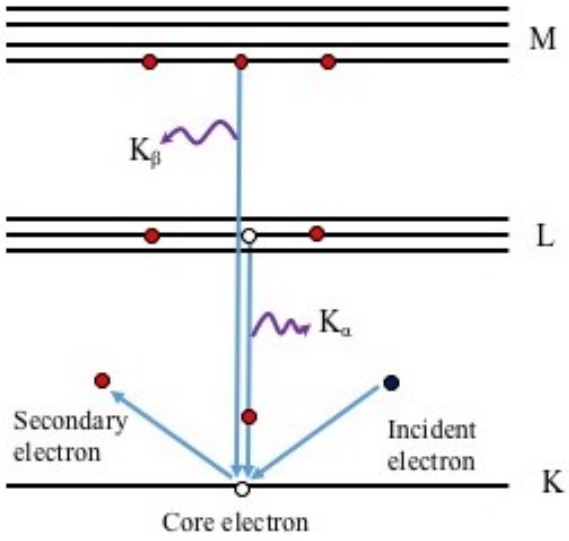


**Figure 1-11.** Emission of characteristic X-rays in which an incident electron ejects a core electron and the resulting vacancy is filled by a higher level electron.

## 1.6 Physical Properties

It is important to measure the physical properties of a newly synthesized material to gain an understanding of electronic structure, evaluate the potential for applications such as thermoelectric, semiconducting, and ferromagnetic materials, and develop relationships between structure and properties.

### 1.6.1 Electrical Properties

The electrical properties of an extended solid originate from the electronic structure, which must be described in terms of energy continua called bands. Just as atomic orbitals overlap to form molecular orbitals in discrete molecules, so too do they combine to form Bloch functions in solids, as discussed later.

Electrical resistivity (in units of Ω·cm) is measured through a four-probe technique (**Figure 1-12**) in which leads are attached to a sample:

$$\rho = \frac{VA}{Il} \qquad (1\text{-}4)$$

where $V$ is the applied voltage across the two inner leads, $I$ is the current applied between two terminal leads, $A$ is the cross-sectional area, and $l$ is the length (**Figure 1-12**). The advantage of a four-probe configuration is that it eliminates the effect of contact resistance that would otherwise need to be corrected in a two-probe configuration.

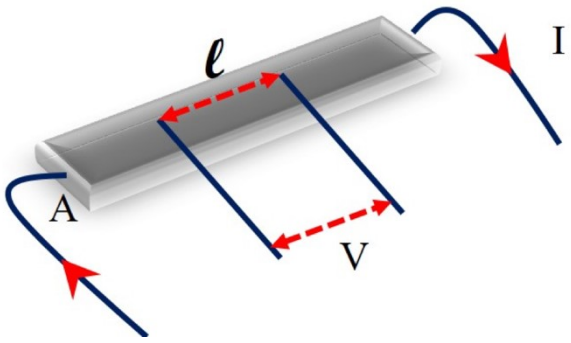


**Figure 1-12.** The four-probe measurement for resistivity measurement

The electrical resistivity was measured on a large single crystal (~1 mm) to avoid grain boundary problems associated with powder samples. The crystals are mounted to four graphite fibers with Ag paint attached to gold wires which are already connected on a holder. The electrical resistivity is then measured as a function of temperature (typically 2 and 300 K) on a Quantum Design Physical Property Measurement System.

The temperature dependence of the electrical resistivity can fall into three basic categories: metallic, semiconducting, and superconducting **Figure 1-13**. In a metal, there is no energy gap in the electronic density of states and the motion of conduction electrons becomes increasingly impeded through scattering by lattice vibrations at higher temperature; thus, the resistivity (inverse of conductivity) rises at higher temperature. At very low temperatures, the resistivity attains a limiting value determined by the concentration of defects in the sample. In a semiconductor, there is a small energy gap (<3 eV) and electrical conduction is conveyed by electrons that have been thermally excited across this gap; the concentration of conduction electrons increases at higher temperature and thus the resistivity decreases at higher temperature. In a superconductor, the behaviour is initially like a metal, but below a transition temperature, the resistivity vanishes and goes to zero.

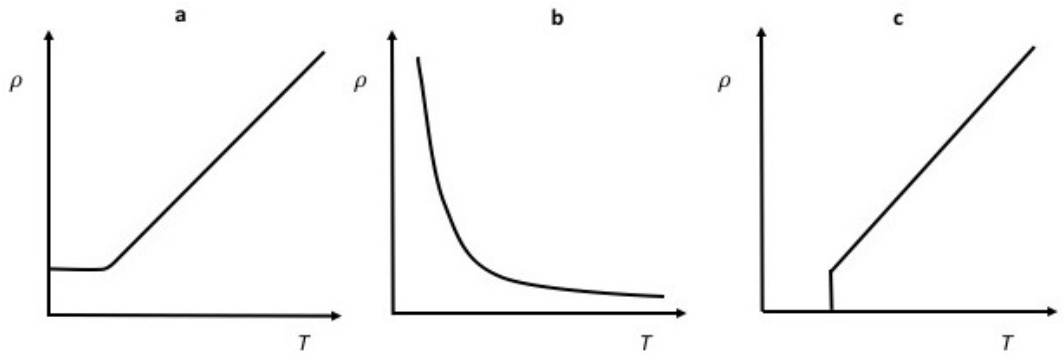


**Figure 1-13.** Relationship of resistivity ($\rho$) vs. temperature ($T$) in (a) metal; (b) semiconductor; and (c) superconductor.

In principle, many of the polyanionic phosphides and arsenides discussed in this thesis can be considered to be Zintl phases, which are expected to be semiconducting, whereas the metal-rich phases will no doubt exhibit metallic behaviour. However, these predictions need to be confirmed by experiment, and it is not so clear whether the electronegativity difference in the polyanionic compounds is large enough to create a band gap.

In some cases, when magnetic ordering occurs, the temperature dependence of resistivity can be affected if there is strong interaction between the conduction electrons and the spins of the magnetically active species. A related phenomenon is the Kondo effect, often found in Ce-containing intermetallics, in which the resistivity reaches a local minimum at some temperature. Here the localized spins from impurities interact with conduction electrons, leading to resonant scattering of the conduction electrons and thus increasing resistivity.[44]

### 1.6.2 Magnetism

Magnetic properties originate from the spins of unpaired electrons, which could be localized on atoms or delocalized on the conduction electrons within the entire solid. The basic ideas are discussed here, but more details can be found elsewhere.[1,62,63] Compounds containing rare-earth or transition-metal atoms or metal-rich phases such as those described in this thesis can thus exhibit diverse magnetic behaviour depending on the ways that these electrons interact.

Magnetic measurements, which must be made on phase-pure samples, were performed on Quantum Design PPMS system. Typically, ~50 mg (more if the magnetic response is weak) of a finely powdered sample are placed in a gelatin capsule, which in turn is placed in a plastic straw. The sample is centred in the magnetometer using ac and dc magnetization modes. When the sample is subjected to an external magnetic field (*H*), the magnetic response or magnetization (*M*) is measured, and the magnetic susceptibility is evaluated as the ratio:

$$\chi = \frac{M}{H} \qquad (1\text{-}5)$$

The most common measurements are the temperature dependence of the magnetization at constant field and the field dependence of the magnetization at constant temperature. (It is also possible to measure the frequency dependence of the magnetization to probe spin dynamics.)

For a free atom or ion, the effective magnetic moment (in Bohr magnetons, $\mu_B$) is given by:

$$\mu_{eff} = g_J\sqrt{J(J+1)} \qquad (1\text{-}6)$$

where *J* is the total angular momentum quantum number and $g_J$ is Landé factor:

$$g_J = g_L \frac{J(J+1)-S(S+1)+L(L+1)}{2J(J+1)} + g_S \frac{J(J+1)+S(S+1)-L(L+1)}{2J(J+1)} \qquad (1\text{-}7)$$

For a free electron, $g_s$ has a value of 2 and from the definition of the gyromagnetic ratio, $g_L$ is 1. Then $g_J$ simplifies to:

$$g_J = \frac{3}{2} + \frac{S(S+1) - L(L+1)}{2J(J+1)} \quad (1\text{-}8)$$

For atoms containing *f* electrons, this general expression can be used, but for atoms containing *d* electrons, the orbital angular momentum is quenched and *J* can be replaced with *S* to result in the spin-only formula:

$$\mu_{eff} = 2.00\sqrt{S(S+1)} \quad (1\text{-}9)$$

For compounds containing more than one magnetic component, the total effective magnetic moment is given by:

$$\mu_{eff} = \sqrt{n_1\mu_1^2 + n_2\mu_2^2 + n_3\mu_3^2 + \cdots} \quad (1\text{-}10)$$

where $n_k$ is the stoichiometric ratio of each component.

When an external magnetic field is applied in a paramagnetic material, the magnetic moments become increasingly aligned as the temperature decreases overcoming the effects of thermal agitation. In contrast, long-range ordering of magnetic moments occurs in parallel or antiparallel fashion in ferromagnetic or antiferromagnetic materials, respectively, even in the absence of an external magnetic field. The temperature dependence of the magnetic susceptibility shows three basic kinds of behaviour **Figure 1-14**.

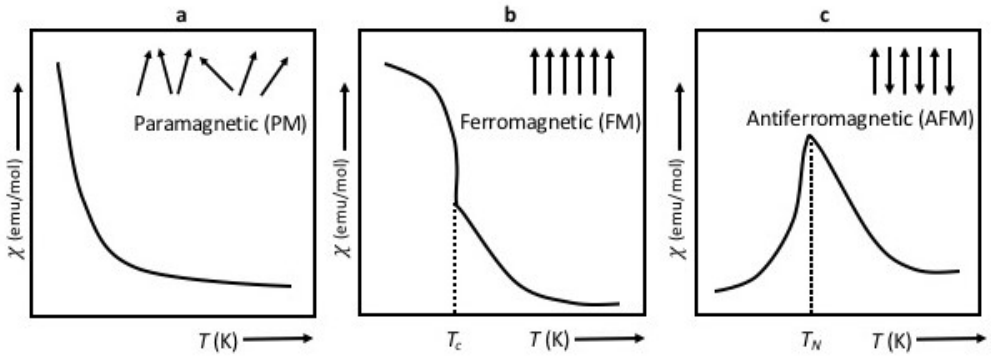


**Figure 1-14.** Temperature dependent magnetic susceptibility for (a) paramagnetism, (b) ferromagnetism, and (c) antiferromagnetism. (Inset: corresponding alignment of magnetic moments.)

A random arrangement of noninteracting magnetic moments gives rise to paramagnetism, which follows the Curie law:

$$\chi = \frac{C}{T} \qquad (1\text{-}11)$$

where $C$ is the Curie constant (in units of emu·K·mol$^{-1}$) and $T$ is the temperature (in units of K). The Curie constant can be obtained from the slope of a plot of the inverse susceptibility, which is linear and goes through the origin **Figure 1-15**.

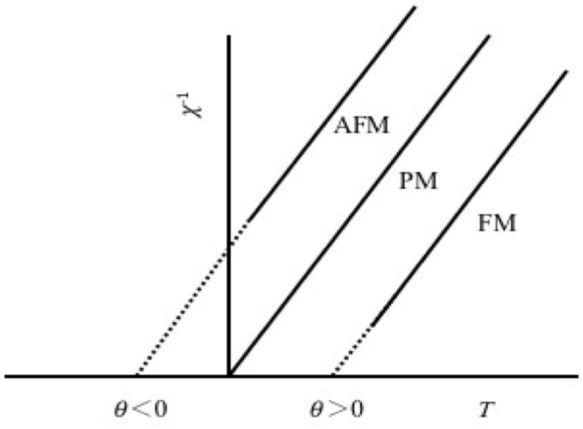


**Figure 1-15.** Inverse susceptibility with temperature in paramagnetic, ferromagnetic and antiferromagnetic materials.

From the Curie constant, the effective magnetic moment can be obtained:

$$\mu_{\text{eff}} = \sqrt{8C} \qquad (1\text{-}12)$$

In other cases, long-range magnetic ordering occurs when the magnetic moments spontaneously align in either a parallel or antiparallel fashion, below the Curie temperature $T_c$ in a ferromagnet or the Néel temperature $T_N$ in an antiferromagnet, respectively. In these cases, the plots of inverse susceptibility in the paramagnetic regime have a non-zero intercept with the *x*-axis. Fitting to the Curie-Weiss law:

$$\chi = \frac{C}{T-\theta_P} \quad \text{or by rearranging} \quad \chi^{-1} = \left(\frac{1}{C}\right)T - \frac{\theta_P}{C} \qquad (1\text{-}13)$$

allows the Curie constant $C$ and the Weiss constant $\theta_P$ to the evaluated. The sign of the Weiss constant is indicative of the type of coupling interaction, ferromagnetic or antiferromagnetic.

Usually magnetic measurements are performed under zero-field-cooled (ZFC) conditions, but it may be useful also to perform them under field-cooled (FC) conditions to characterize magnetic transition more carefully. A difference between ZFC and FC measurements implies an irreversibility in the transition. For example, in exotic materials like spin glasses, the magnetization may be higher under FC conditions because the magnetic moments are frozen.

## 1.7 Optical Diffuse Reflectance Spectroscopy

When light strikes a large flat surface, like that of a crystal, most of it is reflected specularly, like a mirror. In contrast, when light strikes an uneven surface or a collection of randomly oriented small particles, it is reflected back at all angles, a phenomenon called diffuse reflectance **Figure 1-16**.

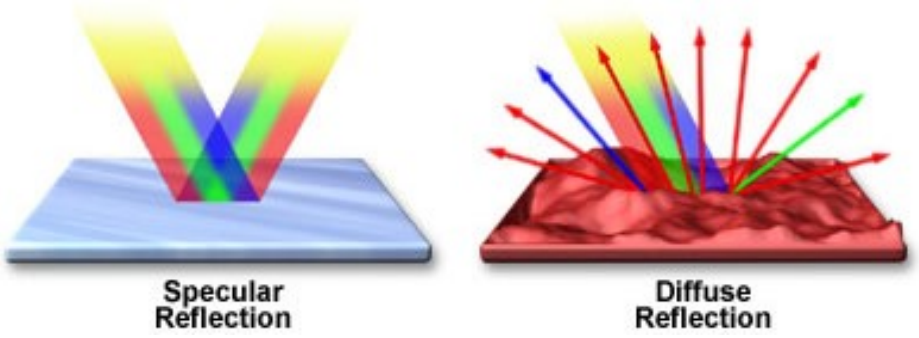


**Figure 1-16.** Difference in reflectance of light from smooth and rough surfaces.[45]

When particle sizes are very small, the scattered light has contributions from reflection, refraction, and diffraction, which cannot be separated. The theory of multiple scattering has been worked out by Kubelka and Munk,[46] and the essential equation is given by:

$$\frac{K}{S} = \frac{(1-R_\infty)^2}{2R_\infty} = F(R_\infty) \qquad (1\text{-}14)$$

where $R$ is the reflectance, $F(R_\infty)$ is the *remission* or *Kubelka-Munk (K-M)* function, $K$ is the absorption coefficient, and $S$ is the scattering coefficient of the sample.

Optical diffuse reflectance spectra reported in this thesis were carried out in the lab of Prof. J. Aitken (Duquesne University). They were measured on a Varian Cary 5000 UV-Vis-NIR spectrometer equipped with a Harrick Praying Mantis diffuse reflectance accessory. $BaSO_4$ was used as a 100% reflectance standard. Scans were made from 2500 to 200 nm at a rate of 600 nm/min generally. The percent reflectance was converted to absorbance through the Kubelka-Munk equation and the wavelength was converted to energy. The optical band gaps were estimated by extrapolating the absorption edge to the baseline.

Although the band gap can be obtained crudely by extrapolating the absorption edge, it is more properly extracted by fitting to an Urbach tail **Figure 1-17**, an exponential function given by:

$$\alpha = A \bullet e^{(E-E_g)/E_u} \qquad (1\text{-}15)$$

where $\alpha$ is absorption coefficient, $A$ is a constant, $E$ is the photon energy in eV, $E_g$ is the band gap, and $E_u$ is the Urbach energy.[47] This tail arises from disorder within the structure (e.g., defects) and fluctuations of bands due to lattice vibration.[48] When the logarithm of the absorption coefficient is plotted against photon energy, the linear region is fitted to:[49]

$$\alpha \propto A \cdot (E - E_g)^n \qquad (1\text{-}16)$$

where $A$ is a constant, $E$ is the photon energy in eV, and $E_g$ is the band gap. If the exponent $n$ is 1/2, the band gap is direct, meaning that the bottom of the conduction band is located at the same point in $k$-space as the top of the valence band, as manifested in a relatively sharp absorption edge. If the exponent $n$ is 2, the band gap is indirect, meaning that the bottom of the conduction band and the top of the valence band do not coincide at the same $k$-point, as manifested by a more gradual onset of the absorption edge.

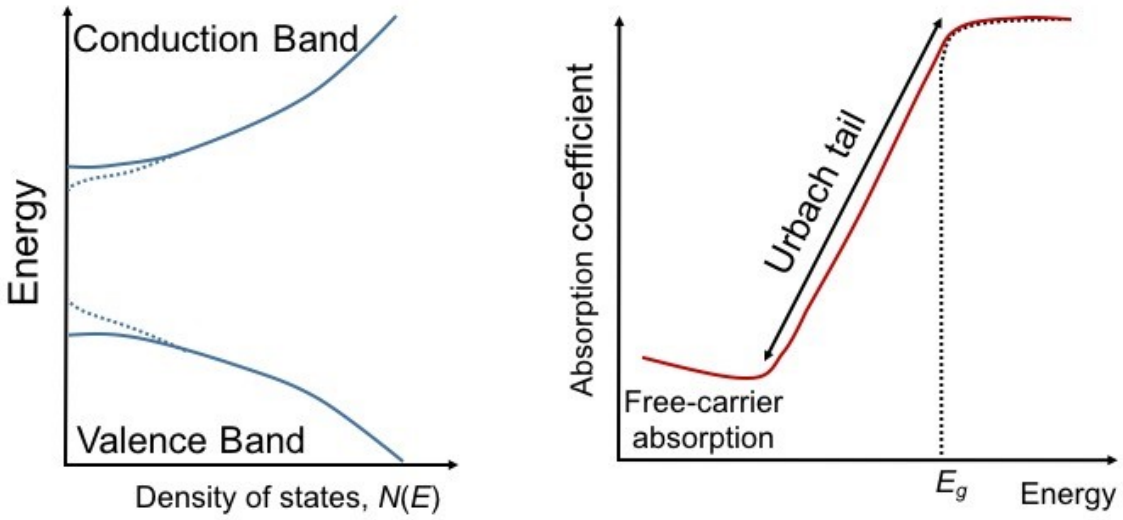


**Figure 1-17** A graphical representation of density of states showing narrowing of the band gap (dotted line) due to defects and lattice vibrations (left)[64], and the corresponding Urbach tail observed in the absorption spectra of a semiconductor (right).[65]

## 1.8 Band Structure Calculations

To evaluate bonding character, orbital interactions, and electrical properties, band structure calculations were performed. Unlike a molecule, in which few atoms interact to result in a finite number of energy levels in a molecular orbital diagram, an extended solid

contains many atoms which interact to form an infinite number of energy levels called bands. Although it appears tedious or impossible to calculate the electronic structure of a solid, the problem is considerably simplified by making several assumptions. Instead of treating all possible interactions between many electrons, each electron is assumed to move independently in an effective field created by the other electrons; that is, there is an effective one-particle Kohn-Sham equation which combines the Coulomb potential of nuclei, the Hartree potential, and the exchange-correlation potential.[50] Similar to molecules, atomic orbitals can be taken as basis functions $\chi_n$ and combine linearly in a solid.[51] The most important simplification takes advantage of the periodicity of crystalline materials. If the unit cell repeat is *a*, the permitted linear combinations of the basis functions that conform to the translational symmetry, called Bloch functions, are restricted to:

$$\psi_k = \sum_n e^{-ikna} \chi_n \qquad (1\text{-}17)$$

where the wavevector, *k*, is quantized and is restricted to the values in the range $-\frac{\pi}{a} \leq k \leq \frac{\pi}{a}$ called the first Brillouin zone.[51] A Bloch function is analogous to a molecular orbital involving the interaction of all atoms in the solid and is sometimes also called a "crystal orbital." A plot of the energies of $\psi_k$ vs. *k* is called a band dispersion diagram (**Figure 1-18**). The states are filled with electrons up to a highest energy level called the Fermi level. The *k* points are so closely spaced and numerous that these plots appear to be continuous. The number of states per energy increment is called the density of states (DOS). It is useful also to plot the atomic projections of the DOS, that is, the contribution of specified atoms to different parts of this curve. The bonding character for specified contacts in the structure

can be evaluated through a population analysis of the Bloch functions, resulting in plots of the crystal orbital overlap population (COOP).[51]

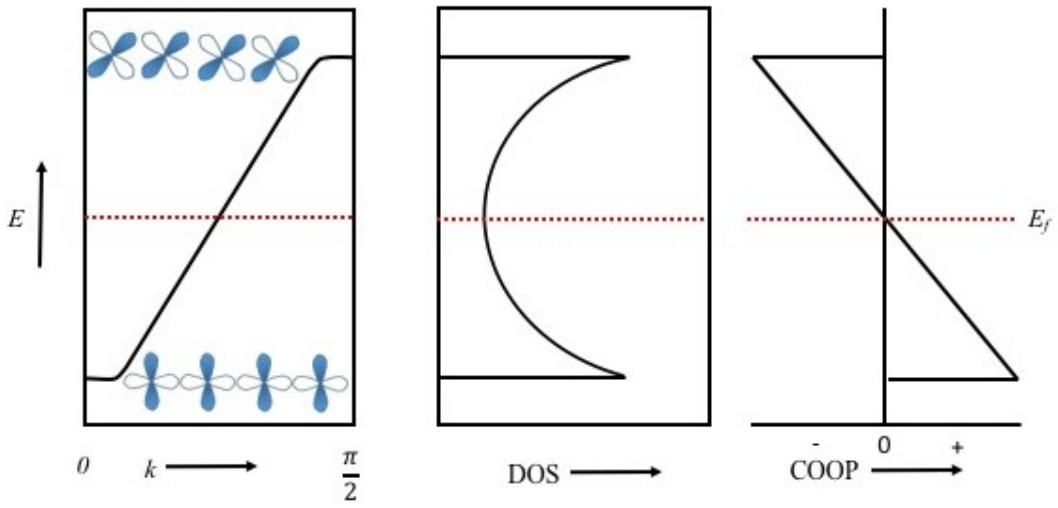


**Figure 1-18.** Graphical representations of the band structure, density of states (DOS), and crystal orbital overlap population (COOP) for the d orbitals in a 1D chain of equally spaced transition metal atoms.[51]

In this thesis, density functional calculations were performed using the Stuttgart tight-binding linear muffin-tin orbital (TB-LMTO) program, which makes two approximations. In the atomic spheres approximation (ASA), the Wigner-Seitz cell, which is a polyhedron constructed around each lattice point to represent a unit cell, is approximated as a spherical shape. The potential is constructed as a sum of the contributions of individual atoms modeled as spheres of specific radius but truncated near the nuclei to finite values (instead of approaching negative infinity), hence the name "muffin tin," and if neighbouring spheres do not overlap, empty spheres with zero potential must be included. In the local density approximation (LDA), the exchange correlation is simplified as a uniform electron gas, which is more easily calculated. In this program, the

COOP curve is replaced by a crystal orbital Hamiltonian populations (COHP) curve, in which the DOS is weighted by matrix elements of the Hamiltonian instead of the overlap integral. COOP is calculated as an average overall bonds in the unit cell, whereas the COHP curve involves the summation of bonds within the unit cell.

## 1.9 Motivation and Objectives

The primary goal of this thesis is to synthesize new quaternary phosphides and arsenides that are both metal-rich and pnicogen-rich and that incorporate rare-earth and transition metals. To date, there are relatively few of these compounds known. It is not obvious whether these compounds will satisfy normal valence rules because the electronegativity differences are not pronounced. Moreover, it is not clear under what conditions *M–M* or *Pn–Pn* bonding, or both, will occur in these compounds. Thus, detailed crystal structures must be determined and constitute a large body of the experimental work. Unlike molecular chemistry, the structures of extended inorganic solids are not easily predictable (which is why solid-state chemistry is so much more fun and exciting); structure determination is the most essential characterization technique. After examining these structures carefully, we hope to be able to discern recurring motifs that will allow us to express some general structural principles about these compounds.

A secondary goal of this thesis is to measure the electrical, magnetic, and optical properties of these quaternary phosphides and arsenides. The combination of rare-earth and transition metals in these compounds introduces the possibility for complex interactions between *f* and *d* electrons, occurring in either metallic or semiconducting materials. The phosphides and arsenides that are normal valence compounds are likely to exhibit small

band gaps, but this is by no means guaranteed or commonly validated experimentally. By relating these properties to the composition and structures of these compounds, we hope to be able to understand what factors need to be controlled to modify the properties.

Although not an explicit goal of this thesis, a potentially useful outcome of this work is that these phosphides and arsenides may be attractive candidates for applications in thermoelectric materials. Some related ternary phosphides and arsenides, especially those with the $CaAl_2Si_2$-type structure, have been implicated as promising thermoelectric materials. Extension to quaternary phosphides and arsenides provides more flexibility to control properties.

## 1.10 References


1. West, A. R., *Solid State Chemsitry and its Applications*, 2nd Ed., Wiley: United Kingdom, 2014.
2. Castillo-Ojeda, R.; Díaz-Reyes, J.; Galván-Arellano, M.; Peña-Sierra, R. *Advanced Material Research* **2014***, 976*, 25-29.
3. Hudl, M.; Campanini, D.; Caron, L.; Höglin, V.; Sahlberg, M.; Nordblad, P.; Rydh, A. *Phys. Rev. B* **2014**, *90***,** 144432 (1-5).
4. Saparov, B.; Mitchell, J.; Sefat, A. *Supercond. Sci. Technol.* **2012**, *25,* 084016 (1-10).
5. Spitzer, D. P.; Castellion, G. A.; Haacke, G. *J. Appl. Phys.* **1966**, *37*, 3795-3801.
6. Oyama; S. T.; Gott, T.; Zhao, H.; Lee, Y. K. *Catal. Today* **2009**, *143*, 94-107.
7. Oyama; S. T. *J. Catal* **2003**, *216*, 343-352.
8. Chen, J.; Zhou, S.; Ci, D.; Zhang, J.; Wang, R.; Zhang, *J. Ind. Eng. Chem. Res.* **2009**, *48*, 3812-3819.
9. Liu, X.; Chen, J.; Zhang, *J. Catal. Commun.* **2007**, *8*, 1905-1909.
10. Chen, J.; Han, M.; Zhao, S.; Pan, Z.; Zhang, Z. *Catal. Sci. Technol.* **2016**, DOI**:**10.1039/C5CY01751C.
11. Habas, S. E.; Baddour, F. G.; Ruddy, D. A.; Nash, C. P.; Wang, J.; Pan, M.; Hensley, J. E.; Schaidle, J. A. *Chem. Mater.* **2015**, *27*, 7580−7592.

12. Pfeiffer, H.; Tancret, F.; Brousse; T. *Mater. Chem. Phys.* **2005**, *92*, 534-539.

13. Stern, L.; Feng, L.; Song, F.; Hu, X.; *Energy Environ. Sci.* **2015**, *8*, 2347--2351.

14. Zhou, A.; Yang, B.; Wang, W.; Dai, X.; Zhao, M.; Xue, J.; Han, M.; Fan, C.; Li, J. *RSC Adv.* **2016**, *6*, 26800–26808.

15. Boyanov, S.; Bernardi, J.; Gillot, F.; Dupont, L.; Womes, M.; Tarascon, J. M.; Monconduit, L.; Doublet, M. L. *Chem. Mater.* **2006**, *18*, 3531-3538.

16. Tegus, O.; Brück, E.; Buschow, K.H.J.; de Boer, F.R. *Nature* **2002**, *415*, 150-152.

17. Ren, Z. -A.; Che, G. -C.; Dong, X. -L.; Yang, J.; Lu., W.; Yi., W.; Shen, X. -L.; Li, Z. -C.; Sun, L. -L.; Zhou, F. *Europhys. Lett.* **2008**, *83*, 17002.

18. Villars, P.; Cenzual, K. Pearson's Crystal Data - Crystal Structure Database for Inorganic Compounds, Release 2015/16, ASM international, Materials Park, Ohio, USA.

19. Jeitschko, W.; Glaum, R.; Boonk; L. *J. Solid State Chem*. **1987**, *69*; 93-100.

20. Guo, Q.; Pan, B. J.; Yu, J.; Ruan, B. B.; Chen, D. Y.; Wang, X. C.; Mu, Q. G.; Chen, G. F.; Ren, Z. A. *Sci. Bull.* **2016**, DOI 10.1007/s11434-016-1080-4.

21. Qi, Y.; Gao, Z.; Wang, L.; Wang, D.; Zhang, X.; Ma, Y. *New J. Phys.* **2008**, *10*, 123003 (1-6).

22. Gascoin, F.; Ottensmann, S.; Stark, D.; Haile, S. M.; Snyder, G. J. *Adv. Funct. Mater.* **2005**, *15*, 1860.

23. Yu, C.; Zhu T. J.; Zhang, S. N.; Zhao, X. B.; He, J.; Su, Z.; Tritt, T. M. *J. Appl. Phys.* **2008**, *104*, 013705.

24. Wang, X. J.; Tang, M. B.; Chen, H. H.; Yang, X. X.; Zhao, J. T.; Burkhardt, U.; Grin, Y. *Appl. Phys. Lett*. **2009**, *94*, 092106.

25. Ponnambalam, V.; Lindsey, S.; Xie, W.; Thompson, D.; Drymiotis, F.; Tritt, T. T. *J. Phys. D: Appl. Phys.* **2011**, *44*, 155406.

26. Müller, U. *Inorganic Structural Chemistry*, 2nd Ed.; Wiley: *Cheichester*, 2007.

27. Kauzlarich, S. M., Ed. *Chemistry, Structure, and Bonding of Zintl Phases and Ions*; VCH Publishers: New York, 1996.

28. Rundqvist, S.; Jellinek, F. *Acta. Chem. Scand.* **1959**, *13*, 425-432.

29. Rundqvist, S. *Acta. Chem. Scand.* **1962**, *16*, 287-292.

30. Grosvenor, A. P.; Wik, S. D.; Cavell, R. G.; Mar, A. *Inorg. CHem.* **2005**, *44*, 8988-8998.

31. Hönle, W.; Von Schnering, H. G. *Z. Anorg. Allg. Chem.* **1979**, *34*, 194-206.

32. Iandelli, A.; Franceschi, E. A. **1973**, *30*, 211-216.

33. Bauer, G.; Zintl E. *Z. Phys. Chem.*, *Abt. B* **1937**, *37*, 323-352.

34. Bhella, S. S.; Shafi, S. P.; Trobec, F.; Bieringer, M.; Thangadurai, V. *Inorg. Chem.*, **2010**, *49*, 1699–1704.

35. Kraus, W., Nolze, G. *J. Appl. Cryst.***1996**, *29*, 301-303.

36. Holland, T. J. B.; Redfern, S. A. T. *Mineral. Mag.* **1997**, *61*, 65-77.

37. Diamond - Crystal and Molecular Structure Visualization Crystal Impact - Dr. H. Putz & Dr. K. Brandenburg GbR, Kreuzherrenstr. 102, 53227 Bonn, Germany <http://www.crystalimpact.com/diamond>.

38. Clegg, W. *Crystal Structure Determination;* Oxford University Press: Oxford, 1998.

39. Giacovazzo, C. *Fundamentals of Crystallography,* 3rd Ed. Oxford University Press: Oxford, 1992.

40. Massa, W. *Crystal Structure Determination,* 2nd Ed. Springer-Verlag: Berlin, 2004.

41. Sheldrick, G. M. SHELXTL. *Bruker AXS Inc.: Madison, WI* **2001***, 6.12*.

42. Gelato, L. M.; Parthé, E. *J. Appl. Crystallogr.* **1987***, 20*, 139-143.

43. Australian Microscopy and Microanalysis Research Facility 2014, accessed 17 June, 2016 <http://www.ammrf.org.au/myscope/sem/introduction/>.

44. Kondo, J. Kondo Effect. *Progr. Theoret. Phys.* **1964***, 32*, 37.

45. Abramowitz, M.; Sutter, R. T.; Davidson, M. W., accessed 5 May 2016 <http://www.olympusmicro.com/primer/java/reflection/specular/>.

46. Kubelka, P.; Munk, F. *Z. Techn. Physik.* **1931***, 12*, 593.

47. Urbach, F. *Phys. Rev.* **1953***, 92*, 1324.

48. Yacobi, B. G. *Semiconductor Materials: An Introduction to Basic Principles*. Springer US: Boston, MA, 2003.

49. Naumkin, A. V.; Kraut-Vass, A.; Gaarenstroom, S. W.; Powell, C. J. NIST X-ray Photoelectron Spectroscopy Database, accessed 5 May, 2016, <http://srdata.nist.gov/xps/>.

50. Dronkowski, R. *Computational Chemistry of Solid State Materials;* Wiley-VCH: Weinheim: 2005.

51. Hoffmann, R. *Angew. Chem. Int. Ed. Engl.* **1987***, 26*, 846-878.

52. Anderson, O. K. *Phys. Rev. B: Condens. Matter* **1975***, 12*, 3060-3083.

53. Ackermann, J.; Wold, A. *J. Phys. Chem. Solids* **1977**, *38*, 1013-1016.

54. Ono, S.; Despault, G. J. G.; Calvert, L. D.; Taylor, J. B. *J. Less-Common Met.* **1970**, *22*, 51-59.

55. Wang, M.; Mar, A. *Acta Crystallogr. C* **2000**, *56*, 138-139.

56. Senko, M. E.; Dunn, H. M.; Weidenborner, J. E.; Cole, H. *Acta Crystallogr.* **1959**, *12*, 76.

57. Jeitschko, W.; Moller, M. H. *Acta Crystallogr. B* **1979**, *35*, 573-579.

58. Trezbiatowski, W.; Lukaszewicz, K; Weglowski, S. *Acta Crystallogr.* **1957**, *10*, 792-793.

59. Furuseth, S.; Kjekshus, A. *Acta Crystallogr.* **1965**, *18*, 320-324.

60. Von Schnering, H. G.; Wichelhaus, W.; Wittmann, M.; Weber, H. P.; Peters, K. *Z. Kristallogr. - New Cryst. Struct.* **1998**, *213*, 460.

61. Chykhrij, S. I.; Kuz'ma, Y. B.; Oryshchyn, S. V. *Dopov. Akad. Nauk Ukr. RSR, Ser. B* **1989**, *3*, 60-62.

62. Martin, D. H. *Magnetism in Solids*, M. I. T. Press, Cambridge, 1967.

63. Kittel, C. *Introduction to Solid State Physics* 8th Ed, John Wiley & Sons, Hoboken, 2005.

64. Malinauskas, M.; Danilecius, P.; Juodkazis, S. *Opt. Express* **2011**, *19*, 5602-5610.

65. Schubert, E. F. *Light-Emitting Diodes* 2nd Ed., Cambridge University Press, Cambridge, 2006.

# Chapter 2

## Rare-Earth Manganese Copper Pnictides $RE_2Mn_3Cu_9Pn_7$ (*Pn* = P, As): Quaternary Ordered Variants of the $Zr_2Fe_{12}P_7$-Type Structure

*A version of this chapter has been published. Stoyko, S. S.; Ramachandran, K. K.; Mullen, C. S.; Mar, A. Inorg. Chem., 2015, 54, 860-866*

### 2.1 Introduction

Among ternary rare-earth transition-metal pnictides *RE–M–Pn*, there are numerous metal-rich phases that have a composition in which the metal-to-nonmetal ratio is close or equal to 2:1. They belong to a homologous series of hexagonal structures with the general formula $RE_{n(n-1)}M_{(n+1)(n+2)}Pn_{n(n+1)+1}$ featuring assemblies constructed from a rapidly expanding number ($n^2$) of triangular units as $n$ is incremented.[1] The first four members correspond to the $Fe_2P$ ($n$ = 1), $Zr_2Fe_{12}P_7$ ($n$ = 2), $Zr_6Ni_{20}P_{13}$ ($n$ = 3), and $(La,Ce)_{12}Rh_{30}P_{21}$ ($n$ = 4) structure types. The $Zr_2Fe_{12}P_7$ family has many representatives among phosphides $RE_2M_{12}P_7$ ($M$ = Mn,[2] Fe,[3–5] Co,[3,6–8] Ni [3,6,9–12]) and, to a lesser extent, arsenides $RE_2M_{12}As_7$ ($M$ = Co,[13] Ni [3,13–17]). The *RE* component generally spans through nearly all possible 4f substituents (apart from Pm, and curiously, La), as well as Sc and Y. Actinide representatives containing U or Th are also known.[2,18–20] The *M* component in these $Zr_2Fe_{12}P_7$-type phases is restricted to first-row transition metals, but there do exist a few examples containing second-row transition metals, $RE_2Rh_{12}Pn_7$ (*Pn* = P, As)[21] and $Eu_2Pd_{12}As_7$,[12] which adopt the closely related $Ho_2Rh_{12}As_7$-type structure. The magnetic

properties measured for these compounds are diverse, with some exhibiting complicated ferromagnetic and antiferromagnetic ordering arrangements.[22–27]

A common strategy for designing new solid-state structures is to take advantage of the different sizes and coordination preferences of metals to occupy available sites. In this regard, ternary $Zr_2Fe_{12}P_7$-type pnictides serve as attractive candidates as host structures amenable to ordered substitution by more than one metal component. Of the four Fe sites (each of threefold multiplicity) in this structure, three of them are coordinated by pnicogen atoms in a tetrahedral geometry (CN4) whereas the fourth is coordinated in a square pyramidal geometry (CN5). Thus, in $Sc_2Fe_{12}P_7$, the Fe atoms in this CN5 site can be partially replaced with excess Sc atoms, leading to the preparation of $Sc_2(Sc_{1.6}Fe_{1.4})Fe_9P_7$ or $Sc_{3.6}Fe_{10.4}P_7$.[28] Similarly, $Yb_2(Yb_{2.6}Pd_{0.4})Pd_9P_7$ or $Yb_{4.6}Pd_{9.4}P_7$ can be regarded as being derived from a hypothetical parent compound "$Yb_2Pd_{12}P_7$" with Yb atoms partially replacing some of the Pd atoms in this site.[29] A complete substitution of Sc for Pt atoms is achieved in the silicide $Sc_2Sc_3Pt_9Si_7$ or $Sc_5Pt_9Si_7$.[30] In view of these examples which illustrate the flexibility of this structure type, it would seem possible to target the preparation of quaternary phases in which two different transition elements order within these metal sites. Following this thought, Dhahri has reported the preparation of quaternary phases $RE_2M_3M'_9Pn_7$ (*RE* = Gd, Er; *M* = Cr, W; *M′* = Fe, Co; *Pn* = P, As), providing cell parameters but no full structure determination to confirm the metal ordering.[31]

This chapter presents the synthesis of twelve new quaternary pnictides $RE_2Mn_3Cu_9Pn_7$ (*Pn* = P, As) adopting the $Zr_2Fe_{12}P_7$-type structure. Crystal structures for all members were determined to give the first definitive evidence for metal ordering within

the four transition-metal sites and to enable systematic trends to be discerned. Chemical bonding was analyzed through band structure calculations on $La_2Mn_3Cu_9P_7$. Preliminary electrical resistivity measurements were made on one member, $Ce_2Mn_3Cu_9P_7$.

## 2.2 Experimental

### 2.2.1 Synthesis

Starting materials were freshly filed *RE* pieces (99.9%, all from Hefa, except Sm, from Alfa-Aesar), Mn powder (99.6%, Alfa-Aesar), Cu powder (99.8%, Alfa-Aesar), red P powder (99.9%, Alfa-Aesar), and As lumps (99.999%, Alfa-Aesar). Stoichiometric mixtures of the elements on a 0.3-g scale were loaded into fused-silica tubes which were evacuated and sealed, and then heated at 800 °C for 2 weeks. Although the title compounds were obtained in powder form after this initial heat treatment, crystal growth could be promoted by regrinding and reheating the resulting powders in the presence of about 30 mg $I_2$ as a mineralizer at 800 °C for 10 d, followed by cooling to room temperature over 1 d. The products were analyzed by powder X-ray diffraction (XRD) patterns collected on an Inel diffractometer equipped with a curved position-sensitive detector (CPS 120) and a Cu $K\alpha_1$ radiation source. Generally, the title compounds constitute >80% of the product. The extent of *RE* substitution is broader for the phosphides $RE_2Mn_3Cu_9P_7$ (*RE* = La–Nd, Sm, Gd–Dy) than the arsenides $RE_2Mn_3Cu_9As_7$ (*RE* = La–Nd). Under these synthetic conditions, extension to further *RE* members was unsuccessful. The compositions of needle-shaped grey crystals were determined by energy-dispersive X-ray (EDX) analysis

with a Zeiss EVO MA 15 scanning electron microscope and are in good agreement with expectations (**Table 2-1**).

**Table 2-1.** EDX analyses of $RE_2Mn_3Cu_9Pn_7$ crystals[a]

| compound | no. of spectra | at. % *RE* | at. % Mn | at. % Cu | at. % *Pn* |
|---|---|---|---|---|---|
| $La_2Mn_3Cu_9P_7$ | 3 | 9(1) | 10(4) | 43(1) | 38(4) |
| $Ce_2Mn_3Cu_9P_7$ | 5 | 10(1) | 13(1) | 42(1) | 36(2) |
| $Pr_2Mn_3Cu_9P_7$ | 5 | 10(1) | 14(1) | 40(3) | 36(3) |
| $Nd_2Mn_3Cu_9P_7$ | 5 | 9(1) | 14(1) | 38(5) | 39(6) |
| $Sm_2Mn_3Cu_9P_7$ | 5 | 10(1) | 14(3) | 40(3) | 36(3) |
| $Gd_2Mn_3Cu_9P_7$ | 5 | 10(1) | 11(3) | 42(1) | 36(3) |
| $Tb_2Mn_3Cu_9P_7$ | 5 | 10(1) | 12(2) | 44(1) | 34(1) |
| $Dy_2Mn_3Cu_9P_7$ | 6 | 12(2) | 10(4) | 45(2) | 34(1) |
| $La_2Mn_3Cu_9As_7$ | 6 | 10(1) | 13(2) | 44(1) | 33(1) |
| $Ce_2Mn_3Cu_9As_7$ | 3 | 10(1) | 13(1) | 45(2) | 31(2) |
| $Pr_2Mn_3Cu_9As_7$ | 6 | 10(1) | 13(1) | 45(2) | 32(2) |
| $La_2Mn_3Cu_9As_7$ | 5 | 10(1) | 14(1) | 45(2) | 31(2) |

[a] Expected composition is 10% *RE*, 14% Mn, 43% Cu, and 33% *Pn*.

### 2.2.2 Structure Determination

Suitable crystals for all $RE_2Mn_3Cu_9Pn_7$ compounds were available. Intensity data were collected at 173 K on a Bruker PLATFORM diffractometer equipped with a SMART APEX II CCD area detector and a Mo $K\alpha$ radiation source, using $\omega$ scans at 4–8 different $\phi$ angles with a frame width of 0.3° and an exposure time of 15 or 20 s per frame. Face-

indexed numerical absorption corrections were applied. Structure solution and refinement were carried out with use of the SHELXTL (version 6.12) program package.[32]

The problem of choosing between the centrosymmetric space group $P6_3/m$ vs. the noncentrosymmetric space group $P\bar{6}$ for $Zr_2Fe_{12}P_7$-type structures has been well documented.[20] In the centrosymmetric model, pnicogen atoms are placed within 2*a* sites (0, 0, ±1/4), which must be half-occupied to preclude unphysically short *Pn*–*Pn* distances along the *c*-direction. In the noncentrosymmetric model, these sites become nonequivalent (1*a* (0, 0, 0); 1*b* (0, 0, ½)) so that one set can be fully occupied while the other remains empty. The centrosymmetric model thus represents an average structure, equivalent to the superposition of multiple domains of the noncentrosymmetric model. The consensus has been to refine $Zr_2Fe_{12}P_7$-type structures in $P\bar{6}$. Initial positions were taken from the structure of $Zr_2Fe_{12}P_7$ itself.[33] Atomic coordinates were standardized with use of the program STRUCTURE TIDY[34] and atom numbering was chosen to conform to literature precedent (i.e., the four Fe atoms in $Zr_2Fe_{12}P_7$ are labeled as *M*1, *M*2, *M*3 in the CN4 sites and *M*4 in the CN5 site). Refinements were performed in which each of these four sites could be occupied by a mixture of Cu and Mn atoms. For example, in $La_2Mn_3Cu_9P_7$, the occupancies converged to 0.97(3) Cu / 0.03(3) Mn in *M*1, 1.00(3) Cu / 0.00(3) Mn in *M*2, 0.93(2) Cu / 0.07(2) Mn in *M*3, and 0.11(3) Cu / 0.91(2) Mn in *M*4, with reasonable displacement parameters for all sites. The results indicate a clear preference for Cu atoms in the CN4 sites and Mn atoms in the CN5 site, although we cannot completely discount the possibility that some Cu atoms partially disorder into the latter site. Nevertheless, the evidence seems to support strong ordering of the Cu and Mn atoms, and for simplicity we

consider only this fully ordered model in the final refinements. A Flack parameter is introduced into these refinements in $P\bar{6}$ and can be interpreted as the fractional contribution of one twin component in these crystals, assumed to be racemic twins.

Full crystallographic details are provided in **Tables 2-2 to 2-9**. They are also available in the form of crystallographic information files (CIFs) as Supporting Information or may be obtained from Fachinformationszentrum Karlsruhe, Abt. PROKA, 76344 Eggenstein-Leopoldshafen, Germany (CSD-425296 to 425307).

**Table 2-2.** Crystallographic Data for $RE_2Mn_3Cu_9P_7$ ($RE$ = La–Nd, Sm, Gd–Dy)

| formula | $La_2Mn_3Cu_9P_7$ | $Ce_2Mn_3Cu_9P_7$ | $Pr_2Mn_3Cu_9P_7$ | $Nd_2Mn_3Cu_9P_7$ | $Sm_2Mn_3Cu_9P_7$ | $Gd_2Mn_3Cu_9P_7$ | $Tb_2Mn_3Cu_9P_7$ | $Dy_2Mn_3Cu_9P_7$ |
|---|---|---|---|---|---|---|---|---|
| formula mass (amu) | 1231.29 | 1233.71 | 1235.29 | 1241.95 | 1254.17 | 1267.97 | 1271.31 | 1278.47 |
| space group | $P\bar{6}$ (No. 174) | $P\bar{6}$ (No. 174) | $P\bar{6}$ (No. 174) | $P\bar{6}$ (No. 174) | $P\bar{6}$ (No. 174) | $P\bar{6}$ (No. 174) | $P\bar{6}$ (No. 174) | $P\bar{6}$ (No. 174) |
| $a$ (Å) | 9.6444(3) | 9.6592(3) | 9.6468(4) | 9.642(4) | 9.6356(2) | 9.5977(7) | 9.6016(7) | 9.5970(7) |
| $c$ (Å) | 3.9027(1) | 3.8686(1) | 3.8508(2) | 3.8404(15) | 3.8188(2) | 3.7981(3) | 3.7867(3) | 3.7761(3) |
| $V$ (Å$^3$) | 314.37(2) | 312.58(2) | 310.35(2) | 309.2(2) | 307.05(2) | 302.99(4) | 302.33(4) | 301.19(4) |
| $Z$ | 1 | 1 | 1 | 1 | 1 | 1 | 1 | 1 |
| $T$ (K) | 173 | 173 | 173 | 173 | 173 | 173 | 173 | 173 |
| $\rho_{calcd}$ (g cm$^{-3}$) | 6.504 | 6.554 | 6.610 | 6.670 | 6.783 | 6.949 | 6.983 | 7.048 |
| crystal dimensions (mm) | 0.02 × 0.04 × 0.36 | 0.05 × 0.05 × 0.24 | 0.04 × 0.05 × 0.12 | 0.02 × 0.03 × 0.28 | 0.05 × 0.06 × 0.14 | 0.03 × 0.03 × 0.20 | 0.03 × 0.03 × 0.27 | 0.02 × 0.04 × 0.26 |
| $\mu$(Mo $K\alpha$) (mm$^{-1}$) | 25.24 | 25.83 | 26.54 | 27.15 | 28.45 | 30.08 | 30.88 | 31.66 |
| transmission factors | 0.133–0.633 | 0.048–0.452 | 0.179–0.558 | 0.119–0.582 | 0.133–0.426 | 0.127–0.546 | 0.106–0.563 | 0.109–0.658 |
| $2\theta$ limits | 4.88–66.34° | 4.86–66.38° | 4.88–66.40° | 4.88–65.80° | 4.88–66.10° | 4.90–66.20° | 4.90–66.26° | 4.90–66.42° |
| data collected | $-14 \le h \le 14$, $-14 \le k \le 14$, $-5 \le l \le 5$ | $-14 \le h \le 14$, $-14 \le k \le 14$, $-5 \le l \le 5$ | $-14 \le h \le 14$, $-14 \le k \le 14$, $-5 \le l \le 5$ | $-14 \le h \le 14$, $-14 \le k \le 14$, $-5 \le l \le 5$ | $-14 \le h \le 14$, $-14 \le k \le 14$, $-5 \le l \le 5$ | $-14 \le h \le 14$, $-14 \le k \le 14$, $-5 \le l \le 5$ | $-14 \le h \le 14$, $-14 \le k \le 14$, $-5 \le l \le 5$ | $-14 \le h \le 14$, $-14 \le k \le 14$, $-5 \le l \le 5$ |
| no. of data collected | 4365 | 4411 | 4339 | 4260 | 4266 | 4191 | 4266 | 4288 |
| no. of unique data, including $F_o^2 < 0$ | 882 ($R_{int}$ = 0.020) | 884 ($R_{int}$ = 0.021) | 871 ($R_{int}$ = 0.033) | 859 ($R_{int}$ = 0.046) | 861 ($R_{int}$ = 0.020) | 850 ($R_{int}$ = 0.038) | 861 ($R_{int}$ = 0.024) | 862 ($R_{int}$ = 0.046) |
| no. of unique data, with $F_o^2 > 2\sigma(F_o^2)$ | 868 | 878 | 843 | 808 | 856 | 823 | 845 | 819 |
| no. of variables | 45 | 45 | 45 | 45 | 45 | 45 | 45 | 45 |
| Flack parameter | 0.44(3) | 0.49(2) | 0.76(3) | 0.61(4) | 0.50(2) | 0.60(3) | 0.50(2) | 0.51(3) |
| $R(F)$ for $F_o^2 > 2\sigma(F_o^2)$ [a] | 0.023 | 0.013 | 0.023 | 0.025 | 0.012 | 0.023 | 0.017 | 0.025 |
| $R_w(F_o^2)$ [b] | 0.057 | 0.029 | 0.056 | 0.050 | 0.028 | 0.055 | 0.038 | 0.049 |

| | | | | | | | | |
|---|---|---|---|---|---|---|---|---|
| goodness of fit | 1.212 | 1.147 | 1.245 | 1.149 | 1.134 | 1.068 | 1.151 | 1.118 |
| $(\Delta\rho)_{max}$, $(\Delta\rho)_{min}$ (e Å$^{-3}$) | 1.76, –2.79 | 1.20, –1.49 | 1.96, –2.88 | 1.97, –1.65 | 1.35, –0.92 | 2.68, –2.06 | 2.00, –1.55 | 2.43, –1.60 |

[a] $R(F) = \sum||F_o| - |F_c|| / \sum|F_o|$. [b] $R_w(F_o^2) = [\sum[w(F_o^2 - F_c^2)^2] / \sum wF_o^4]^{1/2}$; $w^{-1} = [\sigma^2(F_o^2) + (Ap)^2 + Bp]$, where $p = [\max(F_o^2,0) + 2F_c^2] / 3$.

**Table 2-3.** Crystallographic Data for $RE_2Mn_3Cu_9As_7$ ($RE$ = La–Nd)

| formula | $La_2Mn_3Cu_9As_7$ | $Ce_2Mn_3Cu_9As_7$ | $Pr_2Mn_3Cu_9As_7$ | $Nd_2Mn_3Cu_9As_7$ |
|---|---|---|---|---|
| formula mass (amu) | 1538.94 | 1541.36 | 1542.94 | 1549.60 |
| space group | $P\bar{6}$ (No. 174) | $P\bar{6}$ (No. 174) | $P\bar{6}$ (No. 174) | $P\bar{6}$ (No. 174) |
| $a$ (Å) | 9.9376(6) | 9.9226(5) | 9.9196(3) | 9.9130(3) |
| $c$ (Å) | 4.0194(2) | 3.9912(2) | 3.9748(1) | 3.9611(1) |
| $V$ (Å$^3$) | 343.76(3) | 340.32(3) | 338.72(2) | 337.10(2) |
| $Z$ | 1 | 1 | 1 | 1 |
| $T$ (K) | 173 | 173 | 173 | 173 |
| $\rho_{calcd}$ (g cm$^{-3}$) | 7.434 | 7.521 | 7.564 | 7.633 |
| crystal dimensions (mm) | 0.03 × 0.04 × 0.21 | 0.03 × 0.05 × 0.12 | 0.05 × 0.05 × 0.26 | 0.05 × 0.06 × 0.26 |
| $\mu$(Mo $K\alpha$) (mm$^{-1}$) | 38.99 | 39.79 | 40.45 | 41.12 |
| transmission factors | 0.066–0.448 | 0.113–0.478 | 0.042–0.289 | 0.031–0.265 |
| $2\theta$ limits | 4.74–66.34° | 4.74–66.52° | 4.74–66.50° | 4.74–66.46° |
| data collected | $-15 \le h \le 14$, $-14 \le k \le 14$, $-6 \le l \le 6$ | $-14 \le h \le 14$, $-15 \le k \le 15$, $-6 \le l \le 6$ | $-15 \le h \le 15$, $-15 \le k \le 15$, $-6 \le l \le 6$ | $-15 \le h \le 15$, $-15 \le k \le 15$, $-6 \le l \le 6$ |
| no. of data collected | 4792 | 4766 | 4881 | 4797 |
| no. of unique data, including $F_o^2 < 0$ | 969 ($R_{int}$ = 0.048) | 970 ($R_{int}$ = 0.037) | 971 ($R_{int}$ = 0.018) | 962 ($R_{int}$ = 0.024) |
| no. of unique data, with $F_o^2 > 2\sigma(F_o^2)$ | 868 | 925 | 970 | 960 |
| no. of variables | 45 | 45 | 45 | 45 |
| Flack parameter | 0.31(3) | 0.18(3) | 0.28(3) | 0.51(3) |
| $R(F)$ for $F_o^2 > 2\sigma(F_o^2)$ [a] | 0.024 | 0.022 | 0.019 | 0.022 |

| | | | | |
|---|---|---|---|---|
| $R_w(F_o^2)$ [b] | 0.051 | 0.047 | 0.047 | 0.054 |
| goodness of fit | 1.080 | 1.170 | 1.306 | 1.369 |
| $(\Delta\rho)_{max}$, $(\Delta\rho)_{min}$ (e Å$^{-3}$) | 1.95, –1.72 | 1.62, –2.29 | 2.47, –3.15 | 3.07, –3.89 |

[a] $R(F) = \sum||F_o| - |F_c|| / \sum|F_o|$. [b] $R_w(F_o^2) = [\sum[w(F_o^2 - F_c^2)^2] / \sum wF_o^4]^{1/2}$; $w^{-1} = [\sigma^2(F_o^2) + (Ap)^2 + Bp]$, where $p = [\max(F_o^2,0) + 2F_c^2] / 3$.

**Table 2-4.** Crystallographic Data for $RE_2Mn_3Cu_9Pn_7$ [a]

| formula | fw (amu) | $a$ (Å) | $c$ (Å) | $V$ (Å$^2$) | $\rho_c$ (g cm$^{-3}$) | $\mu$ (mm$^{-1}$) | Flack parameter | $R(F)$ [b] | $R_w(F_o^2)$ [c] |
|---|---|---|---|---|---|---|---|---|---|
| $La_2Mn_3Cu_9P_7$ | 1231.29 | 9.6444(3) | 3.9027(1) | 314.37(2) | 6.504 | 25.24 | 0.44(3) | 0.023 | 0.057 |
| $Ce_2Mn_3Cu_9P_7$ | 1233.71 | 9.6592(3) | 3.8686(1) | 312.58(2) | 6.554 | 25.83 | 0.49(2) | 0.013 | 0.029 |
| $Pr_2Mn_3Cu_9P_7$ | 1235.29 | 9.6468(4) | 3.8508(2) | 310.35(2) | 6.610 | 26.54 | 0.76(3) | 0.023 | 0.056 |
| $Nd_2Mn_3Cu_9P_7$ | 1241.95 | 9.642(4) | 3.8404(15) | 309.2(2) | 6.670 | 27.15 | 0.61(4) | 0.025 | 0.050 |
| $Sm_2Mn_3Cu_9P_7$ | 1254.17 | 9.6356(2) | 3.8188(2) | 307.05(2) | 6.783 | 28.45 | 0.50(2) | 0.012 | 0.028 |
| $Gd_2Mn_3Cu_9P_7$ | 1267.97 | 9.5977(7) | 3.7981(3) | 302.99(4) | 6.949 | 30.08 | 0.60(3) | 0.023 | 0.055 |
| $Tb_2Mn_3Cu_9P_7$ | 1271.31 | 9.6016(7) | 3.7867(3) | 302.33(4) | 6.983 | 30.88 | 0.50(2) | 0.017 | 0.038 |
| $Dy_2Mn_3Cu_9P_7$ | 1278.47 | 9.5970(7) | 3.7761(3) | 301.19(4) | 7.048 | 31.66 | 0.51(3) | 0.025 | 0.049 |
| $La_2Mn_3Cu_9As_7$ | 1538.94 | 9.9376(6) | 4.0194(2) | 343.76(3) | 7.434 | 38.99 | 0.31(3) | 0.024 | 0.051 |
| $Ce_2Mn_3Cu_9As_7$ | 1541.36 | 9.9226(5) | 3.9912(2) | 340.32(3) | 7.521 | 39.79 | 0.18(3) | 0.022 | 0.047 |
| $Pr_2Mn_3Cu_9As_7$ | 1542.94 | 9.9196(3) | 3.9748(1) | 338.72(2) | 7.564 | 40.45 | 0.28(3) | 0.019 | 0.047 |
| $Nd_2Mn_3Cu_9As_7$ | 1549.60 | 9.9130(3) | 3.9611(1) | 337.10(2) | 7.633 | 41.12 | 0.51(3) | 0.022 | 0.054 |

[a] For all structures, $Z = 1$, $T = 173(2)$ K, $\lambda = 0.71073$ Å, space group $P\bar{6}$ (No. 174). [b] $R(F) = \sum||F_o| - |F_c|| / \sum|F_o|$ for $F_o^2 > 2\sigma(F_o^2)$. [c] $R_w(F_o^2) = [\sum[w(F_o^2 - F_c^2)^2] / \sum wF_o^4]^{1/2}$; $w^{-1} = [\sigma^2(F_o^2) + (Ap)^2 + Bp]$, where $p = [\max(F_o^2,0) + 2F_c^2] / 3$.

**Table 2-5.** Ranges of Interatomic Distances (Å) for $RE_2Mn_3Cu_9Pn_7$

| compound | *RE*1–*Pn* (CN6) | *RE*2–*Pn* (CN6) | Cu1–*Pn* (CN4) | Cu2–*Pn* (CN4) | Cu3–*Pn* (CN4) | Mn4–*Pn* (CN5) |
|---|---|---|---|---|---|---|
| $La_2Mn_3Cu_9P_7$ | 3.0190(15) | 2.9984(15) | 2.429(2)–2.4387(14) | 2.3453(8)–2.4715(14) | 2.4039(12)–2.481(2) | 2.488(2)–2.7419(18) |
| $Ce_2Mn_3Cu_9P_7$ | 2.9871(8) | 2.9682(7) | 2.4210(11)–2.4427(7) | 2.3562(5)–2.4582(7) | 2.4137(7)–2.4770(11) | 2.5164(11)–2.7284(9) |
| $Pr_2Mn_3Cu_9P_7$ | 2.9738(16) | 2.9521(15) | 2.409(2)–2.4411(15) | 2.3584(9)–2.4484(14) | 2.4156(14)–2.474(2) | 2.514(2)–2.7132(17) |
| $Nd_2Mn_3Cu_9P_7$ | 2.957(2) | 2.943(2) | 2.397(3)–2.4438(19) | 2.3588(14)–2.4513(18) | 2.4219(19)–2.472(3) | 2.523(3)–2.702(2) |
| $Sm_2Mn_3Cu_9P_7$ | 2.9358(9) | 2.9211(9) | 2.3969(14)–2.4432(9) | 2.3643(5)–2.4404(8) | 2.4170(9)–2.4603(14) | 2.5235(13)–2.7051(10) |
| $Gd_2Mn_3Cu_9P_7$ | 2.919(2) | 2.903(2) | 2.381(3)–2.438(2) | 2.3574(11)–2.4275(17) | 2.4113(19)–2.445(3) | 2.502(3)–2.695(2) |
| $Tb_2Mn_3Cu_9P_7$ | 2.9066(14) | 2.8921(14) | 2.386(2)–2.4375(15) | 2.3614(8)–2.4261(13) | 2.4082(14)–2.442(2) | 2.503(2)–2.6913(17) |
| $Dy_2Mn_3Cu_9P_7$ | 2.894(2) | 2.879(2) | 2.375(4)–2.435(2) | 2.3614(12)–2.429(2) | 2.414(2)–2.441(4) | 2.506(3)–2.686(3) |
| $La_2Mn_3Cu_9As_7$ | 3.0975(7) | 3.0773(7) | 2.4944(15)–2.5087(9) | 2.4456(12)–2.5396(9) | 2.4918(9)–2.5324(14) | 2.6139(18)–2.8125(14) |
| $Ce_2Mn_3Cu_9As_7$ | 3.0706(6) | 3.0501(6) | 2.4848(13)–2.5070(8) | 2.4457(10)–2.5254(7) | 2.4892(8)–2.5265(12) | 2.6190(15)–2.8016(12) |
| $Pr_2Mn_3Cu_9As_7$ | 3.0542(5) | 3.0349(5) | 2.4827(10)–2.5062(6) | 2.4453(8)–2.5218(6) | 2.4901(6)–2.5252(9) | 2.6235(12)–2.7969(9) |
| $Nd_2Mn_3Cu_9As_7$ | 3.0406(5) | 3.0229(5) | 2.4773(10)–2.5066(6) | 2.4455(8)–2.5165(6) | 2.4902(6)–2.5231(10) | 2.6256(12)–2.7909(9) |

**Table 2-6.** Atomic Coordinates and Equivalent Isotropic Displacement Parameters (Å$^2$) a for $RE_2Mn_3Cu_9P_7$ (*RE* = La–Nd, Sm, Gd–Dy)

| | $La_2Mn_3Cu_9P_7$ | $Ce_2Mn_3Cu_9P_7$ | $Pr_2Mn_3Cu_9P_7$ | $Nd_2Mn_3Cu_9P_7$ | $Sm_2Mn_3Cu_9P_7$ | $Gd_2Mn_3Cu_9P_7$ | $Tb_2Mn_3Cu_9P_7$ | $Dy_2Mn_3Cu_9P_7$ |
|---|---|---|---|---|---|---|---|---|
| *RE*1 in 1*c* (1/3, 2/3, 0) | | | | | | | | |
| $U_{eq}$ | 0.00558(14) | 0.00518(7) | 0.00551(15) | 0.00587(17) | 0.00529(8) | 0.00654(15) | 0.00611(11) | 0.00635(17) |
| *RE*2 in 1*f* (2/3, 1/3, 1/2) | | | | | | | | |
| $U_{eq}$ | 0.00644(13) | 0.00635(7) | 0.00739(15) | 0.00727(16) | 0.00662(8) | 0.00748(15) | 0.00690(11) | 0.00683(16) |
| Cu1 in 3*j* (*x*, *y*, 0) | | | | | | | | |

| | | | | | | | | |
|---|---|---|---|---|---|---|---|---|
| *x* | 0.42256(11) | 0.42357(6) | 0.42455(12) | 0.42561(14) | 0.42549(7) | 0.42599(15) | 0.42625(11) | 0.42652(17) |
| *y* | 0.05102(11) | 0.04915(6) | 0.04897(12) | 0.04908(15) | 0.04761(7) | 0.04748(16) | 0.04651(12) | 0.04613(19) |
| $U_{eq}$ | 0.00923(18) | 0.00823(9) | 0.0084(2) | 0.0082(2) | 0.00763(11) | 0.0091(2) | 0.00867(18) | 0.0083(3) |
| Cu2 in 3*j* (*x*, *y*, 0) | | | | | | | | |
| *x* | 0.16000(9) | 0.16185(5) | 0.16265(10) | 0.16345(12) | 0.16506(6) | 0.16604(12) | 0.16692(9) | 0.16774(14) |
| *y* | 0.27984(10) | 0.28057(5) | 0.28114(11) | 0.28126(13) | 0.28196(6) | 0.28215(14) | 0.28243(10) | 0.28247(15) |
| $U_{eq}$ | 0.00830(16) | 0.00711(8) | 0.00754(17) | 0.00683(19) | 0.00677(9) | 0.0087(2) | 0.00760(14) | 0.0080(2) |
| Cu3 in 3*k* (*x*, *y*, 1/2) | | | | | | | | |
| *x* | 0.37998(12) | 0.38380(6) | 0.38521(13) | 0.38607(14) | 0.38737(7) | 0.38800(16) | 0.38845(12) | 0.38901(18) |
| *y* | 0.42394(11) | 0.42646(5) | 0.42749(11) | 0.42837(13) | 0.42845(7) | 0.42883(14) | 0.42841(11) | 0.42893(17) |
| $U_{eq}$ | 0.00854(18) | 0.00779(9) | 0.00794(19) | 0.0082(2) | 0.00742(11) | 0.0086(2) | 0.00795(17) | 0.0082(3) |
| Mn4 in 3*k* (*x*, *y*, 1/2) | | | | | | | | |
| *x* | 0.21964(18) | 0.21991(7) | 0.22111(14) | 0.22181(16) | 0.22155(8) | 0.2218(2) | 0.22309(14) | 0.2235(2) |
| *y* | 0.09604(15) | 0.09579(7) | 0.09602(14) | 0.09593(16) | 0.09423(8) | 0.09276(18) | 0.09235(13) | 0.0919(2) |
| $U_{eq}$ | 0.0179(3) | 0.00919(11) | 0.0077(2) | 0.0073(3) | 0.00811(12) | 0.0148(3) | 0.0136(2) | 0.0128(3) |
| P1 in 3*j* (*x*, *y*, 0) | | | | | | | | |
| *x* | 0.4155(2) | 0.41743(12) | 0.4181(2) | 0.4182(3) | 0.41995(14) | 0.4203(3) | 0.4213(2) | 0.4221(4) |
| *y* | 0.2994(2) | 0.29666(12) | 0.2954(2) | 0.2939(3) | 0.29355(14) | 0.2927(3) | 0.2925(2) | 0.2913(4) |
| $U_{eq}$ | 0.0068(3) | 0.00566(15) | 0.0054(3) | 0.0054(4) | 0.00530(18) | 0.0071(4) | 0.0069(3) | 0.0072(5) |
| P2 in 3*k* (*x*, *y*, 1/2) | | | | | | | | |
| *x* | 0.1164(3) | 0.12097(12) | 0.1221(3) | 0.1235(3) | 0.12639(15) | 0.1275(3) | 0.1290(2) | 0.1300(4) |
| *y* | 0.4107(2) | 0.41315(12) | 0.4137(2) | 0.4155(3) | 0.41675(14) | 0.4169(3) | 0.4180(2) | 0.4194(3) |
| $U_{eq}$ | 0.0062(3) | 0.00602(15) | 0.0054(3) | 0.0045(4) | 0.00580(18) | 0.0058(4) | 0.0057(3) | 0.0057(5) |
| P3 in 1*a* (0, 0, 0) | | | | | | | | |
| $U_{eq}$ | 0.0070(5) | 0.0059(2) | 0.0055(5) | 0.0047(6) | 0.0056(3) | 0.0059(6) | 0.0069(4) | 0.0057(6) |

**Table 2-7.** Atomic Coordinates and Equivalent Isotropic Displacement Parameters (Å$^2$) for $RE_2Mn_3Cu_9As_7$ (*RE* = La–Nd)

| | $La_2Mn_3Cu_9As_7$ | $Ce_2Mn_3Cu_9As_7$ | $Pr_2Mn_3Cu_9As_7$ | $Nd_2Mn_3Cu_9As_7$ |
|---|---|---|---|---|
| *RE*1 in 1*c* (1/3, 2/3, 0) | | | | |

| | | | | |
|---|---|---|---|---|
| $U_{eq}$ | 0.00743(18) | 0.00665(15) | 0.00620(11) | 0.00581(12) |
| *RE*2 in 1*f* (2/3, 1/3, 1/2) | | | | |
| $U_{eq}$ | 0.00854(17) | 0.00779(14) | 0.00698(11) | 0.00674(12) |
| Cu1 in 3*j* (*x*, *y*, 0) | | | | |
| *x* | 0.42231(14) | 0.42288(11) | 0.42355(9) | 0.42415(9) |
| *y* | 0.05082(14) | 0.04913(11) | 0.04799(9) | 0.04738(9) |
| $U_{eq}$ | 0.0109(2) | 0.0102(2) | 0.00954(15) | 0.00909(16) |
| Cu2 in 3*j* (*x*, *y*, 0) | | | | |
| *x* | 0.16027(12) | 0.16189(10) | 0.16294(8) | 0.16376(9) |
| *y* | 0.28335(14) | 0.28367(11) | 0.28360(9) | 0.28374(9) |
| $U_{eq}$ | 0.0103(2) | 0.00952(17) | 0.00851(14) | 0.00803(14) |
| Cu3 in 3*k* (*x*, *y*, 1/2) | | | | |
| *x* | 0.37620(14) | 0.37918(12) | 0.38092(9) | 0.38240(10) |
| *y* | 0.42272(14) | 0.42374(11) | 0.42452(9) | 0.42522(10) |
| $U_{eq}$ | 0.0116(2) | 0.01046(19) | 0.00963(15) | 0.00909(16) |
| Mn4 in 3*k* (*x*, *y*, 1/2) | | | | |
| *x* | 0.22027(19) | 0.22022(16) | 0.22020(12) | 0.22023(13) |
| *y* | 0.09977(19) | 0.09888(16) | 0.09807(13) | 0.09749(13) |
| $U_{eq}$ | 0.0162(3) | 0.0151(3) | 0.01305(19) | 0.0126(2) |
| As1 in 3*j* (*x*, *y*, 0) | | | | |
| *x* | 0.41691(11) | 0.41825(10) | 0.41905(7) | 0.41950(7) |
| *y* | 0.29908(12) | 0.29720(10) | 0.29600(7) | 0.29492(8) |
| $U_{eq}$ | 0.00820(18) | 0.00707(15) | 0.00628(11) | 0.00591(13) |
| As2 in 3*k* (*x*, *y*, 1/2) | | | | |
| *x* | 0.11675(11) | 0.12003(9) | 0.12198(7) | 0.12355(7) |
| *y* | 0.41321(11) | 0.41444(9) | 0.41554(7) | 0.41631(7) |
| $U_{eq}$ | 0.00780(17) | 0.00712(14) | 0.00640(11) | 0.00603(12) |
| As3 in 1*a* (0, 0, 0) | | | | |
| $U_{eq}$ | 0.0084(3) | 0.0075(2) | 0.00636(17) | 0.00607(18) |

[a] $U_{eq}$ is defined as one-third of the trace of the orthogonalized $U_{ij}$ tensor.

**Table 2-8.** Interatomic Distances (Å) for $RE_2Mn_3Cu_9P_7$ (*RE* = La–Nd, Sm, Gd–Dy)

| | $La_2Mn_3Cu_9P_7$ | $Ce_2Mn_3Cu_9P_7$ | $Pr_2Mn_3Cu_9P_7$ | $Nd_2Mn_3Cu_9P_7$ | $Sm_2Mn_3Cu_9P_7$ | $Gd_2Mn_3Cu_9P_7$ | $Tb_2Mn_3Cu_9P_7$ | $Dy_2Mn_3Cu_9P_7$ |
|---|---|---|---|---|---|---|---|---|
| *RE*1–P2 (×6) | 3.0190(15) | 2.9871(8) | 2.9738(16) | 2.957(2) | 2.9358(9) | 2.919(2) | 2.9066(14) | 2.894(2) |
| *RE*2–P1 (×6) | 2.9984(15) | 2.9682(7) | 2.9521(15) | 2.943(2) | 2.9211(9) | 2.903(2) | 2.8921(14) | 2.879(2) |
| Cu1–P1 | 2.430(2) | 2.4210(11) | 2.409(2) | 2.397(3) | 2.3969(14) | 2.381(3) | 2.386(2) | 2.375(4) |
| Cu1–P1 | 2.429(2) | 2.4314(12) | 2.426(2) | 2.425(3) | 2.4187(14) | 2.410(3) | 2.405(2) | 2.407(3) |
| Cu1–P2 (×2) | 2.4387(14) | 2.4427(7) | 2.4411(15) | 2.4438(19) | 2.4432(9) | 2.438(2) | 2.4375(15) | 2.435(2) |
| Cu2–P3 | 2.3453(8) | 2.3562(5) | 2.3584(9) | 2.3588(14) | 2.3643(5) | 2.3574(11) | 2.3614(8) | 2.3614(12) |
| Cu2–P1 | 2.375(2) | 2.3947(11) | 2.398(2) | 2.397(3) | 2.4021(13) | 2.391(3) | 2.396(2) | 2.400(3) |
| Cu2–P2 (×2) | 2.4715(14) | 2.4582(7) | 2.4484(14) | 2.4513(18) | 2.4404(8) | 2.4275(17) | 2.4261(13) | 2.429(2) |
| Cu3–P1 (×2) | 2.4039(12) | 2.4137(7) | 2.4156(14) | 2.4219(19) | 2.4170(9) | 2.4113(19) | 2.4082(14) | 2.414(2) |
| Cu3–P2 | 2.444(2) | 2.4295(12) | 2.419(2) | 2.403(3) | 2.4061(14) | 2.400(3) | 2.403(2) | 2.392(4) |
| Cu3–P2 | 2.481(2) | 2.4770(11) | 2.474(2) | 2.472(3) | 2.4603(14) | 2.445(3) | 2.442(2) | 2.441(4) |
| Mn4–P2 | 2.488(2) | 2.5164(11) | 2.514(2) | 2.523(3) | 2.5235(13) | 2.502(3) | 2.503(2) | 2.506(3) |
| Mn4–P3 (×2) | 2.6816(10) | 2.6729(4) | 2.6719(8) | 2.6718(12) | 2.6625(5) | 2.6527(12) | 2.6571(9) | 2.6555(13) |
| Mn4–P1 (×2) | 2.7419(18) | 2.7284(9) | 2.7132(17) | 2.702(2) | 2.7051(10) | 2.695(2) | 2.6913(17) | 2.686(3) |
| Cu1–Cu2 | 2.5930(13) | 2.6121(7) | 2.6187(14) | 2.6316(19) | 2.6358(8) | 2.6364(17) | 2.6433(12) | 2.6505(19) |
| Cu1–Cu3 (×2) | 2.8626(7) | 2.8126(4) | 2.7885(8) | 2.7724(11) | 2.7495(4) | 2.7290(9) | 2.7167(6) | 2.7050(9) |
| Cu1–Mn4 (×2) | 2.9455(12) | 2.9497(6) | 2.9420(11) | 2.9395(15) | 2.9312(7) | 2.9130(16) | 2.9055(12) | 2.8998(18) |
| Cu2–Cu3 (×2) | 2.7003(9) | 2.7023(4) | 2.6979(9) | 2.6948(13) | 2.6839(5) | 2.6697(11) | 2.6631(8) | 2.6580(13) |
| Cu2–Mn4 (×2) | 2.8810(12) | 2.8710(6) | 2.8673(11) | 2.8639(16) | 2.8633(7) | 2.8584(15) | 2.8620(11) | 2.8592(18) |
| Cu2–Mn4 (×2) | 2.9078(11) | 2.9082(5) | 2.9058(11) | 2.9051(15) | 2.8958(7) | 2.8784(15) | 2.8770(11) | 2.8743(18) |
| Cu3–Mn4 | 2.7389(15) | 2.7662(7) | 2.7693(15) | 2.776(2) | 2.7890(9) | 2.7934(19) | 2.7946(14) | 2.801(2) |

**Table 2-9.** Interatomic Distances (Å) for $RE_2Mn_3Cu_9As_7$ (*RE* = La–Nd)

| | $La_2Mn_3Cu_9As_7$ | $Ce_2Mn_3Cu_9As_7$ | $Pr_2Mn_3Cu_9As_7$ | $Nd_2Mn_3Cu_9As_7$ |
|---|---|---|---|---|
| *RE*1–As2 (×6) | 3.0975(7) | 3.0706(6) | 3.0542(5) | 3.0406(5) |
| *RE*2–As1 (×6) | 3.0773(7) | 3.0501(6) | 3.0349(5) | 3.0229(5) |
| Cu1–As1 | 2.4944(15) | 2.4848(13) | 2.4827(10) | 2.4773(10) |
| Cu1–As1 | 2.5031(16) | 2.4983(13) | 2.4945(10) | 2.4920(10) |
| Cu1–As2 (×2) | 2.5087(9) | 2.5070(8) | 2.5062(6) | 2.5066(6) |
| Cu2–As3 | 2.4456(12) | 2.4457(10) | 2.4453(8) | 2.4455(8) |
| Cu2–As1 | 2.4759(14) | 2.4794(12) | 2.4813(9) | 2.4816(10) |
| Cu2–As2 (×2) | 2.5396(9) | 2.5254(7) | 2.5218(6) | 2.5165(6) |
| Cu3–As1 (×2) | 2.4918(9) | 2.4892(8) | 2.4901(6) | 2.4902(6) |
| Cu3–As2 | 2.5154(16) | 2.5076(13) | 2.5001(10) | 2.4937(11) |
| Cu3–As2 | 2.5324(14) | 2.5265(12) | 2.5252(9) | 2.5231(10) |
| Mn4–As2 | 2.6139(18) | 2.6190(15) | 2.6235(12) | 2.6256(12) |
| Mn4–As3 (×2) | 2.7646(11) | 2.7525(10) | 2.7463(7) | 2.7409(8) |
| Mn4–As1 (×2) | 2.8125(14) | 2.8016(12) | 2.7969(9) | 2.7909(9) |
| Cu1–Cu2 | 2.6467(16) | 2.6561(13) | 2.6681(10) | 2.6761(11) |
| Cu1–Cu3 (×2) | 2.9726(10) | 2.9288(8) | 2.9010(7) | 2.8786(7) |
| Cu1–Mn4 (×2) | 3.0469(15) | 3.0434(12) | 3.0443(10) | 3.0430(10) |
| Cu2–Cu3 (×2) | 2.7549(11) | 2.7507(9) | 2.7489(7) | 2.7473(8) |
| Cu2–Mn4 (×2) | 2.9682(15) | 2.9565(12) | 2.9504(10) | 2.9458(10) |
| Cu2–Mn4 (×2) | 3.0256(15) | 3.0173(13) | 3.0119(10) | 3.0072(11) |
| Cu3–Mn4 | 2.780(2) | 2.7918(17) | 2.8046(14) | 2.8136(14) |

### 2.2.3 Band Structure Calculation

Tight-binding linear muffin tin orbital band structure calculations were performed on $La_2Mn_3Cu_9P_7$ within the local density and atomic spheres approximation with use of the Stuttgart TB-LMTO-ASA program (version 4.7).[35] The basis set included La 6s/6p/5d/4f, Mn 4s/4p/3d, Cu 4s/4p/3d, and P 3s/3p/3d orbitals, with the La 6p and P 3d orbitals being downfolded. Integrations in reciprocal space were carried out with an improved tetrahedron method over 1728 irreducible *k*-points within the first Brillouin zone.

### 2.2.4 Electrical Resistivity

Crystals of $Ce_2Mn_3Cu_9P_7$ were mounted for standard four-probe electrical resistivity measurements between 2 and 300 K on a Quantum Design Physical Property Measurement System (PPMS) equipped with an ac transport controller (Model 7100). Silver paste (DuPont 4929N) was used as the contacting agent from the crystal to graphite fibres and gold wires. The current was 100 μA and the frequency was 16 Hz. Measurements were repeated twice.

## 2.3 Results and Discussion

The pnictides $RE_2Mn_3Cu_9Pn_7$ (*Pn* = P, As) form readily at 800 °C and are quaternary representatives of the hexagonal $Zr_2Fe_{12}P_7$-type structure.[33] The unit cell volume decreases smoothly with *RE* substitution, with the range extending further for the phosphides $RE_2Mn_3Cu_9P_7$ (*RE* = La–Nd, Sm, Gd–Dy) than the arsenides $RE_2Mn_3Cu_9As_7$ (*RE* = La–Nd) (**Figure 2-1**). Ternary manganese-containing phosphides $RE_2Mn_{12}P_7$ have been previously reported,[2] but not the copper-containing ones "$RE_2Cu_{12}P_7$". Attempts were

made to prepare other members in $RE_2(Mn_{1-x}Cu_x)_{12}P_7$ ($RE$ = La, Nd, Tb; $x$ = 0, 0.25, 0.50, 1.00). The existence of $RE_2Mn_{12}P_7$ ($x$ = 0) was confirmed, but all other members of this hypothetical series, including "$RE_2Cu_{12}P_7$" ($x$ = 1.0) could not be formed. Further attempts were made to substitute Cu with Ag, or Mn with Fe, to target the preparation of $RE_2M_3Ag_9Pn_7$ ($RE$ = La, Nd, Tb, Ho, Lu; $M$ = Mn, Fe; $Pn$ = P, As), to no avail.

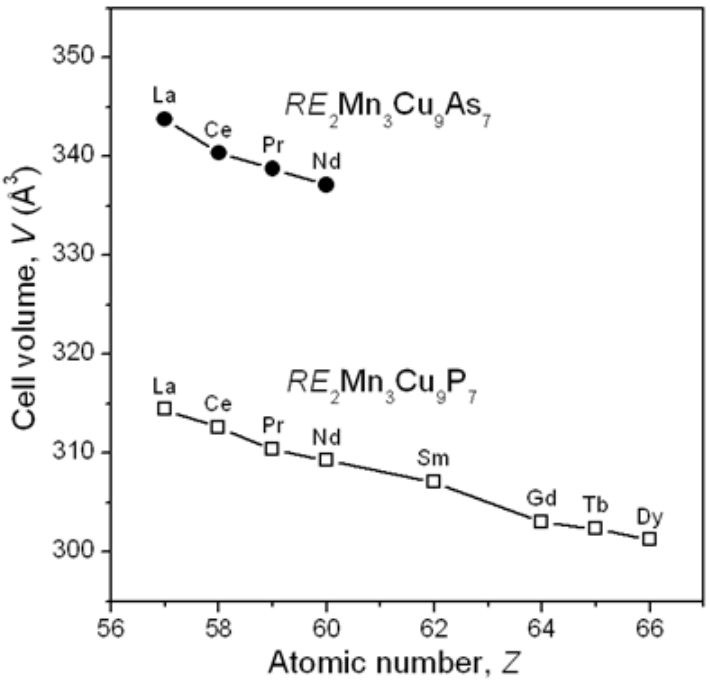


**Figure 2-1.** Plot of unit cell volumes for $RE_2Mn_3Cu_9Pn_7$ ($Pn$ = P, As).

Like other related hexagonal structures of metal-rich phases where the metal-to-nonmetal ratio is close to 2:1,[1] the $Zr_2Fe_{12}P_7$-type structure of $RE_2Mn_3Cu_9Pn_7$ is best understood in terms of the connectivity of $Pn$-centred trigonal prisms (**Figure 2-2**). All atoms in the structure are found on nets lying on the mirror planes at $z$ = 0 or 1/2, which are distinguished by thick or thin rims, respectively. Trigonal prisms of each type share

their triangular faces to form infinite columns aligned parallel to the *c*-direction. The *Pn*1- and *Pn*3-centred trigonal prisms each share two edges along their quadrilateral faces to form a hexagonal framework extending across the *ab*-plane. Three *Pn*2-centred trigonal prisms share a common edge (*RE*2–*RE*2) to form a propeller-shaped unit which lies within the large channels defined by the hexagonal framework. Additional metal atoms are found over the quadrilateral faces, so that the coordination geometry of metal atoms surrounding the *Pn* atoms is actually tricapped trigonal prismatic (CN9) (**Figure 2-3a**).

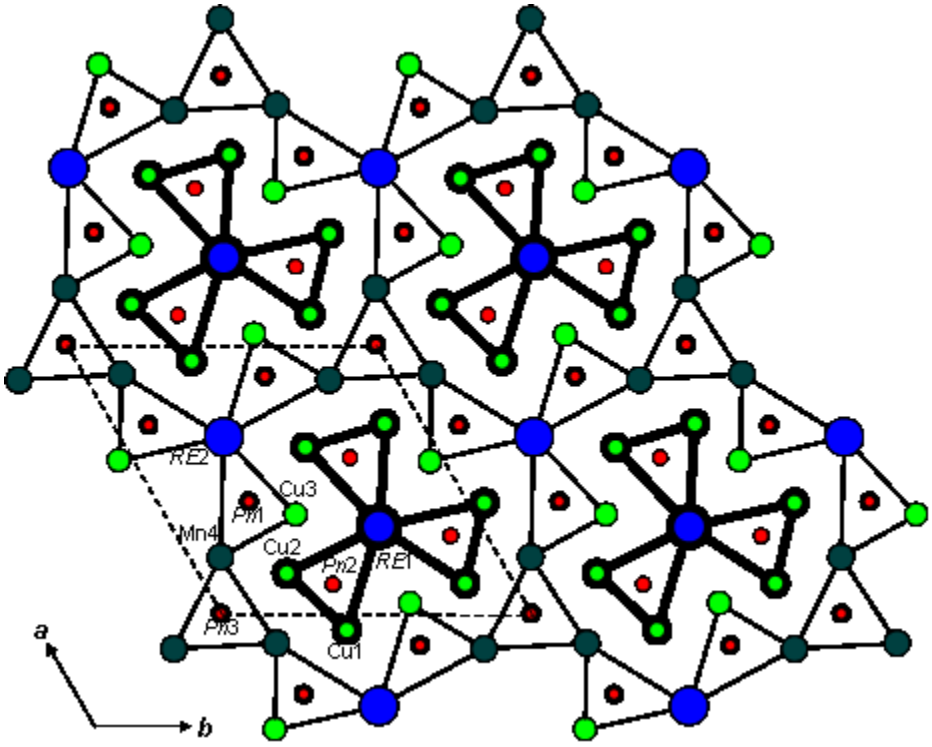


**Figure 2-2.** Structure of $RE_2Mn_3Cu_9Pn_7$ (*Pn* = P, As), in terms of *Pn*-filled trigonal prisms, viewed in projection down the c-axis. Thick and thin lines distinguish between atoms displaced by ½ the c-axis repeat.

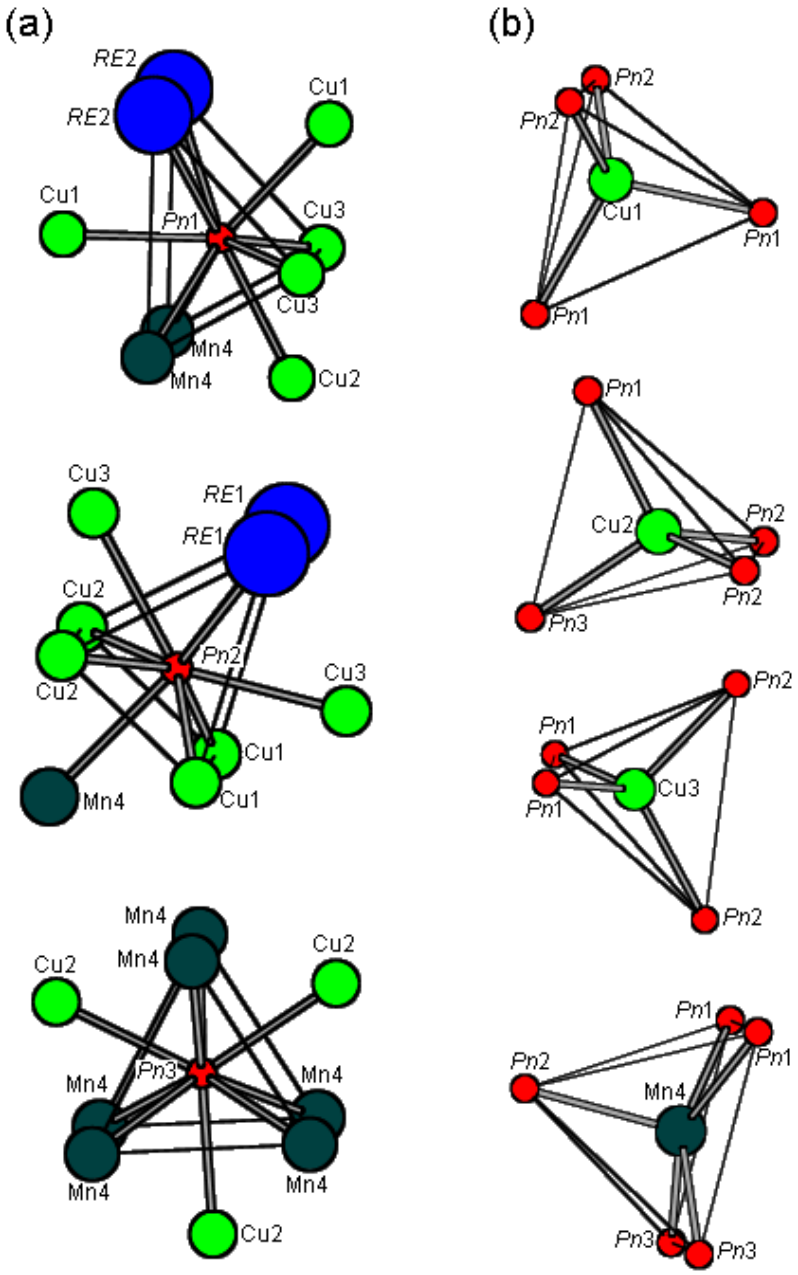


**Figure 2-3.** Coordination geometries in $RE_2Mn_3Cu_9Pn_7$ (*Pn* = P, As): (a) *Pn* atoms (CN9, tricapped trigonal prismatic). (b) Cu (CN4, tetrahedral) and Mn (CN5, square pyramidal) atoms.

Alternatively, it is worthwhile to focus on the coordination of *Pn* atoms around the *RE* or transition-metal atoms. Both *RE* sites have trigonal prismatic coordination (CN6).

The transition-metal atoms occupy four possible sites. The geometry is distorted tetrahedral (CN4) around the first three, but square pyramidal (CN5) around the fourth (**Figure 2-3b**). From the structural refinements, there is a clear preference of Cu atoms for the tetrahedral and Mn atoms for the square pyramidal sites. In $Zr_2Fe_{12}P_7$-type structures, the distances to the CN5 site are generally 0.1–0.2 Å longer than to the CN4 sites, so that larger atoms should prefer the former site. However, it is not so straightforward to apply a size argument to account for the site preferences. If Pauling metallic radii are consulted, they are found to be nearly identical (Mn, 1.178 Å; Cu 1.176 Å).[36] On the other hand, Shannon crystal radii (in which ionic bonding is assumed) tend to suggest that Mn cations are larger than Cu cations, all other things being equal (cf., $Mn^{2+}$, 0.80 Å (CN4), 0.89 (CN5); $Cu^{2+}$, 0.71 Å (CN4), 0.79 Å (CN5); $Cu^{+}$, 0.74 Å (CN4)).[37] Perhaps the most convincing evidence that supports the assignment of Cu vs. Mn sites comes from a comparison to MnCu*Pn* (*Pn* = P, As).[38] These ternary phases adopt the closely related TiNiSi-type structure, in which Cu atoms occupy tetrahedral sites and Mn atoms occupy square pyramidal sites, just as they do in the quaternary phases $RE_2Mn_3Cu_9Pn_7$. Moreover, in MnCu*Pn*, the Mn–*Pn* distances (Mn–P, 2.486–2.719 Å; Mn–As, 2.585–2.793 Å) are also ~0.2 Å longer than the Cu–*Pn* distances (Cu–P, 2.358–2.409 Å; Cu–As, 2.453–2.502 Å),[38] in good agreement with the values observed in $RE_2Mn_3Cu_9Pn_7$ (**Table 2-2**). Dhahri has proposed that the site preferences should be driven not by geometrical factors but rather by the need to maintain electroneutrality; that is, more electropositive and more highly charged metal atoms should prefer the higher CN site, which provides a greater number of anionic *Pn* atoms to satisfy the electroneutrality principle.[31] However, our inability to

prepare Ag-containing analogues suggests that both size and electronegativity are important factors.

The complete structural elucidation of all members of $RE_2Mn_3Cu_9Pn_7$ provides a good opportunity to identify systematic trends as a function of *RE*. As noted above, there is a clear demarcation of longer Mn–*Pn* and shorter Cu–*Pn* distances (**Figure 2-4**). Although the *average* Mn–*Pn* and Cu–*Pn* distances do not change much with *RE* substitution, the *ranges* of these distances, which give a measure of the degree of distortion in the coordination polyhedra, do show smooth trends. Among the three types of Cu-centred tetrahedra, the ones around Cu2 tend to be the most highly distorted. As smaller *RE* atoms are introduced into the structure, the distortions around Cu2, Cu3, and Mn4 become attenuated, but this is counteracted by greater distortion around Cu1. These competing trends define the limits for the largest and smallest *RE* atoms that can be substituted in the series.

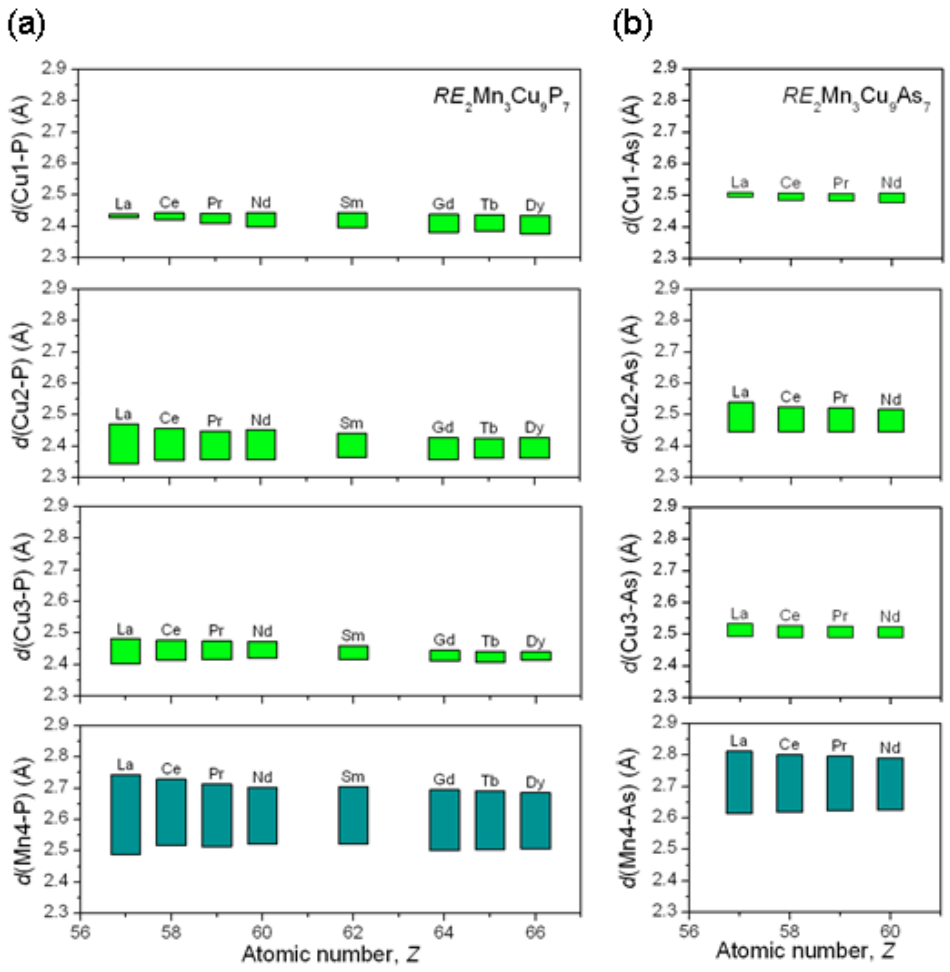


**Figure 2-4.** Ranges of Cu–*Pn* and Mn–*Pn* distances in (a) $RE_2Mn_3Cu_9P_7$ and (b) $RE_2Mn_3Cu_9As_7$ as a function of *RE*.

In $Zr_2Fe_{12}P_7$-type pnictide phases, it has been speculated that metal-pnicogen bonding interactions should be the most important, followed by metal-metal bonding interactions.[20] However, to our knowledge, no electronic structure calculations have been reported previously to quantify these assertions. The electronic band structure has now been calculated for $La_2Mn_3Cu_9P_7$. Consistent with the directions of electron transfer expected from the relative electronegativities of the component elements (La, 1.1; Mn, 1.6; Cu 1.9; P, 2.2),[36] the density of states (DOS) curve reveals nearly empty La states, partly

filled Mn states, mostly filled Cu states, and nearly completely filled P states below the Fermi level (**Figure 2-5a**). The Cu 3d states contribute to the wide energy manifold from –7 to –1 eV, whereas Mn 3d states contribute to the narrower one from –1 to 1 eV; both overlap with P 3p states in this region. (The P 3s states are found deeper in energy, at –12 eV.) The considerable mixing of these states leads to strong bonding interactions for Mn–P (1.28 eV/bond) and Cu–P contacts (1.62 eV/bond). The bonding is not quite optimized, with weakly antibonding Mn–P levels being occupied below the Fermi level and weakly bonding Cu–P levels still available above the Fermi level, as seen in the crystal orbital Hamilton population (–COHP) curves (**Figure 2-5b**). There are also less significant La–P bonding interactions (0.76 eV/bond) arising from the small mixing of La- and P-based states. If metal-metal contacts shorter than 3.0 Å are considered, they are found to be relatively weak (Mn–Cu, 0.41 eV/bond; Cu–Cu, 0.40 eV/bond).

The absence of a band gap in the DOS curve implies metallic behaviour in $La_2Mn_3Cu_9P_7$. A preliminary electrical resistivity measurement on the cerium analogue $Ce_2Mn_3Cu_9P_7$ confirms this prediction (**Figure 2-6**). Although the resistivity decreases as the temperature is lowered, it undergoes two sharp transitions at 165 and 18 K, which are likely related to the onset of long-range magnetic ordering transitions. Fuller interpretation will have to await magnetic measurements, which requires synthetic optimization to improve sample purity.

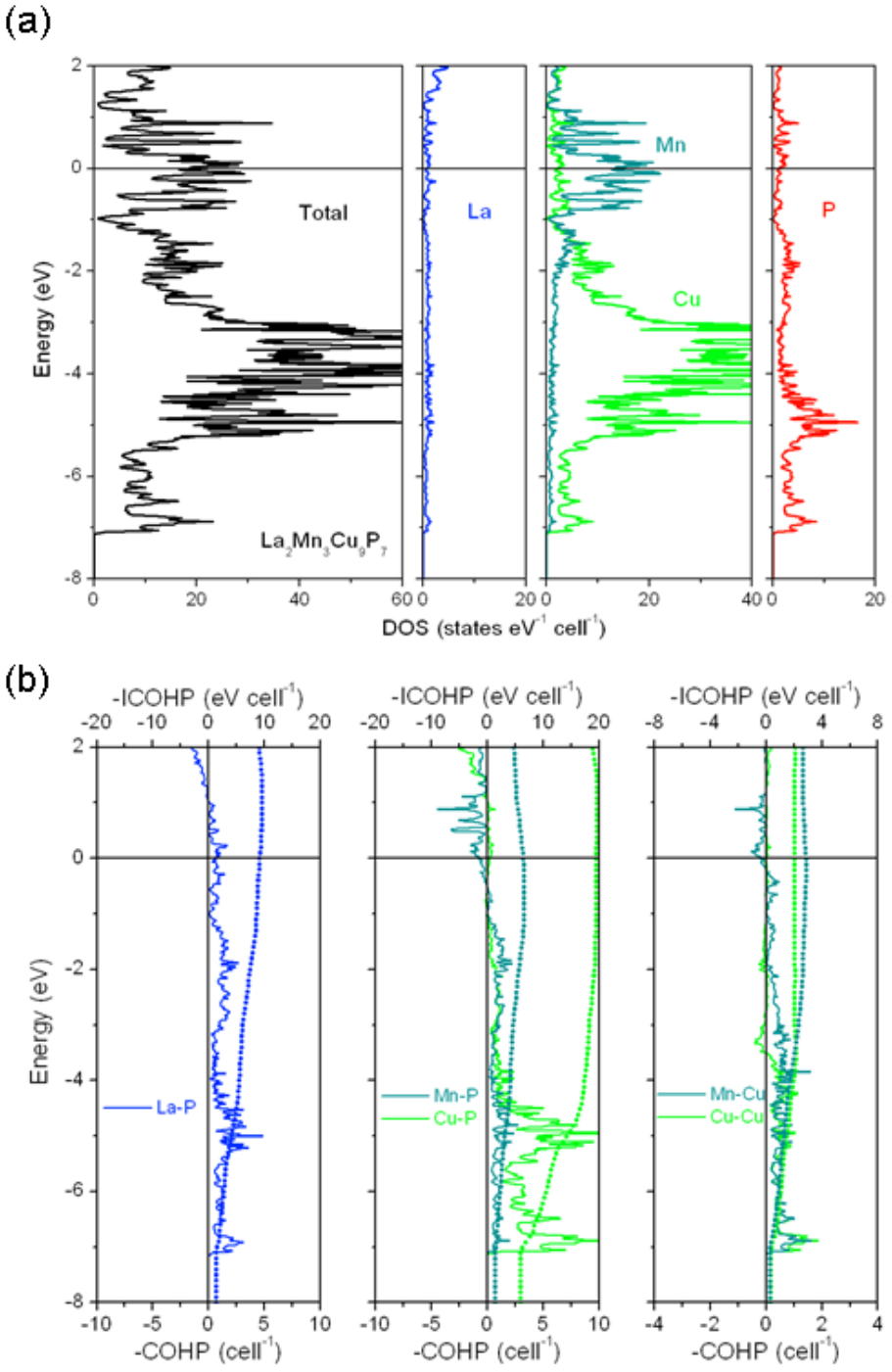


**Figure 2-5.** $La_2Mn_3Cu_9P_7$: (a) Density of states (DOS) and its atomic projections. (b) Crystal orbital Hamilton population (–COHP) curves. The Fermi level is at 0 eV.

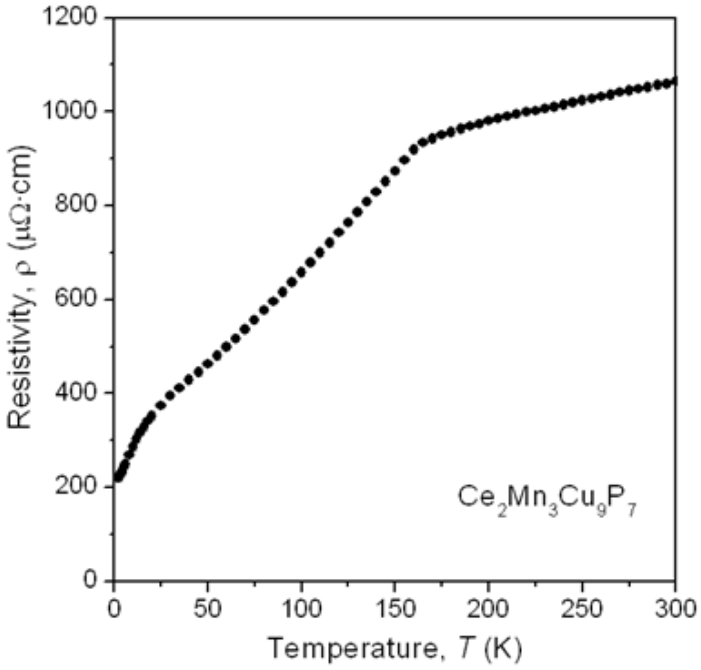


**Figure 2-6.** Plot of electrical resistivity vs. temperature for $Ce_2Mn_3Cu_9P_7$.

## 2.4 Conclusion

The formation of the quaternary pnictides $RE_2Mn_3Cu_9Pn_7$ (*Pn* = P, As) illustrates that cation ordering can be achieved in $Zr_2Fe_{12}P_7$-type structures. Given that the preparation of the corresponding Ag analogues "$RE_2Mn_3Ag_9Pn_7$" fails, this ordering appears to be strictly limited to conditions in which smaller cations occupy the CN4 sites. It would be interesting to determine if higher members of the $RE_{n(n-1)}M_{(n+1)(n+2)}Pn_{n(n+1)+1}$ homologous series are also amenable to ordering if two different *M* components are introduced. The next member after the $Zr_2Fe_{12}P_7$-type ($n$ = 2) is the $Zr_6Ni_{20}P_{13}$-type structure ($n$ = 3), which contains not only square pyramidal and tetrahedral sites, but also trigonal planar sites. We have attempted to synthesize "$RE_6Mn_3Cu_{17}Pn_{13}$" (*RE* = Nd; *Pn* = P, As) in which the Mn atoms would occupy the square pyramidal sites, but obtained

only mixtures of binary and ternary phases. Successful synthesis of these metal-rich phases may be highly sensitive to reaction conditions such as temperature, which will need to be optimized. Nevertheless, this approach of targeting phases based on the predicted compositions of hypothetical structures serves as a useful tool for solid-state synthesis.

## 2.5 References


1. Pivan, J. -Y.; Guérin, R.; Sergent, M. *J. Solid State Chem.* **1987**, *68*, 11–21.
2. Jeitschko, W.; Pollmeier, P. G.; Meisen, U. *J. Alloys Compd.* **1993**, *196*, 105–109.
3. Jeitschko, W.; Braun, D. J.; Ashcraft, R. H.; Marchand, R. *J. Solid State Chem.* **1978**, *25*, 309–313.
4. Jeitschko, W.; Meisen, U.; Scholz, U. D. *J. Solid State Chem.* **1984**, *55*, 331–336.
5. Oryshchyn, S. V.; Zhak, O. V.; Budnyk, S. L.; Kuz'ma, Yu. B. *Russ. J. Inorg. Chem. (Engl. Transl.)* **2002**, *47*, 1411–1414; *Zh. Neorg. Khim.* **2002**, *47*, 1541–1544.
6. Jeitschko, W.; Jaberg, B. *Z. Anorg. Allg. Chem.* **1980**, *467*, 95–104.
7. Jeitschko, W.; Reinbold, E. J. *Z. Naturforsch. B: Anorg. Chem., Org. Chem.* **1985**, *40*, 900–905.
8. Budnyk, S.; Kuz'ma, Yu. B. *Pol. J. Chem.* **2002**, *76*, 1553–1558.
9. Pivan, J. Y.; Guérin, R.; Padiou, J.; Sergent, M. *J. Less-Common Met.* **1986**, *118*, 191–200.
10. Oryshchyn, S.; Babizhetsky, V.; Stoyko, S.; Kuz'ma, Yu. *Z. Kristallogr. – New Cryst. Struct.* **1999**, *214*, 428.
11. Braun, T. P.; DiSalvo, F. J. *J. Alloys Compd.* **2000**, *307*, 111–113.
12. Wurth, A.; Keimes, V.; Johrendt, D.; Mewis, A. *Z. Anorg. Allg. Chem.* **2001**, *627*, 2183–2190.
13. Stoyko, S.; Oryshchyn, S. V. *Coll. Abs. 9th Int. Conf. Crystal Chem. Intermet. Compd. (Lviv)* **2005**, *58*.
14. Jeitschko, W.; Jaberg, B. *J. Less-Common Met.* **1981**, *79*, 311–314.
15. Babizhets'ky, V.; Le Sénéchal, C.; Bauer, J.; Députier, S.; Guérin, R. *J. Alloys Compd.* **1999**, *287*, 174–180.

16. Babizhetskyy, V.; Guérin, R.; Simon, A. *Z. Naturforsch., B: J. Chem. Sci.* **2006**, *61*, 733–740.

17. Zelinska, M.; Zhak, O.; Oryshchyn, S.; Polianska, T.; Pivan, J.-Y. *Z. Naturforsch., B: J. Chem. Sci.* **2007**, *62*, 1143–1152.

18. Probst, H.; Mewis, A. *Z. Anorg. Allg. Chem.* **1991**, *597*, 173–182.

19. Stępień-Damm, H.; Kaczorowski, D.; Wochowski, K. *J. Alloys Compd.* **2001**, *315*, L4–L6.

20. Jeitschko, W.; Meisen, U.; Albering, J. *Dalton Trans.* **2010**, *39*, 6067–6073.

21. Pivan, J. Y.; Guérin, R.; Sergent, M. *J. Less-Common Met.* **1985**, *107*, 249–258.

22. Reehuis, M; Jeitschko, W. *J. Phys. Chem. Solids* **1989**, *50*, 563–569.

23. El Ghadraoui, E. H.; Pivan, J. Y.; Peña, O.; Guérin, R.; Bonville, P. *Physica B* **1990**, *163*, 185–187.

24. Zeppenfeld, K.; Jeitschko, W. *J. Phys. Chem. Solids* **1993**, *54*, 1527–1531.

25. Reehuis, M.; Ouladdiaf, B.; Jeitschko, W.; Vomhof, T.; Zimmer, B.; Ressouche, E. *J. Alloys Compd.* **1997**, *261*, 1–11.

26. Ebel, T.; Albering, J. H.; Jeitschko, W. *J. Alloys Compd.* **1998**, *266*, 71–76.

27. Babizhetskyy, V.; Isnard, O.; Hiebl, K. *Solid State Commun.* **2007**, *142*, 80–84.

28. Jeitschko, W.; Meisen, U.; Reinbold, E. J. *Z. Anorg. Allg. Chem.* **2012**, *638*, 770–778.

29. Budnyk, S.; Prots, Yu.; Schmidt, M.; Schnelle, W.; Kuz'ma, Yu.; Grin, Yu. *Z. Anorg. Allg. Chem.* **2004**, *630*, 1062–1067.

30. Lorenz, P.; Jung, W. *Z. Anorg. Allg. Chem.* **2009**, *635*, 920–925.

31. Dhahri, E. *J. Phys.: Condens. Matter* **1996**, *8*, 4351–4360.

32. Sheldrick, G. M. *SHELXTL*, version 6.12; Bruker AXS Inc.: Madison, WI, 2001.

33. Ganglberger, E. *Monatsh. Chem.* **1968**, *99*, 557–565.

# Chapter 3

## Rare-Earth Manganese Copper Phosphides *RE*$MnCu_4P_3$ (*RE* = Gd–Ho): The First Quaternary Ordered Variants of the $YCo_5P_3$-Type Structure

*A version of this chapter has been published. Ramachandran, K. K.; Stoyko, S. S.; Mullen, C. S.; Mar, A. Inorg. Chem., 2015, 54, 860-866*

### 3.1 Introduction

A large number of ternary rare-earth transition-metal pnictides *RE–M–Pn*, mostly phosphides, have a metal-to-nonmetal ratio equal or close to 2:1, an indication of their close structural relationship to metal-rich binary pnictides $M_2Pn$.[1–3] These binary and ternary pnictides are attractive for their applications in catalysis (e.g. hydrodesulfurization and hydrodenitrogenation by $Ni_2P$ and its ternary derivatives)[4,5] and their exotic magnetic properties (e.g. unconventional quantum criticality in $RE_2M_{12}P_7$).[6] These compounds share a common motif of *Pn*-centred trigonal prisms, which can be connected in many different ways to generate several homologous series of structure types.[1–3] One extensive branch of hexagonal structures has the general formula $RE_{n(n-1)}M_{(n+1)(n+2)}Pn_{n(n+1)+1}$, whose members exhibit increasingly larger triangular assemblies of these trigonal prisms: $Fe_2P$ ($n$ = 1), $Zr_2Fe_{12}P_7$ ($n$ = 2), $Zr_6Ni_{20}P_{13}$ ($n$ = 3), and $(La,Ce)_{12}Rh_{30}P_{21}$ ($n$ = 4). A shorter branch of orthorhombic structures has the general formula $RE_{n(n-1)}M_{(n+1)(n+2)-2}Pn_{n(n+1)}$ and contains the same types of triangular assemblies but arranged in zigzag chains: $Co_2P$ ($n$ = 1) and $YCo_5P_3$ ($n$ = 2). The metal atoms can occupy up to four possible types of coordination environments: trigonal prisms (CN6), square pyramids (CN5), tetrahedra (CN4), and

trigonal planes (CN3). In accordance with the relative sizes of these sites, the general trend is that rare-earth metal atoms occupy CN6 sites, group 4 metal atoms occupy CN6 and CN5 sites, and remaining transition-metal atoms occupy CN5, CN4, and CN3 sites. The variety of available sites offers the possibility of site ordering when several types of metals having different sizes and coordination preferences are introduced. Although there are now hundreds of such ternary pnictides that demonstrate the viability of this principle, to date there have been very few examples of quaternary pnictides. Following up on an earlier report of the quaternary mixed-metal pnictides $RE_2M_3M'_9Pn_7$ ($M$ = Cr, W; $M'$ =Fe, Co; $Pn$ = P, As) for which only cell parameters were provided,[7] we recently prepared the series $RE_2Mn_3Cu_9Pn_7$ ($Pn$ = P, As) and confirmed that they adopt an ordered variant of the hexagonal $Zr_2Fe_{12}P_7$-type structure.[8] With this initial success, we wondered whether complex metal ordering could also be introduced into the orthorhombic branch of these 2:1 phases. The closest related example, with a metal-to-nonmetal ratio of slightly less than 2:1, is $LaZr_2Ni_4As_4$, which has a monoclinic structure resembling that of orthorhombic $YCo_5P_3$.[9]

This chapter discusses the synthesis and characterization of the series of rare-earth manganese copper phosphides $RE MnCu_4P_3$, which are the first examples of quaternary ordered derivatives of the $YCo_5P_3$-type structure. The electronic structure of the hypothetical compound $YMnCu_4P_3$ was examined and the electrical resistivity of $TbMnCu_4P_3$ was measured.

## 3.2 Experimental

### 3.2.1 Synthesis

Starting materials were freshly filed *RE* pieces (99.9%, Hefa), Mn powder (99.6%, Alfa-Aesar), Cu powder (99.8%, Alfa-Aesar), and red P powder (99.9%, Alfa-Aesar). In the course of reactions intended to prepare $RE_2Mn_3Cu_9P_7$ (which forms for *RE* = La–Nd, Sm, Gd–Dy), other quaternary phases with slightly different composition were formed for the later *RE* components starting from Gd, which were subsequently identified to be $REMnCu_4P_3$. Thus, mixtures of the elements in this precise stoichiometry, on a 0.3-g scale, were pressed into pellets and loaded into fused-silica tubes which were evacuated, sealed, and heated at 800 °C for 10 days. To promote crystal growth, the products of these reactions were reground, pressed into pellets, and subjected to the same heat treatment again in the presence of about 30 mg of $I_2$, which acts as a mineralizing agent. Analysis by powder X-ray diffraction (XRD), performed with Cu $K\alpha_1$ radiation on an Inel diffractometer equipped with a curved position-sensitive detector (CPS 120), revealed that the samples generally consisted of not more than ~50% of $REMnCu_4P_3$. It was difficult to obtain phase-pure samples of $REMnCu_4P_3$ because of the closeness of their compositions to those of the competing quaternary phases $RE_2Mn_3Cu_9P_7$, which were often found in smaller amounts in the samples, along with binary phosphides; this is a common problem in the synthesis of other metal-rich phases with metal-to-nonmetal ratio of 2:1.[10] The range of *RE* substitution was found to be limited to Gd–Ho. The corresponding arsenides did not form under the synthetic conditions above. Attempts were also made to elucidate the possibility of a solid solution $RE(Mn_xCu_{1-x})_5P_3$ (*RE* = Tb, Ho; $x$ = 0 to 1 in increments of

0.2); only the $x = 0.2$ member, corresponding to *RE*$MnCu_4P_3$, formed. Energy-dispersive X-ray (EDX) analysis on crystals of *RE*$MnCu_4P_3$ was carried out on a JEOL JSM-6010LA scanning electron microscope, indicating reasonable agreement with expectations (**Table 3-1**). However, distinguishing between crystals of *RE*$MnCu_4P_3$ and $RE_2Mn_3Cu_9P_7$ was challenging because of their similar needle-shaped habits and chemical compositions. Ultimately, single-crystal X-ray diffraction experiments were essential to confirm their identity.

**Table 3-1.** EDX Analyses (atomic %) of *RE*$MnCu_4P_3$ Crystals [a]

| compound | *RE* | Mn | Cu | P |
|---|---|---|---|---|
| $GdMnCu_4P_3$ | 10(1) | 12(1) | 41(2) | 37(3) |
| $TbMnCu_4P_3$ | 11(1) | 12(1) | 44(2) | 33(2) |
| $DyMnCu_4P_3$ | 13(1) | 9(1) | 46(2) | 33(2) |
| $HoMnCu_4P_3$ | 12(1) | 11(1) | 45(2) | 32(4) |

[a] Expected composition is 11.1% *RE*, 11.1% Mn, 44.5% Cu, and 33.3% P.

### 3.2.2 Structure Determination

Intensity data were collected at –100 °C on a Bruker PLATFORM diffractometer equipped with a SMART APEX II CCD area detector and a graphite-monochromated Mo $K\alpha$ radiation source, using $\omega$ scans in 5–8 batches at different $\phi$ angles with a frame width of 0.3° and an exposure time of 15 or 20 s per frame. Face-indexed numerical absorption corrections were applied. Structure refinements were carried out with use of the SHELXTL (version 6.12) program package.[11] The centrosymmetric orthorhombic space

group *Pnma* was chosen on the basis of Laue symmetry and intensity statistics. Direct methods revealed all initial atomic positions, which were standardized with the program STRUCTURE TIDY.[12] Among the five metal sites available, one was occupied by Mn and four by Cu atoms. This ordered model was confirmed by refinements in which each site was allowed to be occupied by a mixture of Mn and Cu atoms with no restriction placed on the overall composition. In $GdMnCu_4P_3$, for example, the nominal Mn site contained 0.89(2) Mn and 0.11(2) Cu, whereas the four nominal Cu sites contained 0.00(2)–0.05(2) Mn and 0.95(2)–1.00(2) Cu. The Mn site consistently exhibited higher displacement parameters than the Cu sites. However, when the occupancy of this site was freely refined, it converged to 1.03(1) Mn in $GdMnCu_4P_3$. Elevated displacement parameters for this site are observed in other $YCo_5P_3$-type structures and are likely inherent to its higher coordination (CN5).[13] After final refinements, agreement factors were acceptable and difference electron density maps were featureless. Abbreviated crystallographic data are listed in **Table 3-2**, atomic coordinates and displacement parameters in **Table 3-4**, and selected interatomic distances in **Table 3-5**. Full crystallographic details are listed in **Table 3-3** and further data in the form of crystallographic information files (CIFs) are available as Supporting Information.

**Table 3-2.** Crystallographic Data for *RE*$MnCu_4P_3$ (*RE* = Gd–Ho)

| | $GdMnCu_4P_3$ | $TbMnCu_4P_3$ | $DyMnCu_4P_3$ | $HoMnCu_4P_3$ |
|---|---|---|---|---|
| fw (amu) | 559.26 | 560.93 | 564.51 | 566.94 |
| space group | *Pnma* (No. 62) | *Pnma* (No. 62) | *Pnma* (No. 62) | *Pnma* (No. 62) |
| *a* (Å) | 12.667(2) | 12.6535(4) | 12.6485(4) | 12.6489(4) |
| *b* (Å) | 3.8119(7) | 3.7955(1) | 3.7841(1) | 3.7755(1) |
| *c* (Å) | 10.895(2) | 10.8761(3) | 10.8680(3) | 10.8632(4) |

| | | | | |
|---|---|---|---|---|
| $V$ (Å$^3$) | 526.05(17) | 522.34(3) | 520.18(3) | 518.78(3) |
| $Z$ | 4 | 4 | 4 | 4 |
| $T$ (K) | 173 | 173 | 173 | 173 |
| $\rho_{calcd}$ (g cm$^{-3}$) | 7.061 | 7.133 | 7.208 | 7.259 |
| $\lambda$ (Å) | 0.71073 | 0.71073 | 0.71073 | 0.71073 |
| $\mu$(Mo $K\alpha$) (mm$^{-1}$) | 31.38 | 32.45 | 33.35 | 34.29 |
| $R(F)$ for $F_o^2 > 2\sigma(F_o^2)$ [a] | 0.019 | 0.020 | 0.022 | 0.016 |
| $R_w(F_o^2)$ [b] | 0.046 | 0.045 | 0.051 | 0.035 |

[a] $R(F) = \sum||F_o| - |F_c|| / \sum|F_o|$. [b] $R_w(F_o^2) = [\sum[w(F_o^2 - F_c^2)^2] / \sum wF_o^4]^{1/2}$; $w^{-1} = [\sigma^2(F_o^2) + (Ap)^2 + Bp]$, where $p = [\max(F_o^2,0) + 2F_c^2] / 3$.

**Table 3-3.** Crystallographic Data for *RE*MnCu$_4$P$_3$ (*RE* = Gd–Ho)

| formula | GdMnCu$_4$P$_3$ | TbMnCu$_4$P$_3$ | DyMnCu$_4$P$_3$ | HoMnCu$_4$P$_3$ |
|---|---|---|---|---|
| fw (amu) | 559.26 | 560.93 | 564.51 | 566.94 |
| space group | *Pnma* (No. 62) | *Pnma* (No. 62) | *Pnma* (No. 62) | *Pnma* (No. 62) |
| $a$ (Å) | 12.667(2) | 12.6535(4) | 12.6485(4) | 12.6489(4) |
| $b$ (Å) | 3.8119(7) | 3.7955(1) | 3.7841(1) | 3.7755(1) |
| $c$ (Å) | 10.895(2) | 10.8761(3) | 10.8680(3) | 10.8632(4) |
| $V$ (Å$^3$) | 526.05(17) | 522.34(3) | 520.18(3) | 518.78(3) |
| $Z$ | 4 | 4 | 4 | 4 |
| $T$ (K) | 173 | 173 | 173 | 173 |
| $\rho_{calcd}$ (g cm$^{-3}$) | 7.061 | 7.133 | 7.208 | 7.259 |
| crystal dimensions (mm) | 0.17 × 0.07 × 0.03 | 0.21 × 0.08 × 0.05 | 0.20 × 0.14 × 0.06 | 0.43 × 0.03 × 0.03 |
| radiation | graphite monochromated Mo $K\alpha$, $\lambda$ = 0.71073 Å | | | |
| $\mu$(Mo $K\alpha$) (mm$^{-1}$) | 31.38 | 32.45 | 33.35 | 34.29 |
| transmission factors | 0.080–0.572 | 0.016–0.307 | 0.029–0.324 | 0.060–0.505 |
| $2\theta$ limits | 4.93–66.49° | 4.94–66.56° | 4.94–66.42° | 4.94–66.39° |
| data collected | $-19 \le h \le 19$, $-5 \le k \le 5$, $-16 \le l \le 16$ | $-19 \le h \le 19$, $-5 \le k \le 5$, $-16 \le l \le 16$ | $-19 \le h \le 19$, $-5 \le k \le 5$, $-16 \le l \le 16$ | $-19 \le h \le 19$, $-5 \le k \le 5$, $-16 \le l \le 16$ |
| no. of data collected | 7031 | 7202 | 7014 | 7113 |
| no. of unique data, including $F_o^2 < 0$ | 1124 ($R_{int}$ = 0.034) | 1129 ($R_{int}$ = 0.023) | 1115 ($R_{int}$ = 0.033) | 1108 ($R_{int}$ = 0.022) |

| | | | | |
|---|---|---|---|---|
| no. of unique data, with $F_o^2 > 2\sigma(F_o^2)$ | 1062 | 1077 | 1087 | 1026 |
| no. of variables | 56 | 56 | 56 | 56 |
| $R(F)$ for $F_o^2 > 2\sigma(F_o^2)$ [a] | 0.019 | 0.020 | 0.022 | 0.016 |
| $R_w(F_o^2)$ [b] | 0.046 | 0.045 | 0.051 | 0.035 |
| Goodness of fit | 1.05 | 1.10 | 1.17 | 1.07 |
| $(\Delta\rho)_{max}$, $(\Delta\rho)_{min}$ (e Å$^{-3}$) | 3.24, –1.58 | 2.81, –2.97 | 2.27, –3.46 | 3.56, –2.01 |

**Table 3-4.** Atomic Coordinates and Equivalent Isotropic Displacement Parameters for *RE*$MnCu_4P_3$ (*RE* = Gd–Ho)

| Atom [a] | *x* | *Y* | *z* | $U_{eq}$ (Å$^2$) [b] |
|---|---|---|---|---|
| $GdMnCu_4P_3$ | | | | |
| Gd | 0.29164(2) | ¼ | 0.92055(2) | 0.00530(7) |
| Mn | 0.01802(6) | ¼ | 0.79141(7) | 0.01327(14) |
| Cu1 | 0.00524(4) | ¼ | 0.41028(5) | 0.00772(11) |
| Cu2 | 0.06429(4) | ¼ | 0.03921(5) | 0.00705(11) |
| Cu3 | 0.30501(4) | ¼ | 0.62889(5) | 0.00761(11) |
| Cu4 | 0.32212(4) | ¼ | 0.21645(5) | 0.00740(11) |
| P1 | 0.11478(8) | ¼ | 0.59499(10) | 0.00540(18) |
| P2 | 0.13005(8) | ¼ | 0.24297(10) | 0.00564(18) |
| P3 | 0.37862(8) | ¼ | 0.42212(9) | 0.00525(18) |
| $TbMnCu_4P_3$ | | | | |
| Tb | 0.29139(2) | ¼ | 0.92061(2) | 0.00559(7) |
| Mn | 0.01840(6) | ¼ | 0.79065(7) | 0.01336(14) |
| Cu1 | 0.00499(4) | ¼ | 0.41080(5) | 0.00792(11) |
| Cu2 | 0.06430(4) | ¼ | 0.03966(5) | 0.00730(11) |
| Cu3 | 0.30535(4) | ¼ | 0.62915(5) | 0.00781(11) |
| Cu4 | 0.32170(4) | ¼ | 0.21628(5) | 0.00761(11) |
| P1 | 0.11560(8) | ¼ | 0.59406(10) | 0.00557(18) |
| P2 | 0.12981(8) | ¼ | 0.24431(10) | 0.00562(17) |
| P3 | 0.37815(8) | ¼ | 0.42199(9) | 0.00540(18) |
| $DyMnCu_4P_3$ | | | | |
| Dy | 0.29123(2) | ¼ | 0.92067(2) | 0.00506(8) |

| | | | | |
|---|---|---|---|---|
| Mn | 0.01841(6) | ¼ | 0.79074(7) | 0.01228(15) |
| Cu1 | 0.00497(4) | ¼ | 0.41102(5) | 0.00727(12) |
| Cu2 | 0.06443(4) | ¼ | 0.03997(5) | 0.00667(12) |
| Cu3 | 0.30531(4) | ¼ | 0.62922(5) | 0.00709(12) |
| Cu4 | 0.32149(5) | ¼ | 0.21631(5) | 0.00697(11) |
| P1 | 0.11606(9) | ¼ | 0.59359(10) | 0.00500(19) |
| P2 | 0.12967(8) | ¼ | 0.24496(10) | 0.00495(18) |
| P3 | 0.37780(9) | ¼ | 0.42193(9) | 0.00486(19) |
| $HoMnCu_4P_3$ | | | | |
| Ho | 0.29110(2) | ¼ | 0.92089(2) | 0.00643(5) |
| Mn | 0.01874(6) | ¼ | 0.78984(7) | 0.01396(13) |
| Cu1 | 0.00493(4) | ¼ | 0.41148(5) | 0.00867(10) |
| Cu2 | 0.06436(4) | ¼ | 0.04035(5) | 0.00808(10) |
| Cu3 | 0.30550(4) | ¼ | 0.62948(5) | 0.00841(10) |
| Cu4 | 0.32111(4) | ¼ | 0.21632(5) | 0.00839(10) |
| P1 | 0.11648(8) | ¼ | 0.59317(10) | 0.00637(17) |
| P2 | 0.12968(8) | ¼ | 0.24582(10) | 0.00657(17) |
| P3 | 0.37753(8) | ¼ | 0.42185(10) | 0.00637(17) |

[a] All atoms in Wyckoff position 4*c*. [b] $U_{eq}$ is defined as one-third of the trace of the orthogonalized $U_{ij}$ tensor.

**Table 3-5.** Interatomic Distances (Å) for *RE*$MnCu_4P_3$ (*RE* = Gd–Ho)

| | $GdMnCu_4P_3$ | $TbMnCu_4P_3$ | $DyMnCu_4P_3$ | $HoMnCu_4P_3$ |
|---|---|---|---|---|
| *RE*–P3 (×2) | 2.8783(9) | 2.8642(8) | 2.8550(9) | 2.8484(8) |
| *RE*–P2 (×2) | 2.8913(9) | 2.8761(8) | 2.8683(9) | 2.8609(8) |
| *RE*–P1 (×2) | 2.9409(9) | 2.9233(8) | 2.9132(8) | 2.9038(8) |
| Mn–P1 | 2.4661(13) | 2.4666(13) | 2.4731(13) | 2.4684(13) |
| Mn–P2 (×2) | 2.7001(10) | 2.6950(9) | 2.6904(9) | 2.6904(9) |
| Mn–P3 (×2) | 2.7156(10) | 2.7121(9) | 2.7086(10) | 2.7095(9) |
| Cu1–P2 | 2.4129(12) | 2.4027(12) | 2.3969(12) | 2.3934(12) |
| Cu1–P1 (×2) | 2.4387(8) | 2.4357(8) | 2.4343(8) | 2.4341(7) |
| Cu1–P1 | 2.4443(12) | 2.4355(12) | 2.4313(12) | 2.4263(12) |

| | | | | |
|---|---|---|---|---|
| Cu2–P2 | 2.3710(13) | 2.3752(12) | 2.3758(12) | 2.3801(12) |
| Cu2–P3 | 2.3892(12) | 2.3922(12) | 2.3966(12) | 2.3987(12) |
| Cu2–P3 (×2) | 2.4048(8) | 2.4020(7) | 2.3999(7) | 2.4003(7) |
| Cu3–P2 (×2) | 2.4195(8) | 2.4173(8) | 2.4163(8) | 2.4152(8) |
| Cu3–P1 | 2.4377(13) | 2.4311(12) | 2.4249(13) | 2.4232(12) |
| Cu3–P3 | 2.4380(12) | 2.4341(12) | 2.4322(12) | 2.4325(12) |
| Cu4–P3 | 2.3521(12) | 2.3486(12) | 2.3455(11) | 2.3439(12) |
| Cu4–P2 | 2.4501(12) | 2.4472(12) | 2.4461(12) | 2.4426(12) |
| Cu4–P1 (×2) | 2.4541(8) | 2.4490(7) | 2.4460(8) | 2.4446(7) |
| Mn–Cu2 | 2.7626(11) | 2.7698(12) | 2.7705(10) | 2.7189(9) |
| Mn–Cu3 | 2.8345(11) | 2.8335(10) | 2.8323(10) | 2.8361(9) |
| Mn–Cu2 (×2) | 2.8504(8) | 2.8465(7) | 2.8395(7) | 2.8410(7) |
| Mn–Cu4 (×2) | 2.8982(8) | 2.8895(7) | 2.8871(7) | 2.8818(7) |
| Mn–Cu1 (×2) | 2.9236(8) | 2.9137(7) | 2.9113(7) | 2.9045(7) |
| Cu1–Cu4 | 2.6993(9) | 2.6999(8) | 2.7020(8) | 2.7080(8) |
| Cu1–Cu1 (×2) | 2.7335(8) | 2.7171(8) | 2.7085(8) | 2.6978(8) |
| Cu2–Cu2 (×2) | 2.6486(8) | 2.6445(7) | 2.6441(8) | 2.6426(7) |
| Cu2–Cu3 (×2) | 2.7071(6) | 2.6962(5) | 2.6899(6) | 2.6852(5) |
| Cu3–Cu4 (×2) | 2.6714(6) | 2.6616(5) | 2.6548(6) | 2.6493(5) |

### 3.2.3 Band Structure Calculation

Tight-binding linear muffin tin orbital band structure calculations were performed on a hypothetical $YMnCu_4P_3$ model within the local density and atomic spheres approximation with use of the Stuttgart TB-LMTO-ASA program (version 4.7).[14] The basis set consisted of Y 5s/5p/4d/4f, Mn 4s/4p/3d, Cu 4s/4p/3d, and P 3s/3p/3d orbitals, with the Y 5p/4f and P 3d orbitals being downfolded. Integrations in reciprocal space were

carried out with an improved tetrahedron method over 576 irreducible *k*-points with the first Brillouin zone. The calculations were repeated with spin-polarization included.

### 3.2.4 Electrical Resistivity

From a relatively long crystal (~1 mm) of $TbMnCu_4P_3$, a small fragment was cut off and confirmed by single-crystal X-ray diffraction to be the desired phase. The remainder of this crystal was mounted for standard four-probe electrical resistivity measurements, made between 2 to 300 K on a Quantum Design Physical Property Measurement System (PPMS) equipped with an ac transport controller (Model 7100). The current was 100 μA and the frequency was 16 Hz. The measurement was repeated twice on this sample and was reproducible on a second sample.

## 3.3 Results and Discussion

The quaternary rare-earth phosphides $REMnCu_4P_3$ could be obtained by reactions of the elements at 800 °C for later *RE* members (Gd–Ho), whose unit cell volumes decrease regularly in accordance with the lanthanide contraction (**Figure 3-1**). There was no evidence for existence of a solid solution $RE(Mn_xCu_{1-x})_5P_3$ and the hypothetical end-members $REMn_5P_3$ and $RECu_5P_3$ are unknown. They are the first well-characterized examples of quaternary ordered representatives of the orthorhombic $YCo_5P_3$-type structure.[13] Previous examples of this structure type were restricted to ternary phases, mostly phosphides ($REFe_5P_3$, $RECo_5P_3$, $ThFe_5P_3$, $UMn_5P_3$)[10,13,15–19] but also a few arsenides ($YCo_5As_3$),[20] germanides ($TbMn_5Ge_3$),[21] and indides ($AMg_5In_3$ (*A* = Sr, Ba) and $Ca_2Au_3In_4$ having a different site ordering).[22,23] The possibility for more complex ordering was already suggested with the initial discovery of $YCo_5P_3$ itself several decades ago

(through the proposal of a compound such as $YRhCo_4P_3$), but no evidence had been forthcoming.[13] Site ordering in the closely related hexagonal $Zr_2Fe_{12}P_7$-type structure was recently demonstrated in the quaternary phosphides $RE_2Mn_3Cu_9P_7$, which forms for a much wider range of *RE* members (La–Nd, Sm, Gd–Dy).[8] In fact, these two types of quaternary phases are often found together during synthesis and, as has been noted previously, it is difficult in general to obtain single-phase samples of $YCo_5P_3$- or $Zr_2Fe_{12}P_7$-type phases given their similar compositions.[10]

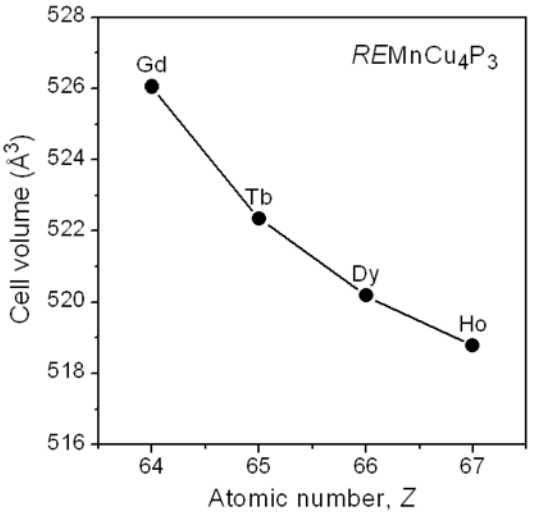


**Figure 3-1.** Plot of unit cell volumes for $REMnCu_4P_3$ (*RE* = Gd–Ho).

In the structure of $REMnCu_4P_3$, all P atoms are located within centres of trigonal prisms with metal atoms at the vertices; this coordination geometry is augmented by three further metal atoms capping the rectangular faces of the trigonal prisms to give CN9 (**Figure 3-2**). The P-centred trigonal prisms are arranged in groups of three sharing a common *RE–RE* edge, forming propellor-shaped units. The trigonal prisms extend as confacial columns along the *b*-direction and the propellor-shaped units are connected in a zigzag manner along the *a*-direction, resulting in corrugated layers parallel to the *ab*-plane.

(In the related orthorhombic $LaCo_5P_3$- and $UNi_5Si_3$-type structures, similar propellor-shaped units are also present but they are connected in different ways.[13]) All atoms are located at either $y$ = ¼ or ¾, such that these layers are alternately displaced as they stack along the *c*-direction. Within the five transition-metal sites, Mn atoms occupy the larger one coordinated by P atoms in a square-pyramidal geometry (CN5; 2.47–2.72 Å) and Cu atoms occupy the remaining four coordinated in a tetrahedral geometry (CN4; 2.34–2.45 Å) (**Figure 3-3**). There is no tendency for site mixing, as confirmed by the structural refinements and by the inability to prepare other members of the hypothetical solid solutions $RE(Mn_xCu_{1-x})_5P_3$.

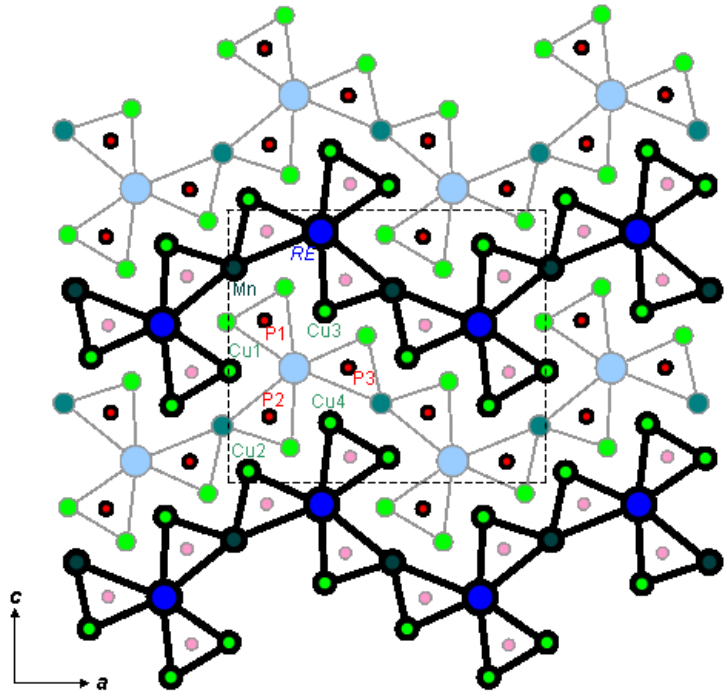


**Figure 3-2.** Structure of $RE$MnCu$_4$P$_3$ ($RE$ = Gd–Ho) built up of propellor-shaped units of trigonal prisms with P atoms (red) at centers and RE (blue), Mn (dark cyan), and Cu atoms (green) at vertices. Thick and thin lines distinguish between atoms displaced by half the b-parameter.

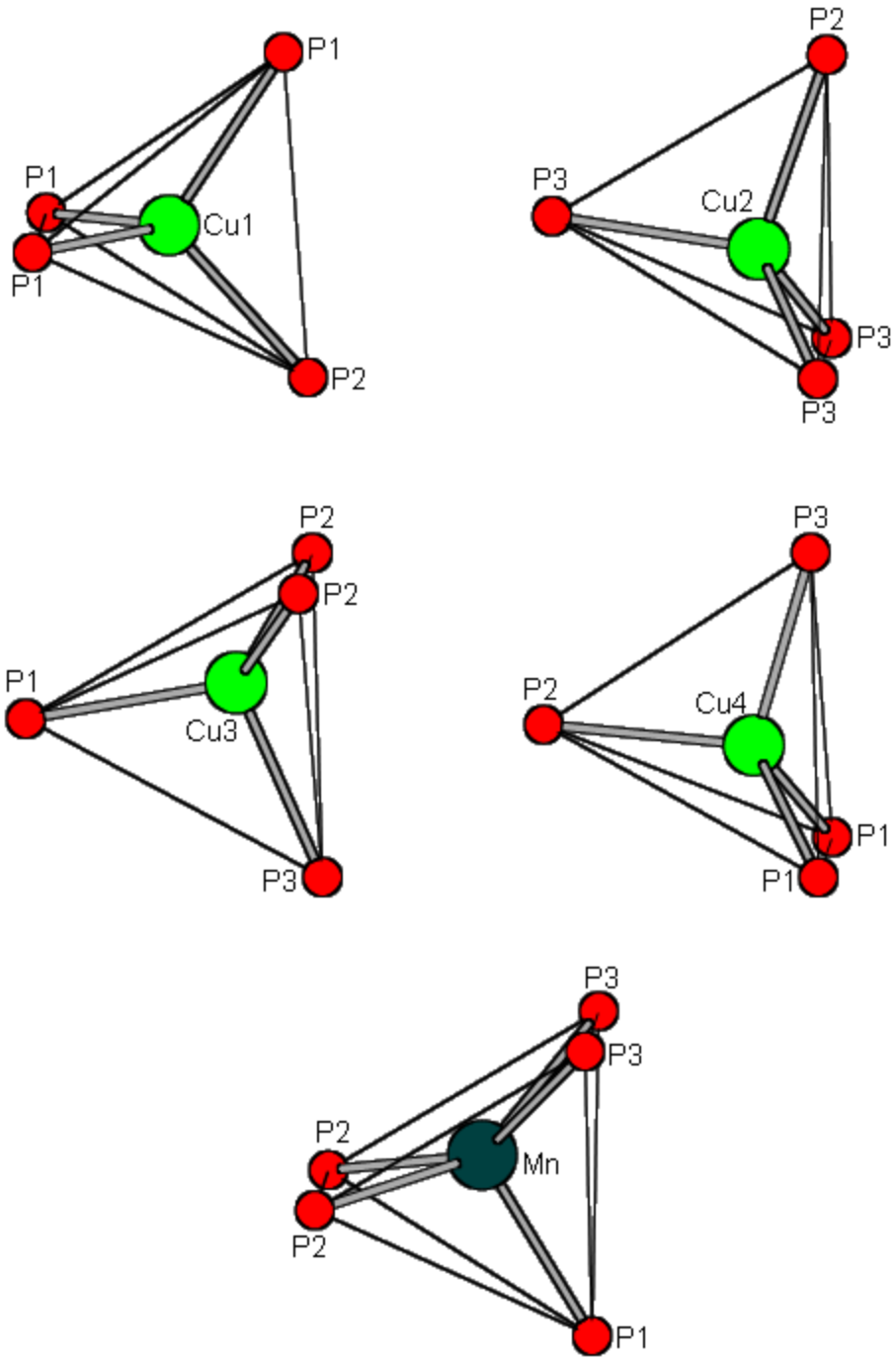


**Figure 3-3.**Coordination geometries of Cu and Mn atoms in *RE*$MnCu_4P_3$.

An alternate way to describe the structure is to focus on large triangular assemblies "$AB_6C_3$" (where $A$ = *RE*, $B$ = Mn/Cu, and $C$ = P);[3] this approach draws attention to the close relationship between the orthorhombic $YCo_5P_3$-type structure adopted by *RE*$MnCu_4P_3$ and the hexagonal $Zr_2Fe_{12}P_7$-type structure adopted by $RE_2Mn_3Cu_9P_7$ (**Figure 3-4**). The six $B$ atoms lie at the corners of four smaller triangles. In *RE*$MnCu_4P_3$, two corners of the large triangular assemblies are Cu atoms and are shared with adjacent assemblies, giving the formula $AB_4B_{2/2}C_3$, or $AB_5C_3$ corresponding to the $YCo_5P_3$-type structure. In $RE_2Mn_3Cu_9P_7$, all three corners of the large triangular assemblies are Mn atoms, which are not shared with adjacent assemblies; the unit cell contains two of these assemblies and one isolated P atom (located along the *c*-axis), giving the formula 2 $AB_6C_3$ + $C$, or $A_2B_{12}C_7$ corresponding to the $Zr_2Fe_{12}P_7$-type structure. These two descriptive schemes, the first based on coordination polyhedra and the second based on triangular assemblies, are valuable for systematizing a large number of structures of many metal-rich pnictides and for predicting new ones.[1–3]

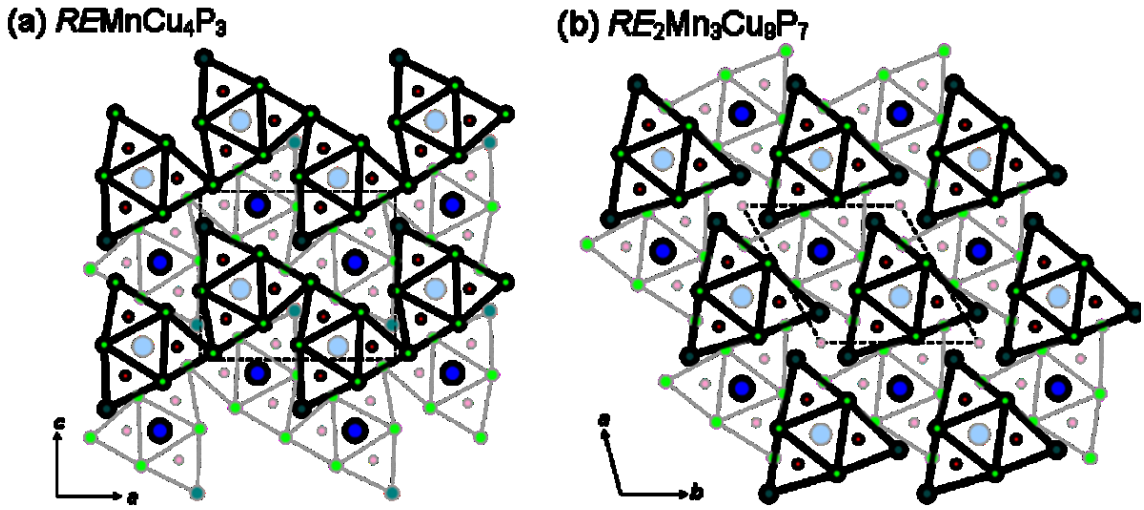


**Figure 3-4.** Comparison of (a) *RE*$MnCu_4P_3$ (*RE* = Gd–Ho; ordered $YCo_5P_3$-type) and (b) $RE_2Mn_3Cu_9P_7$ (*RE* = La–Nd, Sm, Gd–Dy; ordered $Zr_2Fe_{12}P_7$-type) structures, built up of triangular assemblies AB6C3 as proposed by Pivan *et al*.[3] Thick and thin lines distinguish between atoms displaced by half the cell parameter along the viewing direction.

The extent of *RE* substitution in the orthorhombic *RE*$MnCu_4P_3$ series is restricted to smaller *RE* atoms (Gd–Ho), in contrast to the hexagonal $RE_2Mn_3Cu_9P_7$ series, which forms for larger *RE* atoms (La–Nd, Sm, Gd–Dy) and can be extended to the arsenides $RE_2Mn_3Cu_9As_7$ (*RE* = La–Nd).[8] The *RE* atoms are coordinated identically in both structures by P atoms in a trigonal prismatic geometry (CN6). However, if Cu atoms (within ~3.3 Å) are included in the coordination sphere, the unique *RE* atom has CN16 in *RE*$MnCu_4P_3$, whereas the two *RE* atoms have CN15 and CN18 in $RE_2Mn_3Cu_9P_7$. The distinction is subtle, but evidently the formation of $RE_2Mn_3Cu_9P_7$ with larger *RE* atoms is consistent with the presence of the higher CN18 site. In general, compounds with the $YCo_5P_3$-type structure tend to be found with smaller *RE* atoms, although there are a few exceptions.[10,13,15–19]

The quaternary phosphides are formally charge-balanced as $RE^{3+}Mn^{2+}(Cu^{+})_4(P^{3-})_3$ and thus conform to a generalized relationship, followed by many other metal-rich pnictides $M_2Pn$, between valences and site occupations of the metal atoms: +3 in trigonal prisms (CN6), +2 in square pyramids (CN5), +1 in tetrahedra (CN4), and 0 in trigonal planes (CN3).[2,24] Bond valence sum calculations[25] are useful to further evaluate the propensity for the one CN5 and four CN4 sites to be occupied by Mn vs Cu atoms. If Mn atoms are placed in these sites, the bond valence sums are 1.69 in the CN5 site and 2.45–2.63 in the CN4 sites; conversely, if Cu atoms are placed in these sites, the bond valence sums are 0.82 in the CN5 site and 1.18–1.27 in the CN4 sites. In other words, the Mn atoms are slightly underbonded in the CN5 site but severely overbonded in the CN4 sites. If we accept at face value that the CN5 site really prefers a divalent metal atom, then Cu atoms would be severely underbonded in the CN5 site but only slightly overbonded in the CN4 sites; of course, divalent Cu atoms are highly unlikely to occur in pnictides. This bond valence sum analysis accounts neatly for coordination preferences. However, even a rudimentary analysis based on Pauling's electroneutrality principle[26] reveals that the sum of electrostatic bond strengths of the surrounding metal atoms (2.9–3.0) compensates exactly for the valence of each of the P atoms; any exchange of the Mn and Cu atoms within the CN5 vs CN4 sites only exacerbates deviations from electroneutrality.

A more rigorous band structure calculation was performed on the hypothetical compound $YMnCu_4P_3$, which contains a non-magnetic *RE* component. To a first approximation, the simple formulation $RE^{3+}Mn^{2+}(Cu^{+})_4(P^{3-})_3$ is correctly reflected by the occurrence of mostly empty Y states found above the Fermi level, partly filled Mn 3d states

(–1 to +1 eV), mostly filled Cu 3d states (the large peak straddling –4 eV), and filled P 3p (–7 to –1 eV) and 3s states (–12 eV, not shown) in the density of states (DOS) curve (**Figure 3-5a**). Bonding interactions between transition-metal and phosphorus atoms are nearly optimized, as seen by the occupation of all bonding levels in the crystal orbital Hamilton population (COHP) curves (**Figure 3-5b**), which results in large integrated COHP values (–ICOHP) of 1.38 eV/bond for Mn–P and 1.59 eV/bond for Cu–P contacts. Weaker Y–P (0.74 eV/bond) and metal-metal interactions (Mn–Cu, 0.41 eV/bond; Cu–Cu, 0.49 eV/bond) supplement the bonding stability of the structure  A spin-polarized calculation reveals that the Mn 3d states become split by ~3 eV, reflecting strong polarization, but there is nonzero DOS at the Fermi level for both spin directions (**Figure 3-6**). That is, $YMnCu_4P_3$ is predicted to be a ferromagnetic metal, with a sizeable magnetic moment of 3.6 $\mu_B$/f.u. The shortest Mn–Mn distances are 3.8 Å, corresponding to the *b*-parameter, which are too long for direct interactions between spins; the most likely mechanism thus involves indirect interactions mediated through the conduction electrons (RKKY interactions). . A comparison of DOS of $YCo_5P_3$, $YMnCuP_3$, and $YCu_5P_3$ is shown in **Figure 3-7**.

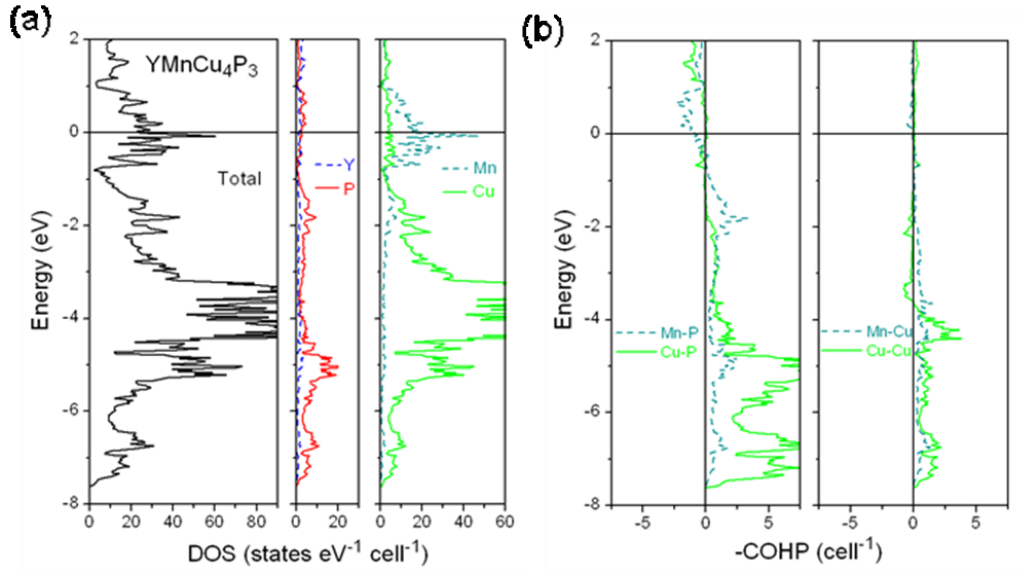


**Figure 3-5.** (a) Density of states and its atomic projections for YMnCu4P3. (b) Crystal orbital Hamilton population (COHP) curves for Mn–P, Cu–P, Mn–Cu, and Cu–Cu interactions. The Fermi level is at 0 eV.

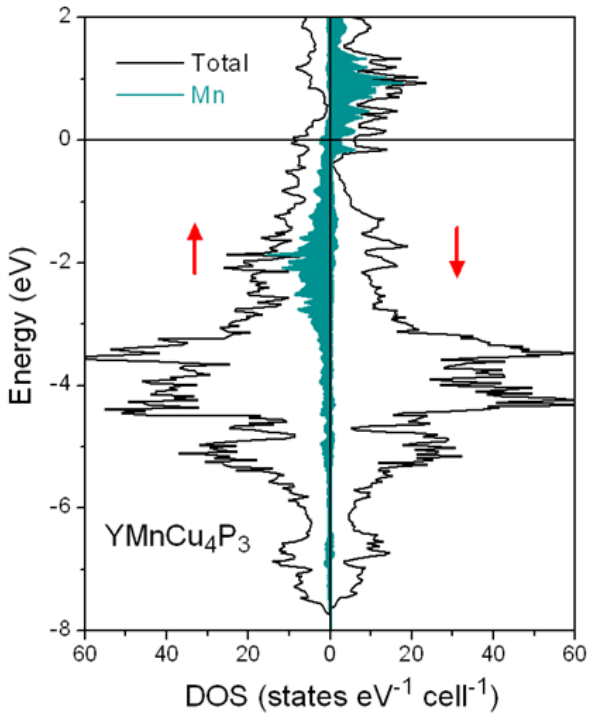


**Figure 3-6.** DOS curve for spin-polarized $YMnCu_4P_3$, with contributions from Mn states identified by the shaded region.

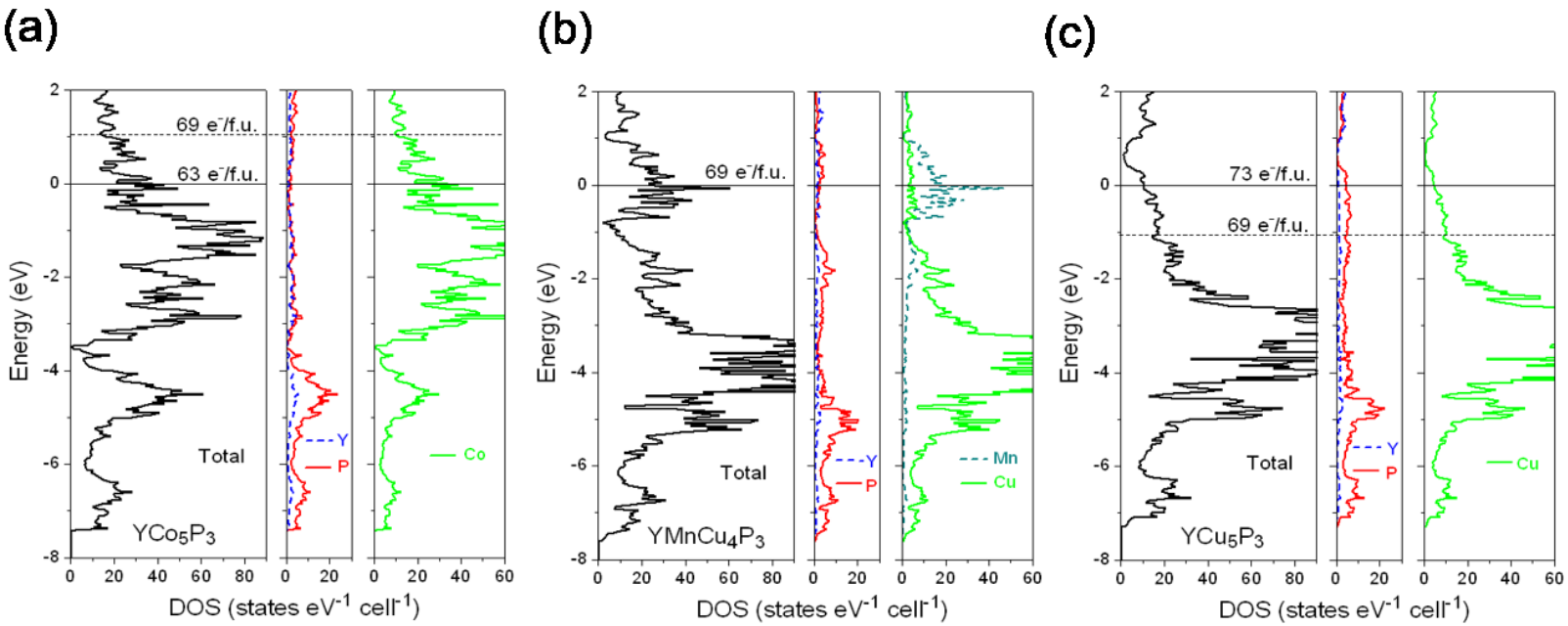


**Figure 3-7.** Density of states (DOS) and its atomic projections for (a) $YCo_5P_3$, (b) $YMnCu_4P_3$, and (c) hypothetical $YCu_5P_3$.

The expectation for metallic behaviour was confirmed in a measurement of the electrical resistivity for a single crystal of $TbMnCu_4P_3$ (**Figure 3-8**). There is a distinct change in curvature below ~100 K, which is probably associated with loss of spin-disorder scattering below a magnetic ordering transition. Further work is in progress to prepare phase-pure samples of *RE*$MnCu_4P_3$ to measure their magnetic properties.

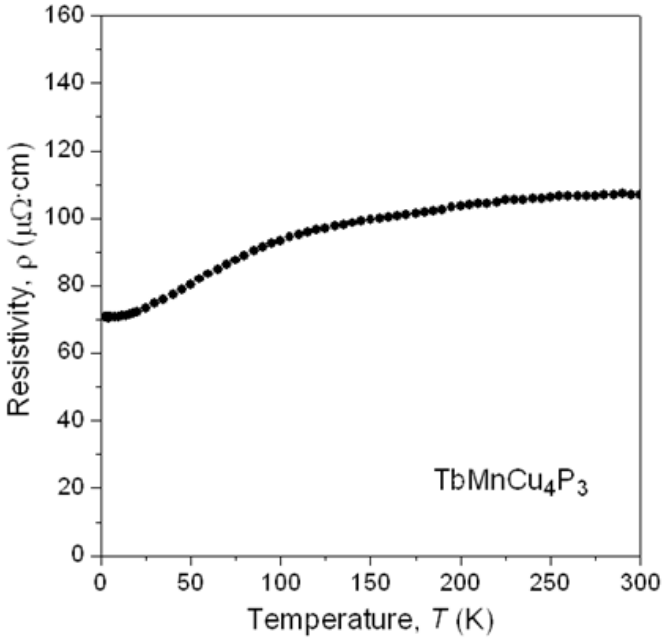


**Figure 3-8.** Plot of electrical resistivity vs temperature for $TbMnCu_4P_3$.

## 3.4 Conclusion

Cation ordering appears to be a viable strategy to introduce further complexity in metal-rich pnictides $M_2Pn$, which can be readily extended to ternary and now quaternary phases, as demonstrated here. It might even be possible to prepare quinary phases, if all four types of metal sites (with coordination geometries ranging from CN6 to CN3) are occupied by different atoms. Notwithstanding the apparent adherence to charge-balanced

formulations, many of these phases lack a band gap in their electronic structure because of the presence of partly filled d-bands of transition-metal components such as Mn. Physical properties of these ternary and quaternary phases remain underexplored and deserve further investigation.

## 3.5 References


1. Gladyshevskii, E. I.; Grin, Yu. N. *Kristallografiya* **1981**, *26*, 1204–1214.
2. Madar, R.; Ghetta, V.; Dhahri, E.; Chaudouet, P.; Senateur, J. P. *J. Solid State Chem.* **1987**, *66*, 73–85.
3. Pivan, J.-Y.; Guérin, R.; Sergent, M. *J. Solid State Chem.* **1987**, *68*, 11–21.
4. Oyama, S. T.; Gott, T.; Zhao, H.; Lee, Y.-K. *Catal. Today* **2009**, *143*, 94–107.
5. Prins, R.; Bussell, M. E. *Catal. Lett.* **2012**, *142*, 1413–1436.
6. Maple, M. B.; Hamlin, J. J.; Zocco, D. A.; Janoschek, M.; Baumbach, R. E.; White, B. D.; Fisher, I. R.; Chu, J.-H. *EPJ Web Conf.* **2012**, *23*, 00012-1–00012-8.
7. Dhahri, E. *J. Phys.: Condens. Matter* **1996**, *8*, 4351–4360.
8. Stoyko, S. S.; Ramachandran, K. K.; Mullen, C. S.; Mar, A. *Inorg. Chem.* **2013**, *52*, 1040–1046.
9. El Ghadraoui, E. H.; Pivan, J.-Y.; Guérin, R. *J. Solid State Chem.* **1989**, *78*, 262–270.
10. Jeitschko, W.; Meisen, U.; Scholz, U. D. *J. Solid State Chem.* **1984**, *55*, 331–336.
11. Sheldrick, G. M. *SHELXTL*, version 6.12; Bruker AXS Inc.: Madison, WI, 2001.
12. Gelato, L. M.; Parthé, E. *J. Appl. Crystallogr.* **1987**, *20*, 139–143.
13. Meisen, U.; Jeitschko, W. *J. Less-Common Met.* **1984**, *102*, 127–134.
14. Tank, R.; Jepsen, O.; Burkhardt, A.; Andersen, O. K. *TB-LMTO-ASA Program*, version 4.7; Max Planck Institut für Festkörperforschung: Stuttgart, Germany, 1998.
15. Jeitschko, W.; Reinbold, E. J. *Z. Naturforsch., B: Anorg. Chem., Org. Chem.* **1985**, *40*, 900–905.
16. Jakubowski-Ripke, U.; Jeitschko, W. *J. Less-Common Met.* **1988**, *136*, 261–270.
17. Jeitschko, W.; Brink, R.; Pollmeier, P. G. *Z. Naturforsch., B: J. Chem. Sci.* **1993**, *48*, 52–57.

18. Albering, J. H.; Jeitschko, W. *J. Solid State Chem.* **1995**, *117*, 80–87.

19. Thompson, C. M.; Kovnir, K.; Zhou, H.; Shatruk, M. *Z. Anorg. Allg. Chem.* **2011**, *637*, 2013–2017.

20. Stoyko, S.; Oryshchyn, S. V. *Coll. Abs. 9th Int. Conf. Crystal Chem. Intermet. Compd. (Lviv)* **2005**, *58*.

21. Venturini, G.; Malaman, B. *J. Alloys Compd.* **1997**, *261*, 19–25.

22. Li, B.; Corbett, J. D. *Inorg. Chem.* **2007**, *46*, 2237–2242.

23. Hoffmann, R. -D.; Pöttgen, R. *Z. Anorg. Allg. Chem.* **1999**, *625*, 994–1000.

24. Zhao, J. T.; Chabot, B.; Parthé, E. *Acta Crystallogr., Sect. C* **1987**, *43*, 1458–1461.

25. Brese, N. E.; O'Keeffe, M. *Acta Crystallogr., Sect. B* **1991**, *47*, 192–197.

26. Pauling, L. *The Nature of the Chemical Bond*, 3rd ed.; Cornell University Press: Ithaca, NY, 1960.

# Chapter 4

## Quaternary Rare-Earth Arsenides $RE\mathrm{Ag}_{1-x}\mathrm{Zn}_y\mathrm{As}_2$ ($RE$ = La–Nd, Sm, Gd–Dy) with Tetragonal $\mathrm{SrZnBi}_2$- and $\mathrm{HfCuSi}_2$-Type Structures

*A version of this chapter has been published. Ramachandran, K. K.; Genet, C.; Mar, A. J. Solid State Chem., 2015, 231, 204-211.*

### 4.1 Introduction

The new classes of iron-based pnictide superconductors adopt similar tetragonal structures (e.g., $\mathrm{ThCr}_2\mathrm{Si}_2$-type for $\mathrm{BaFe}_2\mathrm{As}_2$[1]; ZrCuSiAs-type for LaFeAsO[2]; PbFCl-type for LiFeAs[3]). Phases with the closely related $\mathrm{HfCuSi}_2$-type structure have also been recently identified as superconductors when doped with transition-metal (e.g., $\mathrm{CaFe}_{1-x}\mathrm{Pt}_x\mathrm{As}_2$[4]) or rare-earth components (e.g., $\mathrm{Ca}_{1-x}RE_x\mathrm{FeAs}_2$[5–8]). Indeed, the most prevalent ternary rare-earth transition-metal pnictides are $\mathrm{HfCuSi}_2$-type phases $REM_{1-x}Pn_2$, where the $M$ site is generally defective if it is occupied by a d-block element other than a monovalent one (i.e., from the Cu triad).[9–11] Among arsenides, the only known representatives thus far are $RE\mathrm{MAs}_2$ ($M$ = Cu[12,13], Ag[14–16], Au[15]), which are stoichiometric, and $RE\mathrm{Zn}_{1-x}\mathrm{As}_2$, which are substoichiometric ($RE\mathrm{Zn}_{0.67}\mathrm{As}_2$)[17,18]. However, a small Cu excess can be accommodated in lightly stuffed $\mathrm{HfCuSi}_2$-type phases $RE\mathrm{Cu}_{1.1}\mathrm{As}_2$.[19,20] Structural complications are possible because these phases can be subject to symmetry-lowering distortions within square nets of $Pn$ atoms[16,21–25] and vacancy ordering within the $M$ sites.[17]

To a first approximation, the occurrence of nondefective vs. defective structures among these ternary pnictides can be rationalized in a simple way. For monovalent *M*, the valence-precise formula $(RE^{3+})(M^{+})(Pn^{1-})(Pn^{3-})$ is obtained, in which $Pn^{1-}$ is assigned for the atoms bonded within the square net.[26,27] For divalent *M*, charge balance can be attained by invoking defects in the *M* site, ideally according to the formula $(RE^{3+})(M^{2+})_{0.5}(Pn^{1-})(Pn^{3-})$. In practice, the degree of substoichiometry is rarely as extreme as this; the observed formulas are typically $REM_{0.6–0.8}Pn_2$, where single-crystal structures have been determined.[28–33]

This study addresses the question of what will happen when the *M* site is occupied by two types of components, one that favours full stoichiometry (*M* = Ag) and one that does not (*M* = Zn). By targeting the preparation of quaternary arsenides $RE\mathrm{Ag}_{1-x}\mathrm{Zn}_x\mathrm{As}_2$, can give insight on the tolerance of the $\mathrm{HfCuSi}_2$-type structure to changes in electron count induced by chemical substitution within the *M* site.

## 4.2 Experimental

### 4.2.1 Synthesis

Starting materials were freshly filed *RE* pieces (99.9%, Hefa), Ag powder (99.9%, A.D. Mackay), Zn filings (99.995%, Alfa), and As lumps (99.999%, Alfa-Aesar). The title compounds were initially observed during attempts to prepare "$RE_4\mathrm{AgZnAs}_5$," in analogy to $RE_4\mathrm{Mn}_2\mathrm{As}_5$[34] and $RE_4\mathrm{Zn}_{2-x}\mathrm{As}_5$.[35] Subsequently, reactions with the loading composition "$RE\mathrm{Ag}_{0.5}\mathrm{Zn}_{0.5}\mathrm{As}_2$" were carried out for various trivalent *RE* components (Y, La–Nd, Sm, Gd–Tm, Lu). Stoichiometric mixtures of the elements on a 0.3-g scale were ground,

pressed into pellets, and loaded into fused-silica tubes, which were evacuated and sealed. The tubes were heated at 800 ºC for 10 days and then cooled to room temperature over 1 day. The products were analyzed by powder X-ray diffraction (XRD), performed on an Inel powder diffractometer equipped with a curved position-sensitive detector (CPS 120) and a Cu $K\alpha_1$ radiation source operated at 40 kV and 20 mA. Quaternary tetragonal phases were formed for *RE* = La–Nd, Sm, Gd–Dy; the most common accompanying phase was the binary arsenide *RE*As, but other quaternary phases with different structures such as *RE*AgZnAs$_2$ (trigonal $CaAl_2Si_2$-type)[36] and *RE*$_4$AgZnAs$_5$ (trigonal $Ce_4Zn_{2-x}P_5$-type)[37] were also found (**Figure 4-1**). Cell parameters refined from the powder XRD patterns are listed in **Table 4-1**.

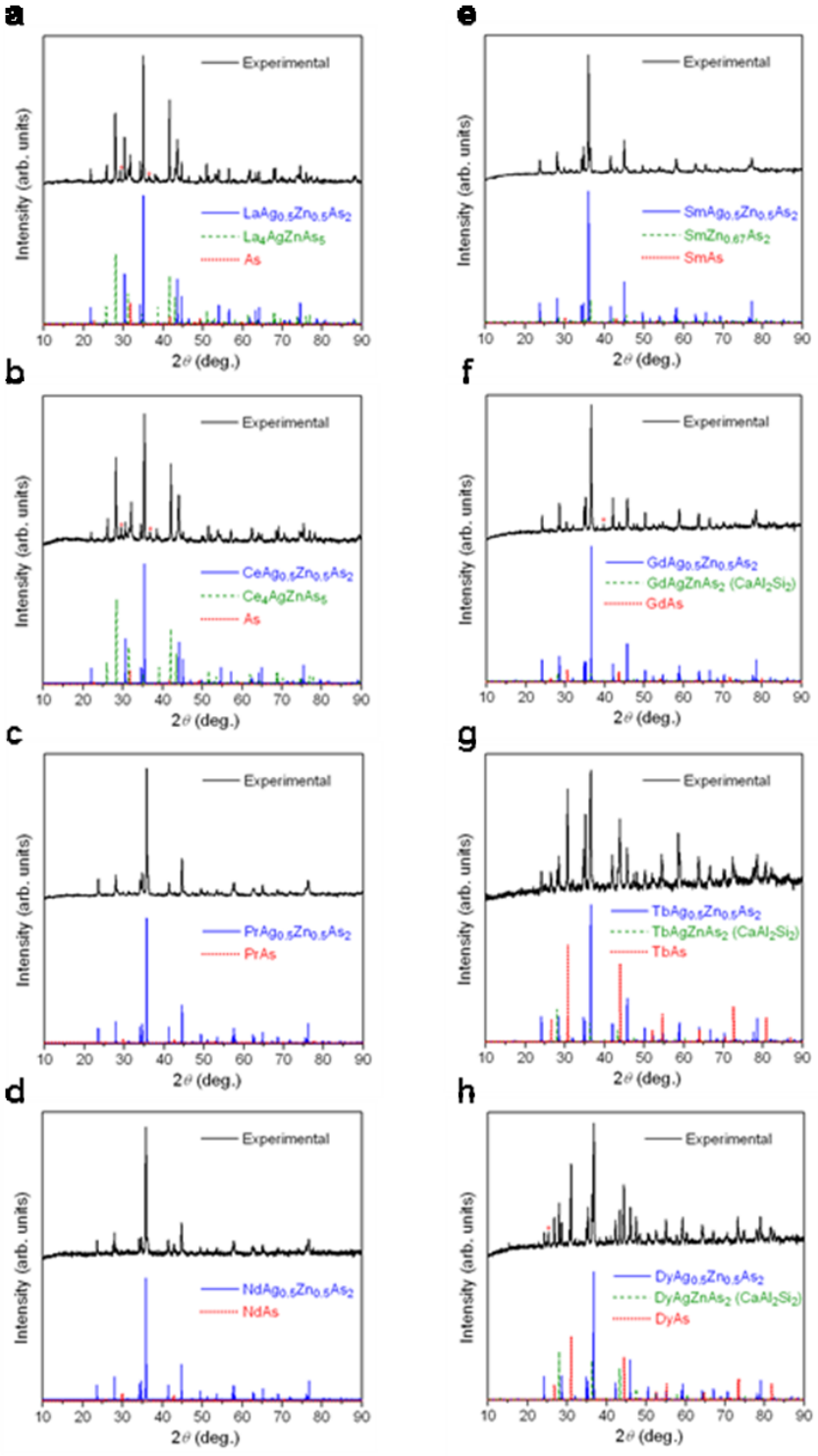


**Figure 4-1.** Powder XRD patterns for reactions *RE*$Ag_{0.5}Zn_{0.5}As_2$ (*RE* = La–Nd, Sm, Gd–Dy).

**Table 4-1.** Cell parameters refined from powder XRD data for quaternary $SrZnBi_2$- or $HfCuSi_2$-type phases obtained from reactions $RE Ag_{0.5}Zn_{0.5}As_2$.

| Loading composition | $a$ (Å) | $c$ (Å) | $V$ (Å$^3$) | $V/Z$ (Å$^3$) |
|---|---|---|---|---|
| $LaAg_{0.5}Zn_{0.5}As_2$ | 4.1482(1) | 20.908(2) | 359.77(3) | 89.94(1) |
| $CeAg_{0.5}Zn_{0.5}As_2$ | 4.0999(1) | 20.725(2) | 348.38(3) | 87.10(1) |
| $PrAg_{0.5}Zn_{0.5}As_2$ | 4.0662(1) | 10.3684(5) | 171.43(1) | 85.72(1) |
| $NdAg_{0.5}Zn_{0.5}As_2$ | 4.0407(2) | 10.3206(7) | 168.51(1) | 84.26(1) |
| $SmAg_{0.5}Zn_{0.5}As_2$ | 4.0178(1) | 10.2883(7) | 166.08(1) | 83.04(1) |
| $GdAg_{0.5}Zn_{0.5}As_2$ | 3.9613(1) | 10.1763(5) | 159.69(1) | 79.84(1) |
| $TbAg_{0.5}Zn_{0.5}As_2$ | 3.9602(2) | 10.2165(5) | 160.23(1) | 80.12(1) |
| $DyAg_{0.5}Zn_{0.5}As_2$ | 3.9430(1) | 10.1536(7) | 157.86(1) | 78.93(1) |

As no suitable single crystals were obtained from the reactions above, the samples were reground, a few mg of $I_2$ was added, and the same heat treatment was applied as before. Block-shaped crystals were obtained for $RE$ = La–Nd, but the Ce-containing ones were still too small for single-crystal X-ray diffraction analysis. To investigate the extent of solid solubility, further reactions were also conducted within the Nd-containing series using loading compositions $NdAg_{1-x}Zn_xAs_2$ ($0 \le x \le 1$ in increments of 0.2), with two heat treatments applied including the addition of $I_2$ in the second step. The crystals obtained from both series of reactions were examined on a JEOL JSM-6010LA scanning electron microscope and their compositions were determined by energy-dispersive X-ray (EDX) analysis. No iodine was detected in these crystals. In general, about six points were examined on each crystal, and the compositions were averaged over 2 to 5 crystals. The

resulting formulas were normalized so that the content of *RE* and As sums to 3 per formula unit (**Table 4-2**). As discussed later, this analysis provides evidence that Zn-richer samples lead to substoichiometric formulas; that is, the quaternary phases formed from the reactions $NdAg_{1-x}Zn_xAs_2$ actually have a combined Ag and Zn content that can be less than one per formula unit and should be properly expressed as $NdAg_{1-x}Zn_yAs_2$.

**Table 4-2.** EDX analyses (atomic %) for crystals obtained from various reactions.

| Loading composition | *RE* | Ag | Zn | As | No. of crystals | Normalized formula |
|---|---|---|---|---|---|---|
| $LaAg_{0.5}Zn_{0.5}As_2$ | 28(1) | 13(1) | 11(1) | 49(1) | 4 | $La_{1.1}Ag_{0.5}Zn_{0.4}As_{1.9}$ |
| $CeAg_{0.5}Zn_{0.5}As_2$ | 28(1) | 13(1) | 11(1) | 49(1) | 2 | $Ce_{1.1}Ag_{0.5}Zn_{0.4}As_{1.9}$ |
| $PrAg_{0.5}Zn_{0.5}As_2$ | 29(1) | 12(1) | 11(1) | 48(1) | 15 | $Pr_{1.1}Ag_{0.5}Zn_{0.4}As_{1.9}$ |
| $NdAgAs_2$ | 27(1) | 25(1) | 0 | 49(1) | 3 | $Nd_{1.1}Ag_{1.0}As_{1.9}$ |
| $NdAg_{0.8}Zn_{0.2}As_2$ | 27(1) | 21(1) | 5(1) | 47(1) | 2 | $Nd_{1.1}Ag_{0.8}Zn_{0.2}As_{1.9}$ |
| $NdAg_{0.6}Zn_{0.4}As_2$ | 27(1) | 16(1) | 8(1) | 49(1) | 3 | $Nd_{1.1}Ag_{0.6}Zn_{0.3}As_{1.9}$ |
| $NdAg_{0.4}Zn_{0.6}As_2$ | 28(1) | 12(1) | 11(1) | 50(1) | 5 | $Nd_{1.1}Ag_{0.5}Zn_{0.4}As_{1.9}$ |
| $NdAg_{0.2}Zn_{0.8}As_2$ | 28(1) | 7(1) | 14(1) | 51(1) | 4 | $Nd_{1.1}Ag_{0.3}Zn_{0.5}As_{1.9}$ |
| $NdZnAs_2$ | 30(1) | 0 | 18(1) | 52(1) | 2 | $Nd_{1.1}Zn_{0.6}As_{1.9}$ |

### 4.2.2 Structure Determination

Single crystals obtained from the reactions $REAg_{0.5}Zn_{0.5}As_2$ (*RE* = La, Pr, Nd) and $NdAg_{1-x}Zn_xAs_2$ ($x$ = 0.2, 0.4, 0.6, 0.8) were mounted on a Bruker PLATFORM diffractometer equipped with a SMART APEX II CCD area detector and a graphite-monochromated Mo $K\alpha$ radiation source. Intensity data were collected at room

temperature using $\omega$ scans in 5–8 batch runs at different $\phi$ angles with a frame width of 0.3º and an exposure time of 10–15 s per frame. Face-indexed numerical absorption corrections were applied. Structure solution and refinement were carried out with use of the SHELXTL (version 6.12) program package.[38]

Crystals within the series $RE$Ag$_{0.5}$Zn$_{0.5}$As$_2$ ($RE$ = La, Pr, Nd) exhibit tetragonal symmetry with unit cells having similar $a$-parameters (4.1 Å) but the La-containing member has a doubled $c$-parameter (20.8 Å) relative to the Pr- and Nd-containing members (10.4 Å). Direct methods suggested a SrZnBi$_2$-type structure[39] for the La-containing member and a HfCuSi$_2$-type structure[40] for the Pr- and Nd-containing members. Both types of structure are simple, containing four sites in space group $I4/mmm$ (La (4$e$), Ag/Zn (4$d$), As1 (4$e$), As2 (4$c$)) or $P4/nmm$ (Pr or Nd (2$c$), Ag/Zn (2$b$), As1 (2$c$), As2 (2$a$)), respectively. The atomic positions were standardized with the program STRUCTURE TIDY.[41] We make the assumption that the nominal, fully stoichiometric formulas $RE$Ag$_{0.5}$Zn$_{0.5}$As$_2$ are roughly correct on the basis of the EDX analyses (for all three samples) and the observation of nearly pure phase (for the Pr and Nd samples). In principle, the occupancies of Ag and Zn atoms within the same site can be refined given their different X-ray scattering factors. For example, these occupancies converged to 0.49(2) Ag / 0.51(2) Zn in the La-containing crystal. In subsequent refinements, we treated all three cases identically by fixing the occupancies to be exactly 0.50 Ag and 0.50 Zn.

Crystals obtained from the reactions NdAg$_{1-x}$Zn$_x$As$_2$ ($x$ = 0.2, 0.4, 0.6, 0.8), all of which exhibited HfCuSi$_2$-type structures, were analyzed in a similar way as above. The EDX analyses of these crystals suggested that the Zn-richer samples may be

substoichiometric in the combined Ag and Zn content. This poses a problem because it is impossible to implement a refinement in which the individual occupancies of Ag and Zn, as well as their total, can be treated simultaneously as free variables. To circumvent this problem, the total occupancy was fixed at different values and the refined Ag/Zn occupancies were evaluated for their consistency with the EDX analyses. For the crystals obtained from the reactions $NdAg_{0.8}Zn_{0.2}As_2$ and $NdAg_{0.6}Zn_{0.4}As_2$, the refined formulas from the X-ray data were $NdAg_{0.81(2)}Zn_{0.19(2)}As_2$ and $NdAg_{0.60(2)}Zn_{0.40(2)}As_2$, respectively, if the total occupancy was constrained to unity; these results agree with the formulas $Nd_{1.1}Ag_{0.8}Zn_{0.2}As_{1.9}$ and $Nd_{1.1}Ag_{0.6}Zn_{0.3}As_{1.9}$, respectively, deduced from the EDX analyses. For the crystal obtained from the reaction $NdAg_{0.4}Zn_{0.6}As_2$, the refined formula was $NdAg_{0.13(2)}Zn_{0.87(2)}As_2$ if the total occupancy was unity; constraining the total occupancy to 0.9 gave a refined formula of $NdAg_{0.38(2)}Zn_{0.50(2)}As_2$, which is in better agreement with the EDX formula $Nd_{1.1}Ag_{0.5}Zn_{0.4}As_{1.9}$. For the crystal obtained from the reaction $NdAg_{0.2}Zn_{0.8}As_2$, the refinement was unstable, tending to >1.00 Zn, if full occupancy was assumed; constraining the total occupancy to 0.8 gave a refined formula of $NdAg_{0.20(3)}Zn_{0.60(3)}As_2$, more consistent with the EDX formula $Nd_{1.1}Ag_{0.3}Zn_{0.5}As_{1.9}$. The general conclusion from these structure refinements and the EDX analyses is that the Ag content closely matches what was loaded but the Zn content can be lower. Adopting this principle, we fixed the formulas to be $NdAg_{0.8}Zn_{0.2}As_2$, $NdAg_{0.6}Zn_{0.4}As_2$, $NdAg_{0.4}Zn_{0.5}As_2$, and $NdAg_{0.2}Zn_{0.6}As_2$ in the final refinements.

Some ternary rare-earth transition-metal pnictides $REM_{1-x}Pn_2$ with $SrZnBi_2$- or $HfCuSi_2$-type structures are subject to distortion of a square net of *Pn* atoms.[16,21–25] This

phenomenon is often signalled by abnormally large displacement ellipsoids of the *Pn*2 site within the parent tetragonal structure. The only case in the present study where this is a concern is $LaAg_{0.5}Zn_{0.5}As_2$, in which the displacement ellipsoid of the As2 site is somewhat prolate (ADP max/min ratio of 3.3). Splitting the As2 site into two half-occupied ones (Wyckoff position shifted from 4*c* to 8*j*) barely improved the agreement factors (conventional *R* lowered from 0.0134 to 0.0128) at the expense of one additional parameter. Moreover, there were no detectable superstructure reflections in the reflection frames or obvious peak splitting in the powder XRD pattern.

For $REAg_{0.5}Zn_{0.5}As_2$ (*RE* = La, Pr, Nd), crystal data and experimental details are listed in **Table 4-3**, positional and displacement parameters in **Table 4-4**, and interatomic distances in **Table 4-5**. For $NdAg_{1-x}Zn_yAs_2$ ($x$ = 0.2, 0.4, 0.6, 0.8), these data are listed in **Tables 4-6 to 4-8**. Further data, in CIF format, have been sent to Fachinformationszentrum Karlsruhe, Abt. PROKA, 76344 Eggenstein-Leopoldshafen, Germany, as supplementary material No. CSD-429848 to 429854 and can be obtained by contacting FIZ (quoting the article details and the corresponding CSD numbers).

**Table 4-3.** Crystallographic data for $REAg_{0.5}Zn_{0.5}As_2$ (*RE* = La, Pr, Nd).

| Formula | $LaAg_{0.5}Zn_{0.5}As_2$ | $PrAg_{0.5}Zn_{0.5}As_2$ | $NdAg_{0.5}Zn_{0.5}As_2$ |
|---|---|---|---|
| Formula mass (amu) | 375.37 | 377.37 | 380.70 |
| Space group | *I*4/*mmm* (No. 139) | *P*4/*nmm* (No. 129) | *P*4/*nmm* (No. 129) |
| *a* (Å) | 4.1300(2) | 4.0536(4) | 4.0495(5) |
| *c* (Å) | 20.8160(11) | 10.3542(9) | 10.3571(13) |

| | | | |
|---|---|---|---|
| $V$ (Å$^3$) | 355.06(4) | 170.14(4) | 169.84(5) |
| $Z$ | 4 | 2 | 2 |
| $\rho_{calcd}$ (g cm$^{-3}$) | 7.022 | 7.366 | 7.444 |
| Crystal dimensions (mm) | 0.12 × 0.12 × 0.08 | 0.08 × 0.06 × 0.05 | 0.06 × 0.05 × 0.03 |
| Radiation | Graphite monochromated Mo $K\alpha$, $\lambda$ = 0.71073 Å | | |
| $\mu$(Mo $K\alpha$) (mm$^{-1}$) | 36.22 | 39.56 | 40.57 |
| Transmission factors | 0.062–0.240 | 0.171–0.311 | 0.187–0.308 |
| $2\theta$ limits | 3.91–66.11° | 3.93–66.29° | 3.93–66.31° |
| Data collected | $-6 \le h \le 6$, $-6 \le k \le 6$, $-31 \le l \le 31$ | $-6 \le h \le 6$, $-6 \le k \le 6$, $-15 \le l \le 15$ | $-6 \le h \le 6$, $-6 \le k \le 6$, $-15 \le l \le 15$ |
| No. of data collected | 2499 | 2378 | 2408 |
| No. of unique data, including $F_o^2 < 0$ | 248 ($R_{int}$ = 0.026) | 236 ($R_{int}$ = 0.042) | 236 ($R_{int}$ = 0.041) |
| No. of unique data, with $F_o^2 > 2\sigma(F_o^2)$ | 245 | 228 | 231 |
| No. of variables | 13 | 12 | 11 |
| $R(F)$ for $F_o^2 > 2\sigma(F_o^2)$ [a] | 0.013 | 0.017 | 0.025 |
| $R_w(F_o^2)$ [b] | 0.031 | 0.037 | 0.054 |
| Goodness of fit | 1.14 | 1.17 | 1.29 |
| $(\Delta\rho)_{max}$, $(\Delta\rho)_{min}$ (e Å$^{-3}$) | 1.12, –0.77 | 1.81, –1.49 | 2.74, –2.13 |

[a] $R(F) = \sum||F_o| - |F_c|| / \sum|F_o|$. [b] $R_w(F_o^2) = [\sum[w(F_o^2 - F_c^2)^2] / \sum wF_o^4]^{1/2}$; $w^{-1} = [\sigma^2(F_o^2) + (Ap)^2 + Bp]$, where $p = [\max(F_o^2,0) + 2F_c^2] / 3$.

**Table 4-4.** Atomic coordinates and equivalent isotropic displacement parameters for $RE$Ag$_{0.5}$Zn$_{0.5}$As$_2$ ($RE$ = La, Pr, Nd).

| Atom | Wyckoff position | $x$ | $y$ | $z$ | $U_{eq}$ (Å$^2$) [a] |
|---|---|---|---|---|---|
| LaAg$_{0.5}$Zn$_{0.5}$As$_2$ | | | | | |
| La | 4*e* | 0 | 0 | 0.11185(2) | 0.0085(1) |
| $M$ [b] | 4*d* | 0 | ½ | ¼ | 0.0123(1) |
| As1 | 4*e* | 0 | 0 | 0.33261(3) | 0.0120(2) |
| As2 | 4*c* | 0 | ½ | 0 | 0.0301(2) |
| PrAg$_{0.5}$Zn$_{0.5}$As$_2$ | | | | | |
| Pr | 2*c* | ¼ | ¼ | 0.22659(4) | 0.0099(1) |
| $M$ [b] | 2*b* | ¾ | ¼ | ½ | 0.0149(2) |
| As1 | 2*c* | ¼ | ¼ | 0.67010(8) | 0.0130(2) |
| As2 | 2*a* | ¾ | ¼ | 0 | 0.0173(2) |
| NdAg$_{0.5}$Zn$_{0.5}$As$_2$ | | | | | |
| Nd | 2*c* | ¼ | ¼ | 0.22570(8) | 0.0120(2) |
| $M$ [b] | 2*b* | ¾ | ¼ | ½ | 0.0110(3) |
| As1 | 2*c* | ¼ | ¼ | 0.67463(15) | 0.0134(3) |
| As2 | 2*a* | ¾ | ¼ | 0 | 0.0198(4) |

**Table 4-5.** Interatomic distances (Å) for $RE$Ag$_{0.5}$Zn$_{0.5}$As$_2$ ($RE$ = La, Pr, Nd).

| | LaAg$_{0.5}$Zn$_{0.5}$As$_2$ | PrAg$_{0.5}$Zn$_{0.5}$As$_2$ | NdAg$_{0.5}$Zn$_{0.5}$As$_2$ |
|---|---|---|---|
| $RE$–As1 (×4) | 3.1408(3) | 3.0594(4) | 3.0438(7) |
| $RE$–As2 (×4) | 3.1121(3) | 3.1004(4) | 3.0925(7) |

| | | | |
|---|---|---|---|
| *RE*–*M* (×4) | 3.5403(3) | 3.4817(4) | 3.4887(7) |
| *M*–As1 (×4) | 2.6873(4) | 2.6852(6) | 2.7149(11) |
| *M*–*M* (×4) | 2.9204(1) | 2.8663(3) | 2.8634(4) |
| As2–As2 (×4) | 2.9204(1) | 2.8663(3) | 2.8634(4) |

**Table 4-6.** Crystallographic data for $NdAg_{1-x}Zn_yAs_2$.

| Formula | $NdAg_{0.8}Zn_{0.2}As_2$ | $NdAg_{0.6}Zn_{0.4}As_2$ | $NdAg_{0.4}Zn_{0.5}As_2$ | $NdAg_{0.2}Zn_{0.6}As_2$ |
|---|---|---|---|---|
| Formula mass (amu) | 393.45 | 384.95 | 369.91 | 354.88 |
| Space group | *P*4/*nmm* (No. 129) | *P*4/*nmm* (No. 129) | *P*4/*nmm* (No. 129) | *P*4/*nmm* (No. 129) |
| *a* (Å) | 4.0452(9) | 4.0489(3) | 4.0326(6) | 4.0131(5) |
| *c* (Å) | 10.404(2) | 10.3438(8) | 10.3016(15) | 10.2549(13) |
| *V* (Å$^3$) | 170.25(8) | 169.57(3) | 167.52(6) | 165.15(5) |
| *Z* | 2 | 2 | 2 | 2 |
| $\rho_{calcd}$ (g cm$^{-3}$) | 7.675 | 7.539 | 7.333 | 7.136 |
| Crystal dimensions (mm) | 0.04 × 0.04 × 0.04 | 0.09 × 0.05 × 0.04 | 0.08 × 0.06 × 0.05 | 0.09 × 0.07 × 0.05 |
| Radiation | Graphite monochromated Mo *K*α, $\lambda$ = 0.71073 Å | | | |
| $\mu$(Mo *K*α) (mm$^{-1}$) | 40.08 | 40.50 | 40.56 | 40.70 |
| Transmission factors | 0.276–0.373 | 0.122–0.312 | 0.092–0.278 | 0.122–0.279 |
| 2$\theta$ limits | 3.91–66.56° | 3.94–66.37° | 3.95–66.25° | 3.97–66.22° |
| Data collected | $-6 \le h \le 6$, $-6 \le k \le 6$, | $-6 \le h \le 6$, $-6 \le k \le 6$, | $-6 \le h \le 6$, $-6 \le k \le 6$, | $-6 \le h \le 6$, $-6 \le k \le 6$, |

| | | | | |
|---|---|---|---|---|
| | $-15 \le l \le 15$ | $-15 \le l \le 15$ | $-15 \le l \le 15$ | $-15 \le l \le 15$ |
| No. of data collected | 2244 | 2354 | 2358 | 2293 |
| No. of unique data, including $F_o^2 < 0$ | 229 ($R_{int}$ = 0.157) | 234 ($R_{int}$ = 0.026) | 232 ($R_{int}$ = 0.038) | 228 ($R_{int}$ = 0.028) |
| No. of unique data, with $F_o^2 > 2\sigma(F_o^2)$ | 191 | 234 | 230 | 226 |
| No. of variables | 12 | 12 | 12 | 12 |
| $R(F)$ for $F_o^2 > 2\sigma(F_o^2)$ [a] | 0.070 | 0.011 | 0.028 | 0.025 |
| $R_w(F_o^2)$ [b] | 0.173 | 0.026 | 0.064 | 0.059 |
| Goodness of fit | 1.13 | 1.19 | 1.44 | 1.50 |
| $(\Delta\rho)_{max}$, $(\Delta\rho)_{min}$ (e Å$^{-3}$) | 5.61, –8.07 | 1.35, –0.97 | 4.47, –3.07 | 1.92, –2.55 |

[a] $R(F) = \sum||F_o| - |F_c|| / \sum|F_o|$.

[b] $R_w(F_o^2) = [\sum[w(F_o^2 - F_c^2)^2] / \sum wF_o^4]^{1/2}$; $w^{-1} = [\sigma^2(F_o^2) + (Ap)^2 + Bp]$, where $p = [\max(F_o^2,0) + 2F_c^2] / 3$.

**Table 4-7.** Atomic coordinates and equivalent isotropic displacement parameters (Å$^2$) for $NdAg_{1-x}Zn_yAs_2$.

| | $NdAg_{0.8}Zn_{0.2}As_2$ | $NdAg_{0.6}Zn_{0.4}As_2$ | $NdAg_{0.4}Zn_{0.5}As_2$ | $NdAg_{0.2}Zn_{0.6}As_2$ |
|---|---|---|---|---|
| Nd in 2*c* (¼, ¼, *z*) | | | | |
| *z* | 0.22767(17) | 0.22538(3) | 0.22610(8) | 0.22723(7) |
| $U_{eq}$ | 0.0137(6) | 0.00818(9) | 0.0106(2) | 0.0090(2) |
| *M* in 2*b* (¾, ¼, ½) | | | | |
| $U_{eq}$ | 0.0166(7) | 0.01117(12) | 0.0152(4) | 0.0145(4) |
| As1 in 2*c* (¼, ¼, *z*) | | | | |
| *z* | 0.6764(3) | 0.67377(6) | 0.66894(18) | 0.66444(17) |
| $U_{eq}$ | 0.0141(8) | 0.01059(13) | 0.0139(4) | 0.0133(3) |
| As2 in 2*a* (¾, ¼, 0) | | | | |
| $U_{eq}$ | 0.0206(8) | 0.01533(14) | 0.0155(4) | 0.0127(3) |

[a] $U_{eq}$ is defined as one-third of the trace of the orthogonalized $U_{ij}$ tensor.

**Table 4-8.** Interatomic distances (Å) for $NdAg_{1-x}Zn_yAs_2$.

| | $NdAg_{0.8}Zn_{0.2}As_2$ | $NdAg_{0.6}Zn_{0.4}As_2$ | $NdAg_{0.4}Zn_{0.5}As_2$ | $NdAg_{0.2}Zn_{0.6}As_2$ |
|---|---|---|---|---|
| Nd–As1 (×4) | 3.0294(14) | 3.0471(3) | 3.0496(8) | 3.0474(8) |
| Nd–As2 (×4) | 3.1147(14) | 3.0876(3) | 3.0806(7) | 3.0751(6) |
| Nd–*M* (×4) | 3.4812(16) | 3.4882(3) | 3.4680(8) | 3.4425(7) |
| *M*–As1 (×4) | 2.731(2) | 2.7072(4) | 2.6635(13) | 2.6210(11) |
| *M*–*M* (×4) | 2.8604(6) | 2.8630(2) | 2.8515(4) | 2.8377(4) |
| As2–As2 (×3) | 2.8604(6) | 2.8630(2) | 2.8515(4) | 2.8377(4) |

### 4.2.3 Magnetic Measurements

Samples of $PrAg_{0.5}Zn_{0.5}As_2$ and $NdAg_{0.5}Zn_{0.5}As_2$ were nearly single-phase, permitting magnetic measurements to be made. A sample of $NdAgAs_2$ was also analyzed as a reference to which $NdAg_{0.5}Zn_{0.5}As_2$ can be compared. The dc magnetic susceptibility was measured on 0.1-g powder samples between 2 and 300 K under an applied field of 0.5 T on a Quantum Design 9T-PPMS magnetometer.

### 4.2.4 Band Structure Calculations

Tight-binding linear muffin tin orbital band structure calculations were performed within the local density and atomic spheres approximation with use of the Stuttgart TB-LMTO-ASA program (version 4.7).[42] To understand the experimental results obtained for $NdAg_{1-x}Zn_yAs_2$, a $HfCuSi_2$-type model was chosen in which cell parameters and atomic positions were taken from the crystal structure of $NdAg_{0.5}Zn_{0.5}As_2$, the Nd atoms were replaced by La atoms to avoid computational difficulties associated with 4f orbitals of *RE* atoms, and the Ag and Zn atoms were ordered in a checkerboard pattern within square nets so that nearest neighbour contacts are heteroatomic. This model (in space group $P\bar{4}m2$) contains undistorted square As nets. A related lower-symmetry model (in space group $P2_1/m$) based on the $SrZnSb_2$-type structure[43] was also examined in which the As nets are distorted to give zigzag chains (with 2.6 Å distances) while all other metrical details were kept unchanged. The basis set consisted of La 6s/6p/5d/4f, Ag 5s/5p/4d/4f, Zn 4s/4p/3d, and As 4s/4p/4d orbitals, with the La 6p/4f, Ag 4f, and As 4d orbitals being downfolded. Integrations in reciprocal space were carried out with an improved tetrahedron method over

105 or 182 irreducible *k* points (for the $HfCuSi_2$- or $SrZnSb_2$-type models, respectively) within the first Brillouin zone.

## 4.3 Results and Discussion

Quaternary arsenides were obtained from reactions of the elements at 800 °C with the loading compositions $RE Ag_{0.5}Zn_{0.5}As_2$ for *RE* = La–Nd, Sm, Gd–Dy. For *RE* = Pr and Nd, the products were nearly single-phase and mass balance arguments imply that the formula $RE Ag_{0.5}Zn_{0.5}As_2$ is close to being accurate in these cases. For the other *RE* members, these arsenides were formed in conjunction with other phases; thus, it is important to recognize that the nominal compositions are approximations to the true formulas, which must be established through other independent means. For *RE* = La and Ce, a competing quaternary arsenide $RE_4AgZnAs_5$[37] was formed in significant proportions; for *RE* = Sm and Gd–Dy, binary arsenide *RE*As and a different quaternary arsenide $RE AgZnAs_2$[36] became increasingly prominent on proceeding to the later *RE* members. Although the powder XRD patterns for $RE Ag_{0.5}Zn_{0.5}As_2$ are generally similar, the La and Ce members show additional peaks compared to the others, the most diagnostic being the 105 peak near 31°, that arise from a doubling of the *c*-axis (**Figure 4-1**). The tetragonal cell parameters refined from the powder XRD patterns generally decrease smoothly according to the lanthanide contraction (**Table 4-1**) except that the latest *RE* members (Tb, Dy) exhibit small deviations, seen more clearly in a plot of the normalized unit cell volumes (**Figure 4-2**). This is not surprising considering that the Tb and Dy reactions resulted in significant admixtures of other phases, so that the Ag/Zn content begins to deviate from the formula $RE Ag_{0.5}Zn_{0.5}As_2$.

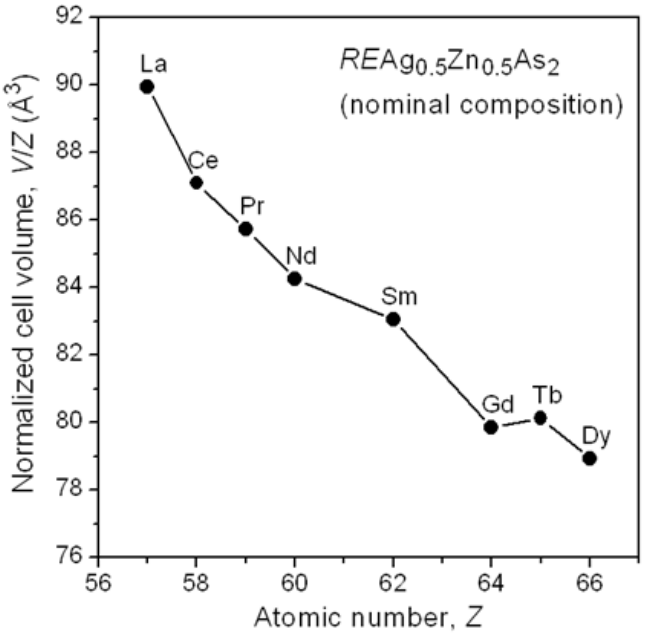


**Figure 4-2.** Plot of unit cell volume, normalized per formula unit, for tetragonal quaternary arsenides obtained from reactions with nominal composition $RE$Ag$_{0.5}$Zn$_{0.5}$As$_2$.

The two series of quaternary arsenides $RE$Ag$_{0.5}$Zn$_{0.5}$As$_2$ adopt closely related structures: SrZnBi$_2$-type (for $RE$ = La, Ce) and HfCuSi$_2$-type (for $RE$ = Pr, Nd, Sm, Gd–Dy) (**Figure 4-3**). The Ag and Zn atoms are disordered within metal-centred tetrahedra, which share edges to form [$M$As] layers that are fragments of the PbO-type structure. These [$M$As] layers are stacked with As square nets along the $c$-direction, separated by $RE$ atoms which are also arranged in square nets that are half as dense. In the SrZnBi$_2$-type members, successive [$M$As] layers alternate in orientation as they stack and are related by reflection across a mirror coplanar with the As square net; in the HfCuSi$_2$-type members, successive [$M$As] layers are always in registry. The $RE$ atoms are centred within square antiprisms which face opposite each other across the shared square face on the As net in

the $SrZnBi_2$-type members, but are staggered and share only common edges in the $HfCuSi_2$-type members. A crossover from $SrZnBi_2$- to $HfCuSi_2$-type structures can also be induced through substitution within the tetrahedral site in $CaFe_{1-x}Pt_xAs_2$,[4] but occurs more commonly through substitution of the *RE* component in ternary arsenides $RECu_{1+x}As_2$,[19] $REAuAs_2$,[15] and $REZn_{0.67}As_2$.[18] Interestingly, such a crossover does not take place in $REAgAs_2$, which basically adopts only $HfCuSi_2$-type structures, subject to symmetry-lowering distortions of the As square net.[15,25] These distortions are flagged by abnormally large displacement ellipsoids of the As atoms within the square net and can be manifested as zigzag chains, cis-trans chains, or other configurations that mimic the higher tetragonal symmetry through twinning operations. In the single-crystal structure determinations of $REAg_{0.5}Zn_{0.5}As_2$ reported here, the displacement parameters of these As nets are not so severely expanded (being slightly elongated for *RE* = La) compared to other more pathological cases (**Figure 4-3**). It is possible to refine the structure of $LaAg_{0.5}Zn_{0.5}As_2$ with split As sites in the square net (with negligible improvement in agreement factors), so that the set of four equidistant As2–As2 distances of 2.920 Å differentiates into unequal pairs, the shorter being 2.693 Å, similar to intrachain distances found in other cases where the distortion can be resolved clearly.[25] For $PrAg_{0.5}Zn_{0.5}As_2$ and $NdAg_{0.5}Zn_{0.5}As_2$, such a splitting of the As sites does not seem justified given that their displacement ellipsoids are unextraordinary. Nevertheless, it is important to regard the structures presented as the average ones. The true structures may have lower symmetry or perhaps even exhibit incommensurate modulations[23,24], but detecting superstructure

reflections will require higher resolution of the powder XRD patterns (e.g., through use of synchrotron radiation) or better quality single crystals.

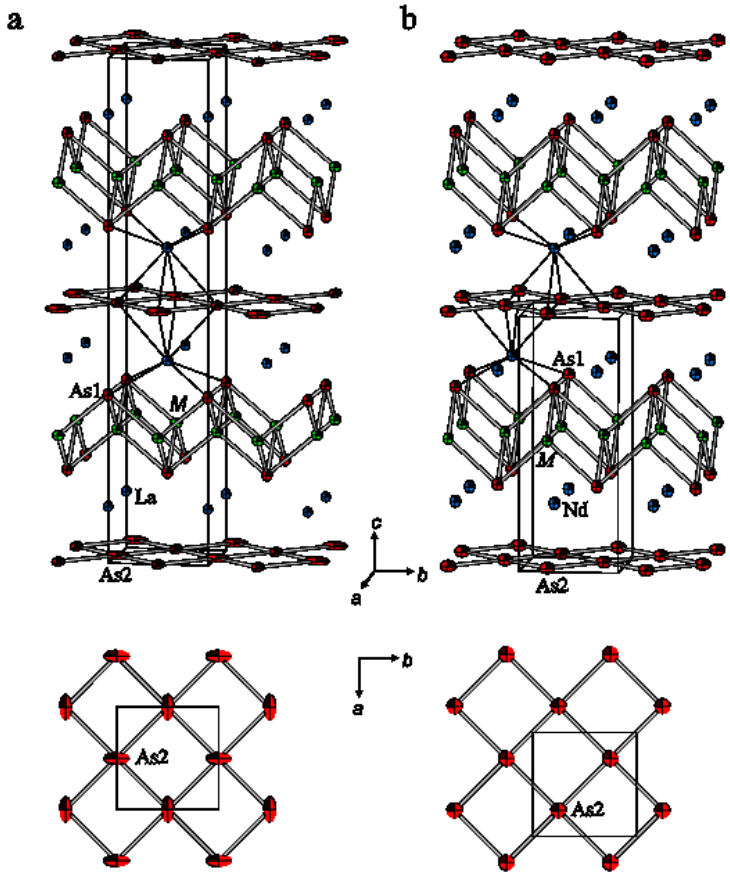


**Figure 4-3.** Views of unit cells and As square nets in $RE$Ag$_{0.5}$Zn$_{0.5}$As$_2$ with (a) SrZnBi$_2$-type ($RE$ = La, Ce) structure, exemplified by LaAg$_{0.5}$Zn$_{0.5}$As$_2$, and (b) HfCuSi$_2$-type (for $RE$ = Pr, Nd, Sm, Gd–Dy) structure, exemplified by NdAg$_{0.5}$Zn$_{0.5}$As$_2$. $RE$ atoms are blue, $M$ atoms (Ag and Zn) are green, and As atoms are red. The displacement ellipsoids are drawn at the 70%

The bonding within square nets of main-group atoms, such as those found in $RE$Ag$_{0.5}$Zn$_{0.5}$As$_2$, has been of considerable theoretical interest.[26,27] If usual electron counting rules are applied in which a four-bonded pnicogen atom within hypervalent square nets is assigned as $Pn^{1-}$, these quaternary arsenides have the formulation ($RE^{3+}$)(Ag$^{+}$)$_{0.5}$(Zn$^{2+}$)$_{0.5}$(As$^{1-}$)(As$^{3-}$), which has an electron excess of 0.5 e$^{-}$ per formula unit.

For the corresponding ternary arsenides, a charge-balanced formulation can be attained for the silver-containing ones, $(RE^{3+})(Ag^{+})(As^{1-})(As^{3-})$, but not for the zinc-containing ones, $(RE^{3+})(Zn^{2+})_{0.67}(As^{1-})(As^{3-})$, which has a slight electron excess of 0.3 $e^-$ per formula unit. An alternative rationalization is that the electron excess in the zinc-containing arsenides is accommodated through reduction of the As atoms within the square net, which recovers charge-balanced formulations $(RE^{3+})(Ag^{+})_{0.5}(Zn^{2+})_{0.5}(As^{1.5-})(As^{3-})$ and $(RE^{3+})(Zn^{2+})_{0.67}(As^{1.3-})(As^{3-})$. The degree of solid solution was thus investigated by preparing samples with nominal compositions $NdAg_{1-x}Zn_xAs_2$ to determine if the combined Ag and Zn content eventually becomes substoichiometric.

The powder XRD patterns indicate that quaternary arsenides with the $HfCuSi_2$-type structure were obtained as pure phase up to about $x = 0.5$, beyond which increasing amounts of other Zn-containing and eventually Ag-containing phases are observed (**Figure 4-4**). The cell parameters for these quaternary arsenides were refined and plotted as a function of $x$ in the nominal reaction composition $NdAg_{1-x}Zn_xAs_2$ (**Figure 4-5a**). As $x$ increases, the $a$-parameter is nearly invariant at 4.1 Å while the $c$-parameter decreases slightly from 10.6 to 10.4 Å; the cell volume does not quite reach a plateau but descends smoothly even past $x \approx 0.5$ when the samples become multiphase. The decrease in cell parameters is consistent with the substitution of Ag with smaller Zn atoms, but we must contend with the possibility that the tetrahedral site may also be decreasing in occupancy. Because the trends in these cell parameters are too subtle to establish if a limiting composition is attained past $x \approx 0.5$, the chemical compositions of crystals obtained from these reactions were evaluated from EDX analyses (**Table 4-1**). The Ag and Zn contents (normalized per

formula unit), as well as the combined content of the two elements, show clearer trends when plotted as a function of $x$ (**Figure 4-5b**). The Ag content decreases linearly and tracks directly with 1–$x$; that is, we can be confident that the Ag content matches with what was loaded in the reaction. In contrast, the Zn content deviates more and more from the loaded content as $x$ increases, eventually reaching the limiting value of 0.6, which is close to the maximum content that can be attained in the ternary zinc-containing arsenides $RE$Zn$_{0.67}$As$_2$.[18] The combined Ag and Zn content becomes less than unity past $x \approx 0.5$, consistent with the observation of multiphase samples past this point in the XRD analyses. In fact, this plot suggests that the quaternary arsenides obtained from reactions with $x = 0.5$ may already be slightly substoichiometric in Zn, with a formula of $RE$Ag$_{0.5}$Zn$_{0.4}$As$_2$; within experimental uncertainties (e.g., from EDX analyses and from weighing), this formula is close to the nominal composition and the single-crystal structure formula $RE$Ag$_{0.5}$Zn$_{0.5}$As$_2$. Given this evidence of Zn substoichiometry, however, we must revise the general formula to $RE$Ag$_{1-x}$Zn$_y$As$_2$ to admit the possibility that the sum of Ag and Zn can be less than one.

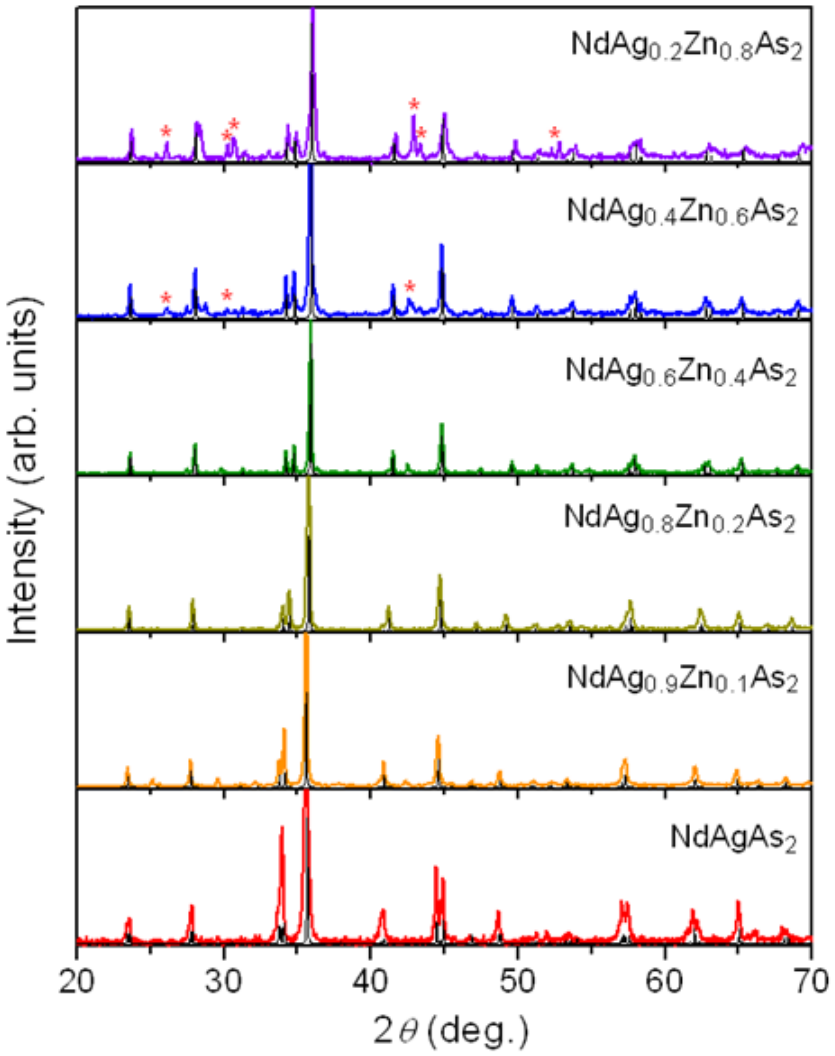


**Figure 4-4.** Powder XRD patterns for reactions with nominal composition $NdAg_{1-x}Zn_xAs_2$. Peaks that do not belong to $HfCuSi_2$-type phases are marked with asterisks.

As further support for the substoichiometric compositions, single-crystal structures were determined for four members of $NdAg_{1-x}Zn_yAs_2$ (**Tables 4-6 to 4-8**). Details on how these structures were refined are discussed in the experimental section. The resulting formulas were $NdAg_{0.8}Zn_{0.2}As_2$, $NdAg_{0.6}Zn_{0.4}As_2$, $NdAg_{0.4}Zn_{0.5}As_2$, and $NdAg_{0.2}Zn_{0.6}As_2$,

which follow the general trend of the substoichiometry becoming increasingly pronounced in the Zn-richer phases. In contrast to these quaternary arsenides, which were modeled with tetragonal $HfCuSi_2$-type structures, the ternary silver-containing end-member $NdAgAs_2$ has been previously reported to adopt an orthorhombic structure in either space group *Pmcn* (an alternate setting of *Pnma*)[15,25] or *Pmmn*.[14] These lower-symmetry structures differ in the distortion of the As square nets. The *Pmcn* variant contains zigzag chains and unequal pairs (short and long) of As–As distances, whereas the *Pmmn* variant contains slightly puckered nets but retaining all equal As–As distances. The powder XRD patterns obtained here clearly reveal peak splitting in $NdAgAs_2$, the most prominent being the 200/020 set near 45°, that does not occur when even a small amount of Zn is introduced in $NdAg_{0.9}Zn_{0.1}As_2$ and in any of the Zn-richer samples (**Figure 4-3**). Additional evidence that the quaternary arsenides are less prone to distortion, if at all, comes from the observation that the displacement parameters of the As atoms in the square net are unremarkable and become similar in magnitude to those of other atoms in the structure with increasing Zn substitution (cf. $U_{eq}$ of 0.0206(8) $Å^2$ in $NdAg_{0.8}Zn_{0.2}As_2$ and $U_{eq}$ of 0.0127(3) $Å^2$ in $NdAg_{0.2}Zn_{0.6}As_2$) (**Table 4-7**).

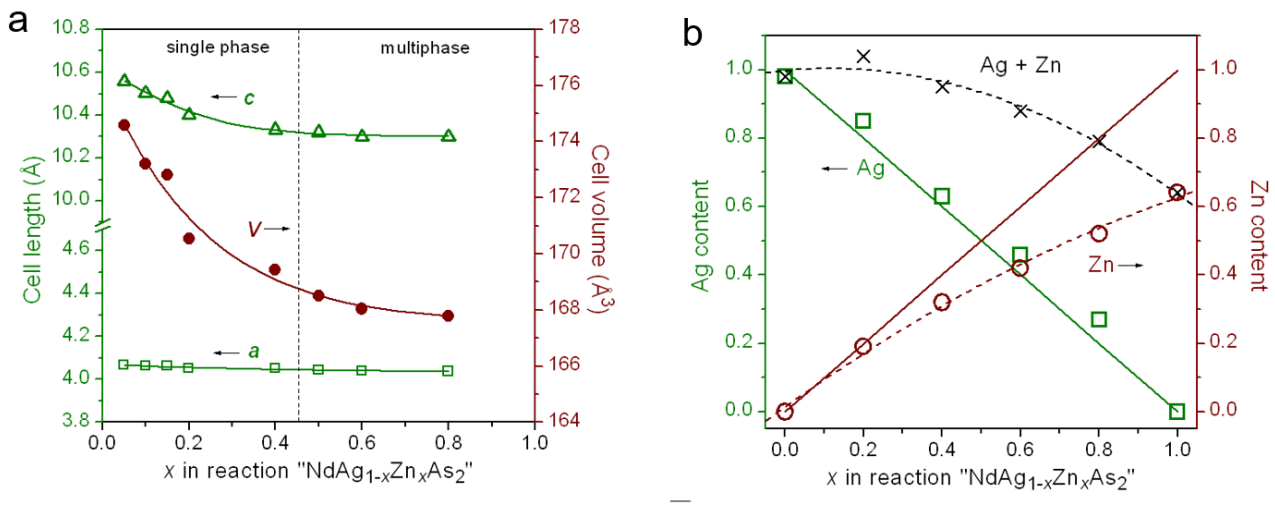


**Figure 4-5.** Plots of (a) cell parameters and (b) Ag and Zn content (and their combined content) for HfCuSi2-type phases obtained from reactions with nominal composition $NdAg_{1-x}Zn_xAs_2$.

Magnetic measurements were performed on $PrAg_{0.5}Zn_{0.5}As_2$ and $NdAg_{0.5}Zn_{0.5}As_2$, as well as on the ternary arsenide $NdAgAs_2$. All appear to exhibit simple paramagnetic behaviour (**Figure 4-6**). The inverse magnetic susceptibility curves are linear and can be fitted to the Curie-Weiss law, $\chi = C / (T - \theta_p)$. The effective magnetic moments (3.65(1) $\mu_B$ for $PrAg_{0.5}Zn_{0.5}As_2$, 3.62(1) $\mu_B$ for $NdAg_{0.5}Zn_{0.5}As_2$, and 3.55(1) $\mu_B$ for $NdAgAs_2$) agree well with the expected free-ion values for $Pr^{3+}$ (3.58 $\mu_B$) and $Nd^{3+}$ (3.62 $\mu_B$). The Weiss parameters (0(1) K for $PrAg_{0.5}Zn_{0.5}As_2$, –6(1) K for $NdAg_{0.5}Zn_{0.5}As_2$, and –16(1) K for $NdAgAs_2$) suggest that weak antiferromagnetic coupling takes place only in the Nd-containing compounds. However, no long-range antiferromagnetic ordering is apparent; in particular, our sample of $NdAgAs_2$ does not show any obvious downturn in the magnetic susceptibility to as low as 2 K, in contrast to previous reports revealing a clear transition at a Néel temperature of 2.7 K.[44] The inverse magnetic susceptibility does show a small

deviation from linearity at low temperatures (<15 K) in our sample of $NdAgAs_2$ but the antiferromagnetic transition is entirely suppressed. The discrepancy in these results could be related to the subtle structural differences (i.e., in the As square nets), which may well arise if the preparative methods differ. In $NdAg_{0.5}Zn_{0.5}As_2$, a small kink in the magnetic susceptibility starts to appear at 2 K, suggesting an incipient antiferromagnetic ordering. It is not surprising that the magnetic coupling between *RE* atoms is weak, given the rather long *RE*–*RE* distances (~4 Å), which corresponds to the *a*-parameter in these compounds. The trend in Weiss parameters implies that this coupling weakens on progressing from $NdAgAs_2$ ($\theta_p$ of –16 K) to $NdAg_{0.5}Zn_{0.5}As_2$ ($\theta_p$ of –6 K), which seems to run counter to expectations that substitution with smaller Zn atoms will contract the entire structure. However, we note that the structural effect of Zn substitution is highly anisotropic, causing a significant contraction along *c* but not along *a* (**Figure 4-3a**). If conduction electrons are assumed to play a role in mediating the magnetic coupling between *RE* atoms, a more important effect may be that the Fermi level is adjusted on progressing from $NdAgAs_2$ to $NdAg_{0.5}Zn_{0.5}As_2$. Related ternary arsenides $REMAs_2$ (*M* = Cu, Ag, Au) also tend to exhibit small negative Weiss parameters and the occurrence of antiferromagnetic ordering (typically at less than 10 K) seems to be quite sensitive to subtle structural features.[45–48]

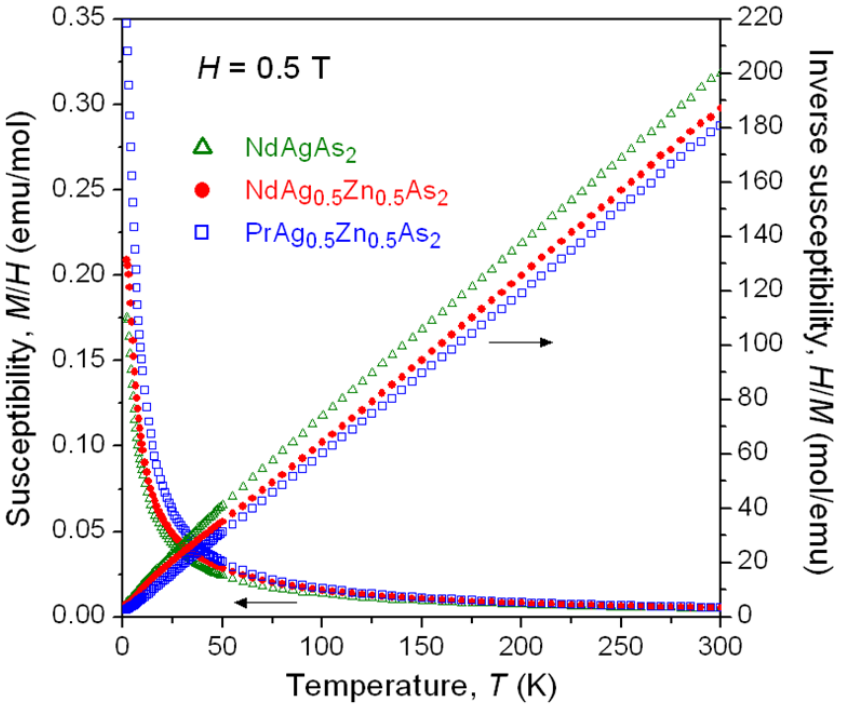


**Figure 4-6.** Magnetic susceptibility curves and their inverse for $NdAgAs_2$, $NdAg_{0.5}Zn_{0.5}As_2$, and $PrAg_{0.5}Zn_{0.5}As_2$.

The electronic band structure was calculated for a hypothetical "$LaAg_{0.5}Zn_{0.5}As_2$" model based on the $HfCuSi_2$-type crystal structure of $NdAg_{0.5}Zn_{0.5}As_2$ except that Nd was replaced by La (for computational reasons) while the Ag and Zn atoms were placed in an ordered checkerboard arrangement (**Figure 4-3**). The formulations $(RE^{3+})(Ag^{+})_{0.5}(Zn^{2+})_{0.5}(As^{1-})(As^{3-})$ or $(RE^{3+})(Ag^{+})_{0.5}(Zn^{2+})_{0.5}(As^{1.5-})(As^{3-})$ presented earlier are essentially equivalent in predicting that the Fermi level will be located just at the bottom of the conduction band, as corroborated in the calculated density of states (DOS) curve. A pseudogap with a very low but nonzero DOS (0.1 states/eV·cell) is found near –0.8 eV, separating a broad valence band that extends down to –6.5 eV and the conduction

band higher in energy. Decreasing the electron count by exactly 1 $e^-$ per cell (or 0.5 $e^-$ per formula unit), which is the electron excess found in the non-charge-balanced formulation, lowers the Fermi level to this pseudogap. Filled d-bands of the Ag and Zn atoms are found well below in energy, consistent with the $d^{10}$ electron configurations of $Ag^+$ and $Zn^{2+}$ species; there is very little contribution of s/p states from these metal atoms near the Fermi level. The As states segregate into a lower-energy s-band (from –8 to –13 eV) and a higher-energy p-band (from –8 eV upwards). Mixing of the Ag and Zn states with the As states provides substantial bonding stability, as seen in population of bonding levels in the crystal orbital Hamilton population curves (COHP). The integrated COHP (–ICOHP) values are 1.53 eV/bond for Ag–As and 1.06 eV/bond for Zn–As interactions within these metal-centred tetrahedra. In accordance with the analysis of bonding of main-group atoms within square nets, which has been well described in the literature,[26,27] the Fermi level cuts through weakly antibonding As–As states involving interactions of As 4p orbitals. The –ICOHP value for these As–As interactions is 0.91 eV/bond. In fact, the COHP curves do not change rapidly over an energy window from –1 to 0 eV, above which the slope of the Zn–As COHP curve rises steeply. The relative insensitivity to changes in electron count over this energy window rationalizes the solid solubility seen in $NdAg_{1-x}Zn_yAs_2$ and permits the small electron excess observed when more Zn substitutes for Ag, up to a limit beyond which deficiencies of the higher-valent Zn atoms must occur as a counteracting effect.

Why some square nets of main-group atoms distort and others do not, as is the case in the quaternary arsenides *RE*$Ag_{0.5}Zn_{0.5}As_2$ here, depends on several factors, including electron count and degree of orbital interactions. The principal driving force for the distortion of the square net is that a net stabilization is gained when filled bonding levels go down in energy and empty antibonding levels go up, while an energy gap opens at the Fermi level. Although such distortions do occur in the ternary arsenides *RE*$AgAs_2$, they are not sufficient to produce an energy gap. [25] On proceeding to the quaternary arsenides *RE*$Ag_{0.5}Zn_{0.5}As_2$, distortions are disfavoured because the strong mixing of metal and As states prevents antibonding As–As states from rising too high in energy and the increase in electron count positions the Fermi level within these antibonding levels, so that there is no energy stabilization to be gained. To test this explanation, the band structure calculation was repeated on a hypothetical "$LaAg_{0.5}Zn_{0.5}As_2$" model constructed as above but based on a $SrZnSb_2$-type structure containing zigzag As–As chains with 2.6 Å distances (**Figure 4-7**). At this electron count, the As–As interactions become even more strongly antibonding, as expected, at the Fermi level; this distorted structure is less stable by about 9 kJ/mol than the undistorted one.

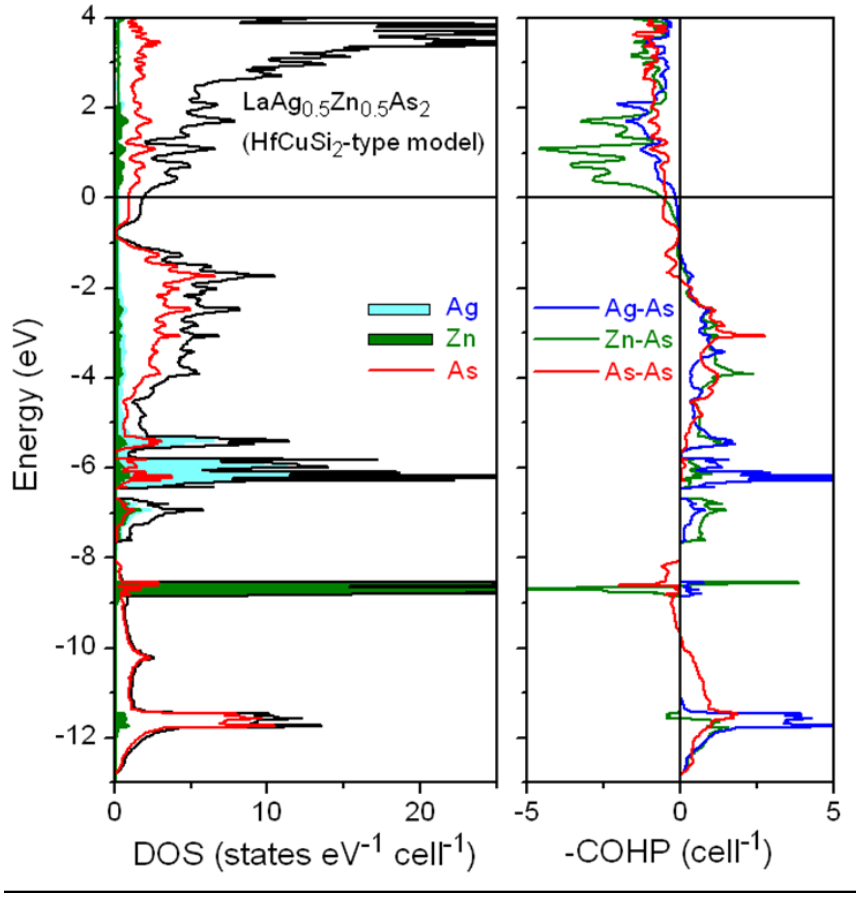


**Figure 4-7.** Density of states (DOS) and crystal orbital Hamilton population (–COHP) curves for hypothetical $LaAg_{0.5}Zn_{0.5}As_2$ model with $HfCuSi_2$-type structure containing undistorted As square net.

## 4.4 Conclusion

The substitution of Zn in stoichiometric ternary arsenides *RE*$AgAs_2$ results in nonstoichiometric quaternary arsenides *RE*$Ag_{1-x}Zn_yAs_2$ in which the combined Ag and Zn content can become less than unity, as demonstrated in a Nd-containing series adopting the $HfCuSi_2$-type structure. This deviation is a response to the increasing electron excess introduced by divalent Zn replacing monovalent Ag. The modest tolerance of the $HfCuSi_2$-

type structure in these quaternary arsenides to a small electron excess (up to 0.5 $e^-$ per formula unit) originates from the presence of only weakly antibonding As–As states which are pinned close to the Fermi level by the strong orbital interactions of metal and As states. Distortions of the square As net appear to be suppressed in these quaternary arsenides.

## 4.5 References


1. Johrendt, D.; Pöttgen, R. *Physica C* **2009**, *469*, 332–339.
2. Pöttgen, R.; Johrendt, D. *Z. Naturforsch., B: J. Chem. Sci.* **2008**, *63*, 1135–1148.
3. Pitcher, M. J.; Parker, D. R.; Adamson, P.; Herkelrath, S. J. C.; Boothroyd, A. T.; Ibberson, R. M.; Brunelli, M.; Clarke, S. J. *Chem. Commun.* **2008**, 5918–5920.
4. Kawamata, T.; Iida, T.; Suzuki, K.; Satomi, E.; Kobayashi, Y.; Itoh, M.; Sato, M. *J. Phys. Soc. Jpn.* **2011**, *80*, 073710-1–0737010-3.
5. Katayama, N.; Kudo, K.; Onari, S.; Mizukami, T.; Sugawara, K.; Sugiyama, Y.; Kitahama, Y.; Iba, K.; Fujimura, K.; Nishimoto, N.; Nohara, M.; Sawa, H. *J. Phys. Soc. Jpn.* **2013**, *82*, 123702-1–123702-4.
6. Yakita, H.; Ogino, H.; Okada, T.; Yamamoto, A.; Kishio, K.; Tohei, T.; Ikuhara, Y.; Gotoh, Y.; Fujihisa, H.; Kataoka, K.; Eisaki, H.; Shimoyama, J. *J. Am. Chem. Soc.* **2014**, *136*, 846–849.
7. Sala, A.; Yakita, H.; Ogino, H.; Okada, T.; Yamamoto, A.; Kishio, K.; Ishida, S.; Iyo, A.; Eisaki, H.; Fujioka, M.; Takano, Y.; Putti, M.; Shimoyama, J. *Appl. Phys. Express* **2014**,*7*, 073102-1–073102-4.
8. Kudo, K.; Kitahama, Y.; Fujimura, K.; Mizukami, T.; Ota, H.; Nohara, M. *J. Phys. Soc. Jpn.* **2014** *83* 093705-1–093705-4.
9. Kuz'ma, Yu.; Chykhrij, S. in: K. A. Gschneidner Jr., K A.; Eyring, L. (Eds.), *Handbook on the Physics and Chemistry of Rare Earths*, vol. 23, Elsevier, Amsterdam, **1996**, pp. 285–434.
10. Sologub, O.L.; Salamakha, P. S. in: Gschneidner Jr., K. A., Bünzli, J. -C. G.; Pecharsky, V. K. (Eds.), *Handbook on the Physics and Chemistry of Rare Earths*, vol. 33, Elsevier, Amsterdam, 2003, pp. 35–146.
11. Mar, A. in: Gschneidner Jr., K. A., Bünzli, J. -C. G.; Pecharsky, V.K. (Eds.), *Handbook on the Physics and Chemistry of Rare Earths*, vol. 36, Elsevier, Amsterdam, 2006, pp. 1–82.
12. Brylak, M.; Möller, M. H.; Jeitschko, W. *J. Solid State Chem.* **1995**, *115*, 305–308.

13. Jemetio Feudjio, J. -P.; Doert, Th.; Böttcher, P. *Z. Kristallogr.–New Cryst. Struct.* **2002**, *217*, 455–457.

14. Demchyna, R. O.; Kuz'ma, Yu. B.; Babizhetsky, V. S. *J. Alloys Compd.* **2001**, *315*, 158–163.

15. Eschen, M.; Jeitschko, W. *Z. Naturforsch., B: J. Chem. Sci.* **2003**, *58*, 399–409.

16. Demchyna, R.; Jemetio, J. P. F.; Prots, Yu.; Doert, Th.; Akselrud, L. G.; Schnelle, W.; Kuz'ma, Yu.; Grin, Yu. *Z. Anorg. Allg. Chem.* **2004**, *630*, 635–641.

17. Nientiedt, A. T.; Jeitschko, W. *J. Solid State Chem.* **1999**, *142*, 266–272.

18. Stoyko, S. S.; Mar, A. *J. Solid State Chem.* **2011**, *184*, 2360–2367.

19. Wang, M.; McDonald, R.; Mar, A. *J. Solid State Chem.* **1999**, *147*, 140–145.

20. Jemetio, J. -P.; Doert, Th.; Rademacher, O.; Böttcher, P. *J. Alloys Compd.* **2002**, *338*, 93–98.

21. Mozharivskyj, Yu.; Pecharsky, A. O.; Bud'ko, S.; Franzen, H .F. *Z. Anorg. Allg. Chem.* **2002**, *628,* 1619–1630.

22. Mozharivskyj, Yu.; Franzen, H. F. *J. Phys. Chem. B* **2002**, *106*, 9528–9535.

23. Rutzinger, D.; Doert, Th.; Ruck, M. *Acta Crystallogr., Sect. B: Struct. Sci.* **2009**, 65, 519–526.

24. Rutzinger, D.; Bartsch, C.; Doert, Th., Ruck, M. *Acta Crystallogr., Sect. B: Struct. Sci.* **2009**, *65*, 527–534.

25. Rutzinger, D.; Bartsch, C.; Doerr, M.; Rosner, H.; Neu, V.; Doert, Th.; Ruck, M. *J. Solid State Chem.* **2010**, *183*, 510–520.

26. Tremel, W.; Hoffmann, R. *J. Am. Chem. Soc.* **1987**, *109,* 124–140.

27. Papoian, G. A.; Hoffmann, R. *Angew. Chem. Int. Ed.* **2000**, *39*, 2408–2448.

28. Cordier, G.; Schäfer, H.; Woll, P. *Z. Naturforsch. B: Anorg. Chem., Org. Chem.* **1985**, *40*, 1097–1099.

29. Sologub, O.; Hiebl, K.; Rogl, P.; Bodak, O. *J. Alloys Compd.* **1985**, *227*, 40–43.

30. Wollesen, P.; Jeitschko, W.; Brylak, M.; Dietrich, L. *J. Alloys Compd.* **1996**, *245*, L5–L8.

31. Flandorfer, H.; Sologub, O.; Godart, C.; Hiebl, K.; Leithe-Jasper, A.; Rogl, P.; Noël, H. *Solid State Commun.* **1996**, *97*, 561–565.

32. Tkachuk, A. V.; Zelinska, O. Ya.; Mar, A. *J. Solid State Chem.* **2006**, *179*, 1506–1512.

33. Zelinska, O. Ya.; Mar, A. *J. Solid State Chem.* **2006**, *179*, 3776–3783.

34. Tabassum, D., Lin, X.; Mar, A. *J. Alloys Compd.* **2015**, *636*, 187–190.

35. Lin, X.; Mar, A. *Inorg. Chem.* **2013**, *52*, 7261–7270.

36. Stoyko, S. S.; Ramachandran, K. K.; Blanchard, P. E. R.; Rosmus, K. A.; Aitken, J. A.; Mar, A. *J. Solid State Chem.* **2014**, *213*, 275–286.

37. Ramachandran, K. K.; Stoyko, S. S.; Mar, A. unpublished results.

38. Sheldrick, G. M. SHELXTL, version 6.12, Bruker AXS Inc., Madison, WI, 2001.

39. Cordier, G.; Eisenmann, B.; Schäfer, H.; *Z. Anorg. Allg. Chem.* **1976**, *426*, 205–214.

40. Andrukhiv, L .S.; Lysenko, L. A.; Yarmolyuk, Ya. P.; Gladyshevskii, E. I.; *Dopov. Akad. Nauk Ukr. RSR, Ser. A: Fiz.-Tekh. Mat. Nauki* **1975**, *7*, 645–648.

41. Gelato, L. M.; Parthé, E. *J. Appl. Crystallogr.* **1987**, *20*, 139–143.

42. Tank, R.; Jepsen, O.; Burkhardt, A.; Andersen, O. K. *TB-LMTO-ASA Program*, version 4.7, Max Planck Institut für Festkörperforschung, Stuttgart, Germany, 1998.

43. Brechtel, E.; Cordier, G.; Schäfer, H.; *Z. Naturforsch., B: Anorg. Chem., Org. Chem.* **1979**, *34*, 251–255.

44. Rutzinger, D. Ph.D. thesis, Technische Universität Dresden, 2009.

45. Sengupta, K.; Rayaprol, S.; Sampathkumaran, E. V.; Doert, Th.; Jemetio, J.P.F. *Physica B* **2004**, *348*, 465–474.

46. Szlawska, M.; Kaczorowski, D. *J. Alloys Compd*. **2008**, *451*, 464–466.

47. Mukherjee, K.; Sampathkumaran, E. V.; Rutzinger, D.; Doert, Th.; Ruck, M. *J. Phys: Condens. Matter* **2009**, *21*, 506004-1–506004-8.

48. Doert, Th.; Schneidewind, A.; Hölzel, M.; Stockert, O.; Rutzinger, D.; Ruck, M. *J. Magn. Magn. Mater*. **2012**, *324*, 1157–1164.

# Chapter 5

## Three Series of Quaternary Rare-Earth Transition-Metal Pnictides with $CaAl_2Si_2$-Type Structures: *RE*CuZn$As_2$, *RE*Ag$ZnP_2$ and *RE*Ag$ZnAs_2$

*A version of this chapter has been published by Stoyko, S.S.; Ramachandran, K. K.; Blanchard, P. E. R.; Rosmus, K. A.; Aitken, J. A.; Mar, A. J. Solid State Chem., 2014, 213, 275-286.*

### 5.1 Introduction

Among ternary phases of the form $AB_2X_2$ ($A$ = alkali, alkaline-earth, or rare-earth metal; $B$ = transition metal or main-group metalloid; $X$ = group 13–16 element), the most commonly occurring ones adopt the tetragonal $ThCr_2Si_2$-type structure[1–3] and are popular for their many exotic physical properties, such as superconductivity.[4–6] $AB_2X_2$ phases adopting the trigonal $CaAl_2Si_2$-type structure are also numerous but slightly less widespread, owing to restrictions on the valence electron count (16 $e^-$/f.u.) and the $B$ component (having $d^0$, $d^5$, or $d^{10}$ configurations).[2,7–13] For many such $CaAl_2Si_2$-type phases, the formally closed-shell electron configurations of the atoms leads to the expectation of small band-gap semiconducting behaviour. The structural and electronic features exhibited by $CaAl_2Si_2$-type phases render them to be excellent candidates for thermoelectric materials.[14–22] Within the structure, the covalently bonded $[B_2X_2]$ framework offers high electronic mobility, while the intervening layers containing ionically bonded $A$ cations inhibit phonon mobility, thus satisfying the "electron-crystal-phonon-glass" criteria often invoked for good thermoelectric properties.[23–25] A major challenge in these investigations is to improve the compositional flexibility of $CaAl_2Si_2$-

type phases, which will be important in their development as thermoelectric materials. A logical step is to explore the preparation of quaternary derivatives of $CaAl_2Si_2$-type phases through aliovalent substitution while preserving the required electron count, and to understand how their properties vary upon systematic chemical changes. This has been achieved previously through introduction of two different *B* components simultaneously with substitution of a trivalent rare-earth metal as the *A* component, resulting in quaternary rare-earth phosphides $YbCuMnP_2$[26] and *RE*$CuZnP_2$ (*RE* = Sc, Y, La–Nd, Sm, Gd–Tm, Lu),[27–32] *RE*$AgZnP_2$ (*RE* = La, Sm);[31] arsenides *RE*$CuZnAs_2$ (*RE* = Y, Yb, Lu);[28,29] and germanides $YMgAlGe_2$ and $GdZnAlGe_2$.[11] Even greater complexity has been demonstrated in quaternary alkali-metal-containing arsenides $AM_{1.5}Tt_{0.5}As_2$ (*A* = Na, K, Rb; *M* = Zn, Cd; *Tt* = Si, Ge, Sn).[33] Recent reports have indicated a good thermoelectric figure of merit (*ZT* of ~0.6 at 1000 K) for $YbCuZnP_2$.[21]

In continuation of our systematic studies of quaternary pnictides with the $CaAl_2Si_2$-type structure, this chapter describes here the elucidation of the three series *RE*$CuZnAs_2$, *RE*$AgZnP_2$, and *RE*$AgZnAs_2$. The range of *RE* substitution has been significantly extended in the *RE*$CuZnAs_2$ and *RE*$AgZnP_2$ series, for which only a handful of members were known previously.[28,29,31] The *RE*$AgZnAs_2$ series is new. X-ray diffraction analysis of these compounds permits a detailed evaluation of factors influencing the crystal chemistry of quaternary pnictides *REMM′Pn*$_2$ (*M* = Cu, Ag; *M′* = Zn; *Pn* = P, As). The bonding and electronic structure of these compounds were further examined through band structure calculations. Core-line and valence band X-ray photoelectron spectra were collected for

the *RE*CuZnAs$_2$ series, and diffuse reflectance spectra were obtained for the *RE*AgZnP$_2$ series. The magnetic properties of the *RE*CuZnAs$_2$ and *RE*AgZnP$_2$ series were measured.

## 5.2 Experimental

### 5.2.1 Synthesis

Starting materials were freshly filed *RE* pieces (99.9%, Hefa or Cerac), Cu powder (99.9999%, Cerac), Ag powder (99.9%, A.D. Mackay), Zn shot or filings (99.99%, Aldrich, or 99.999%, Alfa), red P lumps (99.999%, Aldrich), and As lumps (99.999%, Alfa-Aesar). Stoichiometric mixtures of the elements were loaded into fused-silica tubes, which were evacuated and sealed. The tubes were heated to 500 ºC over 1 day, kept at that temperature for 2 days, heated to 800 ºC over 1 day, kept at that temperature for 7–10 days, and then cooled to room temperature over 1 day. The preheating step at 500 ºC was applied as a precaution to minimize loss of volatile components (such as Zn and As). Sample purity could be improved through subsequent annealing at 800 ºC for 14 d with intermediate grindings. Powder X-ray diffraction (XRD) patterns were collected on an Inel powder diffractometer equipped with a curved position-sensitive detector (CPS 120) and a Cu $K\alpha_1$ radiation source operated at 40 kV and 20 mA. Representative powder XRD patterns are shown in **Figure 5-1**. Substitutions were attempted for all the normally trivalent *RE* metals (Y, La–Nd, Sm, Gd–Tm, Lu), except for Sc, for the *RE*CuZnAs$_2$, *RE*AgZnP$_2$, and *RE*AgZnAs$_2$ series. The products consisted of nearly single-phase quaternary pnictides (generally >97%) which were air-stable. The DyAgZnP$_2$ sample was <30% pure, containing other binary phases and unreacted Ag. Cell parameters refined from the powder XRD patterns, including those of previously reported compounds, are listed in **Table 5-1**.

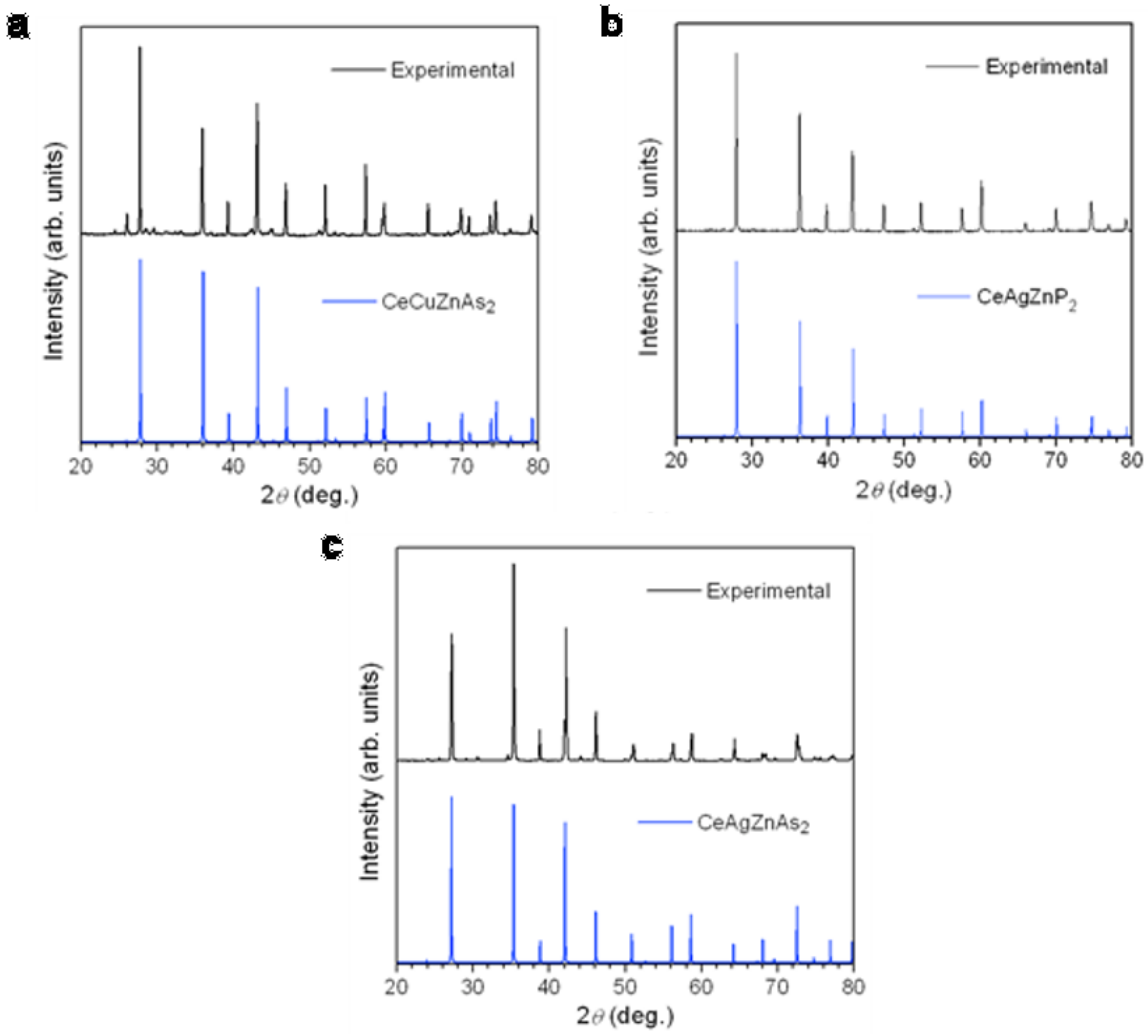


**Figure 5-1.** Representative powder XRD patterns: (a) $CeCuZnAs_2$, (b) $CeAgZnP_2$, and (c) $CeAgZnAs_2$.

**Table 5-1.** Cell parameters *RE*$CuZnAs_2$, *RE*$AgZnP_2$, and *RE*$AgZnAs_2$ [a]

| Compound | *a* (Å) | *c* (Å) | *V* (Å$^3$) | Reference |
|---|---|---|---|---|
| $YCuZnAs_2$ | 4.104(1) | 6.692(1) | 97.61(6) | [28] |
| $LaCuZnAs_2$ | 4.2091(3) | 6.9121(7) | 106.05(3) | This work |
| $CeCuZnAs_2$ | 4.1875(3) | 6.8543(6) | 104.09(2) | This work |
| $PrCuZnAs_2$ | 4.1739(4) | 6.8232(7) | 102.94(3) | This work |

| | | | | |
|---|---|---|---|---|
| $NdCuZnAs_2$ | 4.1621(4) | 6.7995(7) | 102.01(3) | This work |
| $SmCuZnAs_2$ | 4.1417(4) | 6.7562(6) | 100.37(3) | This work |
| $GdCuZnAs_2$ | 4.1222(6) | 6.7260(9) | 98.98(4) | This work |
| $TbCuZnAs_2$ | 4.1130(3) | 6.7037(6) | 98.21(2) | This work |
| $DyCuZnAs_2$ | 4.1050(5) | 6.6911(9) | 97.65(4) | This work |
| $HoCuZnAs_2$ | 4.0937(3) | 6.6731(6) | 96.85(2) | This work |
| $ErCuZnAs_2$ | 4.0853(3) | 6.6614(8) | 96.28(3) | This work |
| $TmCuZnAs_2$ | 4.0775(4) | 6.6481(9) | 95.72(3) | This work |
| $YbCuZnAs_2$ [b] | ——— | ——— | ——— | [29] |
| $LuCuZnAs_2$ | 4.071(1) | 6.634(1) | 95.22(6) | [28] |
| $LaAgZnP_2$ | 4.194(2) | 6.817(2) | 103.8(1) | [31] |
| $CeAgZnP_2$ | 4.188(1) | 6.794(1) | 103.20(6) | This work |
| $PrAgZnP_2$ | 4.1670(7) | 6.758(1) | 101.62(4) | This work |
| $NdAgZnP_2$ | 4.1576(8) | 6.740(2) | 100.90(7) | This work |
| $SmAgZnP_2$ [c] | 4.1247(4) | 6.6920(6) | 98.60(3) | [31] |
| $GdAgZnP_2$ | 4.123(2) | 6.685(3) | 98.4(1) | This work |
| $TbAgZnP_2$ | 4.1054(5) | 6.661(1) | 97.23(4) | This work |
| $DyAgZnP_2$ | 4.075(2) | 6.630(3) | 95.4(1) | This work |
| $LaAgZnAs_2$ | 4.319(2) | 6.989(3) | 112.9(1) | This work |
| $CeAgZnAs_2$ | 4.2876(6) | 6.9354(9) | 110.42(4) | This work |
| $PrAgZnAs_2$ | 4.2805(8) | 6.913(1) | 109.72(5) | This work |
| $NdAgZnAs_2$ | 4.2701(5) | 6.8886(8) | 108.78(4) | This work |
| $SmAgZnAs_2$ | 4.2377(7) | 6.850(1) | 106.55(5) | This work |

| | | | | |
|---|---|---|---|---|
| $GdAgZnAs_2$ | 4.220(1) | 6.832(1) | 105.37(6) | This work |
| $TbAgZnAs_2$ | 4.2169(5) | 6.817(1) | 104.98(4) | This work |
| $DyAgZnAs_2$ | 4.211(1) | 6.805(1) | 104.50(6) | This work |

[a] Refined from powder XRD data. [b] The existence of compound has been reported but not cell parameters, which could not be refined because of poor sample crystallinity. [c]Refined from single-crystal data.

Crystal growth of these compounds was promoted by reheating the samples prepared above in the presence of a few mg of $I_2$ at 800 ºC for 10 days, followed by cooling to room temperature over 1–2 days. The obtained crystals, which were generally small (<0.3 mm), were examined on a scanning electron microscope (Hitachi S-2700, Zeiss EVO MA 15, or JEOL JSM-6010LA). A representative SEM image is shown in **Figure 5-2**. Energy-dispersive X-ray (EDX) analysis on these crystals revealed compositions (20–22% *RE*, 20–21% Cu or Ag, 19–21% Zn, 37–41% P or As) that are in good agreement with expectations (20% *RE*, 20% Cu or Ag, 20% Zn, 40% P or As), with no evidence for iodine incorporation.

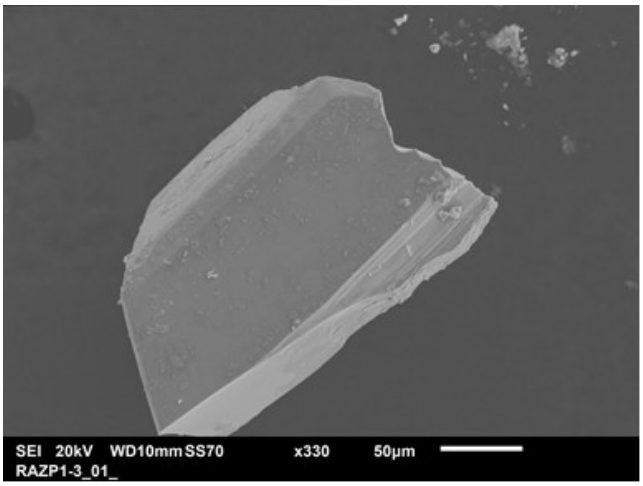


**Figure 5-2.** A representative SEM image of $PrAgZnP_2$.

### 5.2.2 Structure Determination

Where suitable crystals were available, intensity data were collected at room temperature on a Bruker PLATFORM diffractometer equipped with a SMART APEX II CCD area detector and a graphite-monochromated Mo $K\alpha$ radiation source (operated at 50 kV and 30 mA). Data were acquired using $\omega$ scans in 5–8 batch runs at different $\phi$ angles with a frame width of 0.3º and an exposure time of 15–20 s per frame. Face-indexed absorption corrections were applied. Structure solution and refinement were carried out with use of the SHELXTL (version 6.12) program package.[34] The centrosymmetric trigonal space group $P\bar{3}m1$ was chosen. The atomic positions located by direct methods and standardized with the program STRUCTURE TIDY[35] were consistent with the $CaAl_2Si_2$-type structure,[36] which contains only three sites: *RE* atoms in 1*a* (0, 0, 0), Cu or Ag atoms disordered with Zn atoms in 2*d* (1/3, 2/3, ~0.63), and P or As atoms in 2*d* (1/3, 2/3, ~0.25). In *RE*$CuZnAs_2$, the occupancies of the transition-metal site were fixed to be exactly 0.50 Cu and 0.50 Zn. In *RE*$AgZnP_2$ and *RE*$AgZnAs_2$, it should be possible to distinguish between Ag and Zn atoms on the basis of their X-ray scattering factors. When their occupancies were allowed to vary freely, with the constraint that they sum to unity, they generally converged to values of 0.47(1)–0.54(2) Ag and 0.53(1)–0.46(2) Zn, confirming the statistical disorder. In subsequent refinements, these occupancies were similarly fixed to be exactly 0.50 Ag and 0.50 Zn.

Refinements proceeded without complications in all cases except for $CeCuZnAs_2$. Here, the difference Fourier map revealed significant residual electron density of ~9 e/Å$^3$ in 1*b* (0, 0, 1/2) which is surrounded in an octahedral geometry by neighbouring As atoms

at ~2.9 Å. We proposed a structural model in which this site is partially occupied by monovalent Cu atoms, in analogy to known quaternary phases Li*RE*$Cu_2P_2$ in which the same site is interstitially occupied by Li atoms.[30] Refinement of this excess Cu model, with no consideration placed on overall charge balance, led to the formula $CeCu_{1.07(1)}ZnAs_2$ and an improvement in the agreement factors ($R_1$ = 0.011, $wR_2$ = 0.027) relative to the stoichiometric model ($R_1$ = 0.025, $wR_2$ = 0.060). Another possible model is enforce overall charge balance by allowing the occupancies of the mixed Cu/Zn site to deviate from 0.50/0.50 simultaneously as the interstitial Cu atoms are introduced. Refinement of this charge-balanced model led to the formula $CeCu_{1.09(1)}Zn_{0.93(1)}As_2$ and a similar improvement in the agreement factors ($R_1$ = 0.011, $wR_2$ = 0.027). (A third possible model with oxygen atoms entering this interstitial site was tested but rejected on the basis of comparison to reasonable Cu–O distances found in known copper oxides.) The two nonstoichiometric models are close in composition and would be difficult to distinguish experimentally from EDX analyses or cell parameters. In the absence of additional evidence, we report the excess Cu model, recognizing that this is an arbitrary choice.

Crystal data and experimental details of the data collection are summarized in **Tables 5-2 and 5-3**, positional and displacement parameters are listed in **Tables 5-4 and 5-5**, and selected interatomic distances are listed in **Tables 5-6 and 5-7**. Further data, in CIF format, have been sent to Fachinformationszentrum Karlsruhe, Abt. PROKA, 76344 Eggenstein-Leopoldshafen, Germany, as supplementary material No. CSD-427267 to 427281 and can be obtained by contacting FIZ (quoting the article details and the corresponding CSD numbers). Crystallographic data for *RE*$AgZnP_2$ (RE = Ce–Nd)

**Table 5-2.** Crystallographic data for *RE*CuZnAs$_2$ (*RE* = Ce, Nd, Sm, Tb, Dy)

| Formula | $CeCu_{1.07(1)}ZnAs_2$ | $NdCuZnAs_2$ | $SmCuZnAs_2$ | $TbCuZnAs_2$ | $DyCuZnAs_2$ |
|---|---|---|---|---|---|
| Formula mass (amu) | 423.32 | 422.99 | 429.10 | 437.67 | 441.25 |
| Space group | $P\bar{3}m1$ (No. 164) | $P\bar{3}m1$ (No. 164) | $P\bar{3}m1$ (No. 164) | $P\bar{3}m1$ (No. 164) | $P\bar{3}m1$ (No. 164) |
| $a$ (Å) | 4.1862(2) | 4.1629(3) | 4.1449(3) | 4.1200(5) | 4.1069(3) |
| $c$ (Å) | 6.8571(4) | 6.8035(5) | 6.7643(5) | 6.7158(8) | 6.6950(4) |
| $V$ (Å$^3$) | 104.07(1) | 102.11(1) | 100.64(1) | 98.72(2) | 97.79(1) |
| $Z$ | 1 | 1 | 1 | 1 | 1 |
| $\rho_{calcd}$ (g cm$^{-3}$) | 6.755 | 6.879 | 7.080 | 7.362 | 7.492 |
| Crystal dimensions (mm) | 0.10 × 0.09 × 0.03 | 0.18 × 0.13 × 0.04 | 0.15 × 0.08 × 0.03 | 0.11 × 0.11 × 0.03 | 0.14 × 0.07 × 0.04 |
| Radiation | Graphite monochromated Mo $K\alpha$, $\lambda$ = 0.71073 Å | | | | |
| $\mu$(Mo $K\alpha$) (mm$^{-1}$) | 37.42 | 39.35 | 41.61 | 45.46 | 46.92 |
| Transmission factors | 0.110–0.406 | 0.029–0.331 | 0.071–0.389 | 0.080–0.497 | 0.040–0.248 |
| 2$\theta$ limits | 5.94–66.22° | 5.98–66.00° | 6.02–65.70° | 6.06–66.20° | 6.08–66.18° |
| Data collected | $-6 \le h \le 6$, $-6 \le k \le 6$, $-10 \le l \le 10$ | $-6 \le h \le 6$, $-6 \le k \le 6$, $-10 \le l \le 10$ | $-6 \le h \le 6$, $-6 \le k \le 6$, $-10 \le l \le 10$ | $-6 \le h \le 6$, $-6 \le k \le 6$, $-9 \le l \le 10$ | $-6 \le h \le 6$, $-6 \le k \le 6$, $-10 \le l \le 10$ |

| | | | | | |
|---|---|---|---|---|---|
| No. of data collected | 1416 | 1388 | 1399 | 1366 | 1338 |
| No. of unique data, including $F_o^2 < 0$ | 184 ($R_{int}$ = 0.018) | 178 ($R_{int}$ = 0.021) | 176 ($R_{int}$ = 0.017) | 176 ($R_{int}$ = 0.017) | 171 ($R_{int}$ = 0.018) |
| No. of unique data, with $F_o^2 > 2\sigma(F_o^2)$ | 182 | 178 | 175 | 172 | 171 |
| No. of variables | 13 | 10 | 10 | 10 | 10 |
| $R(F)$ for $F_o^2 > 2\sigma(F_o^2)$ [a] | 0.011 | 0.017 | 0.017 | 0.017 | 0.014 |
| $R_w(F_o^2)$ [b] | 0.027 | 0.042 | 0.043 | 0.044 | 0.034 |
| Goodness of fit | 1.18 | 1.31 | 1.17 | 1.31 | 1.28 |
| $(\Delta\rho)_{max}$, $(\Delta\rho)_{min}$ (e Å$^{-3}$) | 1.10, –1.08 | 2.36, –1.46 | 3.42, –1.48 | 1.36, –2.69 | 2.62, –0.68 |



**Table 5-3.** Crystallographic data for *RE*AgZnP$_2$ (*RE* = Ce–Nd) and *RE*AgZnAs$_2$ (*RE* = La–Nd, Sm, Gd, Tb).

| Formula | CeAgZnP$_2$ | PrAgZnP$_2$ | NdAgZnP$_2$ | LaAgZnAs$_2$ | CeAgZnAs$_2$ |
|---|---|---|---|---|---|
| Formula mass (amu) | 375.50 | 376.09 | 379.42 | 461.99 | 463.20 |
| Space group | $P\bar{3}m1$ (No. 164) | $P\bar{3}m1$ (No. 164) | $P\bar{3}m1$ (No. 164) | $P\bar{3}m1$ (No. 164) | $P\bar{3}m1$ (No. 164) |
| *a* (Å) | 4.1846(5) | 4.1687(4) | 4.1535(4) | 4.3130(3) | 4.2904(3) |
| *c* (Å) | 6.7929(9) | 6.7620(6) | 6.7348(7) | 6.9819(5) | 6.9499(4) |

| | | | | | |
|---|---|---|---|---|---|
| $V$ (Å$^3$) | 103.01(2) | 101.77(2) | 100.62(2) | 112.48(1) | 110.79(1) |
| $Z$ | 1 | 1 | 1 | 1 | 1 |
| $\rho_{calcd}$ (g cm$^{-3}$) | 6.050 | 6.137 | 6.262 | 6.821 | 6.942 |
| Crystal dimensions (mm) | 0.06 × 0.04 × 0.03 | 0.05 × 0.05 × 0.04 | 0.04 × 0.04 × 0.04 | 0.28 × 0.27 × 0.13 | 0.23 × 0.21 × 0.10 |
| Radiation | Graphite monochromated Mo $K\alpha$, $\lambda$ = 0.71073 Å | | | | |
| $\mu$(Mo $K\alpha$) (mm$^{-1}$) | 21.88 | 22.94 | 23.99 | 33.30 | 34.44 |
| Transmission factors | 0.455–0.583 | 0.428–0.536 | 0.492–0.562 | 0.018–0.087 | 0.016–0.122 |
| 2$\theta$ limits | 6.00–66.18° | 6.02–65.94° | 6.04–66.22° | 5.84–65.82° | 5.86–66.18° |
| Data collected | $-6 \le h \le 6$, $-6 \le k \le 6$, $-10 \le l \le 10$ | $-6 \le h \le 6$, $-6 \le k \le 6$, $-10 \le l \le 10$ | $-6 \le h \le 5$, $-6 \le k \le 6$, $-10 \le l \le 9$ | $-6 \le h \le 6$, $-6 \le k \le 6$, $-10 \le l \le 10$ | $-6 \le h \le 6$, $-6 \le k \le 6$, $-10 \le l \le 10$ |
| No. of data collected | 1444 | 1452 | 829 | 1578 | 1603 |
| No. of unique data, including $F_o^2 < 0$ | 180 ($R_{int}$ = 0.033) | 179 ($R_{int}$ = 0.021) | 176 ($R_{int}$ = 0.030) | 198 ($R_{int}$ = 0.034) | 198 ($R_{int}$ = 0.023) |
| No. of unique data, with $F_o^2 > 2\sigma(F_o^2)$ | 166 | 170 | 156 | 197 | 197 |
| No. of variables | 10 | 10 | 10 | 10 | 10 |

| | | | | | |
|---|---|---|---|---|---|
| $R(F)$ for $F_o^2 > 2\sigma(F_o^2)$ [a] | 0.014 | 0.010 | 0.022 | 0.022 | 0.021 |
| $R_w(F_o^2)$ [b] | 0.032 | 0.024 | 0.045 | 0.054 | 0.054 |
| Goodness of fit | 1.10 | 1.09 | 1.10 | 1.22 | 1.29 |
| $(\Delta\rho)_{max}$, $(\Delta\rho)_{min}$ (e Å$^{-3}$) | 0.74, –0.96 | 0.71, –0.77 | 1.79, –1.69 | 1.81, –0.65 | 1.47, –2.14 |
| Formula | $PrAgZnAs_2$ | $NdAgZnAs_2$ | $SmAgZnAs_2$ | $GdAgZnAs_2$ | $TbAgZnAs_2$ |
| Formula mass (amu) | 463.99 | 467.32 | 473.43 | 480.33 | 482.00 |
| Space group | $P\bar{3}m1$ (No. 164) | $P\bar{3}m1$ (No. 164) | $P\bar{3}m1$ (No. 164) | $P\bar{3}m1$ (No. 164) | $P\bar{3}m1$ (No. 164) |
| $a$ (Å) | 4.2809(3) | 4.2655(4) | 4.2446(3) | 4.2167(2) | 4.1841(3) |
| $c$ (Å) | 6.9153(5) | 6.8882(7) | 6.8565(4) | 6.8377(4) | 6.8288(5) |
| $V$ (Å$^3$) | 109.75(1) | 108.54(2) | 106.98(1) | 105.29(1) | 103.44(1) |
| $Z$ | 1 | 1 | 1 | 1 | 1 |
| $\rho_{calcd}$ (g cm$^{-3}$) | 7.020 | 7.150 | 7.348 | 7.575 | 7.737 |
| Crystal dimensions (mm) | 0.22 × 0.12 × 0.08 | 0.29 × 0.14 × 0.09 | 0.24 × 0.18 × 0.08 | 0.19 × 0.18 × 0.05 | 0.21 × 0.14 × 0.06 |
| Radiation | Graphite monochromated Mo $K\alpha$, $\lambda$ = 0.71073 Å | | | | |
| $\mu$(Mo $K\alpha$) (mm$^{-1}$) | 35.50 | 36.63 | 38.76 | 41.18 | 42.98 |
| Transmission factors | 0.041–0.189 | 0.027–0.148 | 0.019–0.130 | 0.029–0.169 | 0.027–0.211 |

| | | | | | |
|---|---|---|---|---|---|
| $2\theta$ limits | 5.90–65.88° | 5.92–66.16° | 5.94–66.00° | 5.96–65.96° | 5.98–65.64° |
| Data collected | $-6 \le h \le 6$,<br>$-6 \le k \le 6$,<br>$-10 \le l \le 10$ | $-6 \le h \le 6$,<br>$-6 \le k \le 6$,<br>$-10 \le l \le 10$ | $-6 \le h \le 6$,<br>$-6 \le k \le 6$,<br>$-10 \le l \le 10$ | $-6 \le h \le 6$,<br>$-6 \le k \le 6$,<br>$-10 \le l \le 10$ | $-6 \le h \le 6$,<br>$-6 \le k \le 6$,<br>$-10 \le l \le 10$ |
| No. of data collected | 1514 | 1487 | 1514 | 1445 | 1423 |
| No. of unique data, including $F_o^2 < 0$ | 190 ($R_{int}$ = 0.033) | 191 ($R_{int}$ = 0.021) | 188 ($R_{int}$ = 0.024) | 185 ($R_{int}$ = 0.015) | 179 ($R_{int}$ = 0.017) |
| No. of unique data, with $F_o^2 > 2\sigma(F_o^2)$ | 190 | 190 | 186 | 185 | 177 |
| No. of variables | 10 | 10 | 10 | 10 | 10 |
| $R(F)$ for $F_o^2 > 2\sigma(F_o^2)$ [a] | 0.016 | 0.024 | 0.019 | 0.022 | 0.040 |
| $R_w(F_o^2)$ [b] | 0.036 | 0.063 | 0.047 | 0.056 | 0.100 |
| Goodness of fit | 1.19 | 1.42 | 1.35 | 1.30 | 1.28 |
| $(\Delta\rho)_{max}$, $(\Delta\rho)_{min}$ (e Å$^{-3}$) | 1.02, –0.77 | 3.39, –1.01 | 1.37, –1.49 | 1.51, –2.16 | 3.50, –3.64 |

[a] $R(F) = \sum||F_o| - |F_c|| / \sum|F_o|$. [b] $R_w(F_o^2) = [\sum[w(F_o^2 - F_c^2)^2] / \sum wF_o^4]^{1/2}$; $w^{-1} = [\sigma^2(F_o^2) + (Ap)^2 + Bp]$, where $p = [\max(F_o^2,0) + 2F_c^2] / 3$.

**Table 5-4.** Atomic coordinates and equivalent isotropic displacement parameters (Å$^2$) a for *RE*CuZnAs$_2$ (*RE* = Ce, Nd, Sm, Tb, Dy).

| | CeCuZnAs$_2$ [b] | NdCuZnAs$_2$ | SmCuZnAs$_2$ | TbCuZnAs$_2$ | DyCuZnAs$_2$ |
|---|---|---|---|---|---|
| *RE* in 1*a* (0, 0, 0) | | | | | |
| $U_{eq}$ | 0.0089(1) | 0.0091(2) | 0.0091(2) | 0.0094(2) | 0.0088(2) |
| *M* in 2*d* (1/3, 2/3, *z*) [c] | | | | | |
| *z* | 0.6344(1) | 0.6337(1) | 0.6332(1) | 0.6320(1) | 0.6315(1) |
| $U_{eq}$ | 0.0152(1) | 0.0143(2) | 0.0146(2) | 0.0141(2) | 0.0142(2) |
| As in 2*d* (1/3, 2/3, *z*) | | | | | |
| *z* | 0.2614(1) | 0.2577(1) | 0.2551(1) | 0.2514(1) | 0.2504(1) |
| $U_{eq}$ | 0.0086(1) | 0.0078(2) | 0.0080(2) | 0.0076(2) | 0.0077(2) |

[a] $U_{eq}$ is defined as one-third of the trace of the orthogonalized $U_{ij}$ tensor.

[b] An additional site at 1*b* (0, 0, 1/2) is occupied by 0.072(4) Cu with $U_{eq}$ = 0.017(3) Å$^2$.

[c] 0.50 Cu + 0.50 Zn.

**Table 5-5.** Atomic coordinates and equivalent isotropic displacement parameters (Å$^2$) a for *RE*AgZnP$_2$ (*RE* = Ce–Nd) and *RE*AgZnAs$_2$ (*RE* = La–Nd, Sm, Gd, Tb)

| | CeAgZnP$_2$ | PrAgZnP$_2$ | NdAgZnP$_2$ | LaAgZnAs$_2$ | CeAgZnAs$_2$ |
|---|---|---|---|---|---|
| *RE* in 1*a* (0, 0, 0) | | | | | |
| $U_{eq}$ | 0.0081(2) | 0.0078(1) | 0.0083(2) | 0.0132(2) | 0.0121(2) |
| *M* in 2*d* (1/3, 2/3, *z*) [b] | | | | | |
| *z* | 0.6333(1) | 0.6334(1) | 0.6334(1) | 0.6334(1) | 0.6332(1) |
| $U_{eq}$ | 0.0127(2) | 0.0122(1) | 0.0124(2) | 0.0182(2) | 0.0165(2) |
| *Pn* in 2*d* (1/3, 2/3, *z*) | | | | | |
| *z* | 0.2512(2) | 0.2494(2) | 0.2483(4) | 0.2526(1) | 0.2501(1) |
| $U_{eq}$ | 0.0113(3) | 0.0111(2) | 0.0114(4) | 0.0150(3) | 0.0133(3) |

| | $PrAgZnAs_2$ | $NdAgZnAs_2$ | $SmAgZnAs_2$ | $GdAgZnAs_2$ | $TbAgZnAs_2$ |
|---|---|---|---|---|---|
| *RE* in 1*a* (0, 0, 0) | | | | | |
| $U_{eq}$ | 0.0120(2) | 0.0107(3) | 0.0123(2) | 0.0129(3) | 0.0151(5) |
| *M* in 2*d* (1/3, 2/3, *z*) [b] | | | | | |
| *z* | 0.6330(1) | 0.6332(1) | 0.6325(1) | 0.6319(2) | 0.6316(3) |
| $U_{eq}$ | 0.0164(2) | 0.0153(3) | 0.0164(2) | 0.0168(3) | 0.0192(6) |
| *Pn* in 2*d* (1/3, 2/3, *z*) | | | | | |
| *z* | 0.2479(1) | 0.2467(1) | 0.2440(1) | 0.2432(2) | 0.2441(3) |
| $U_{eq}$ | 0.0136(2) | 0.0120(3) | 0.0134(2) | 0.0122(3) | 0.0100(5) |

[a] $U_{eq}$ is defined as one-third of the trace of the orthogonalized $U_{ij}$ tensor.

[b] 0.50 Ag + 0.50 Zn.

**Table 5-6.** Interatomic distances (Å) for *RE*$CuZnAs_2$ (*RE* = Ce, Nd, Sm, Tb, Dy).

| | $CeCuZnAs_2$ [a] | $NdCuZnAs_2$ | $SmCuZnAs_2$ | $TbCuZnAs_2$ | $DyCuZnAs_2$ |
|---|---|---|---|---|---|
| *RE*–As (×6) | 3.0091(3) | 2.9751(4) | 2.9504(4) | 2.9171(4) | 2.9038(3) |
| *RE*–*M* (×6) | 3.4822(4) | 3.4623(6) | 3.4469(6) | 3.4300(7) | 3.4218(6) |
| *M*–As (×3) | 2.5202(2) | 2.5144(3) | 2.5094(3) | 2.5041(4) | 2.4995(3) |
| *M*–As | 2.5576(7) | 2.5578(11) | 2.5578(10) | 2.5559(11) | 2.5515(9) |
| *M*–*M* (×3) | 3.0396(7) | 3.0142(10) | 2.9960(10) | 2.9671(11) | 2.9534(9) |

[a] The 1*b* site partially occupied by Cu atoms has Cu–As (×6) distances of 2.9185(2) Å and Cu–*M* (×6) distances of 2.5867(2) Å.

**Table 5-7.** Interatomic distances (Å) for *RE*AgZnP$_2$ (*RE* = Ce–Nd) and *RE*AgZnAs$_2$ (*RE* = La–Nd, Sm, Gd, Tb).

| | CeAgZnP$_2$ | PrAgZnP$_2$ | NdAgZnP$_2$ | LaAgZnAs$_2$ | CeAgZnAs$_2$ |
|---|---|---|---|---|---|
| *RE–Pn* (×6) | 2.9579(9) | 2.9389(6) | 2.9234(14) | 3.0515(4) | 3.0262(4) |
| *RE–M* (×6) | 3.4703(5) | 3.4552(3) | 3.4419(6) | 3.5712(5) | 3.5544(5) |
| *M–Pn* (×3) | 2.5402(6) | 2.5340(4) | 2.5270(9) | 2.6143(3) | 2.6064(3) |
| *M–Pn* | 2.5951(16) | 2.5964(11) | 2.594(3) | 2.6583(9) | 2.6624(10) |
| *M–M* (×3) | 3.0191(7) | 3.0077(5) | 2.9964(10) | 3.1095(8) | 3.0927(8) |
| | PrAgZnAs$_2$ | NdAgZnAs$_2$ | SmAgZnAs$_2$ | GdAgZnAs$_2$ | TbAgZnAs$_2$ |
| *RE–Pn* (×6) | 3.0081(4) | 2.9920(5) | 2.9674(5) | 2.9482(6) | 2.9340(12) |
| *RE–M* (×6) | 3.5423(4) | 3.5282(6) | 3.5148(5) | 3.5018(8) | 3.4863(17) |
| *M–Pn* (×3) | 2.6050(3) | 2.5979(4) | 2.5927(4) | 2.5800(5) | 2.5604(11) |
| *M–Pn* | 2.6631(9) | 2.6625(12) | 2.6636(11) | 2.6577(15) | 2.644(3) |
| *M–M* (×3) | 3.0814(7) | 3.0713(10) | 3.0509(9) | 3.0298(13) | 3.010(3) |

### 5.2.3 Band Structure Calculations

Tight-binding linear muffin tin orbital (TB-LMTO) band structure calculations were performed within the local density and atomic spheres approximation with use of the Stuttgart TB-LMTO program.[37] To examine the effects of substituting the rare-earth-metal, transition-metal, or pnicogen components in *REMM′Pn*$_2$ (*M* = Cu, Ag; *M′* = Zn; *Pn* = P, As), the series of four compounds LaCuZnAs$_2$, YCuZnAs$_2$, LaAgZnAs$_2$, and LaAgZnP$_2$ were considered. The mixed occupancy of the transition-metal site was modeled by a hypothetical superstructure in which Cu or Ag atoms alternate with Zn atoms

in an ordered distribution within separate sites in space group *P*3*m*1 (No. 156): *RE* in 1*a* (0, 0, 0); *M* in 1*b* (1/3, 2/3, ~0.37); Zn in 1*c* (2/3, 1/3, ~0.63); *Pn*1 in 1*b* (1/3, 2/3, ~0.75); *Pn*2 in 1*c* (2/3, 1/3, ~0.25). The basis sets included La 6s/6p/5d/4f, Y 5s/5p/4d/4f, Cu 4s/4p/3d, Zn 4s/4p/3d, Ag 5s/5p/4d/4f, As 4s/4p/4d, and P 3s/3p/3d orbitals. The La 6p, Y 4f, Ag 4f, As 4d, and P 3d orbitals were downfolded. Integrations in reciprocal space were carried out with an improved tetrahedron method over 248 irreducible *k* points within the first Brillouin zone.

### 5.2.4 XPS Measurements

XPS spectra were collected for *RE*CuZnAs$_2$ (*RE* = Ce, Sm, Gd, Tb) on a Kratos AXIS 165 spectrometer equipped with a monochromatic Al *K*α source (15 kV, 14 mA) and a hybrid lens with a spot size of 700 μm × 400 μm. The air-stable samples were ground into fine powders, pressed onto In foil, mounted onto a Cu sample holder, and transferred to the XPS instrument. The pressure inside the analysis chamber was maintained at $10^{-7}$ to $10^{-9}$ Pa. The samples were sputter-cleaned with an $Ar^+$ ion beam (4 kV, 10 mA) until all surface oxides were removed; a slight reduction in As was noticeable in the As 3d XPS spectra as a result of this procedure.

Survey spectra, which were collected with a binding energy (BE) range of 1100–0 eV, a pass energy of 160 eV, a step size of 0.7 eV, and a sweep time of 180 s, confirmed the expected compositions. High-resolution core-line (Ce 3d, Cu 2p, and As 3d) spectra were collected for CeCuZnAs$_2$, with energy envelopes of 70, 80, and 20 eV, respectively. Valence band spectra were collected for *RE*CuZnAs$_2$ (*RE* = Ce, Sm, Gd, Tb), with an energy envelope of 30 eV. No charge correction was needed. All spectra were calibrated

against the C 1s line at 284.8 eV arising from adventitious carbon, and they were analyzed with use of the CasaXPS software package.[38] The background, which arises from electron energy loss, was removed by applying a Shirley-type function. The precision in BE values is estimated to be ±0.1 eV, on the basis of previous measurements made on this instrument.

### 5.2.5 Optical Diffuse Reflectance Spectra

Optical diffuse reflectance spectra were collected for *RE*AgZnP$_2$ (*RE* = Ce, Pr, Nd, Gd) on a Varian Cary 5000 UV-Vis-NIR spectrometer equipped with a Harrick Praying Mantis diffuse reflectance accessory. $BaSO_4$ was used as a 100% reflectance standard. Scans were made from 2500 to 200 nm at a rate of 600 nm/min. The percent reflectance was converted to absorption through the Kubelka-Munk equation and the wavelength was converted to energy. The spectra for *RE*AgZnP$_2$ (*RE* = Ce, Pr, Nd, Gd) were normalized to the highest intensity peak and band gaps were estimated by extrapolating the absorption edge to the baseline.

### 5.2.6 Magnetic Measurements

Measurements of dc magnetic susceptibility were made on powders of *RE*CuZnAs$_2$ (*RE* = Ce–Nd, Sm, Gd–Tm) and *RE*AgZnP$_2$ (*RE* = Ce–Nd, Gd, Tb) under an applied field of 0.5 T from 5 to 300 K on a Quantum Design 9T-PPMS dc magnetometer / ac susceptometer. The magnetic susceptibility values were corrected for contributions from the holder and underlying sample core diamagnetism.

## 5.3 Results and Discussion

### 5.3.1 Crystal Structure

Among the four series possible for the quaternary rare-earth transition-metal pnictides *REMM′Pn*$_2$ (*M* = Cu, Ag; *M′* = Zn; *Pn* = P, As), only the *RE*CuZnP$_2$ series had been extensively investigated previously.[27–32] A total of 25 new compounds have now been identified in the remaining three series *RE*CuZnAs$_2$, *RE*AgZnP$_2$, and *RE*AgZnAs$_2$, for which 5 representatives were previously known and, apart from SmAgZnP$_2$, characterized only by powder X-ray diffraction (**Table 5-1**).[28,29,31] Plots of the cell parameters for all compounds, including those from the literature, show a monotonic decrease upon substitution with smaller *RE* components, reflecting the lanthanide contraction (**Figure 5-3**).

Single-crystal structure determinations carried out for *RE*CuAgAs$_2$ (*RE* = Ce, Nd, Sm, Tb, Dy), *RE*AgZnP$_2$ (*RE* = Ce–Nd), and *RE*AgZnAs$_2$ (*RE* = La–Nd, Sm, Gd, Tb) confirm the adoption of the trigonal CaAl$_2$Si$_2$-type structure (space group $P\bar{3}m1$).[36] This relatively simple structure is composed of [*M*$_2$*Pn*$_2$] slabs, which are built up of edge-sharing *M*-centred tetrahedra with Cu or Ag atoms statistically disordered with Zn atoms within the *M* site, alternating with hexagonal nets of octahedrally coordinated *RE* atoms as they stack along the *c*-direction (**Figure 5-4**). The "umbrella" geometry of the four-coordinate *Pn* atoms within the [*M*$_2$*Pn*$_2$] slabs is an unusual feature of the CaAl$_2$Si$_2$-type structure that has been well examined by theoretical considerations; occupation of this site by the more electronegative element (*Pn* atoms in this case) leads to greater dispersion of a filled band in the electronic structure and thus greater energetic stabilization.[2,8] These theoretical

studies also predict that the three lateral or "rib" bonds should be shorter than the one vertical or "handle" bond in these *Pn* coordination environments.[8] Inspection of the bond distances confirms that the lateral *M*–*Pn* distances are generally slightly shorter (by 0.03–0.07 Å) than the vertical *M*–*Pn* distances (**Tables 5-6 and 5-7**). Interestingly, the vertical *M*–*Pn* distances are much less affected than the lateral ones by *RE* substitution within a given *REMM*′*Pn*$_2$ series (cf., vertical *M*–As 2.5515(9)–2.5578(11) Å (×3) and lateral *M*–As 2.4995(3)–2.5202(2) Å in *RE*CuZnAs$_2$ (*RE* = Ce, Nd, Sm, Tb, Dy)). The *M*–*M* distances within these slabs are ~3.0 Å, significantly longer than the sum of the Pauling metallic radii (2.4 Å for Cu–Cu, Cu–Zn, or Zn–Zn contacts).[39]

An alternative description of the structure emphasizes the hcp stacking sequence of the nets of *Pn* atoms, with the octahedral interstices filled by *RE* atoms and the tetrahedral interstices by *M* atoms within every other pair of nets.[32] Because only half the available octahedral and half the tetrahedral interstices are filled within the entire structure, this description highlights the potential for additional atoms to enter the structure. Thus, there is evidence that a small amount of Cu atoms can be introduced into the octahedral site within the [$M_2Pn_2$] slabs in CeCu$_{1.07(1)}$ZnAs$_2$, analogous to what occurs in Li*RE*Cu$_2$P$_2$ []. The Pauling metallic radii ($R_1$) are similar for Li (1.22 Å) and Cu (1.18 Å),[39] and the corresponding distances *M*–*Pn* distances within these octahedra are reasonable (Li–P, 2.795(2) Å in LiTbCu$_2$P$_2$;[30] Cu–As, 2.9185(2) Å in CeCu$_{1.07(1)}$ZnAs$_2$).

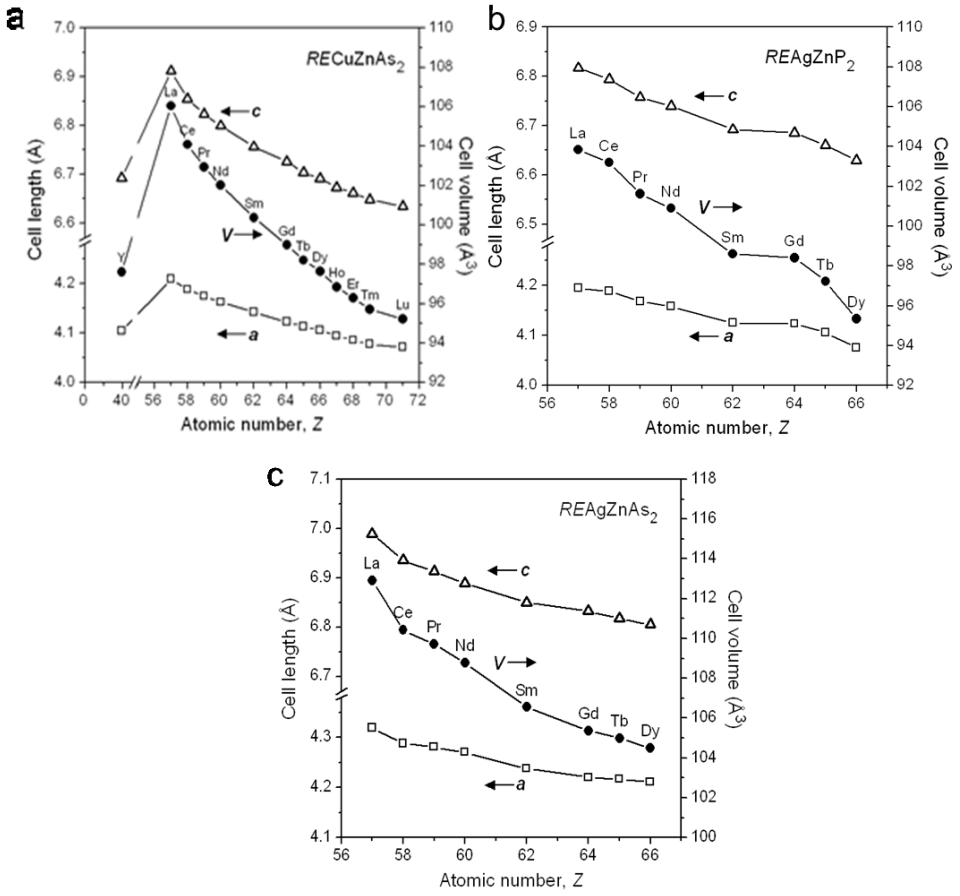


**Figure 5-3.** Plots of cell parameters for (a) *RE*$CuZnAs_2$, (b) *RE*$AgZnP_2$, and (c) *RE*$AgZnAs_2$.

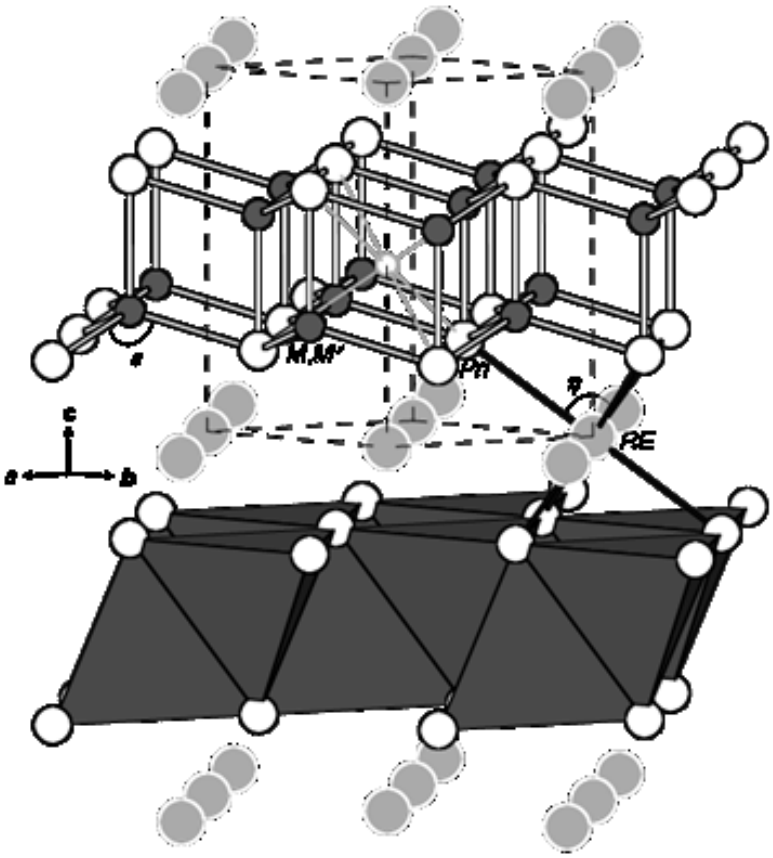


**Figure 5-4.** Structure of *REMM'Pn*$_2$ (*M* = Cu, Ag; *M'* = Zn; *Pn* = P, As) built up of slabs of *M*-centred tetrahedra separated by octahedrally coordinated *RE* atoms. The *M* and *M'* atoms are disordered over the same site. Bond angles are indicated as $\eta$ around the *RE* atoms around the *RE* atoms and $\varepsilon$ around the *M* atoms. Additional interstitial Cu atoms partially occupy octahedral sites located within the slabs in $CeCu_{1.07(1)}ZnAs_2$.

These series of quaternary pnictides can be further analyzed according to crystal chemical principles developed previously by Mewis and co-workers for $AB_2X_2$ phases with the $CaAl_2Si_2$-type structure.[7] They carefully examined distortions in the overall structure, as expressed through the *c*/*a* ratio, and trends in the coordination geometries, as expressed through the bond angles $\eta$ around the octahedrally coordinated *A* atoms and $\varepsilon$ around the

tetrahedrally coordinated *B* atoms (**Figure 5-4**). There are sufficient data from the single-crystal structure determinations to discern trends in the *c*/*a* ratio and the bond angles when they are plotted as a function of *RE–Pn* distances (**Figure 5-5**). Within the *RE*CuZnAs$_2$ and *RE*AgZnP$_2$ series, substitution with a smaller *RE* component reduces the *c*/*a* ratio. This overall contraction results from two competing effects: although the [$M_2Pn_2$] slabs actually become slightly thicker (as seen by the narrowing in $\varepsilon$), these slabs come closer together (as seen by the widening in $\eta$) to maintain reasonable *RE–Pn* distances upon substitution with smaller *RE* atoms. For example, on proceeding from the Ce to the Dy member of the *RE*CuZnAs$_2$ series, the thickness of the [$M_2Pn_2$] slabs increases slightly from 3.272 Å to 3.342 Å, but the separation of these slabs diminishes significantly from 3.585 Å to 3.353 Å. The relatively rigid character of the [$M_2Pn_2$] slabs contrasts with the flexibility of the *RE* interactions to these slabs, as is typical of many $CaAl_2Si_2$-type compounds. The *RE*AgZnAs$_2$ series exhibits a reversal in the trend in the *c*/*a* ratio when the Sm member is reached. In this case, the *c*/*a* ratio initially decreases as the [$M_2Pn_2$] slabs come closer together on progressing from La to Sm; at this point, the octahedral geometry around the *RE* atoms can distort no further, and substitution with a smaller *RE* atom now primarily contracts the structure within the *ab*-plane. The anomaly at the Ce member is noted but is difficult to explain.

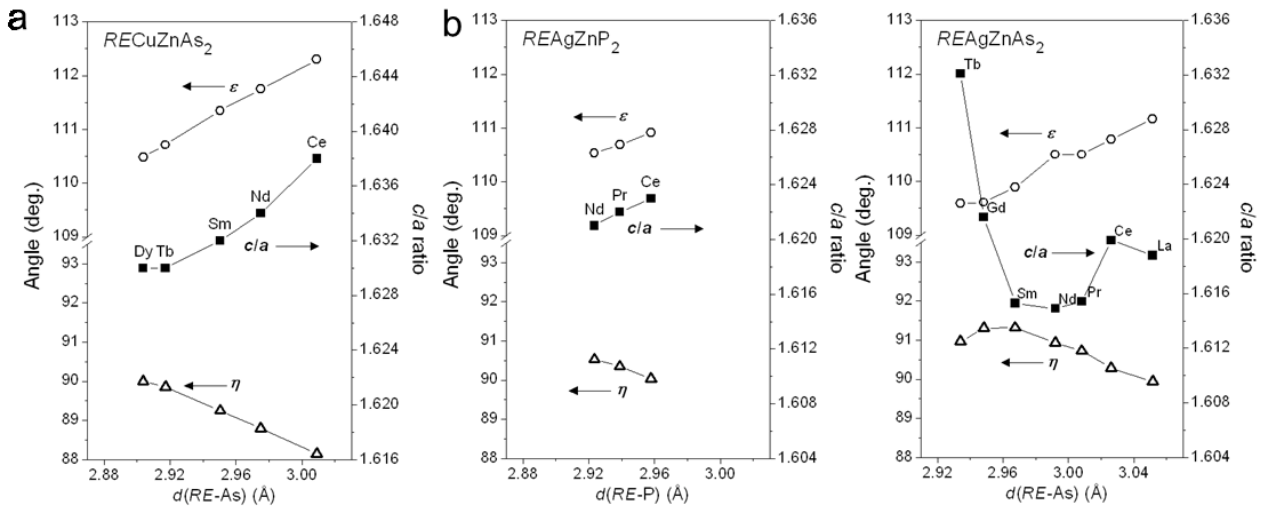


**Figure 5-5.** Plots of *c*/*a* ratio and bond angles ($\eta = \angle(Pn–RE–Pn)$, $\varepsilon = \angle(Pn–M–Pn)$, as defined in **Figure 5-4**) for (a) *RE*CuZnAs$_2$, (b) *RE*AgZnP$_2$, and (c) *RE*AgZnAs$_2$.

The geometrical effects observed above suggest that it may be helpful to envision a hard-sphere model to develop radius-ratio rules, which have been applied previously for many ternary phases $AB_2X_2$ with the $CaAl_2Si_2$-type structure.[7] A structure map based on the average principal quantum number $\bar{n}$ and a weighted function of Slater atomic radii $f = k_n \cdot [r_A/(r_B + 0.2r_X)]$ (where $k_n$ is a factor that scales with the valence of the $A$ component) is effective in delimiting where the $CaAl_2Si_2$-type structure is formed.[7] If an average radius $r_B$ is taken for the mixed Cu/Zn or Ag/Zn sites, the quaternary pnictides $REMM'Pn_2$ ($M$ = Cu, Ag; $M'$ = Zn; $Pn$ = P, As) have parameters in the ranges of $\bar{n}$ = 4.0–4.6 and $f$ = 0.93–1.13, well within the limits of stability of the $CaAl_2Si_2$-type structure (generally $\bar{n}$ = 3–5 and $f$ = 0.9–1.3). A related structure map has been developed for the special case of quaternary arsenides $AM_{1.5}Tt_{0.5}As_2$ ($A$ = alkali metals; $M$ = Zn, Cd; $Tt$ = Si, Ge, Sn); because the $X$ component is fixed to be As, the relevant parameters are the radius ratios $r_A/r_{avg(M+Tt)}$

and $r_M/r_{Tt}$, the latter intended to account for the disorder of differently sized *M* and *Tt* atoms over the same site.[33] For the *REMM*′$As_2$ (*M* = Cu, Zn; *M*′ = Ag) series, the corresponding radius ratios are $r_{RE}/r_{avg(M+M')}$ = 1.3–1.4 and $r_M/r_{M'}$ = 1.0–1.1, which lie within the stability field for the $CaAl_2Si_2$-type structure (1.1–1.6 and 0.9–1.1, respectively, for these parameters).

### 5.3.2 Electronic Structure

Application of the Zintl concept leads to the charge-balanced formulation $RE^{3+}M^{1+}Zn^{2+}(Pn^{3-})_2$ for these series with *M* = Cu, Ag and *Pn* = P, As. Notwithstanding the prediction of semiconducting behaviour, there is growing recognition that the electronic properties of $CaAl_2Si_2$-type phases can depend sensitively on various factors.[13] To examine the role of the rare-earth metal, transition metal, and pnicogen in influencing these properties, band structure calculations were performed on the four compounds $LaCuZnAs_2$, $YCuZnAs_2$, $LaAgZnAs_2$, and $LaAgZnP_2$, modeled as superstructures such that only heteroatomic Cu–Zn or Ag–Zn contacts are present within the [$M_2Pn_2$] slabs.

The band structure for $LaCuZnAs_2$ serves as a convenient reference point to which comparisons can be made with the other compounds. The density of states (DOS) curve is shown together with its atomic projections (**Figure 5-6a**). The most remarkable feature is that the valence and conduction bands nearly touch, with a band gap of <0.02 eV but a zero DOS at the Fermi level (at 0 eV). The general characteristics of the DOS curve conform with the charge-balanced formulation presented above, namely that the filled levels below

the Fermi level are derived largely from Cu 3d (–4 to –2 eV), Zn 3d (–8.5 to –8 eV), As 4s (–12 to –10.5 eV), and As 4p states (–6 to 0 eV), consistent with the closed-shell electron configurations for these atoms. The broad manifold from –6 to 0 eV results from mixing of Cu 3d and some Zn 3d with As 4p states, generating filled metal-arsenic bonding levels that are responsible for most of the stability of the structure, as seen in the crystal orbital Hamilton population (COHP) curves (**Figure 5-6b**). These bonding interactions are just optimized by filling up to the Fermi level, above which they become antibonding within the conduction band. The average integrated COHP value (–ICOHP) for these metal-arsenic bonds is 1.67 eV/bond, but closer inspection reveals a distinction between the stronger "rib" (2.54 Å; Cu–As, 1.73 eV/bond; Zn–As, 1.78 eV/bond) vs. "handle" bonds (2.58 Å; Cu–As, 1.40 eV/bond; Zn–As, 1.40 eV/bond). In particular, the conduction band just above the Fermi level has strongly antibonding character of the Zn–As rib bonds (**Figure 5-7**). Although most of the La states are also found above the Fermi level, there are small contributions to the filled bands such that the –ICOHP value for La–As bonds is significant, 1.08 eV/bond, indicating some covalent character. Metal-metal bonding in the form of Cu–Zn contacts is rather weak, with an –ICOHP value of 0.19 eV/bond; however, it is important for providing additional stability to account for the corrugation of the [$M_2Pn_2$] slabs in $CaAl_2Si_2$-type structures.

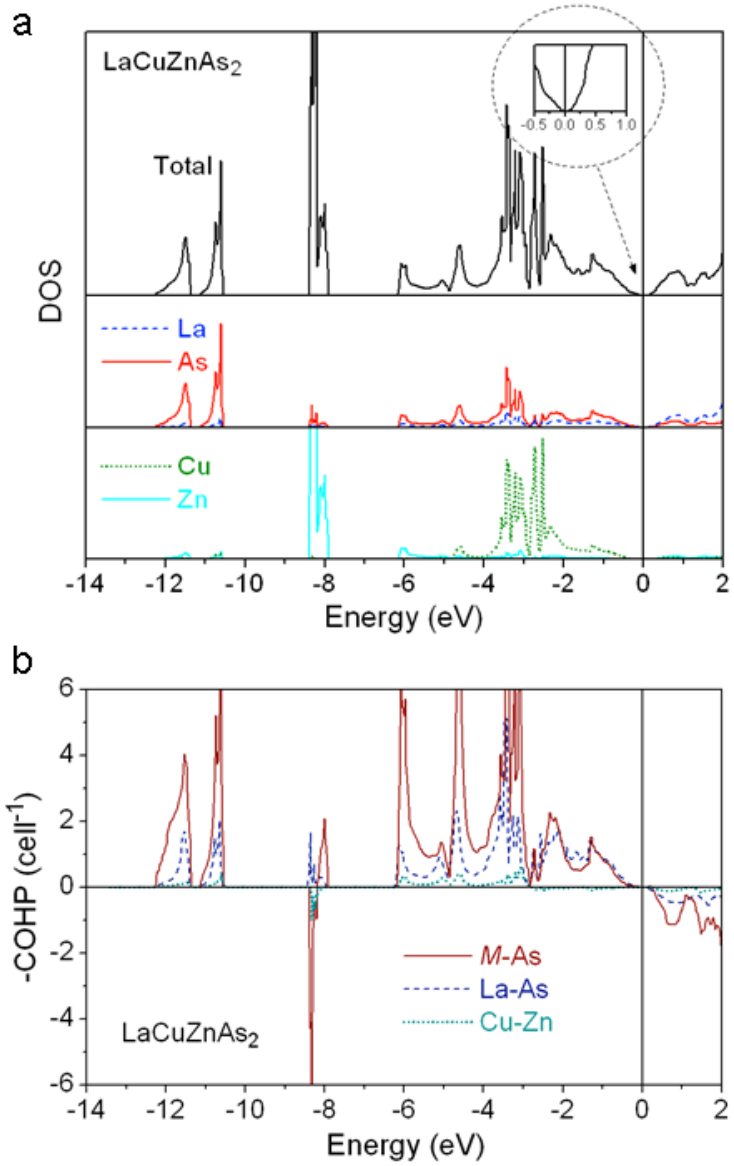


**Figure 5-6.** (a) Density of states (DOS) and its atomic projections for $LaCuZnAs_2$ in an ordered superstructure model. The inset shows details near the Fermi level (at 0 eV). (b) Crystal orbital Hamilton population (–COHP) curves for *M*–As, La–As, and Cu–Zn contacts

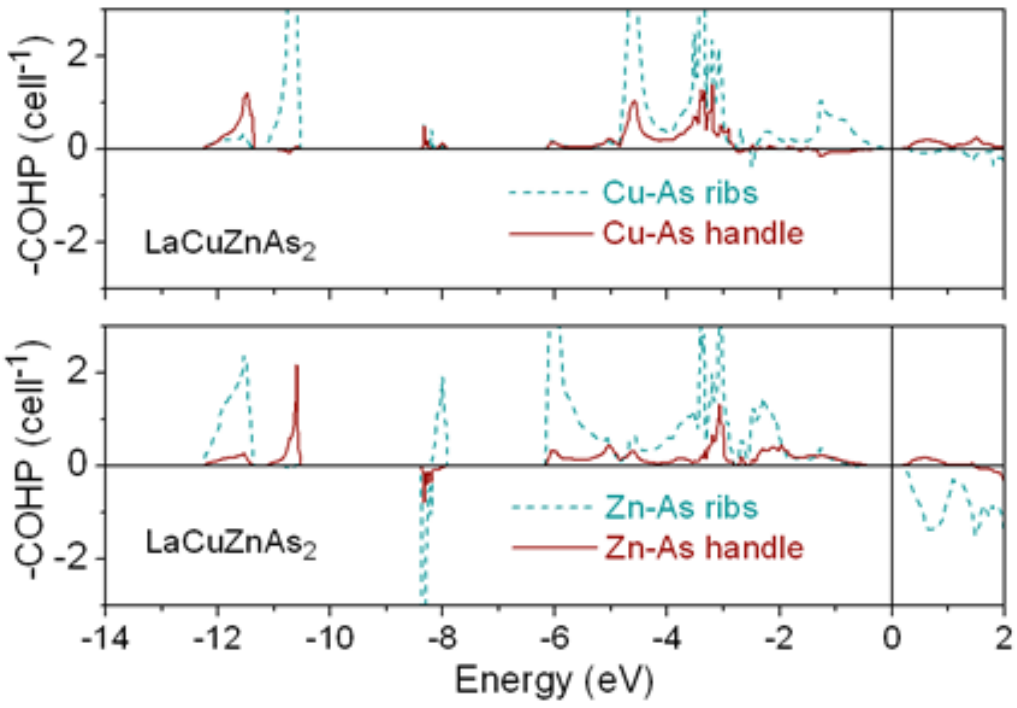


**Figure 5-7.** COHP curves for Cu–As and Zn–As bonds in $LaCuZnAs_2$.

Comparison of the band structure of $LaCuZnAs_2$ with those of $YCuZnAs_2$, $LaAgZnAs_2$, and $LaAgZnP_2$ (**Figure 5-8 to 5-10**) shows interesting trends in the band gap. On proceeding to a smaller *RE* component, from $LaCuZnAs_2$ to $YCuZnAs_2$, the gap between valence and conduction bands now closes and there is a small but nonzero DOS of 0.07 states/eV (per cell) at the Fermi level. This effect was also seen previously in the corresponding phosphides $LaCuZnP_2$ (with a 0.2 eV gap) and $YCuZnP_2$ (with no gap and a DOS of 0.05 states/eV at the Fermi level).[32] Substitution of Cu with Ag to form $LaAgZnAs_2$ results in a wider gap of 0.24 eV. This gap broadens to 0.55 eV upon substitution of As with P in $LaAgZnP_2$. It has been previously proposed that the primary factor that controls the presence or absence of a band gap in $CaAl_2Si_2$-type phases of the

form $AB_2X_2$ is the difference in electronegativity between the $B$ and $X$ atoms within the $[B_2X_2]$ slabs.[13] For disparate types of compounds, this observation is generally valid, but in the case of these quaternary pnictides $REMM'Pn_2$ ($M$ = Cu, Ag; $M'$ = Zn; $Pn$ = P, As), there is little distinction in the electronegativities (cf. Pauling values of 1.9 for Cu, 1.9 for Ag, 1.6 for Zn, 2.1 for P, and 2.0 for As).[39] Band dispersion diagrams for these compounds in the vicinity of the Fermi level reveal that the effects are more subtle (**Figure 5-11**). It appears that the identity of the transition-metal atoms in the $[M_2Pn_2]$ slabs is the more important factor. In the Cu–Zn combinations, the valence and conduction bands nearly touch or just overlap indirectly (with the top of the valence band at Γ and the bottom of the conduction band at L). All other things being equal, Ag–Zn combinations tend to increase the separation between the valence and conduction bands by 0.2–0.3 eV relative to the Cu–Zn combinations, mainly through destabilizing the antibonding levels in the conduction bands. The *RE* atoms act secondarily by virtue of their role as spacers between the $[M_2Pn_2]$ slabs; smaller *RE* atoms tend to shorten all bonds within these slabs, thereby enhancing the dispersion of both valence and conduction bands to increase the likelihood of band overlap.

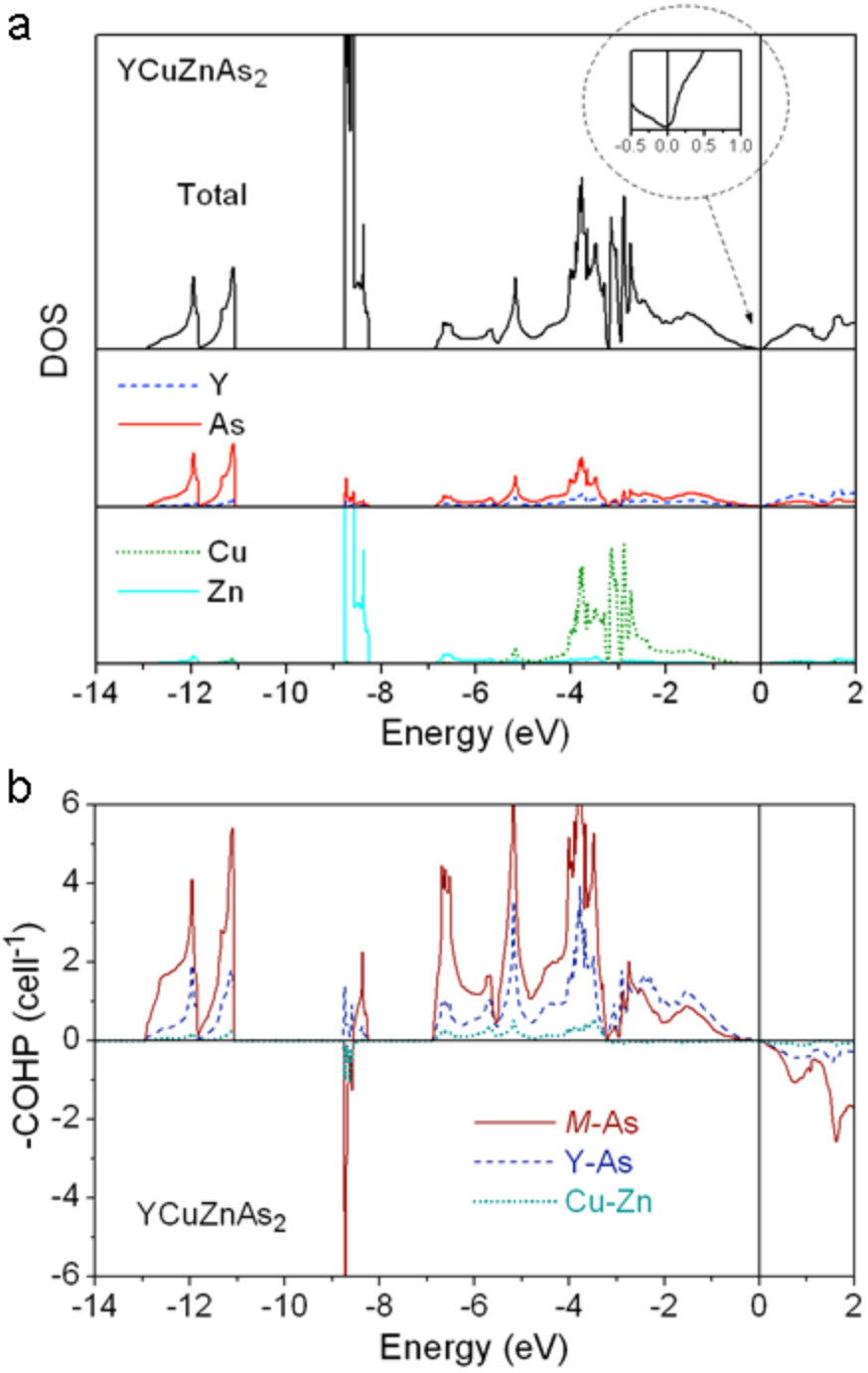


**Figure 5-8.** (a) DOS curves and (b) COHP curves for $YCuZnAs_2$.

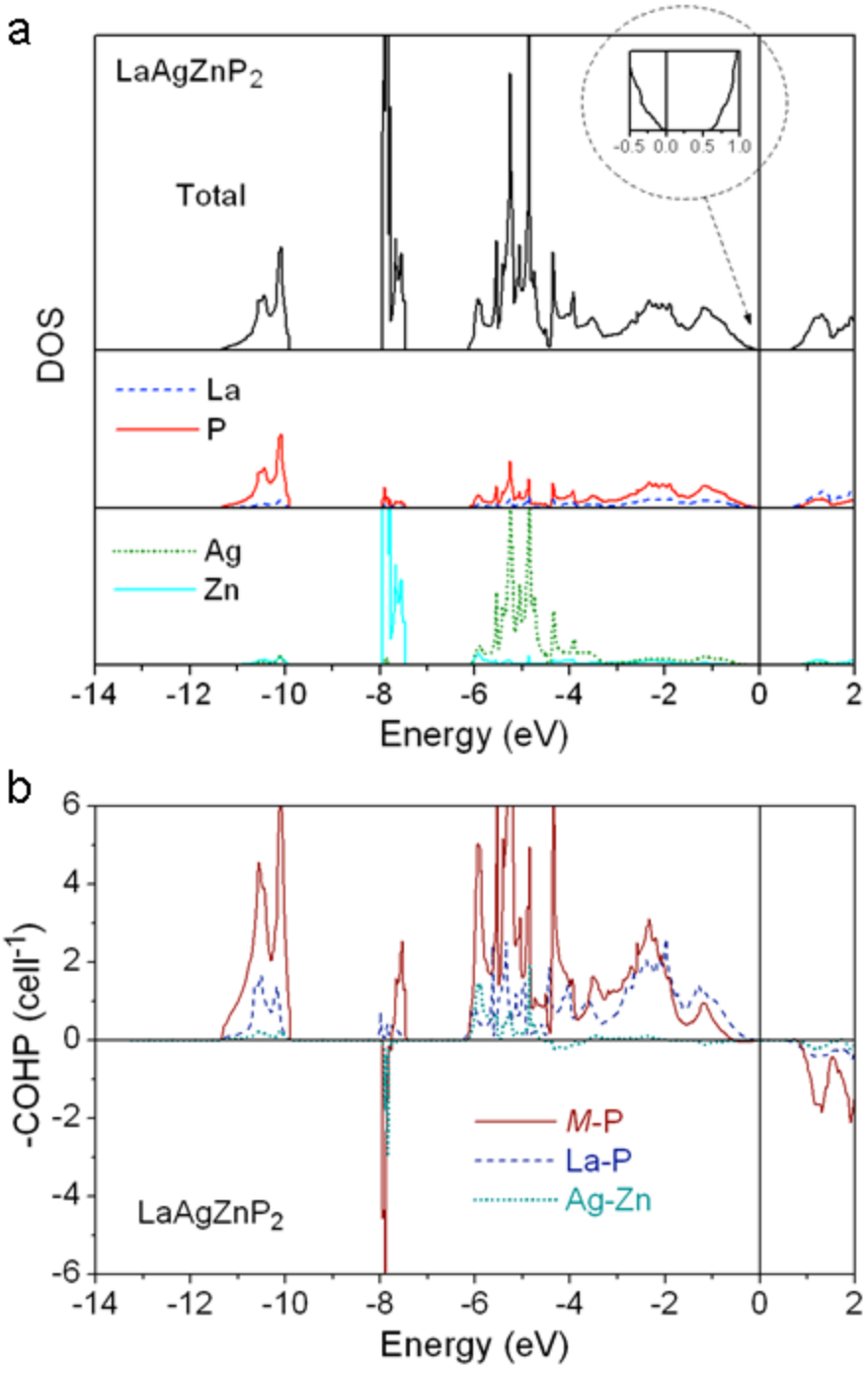


**Figure 5-9.** (a) DOS curves and (b) COHP curves for $LaAgZnAs_2$.

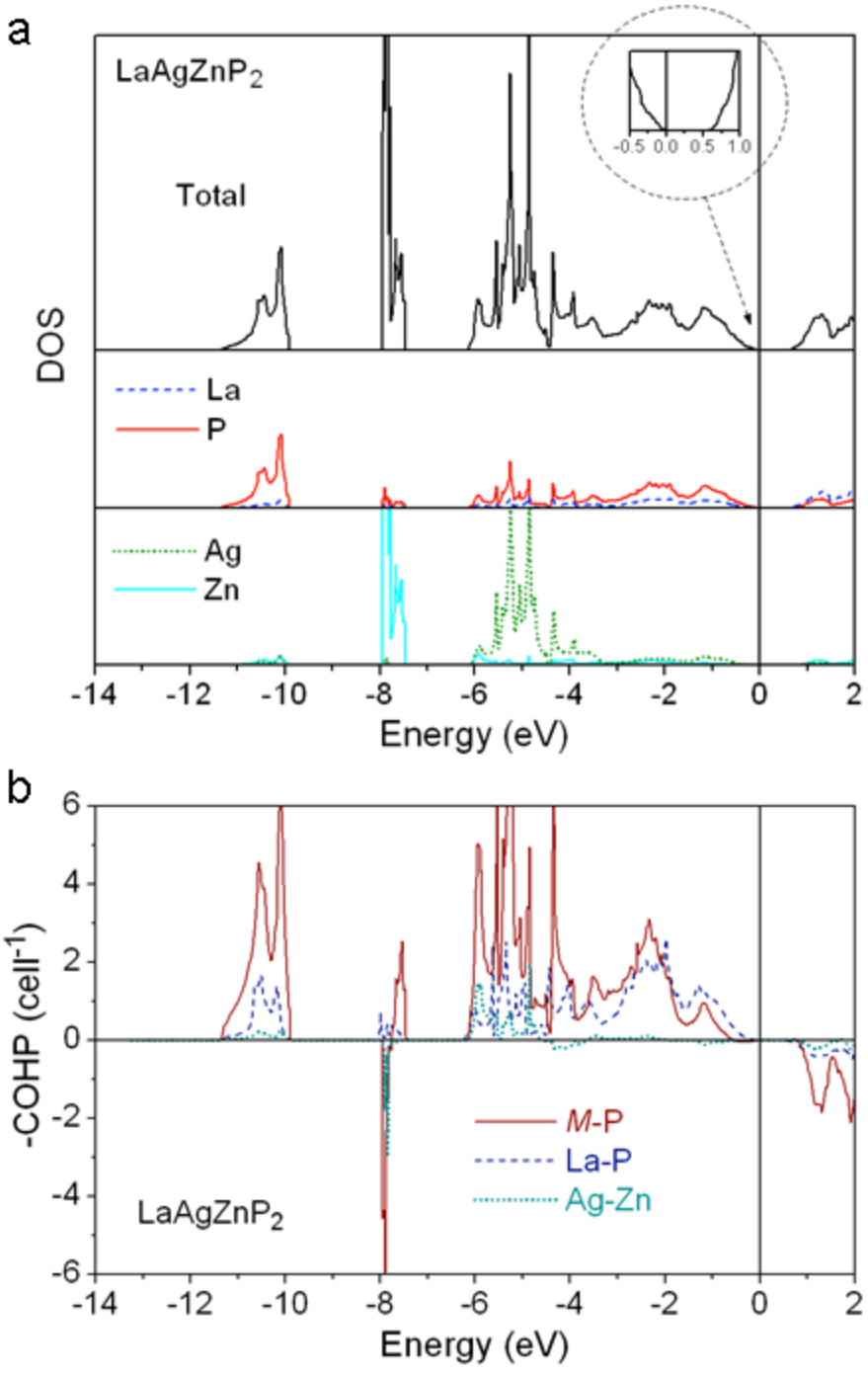


**Figure 5-10.** (a) DOS curves and (b) COHP curves for $LaAgZnP_2$.

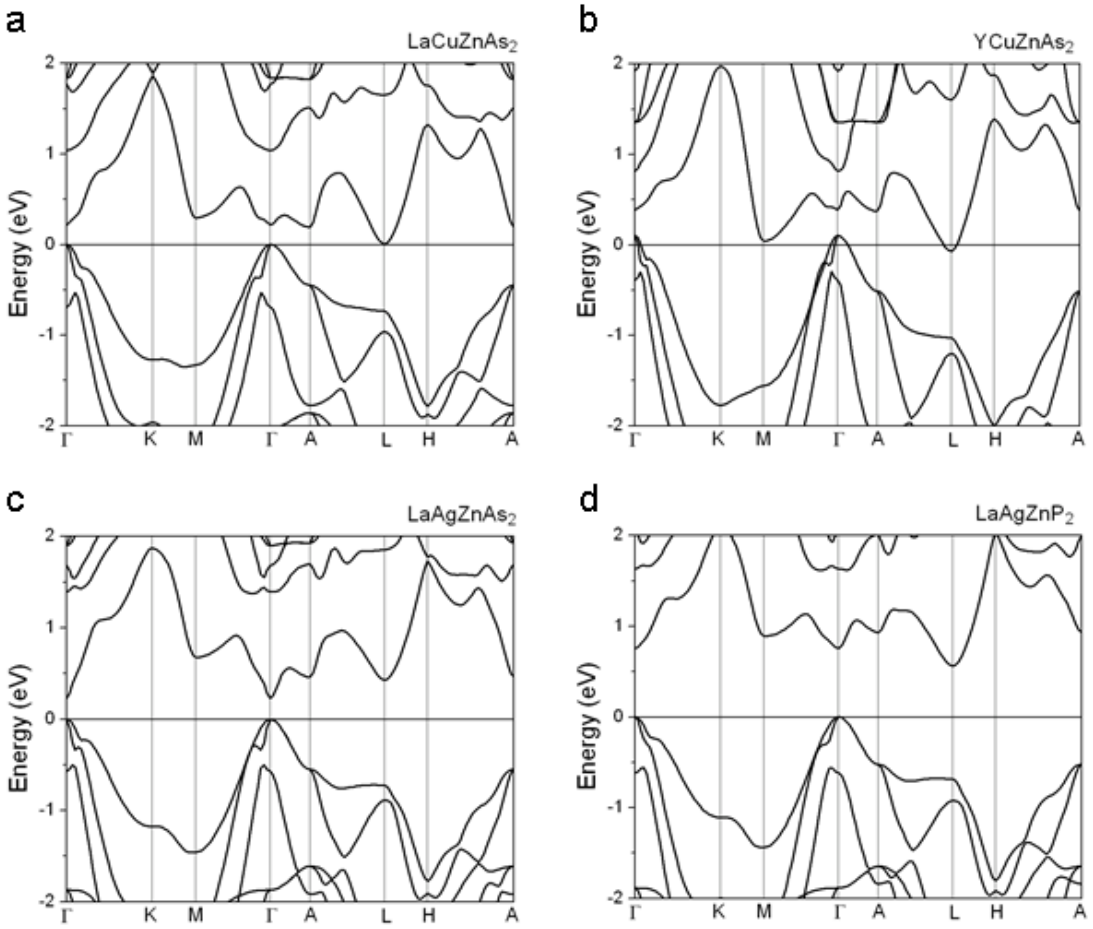


**Figure 5-11.** Band dispersion diagrams for (a) $LaCuZnAs_2$, (b) $YCuZnAs_2$, (c) $LaAgZnAs_2$, and (d) $LaAgZnP_2$.

### 5.3.3 XPS Core Electron and Valence Band Spectra

The charge formulation $RE^{3+}M^{1+}Zn^{2+}(Pn^{3-})_2$ and the band structures discussed above can be verified experimentally through XPS measurements. Core-line XPS spectra reveal information about the localized electronic states of individual atoms, which experience different degrees of shielding depending on their environments within the solid giving rise to binding energies (BE) that should in principle be diagnostic of oxidation

states, whereas valence band XPS spectra probe the delocalized electronic states involved in bonding interactions and can thus be compared to calculated DOS curves.[40] The series *RE*CuZnAs$_2$ (*RE* = Ce, Sm, Gd, Tb) was chosen for analysis.

Core-line Ce 3d, Cu 2p, and As 3d XPS spectra were collected (**Figure 5-12**). (The *RE* 3d spectra for the later *RE* atoms were inaccessible because their peaks lie at energies that are too close to the maximum kinetic energy of the X-ray source.) The Ce 3d spectrum for CeCuZnAs$_2$ consists of a doublet of core-line peaks representing the 3d$_{5/2}$ and 3d$_{3/2}$ spin-orbit-split final states, along with intense satellite features (**Figure 5-12a**). This fine structure is typical of *RE* spectra, for which multiplet splitting arising from coupling with the poorly screened 4f electrons as well as other relaxation mechanisms can lead to difficulties in interpretation. Thus, the BE of the Ce 3d$_{5/2}$ peak (882.1 eV) is not a reliable indicator of oxidation state.[41] Instead, we note the similarity of this spectrum to those of other cerium-containing compounds (such as $CeF_3$, $CeFe_4P_{12}$, CeFeAsO, and $CeCrSb_3$),[41–43] especially in terms of lineshape, to argue for the presence of trivalent cerium in CeCuZnAs$_2$. It is assumed that the main core-line peaks are found at lower BE and the satellite features (caused by a ligand-to-metal shake-up process)[44] are the more intense peaks found at higher BE within the 3d$_{5/2}$ or 3d$_{3/2}$ set of peaks.

The Cu 2p spectra are identical for the entire series *RE*CuZnAs$_2$ (*RE* = Ce, Sm, Gd, Tb) (**Figure 5-12b**). There are two peaks corresponding to the 2p$_{3/2}$ and 2p$_{1/2}$ spin-orbit-split final states in an intensity ratio of 2:1. The Cu 2p$_{3/2}$ BE is essentially constant at 933.2–933.3 eV, indicating that substitution of the *RE* component has little or no effect on the electronic structure of the Cu atoms. Again, these BE values alone cannot be used to

assign oxidation states. Rather, the linewidths of the core-line peaks (FWHM of 1.1–1.2 eV) are similar to those in CuBr and CuI, containing monovalent copper species,[45,46] but much narrower than in CuO (FWHM of ~3 eV), containing divalent copper species.[47] However, the key criterion is that a satellite peak at the high BE side of the $2p_{3/2}$ core-line peak (945–940 eV) is absent in $Cu^{+}$ systems (having a completely filled $3d^{10}$ subshell), as is the case here, but would be present in $Cu^{2+}$ systems (having a partly filled $3d^{9}$ subshell), for which a shake-up process can take place involving excitation of valence electrons into available empty Cu 3d conduction states.[48–50]

The As 3d spectra show a broad envelope that was fit to two peaks corresponding to the $3d_{5/2}$ and $3d_{3/2}$ spin-orbit-split final states, each with a FWHM of 1.0 eV, in an intensity ratio of 3:2 and with a BE separation of 0.7 eV (**Figure 5-12c**). Although the As atoms are directly bonded to the *RE* atoms, no shifts could be resolved among the different *RE* members, with the As $3d_{5/2}$ BE remaining unchanged at 40.7–40.8 eV. This BE is lower than in elemental As (41.7(2) eV),[51] indicating the presence of anionic As species in *RE*$CuZnAs_2$, and is the same as in $BaAg_2As_2$ ($ThCr_2Si_2$-type), which also contains metal centres coordinated tetrahedrally by As atoms.[52]

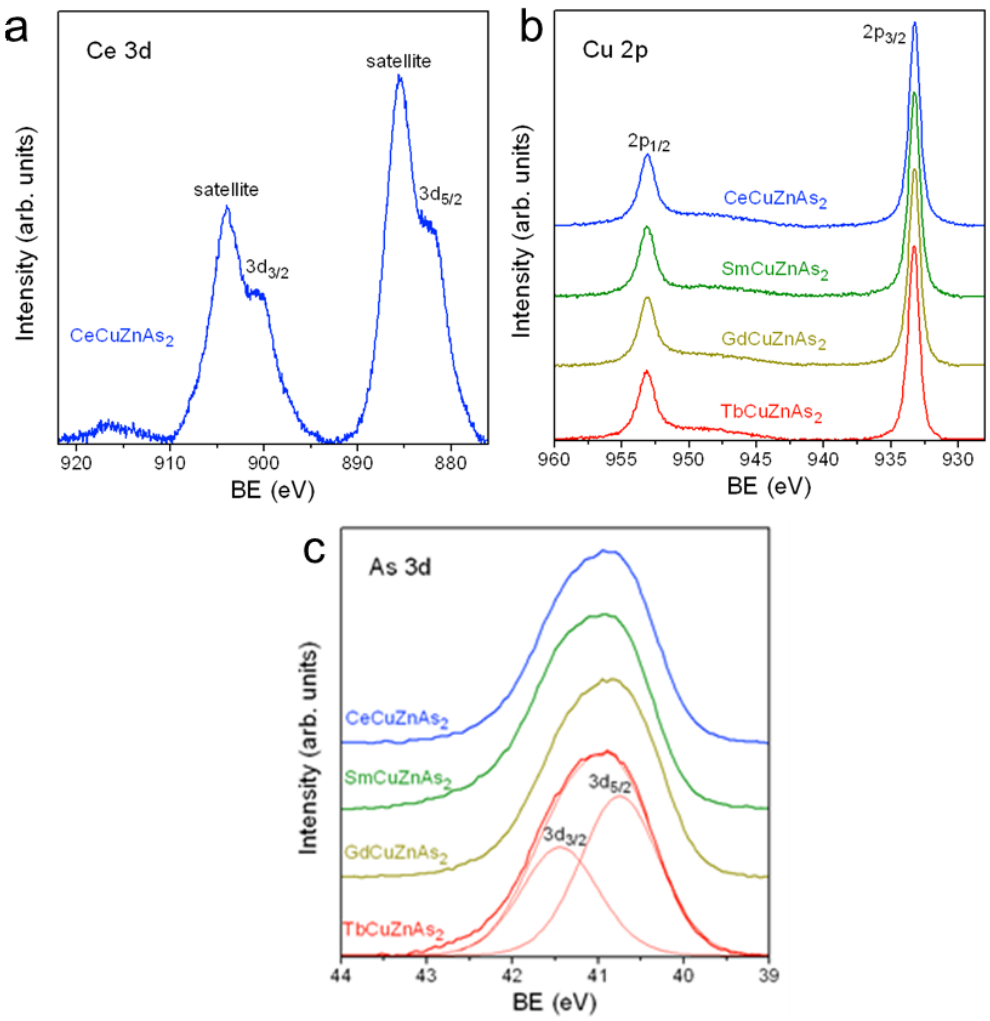


**Figure 5-12.** Core-line XPS spectra: (a) Ce 3d spectrum for $CeCuZnAs_2$, (b) Cu 2p spectra for *RE*$CuZnAs_2$ (*RE* = Ce, Sm, Gd, Tb), and (c) As 3d spectra for *RE*$CuZnAs_2$ (*RE* = Ce, Sm, Gd, Tb).

The valence band spectra for *RE*$CuZnAs_2$ (*RE* = Ce, Sm, Gd, Tb) (**Figure 5-13**) can be interpreted with the aid of the calculated DOS curves for $LaCuZnAs_2$ or $YCuZnAs_2$. However, the XPS intensities will depend strongly on photoionization cross-sections for different types of atoms. Moreover, final state effects (especially multiplet splitting of the *RE* 4f states) may produce additional complex features in the spectra that make detailed

interpretation difficult. There are three general regions (labeled A, B, and C) identified in these spectra of these arsenides, very similar to the phosphides *RE*CuZn$P_2$ (*RE* = Gd, Tb, Dy, Ho, Er).[32] The broad region A found at low BE (6 to 0 eV) corresponds to the wide manifold of mixed Cu 3d and As 4p states seen in the DOS curve (–6 to 0 eV). The narrower region B found at high BE (14 to 8 eV) is composed of Zn 3d and As 4s states. Because of the larger cross-section associated with Zn 3d states,[53,54] they dominate the intensity in this region. These two regions correspond to the states arising from the [CuZn$As_2$] slabs common to all four compounds, and thus they remain largely unchanged. Region C shifts in energy depending on the compound, and must thus be attributed to *RE* 4f states. In the case of CeCuZn$As_2$, this region is probably subsumed within the broad peak A; valence band spectra of related Ce-containing compounds ($CeFe_4P_{12}$, $CeCrSb_3$, CeFeAsO)[41–43] suggest that the Ce 4f states should be located around 2 eV. In all spectra, the intensity does not show a sharp cutoff at 0 eV, but rather decreases smoothly as the BE increases to 0 eV and vanishes so that there are no states at the Fermi edge. This observation agrees with the prediction of a semimetal with very low or zero DOS at the Fermi level, as seen in the DOS curves for $LaCuZnAs_2$ or $YCuZnAs_2$.

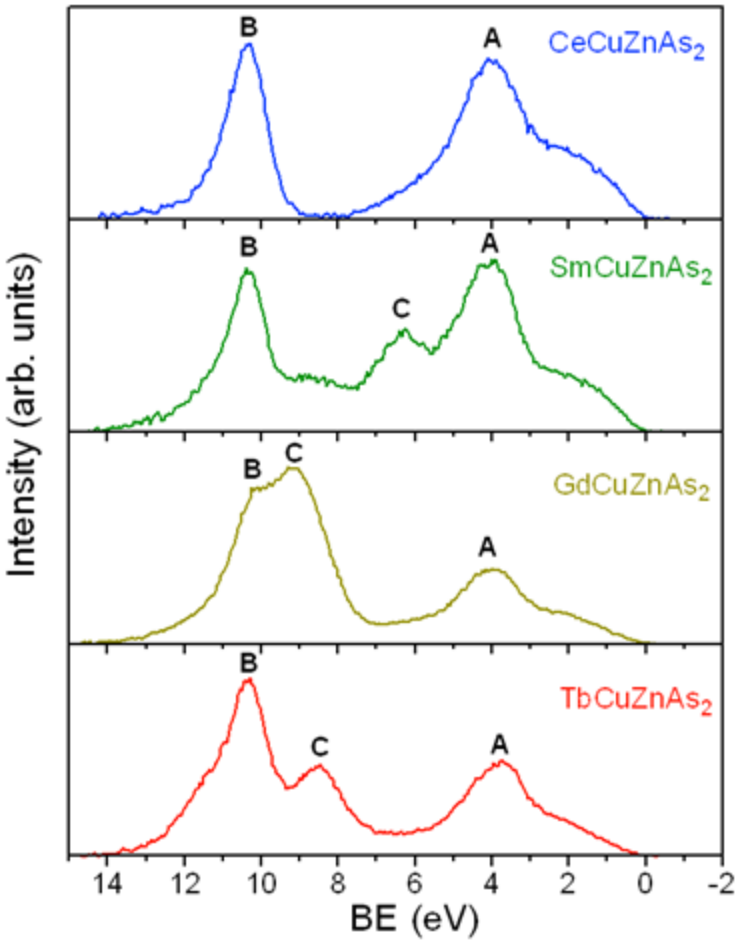


**Figure 5-13** XPS valence band spectra for *RE*CuZnAs$_2$ (*RE* = Ce, Sm, Gd, Tb). The peaks labeled A, B, and C are discussed in the text.

### 5.3.4 Diffuse Reflectance Spectra

From the band structure results above, the *RE*AgZnP$_2$ series are clearly shown to be semiconductors; the calculated band gap of 0.55 eV for the La member is expected to diminish only slightly on proceeding to later *RE* members. The diffuse reflectance spectra for *RE*AgZnP$_2$ (*RE* = Ce, Pr, Nd, Gd) indicate optical band gaps of 0.6–0.8 eV (**Figure 5-**

**14**), considerably larger than the value of 0.12 eV previously reported for $LaAgZnP_2$[31] but in better agreement with the calculated values here.

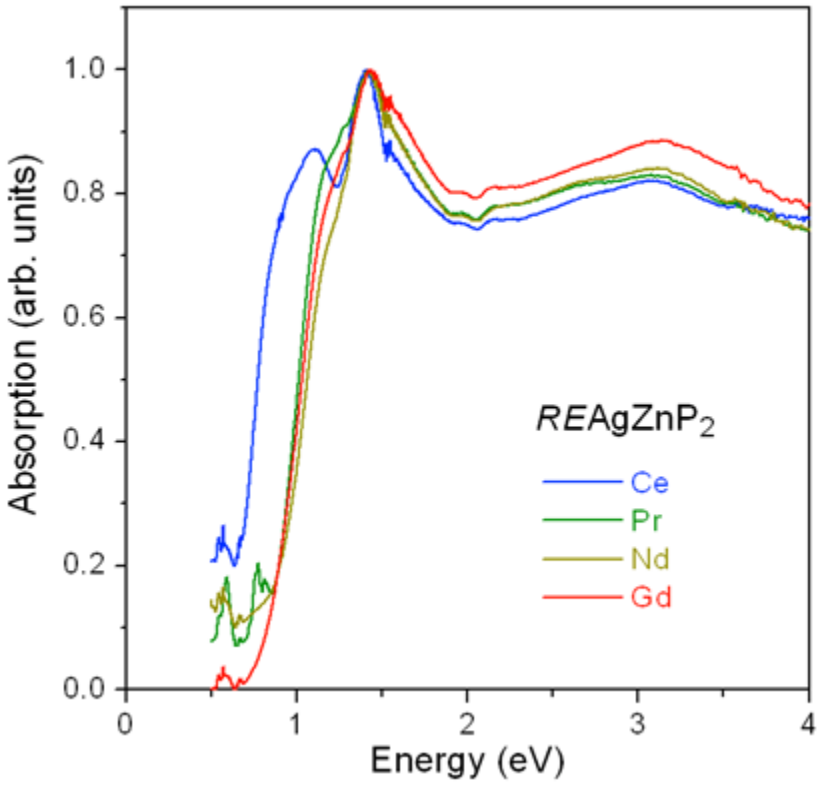


**Figure 5-14.** Diffuse reflectance spectra for *RE*$AgZnP_2$ (*RE* = Ce, Pr, Nd, Gd).

### 5.3.5 Magnetic Properties

For several members of the *RE*$CuZnAs_2$ (*RE* = Ce–Nd, Sm, Gd–Tm) and *RE*$AgZnP_2$ (*RE* = Ce–Nd, Gd, Tb) series, the samples were sufficiently pure to permit magnetic measurements. They generally display simple paramagnetism with no transitions evident in the magnetic susceptibility curves in most cases (**Figure 5-15**). Typical of Sm-containing compounds, $SmCuZnAs_2$ does not exhibit simple magnetic behaviour because of the presence of low-lying excited states (**Figure 5-16**). A weak downturn in magnetic

susceptibility was observed only in the case of $GdCuZnAs_2$ (at 5 K) and $GdAgZnP_2$ (at 3 K); it appears that $TbCuZnAs_2$ may undergo a downturn below 2 K. The inverse magnetic susceptibilities were fit to the Curie-Weiss law, $\chi = C / (T - \theta_p)$, in the linear portion of the curves (typically 50 to 300 K), allowing effective magnetic moments to be evaluated from the Curie constant via $\mu_{eff} = (8C)^{1/2}$. The magnetic data obtained from these fittings are summarized in **Table 5-8**. The effective magnetic moments agree well with the theoretical free-ion values for $RE^{3+}$ species and are consistent with the expectation that there will be no contributions from the other components ($Cu^+$, $Zn^{2+}$, $Pn^{3-}$) because of their closed-shell electron configurations. The Weiss parameters are small and tend to change from positive to negative values on proceeding from the early to late *RE* members within a series. In comparison, the previously measured $RECuZnP_2$ series show only positive Weiss parameters for *RE* = Gd–Er but a highly negative value (–108 K) for *RE* = Yb.[32] With the assumption that the Weiss parameter scales with the strength of the magnetic coupling interactions, it is interesting to note that its magnitude diminishes on proceeding from $GdCuZnP_2$ (+12.8 K) to $GdCuZnAs_2$ (+4.1 K) or to $GdAgZnP_2$ (–0.7 K), consistent with greater separation between Gd atoms.

**Table 5-8.** Magnetic data for $RECuZnAs_2$ and $REAgZnP_2$.

| Compound | $\theta_p$ (K) | $\mu_{eff,\ meas}$ ($\mu_B$/f.u.) | $\mu_{eff,\ theor}$ for $RE^{3+}$ ($\mu_B$) |
|---|---|---|---|
| $CeCuZnAs_2$ | –4(1) | 2.64(1) | 2.54 |
| $PrCuZnAs_2$ | –12.4(5) | 3.71(1) | 3.58 |
| $NdCuZnAs_2$ | –13.3(5) | 3.80(1) | 3.62 |
| $GdCuZnAs_2$ | +4.1(3) | 7.99(1) | 7.94 |

| | | | |
|---|---|---|---|
| $TbCuZnAs_2$ | +7.9(2) | 9.87(1) | 9.72 |
| $DyCuZnAs_2$ | +3.8(3) | 10.88(1) | 10.64 |
| $HoCuZnAs_2$ | +3.6(2) | 10.80(1) | 10.61 |
| $ErCuZnAs_2$ | –0.1(2) | 9.83(1) | 9.58 |
| $TmCuZnAs_2$ | +25(1) | 7.38(1) | 7.56 |
| $CeAgZnP_2$ | –19(1) | 2.43(1) | 2.54 |
| $PrAgZnP_2$ | –16.5(5) | 3.63(1) | 3.58 |
| $NdAgZnP_2$ | –14.7(2) | 3.67(1) | 3.62 |
| $GdAgZnP_2$ | –0.7(2) | 8.08(1) | 7.94 |
| $TbAgZnP_2$ | –1.4(2) | 9.92(1) | 9.72 |

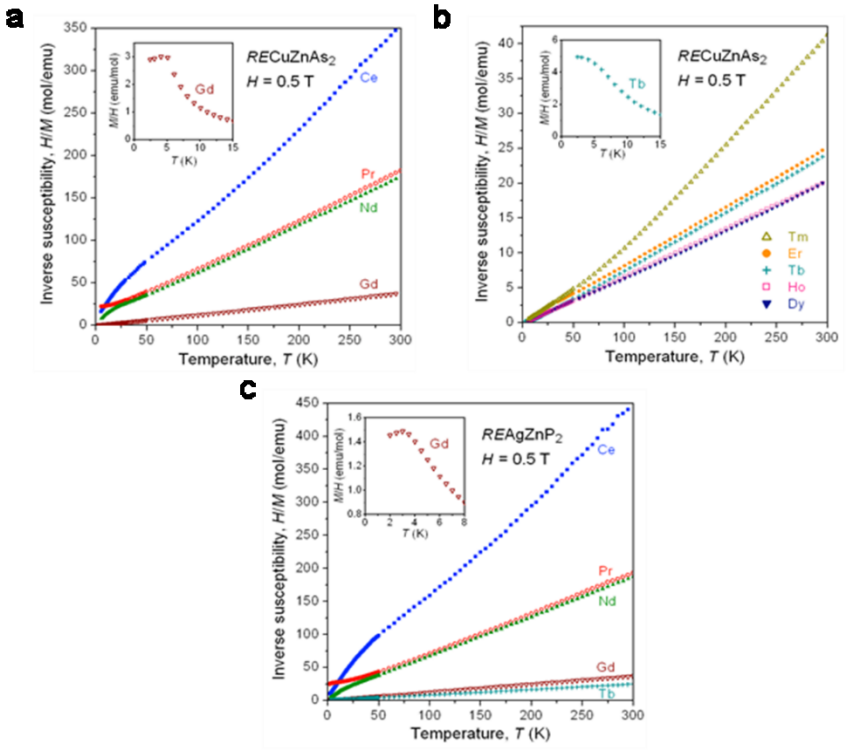


**Figure 5-15.** Plots of inverse magnetic susceptibility vs. temperature for (a) *RE*$CuZnAs_2$ (*RE* = Ce–Nd, Gd), (b) *RE*$CuZnAs_2$ (*RE* = Tb–Tm), and (c) *RE*$AgZnP_2$ (*RE* = Ce–Nd, Gd, Tb). Insets show details of the low-temperature magnetic susceptibility for selected members.

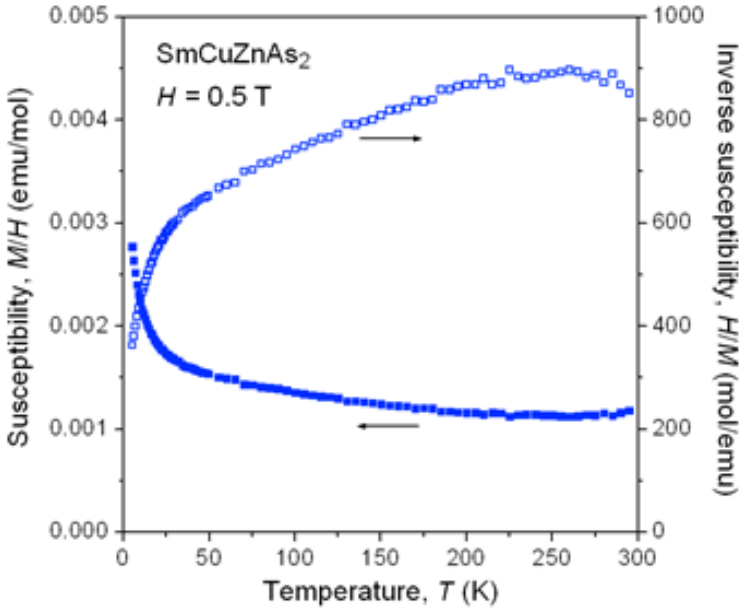


**Figure 5-16.** Magnetic susceptibility and its inverse for $SmCuZnAs_2$.

## 5.4 Conclusion

The characterization of the three series *RE*$CuZnAs_2$, *RE*$AgZnP_2$, and *RE*$AgZnAs_2$ completes a thorough investigation of the quaternary pnictides *REMM*′$Pn_2$ (*M* = Cu, Ag; *M*′ = Zn; *Pn* = P, As), allowing clear trends to be discerned. The main structural effect of substituting with smaller *RE* components is to contract the *c*/*a* ratio, largely by bringing the relatively rigid [$M_2Pn_2$] slabs closer together. Significant changes in the electronic structure are brought about by substitution within these [$M_2Pn_2$] slabs, which dominate the states involved in the valence and conduction bands. In general, these compounds are small gap semiconductors, but the gap is narrower in the Cu–Zn combinations and in the arsenides, to the extent that semimetallic behaviour can be attained in the *RE*$CuZnAs_2$ series as well as the previously known *RE*$CuZnP_2$ series. Further narrowing of the band

gap can be achieved by substitution with smaller *RE* components. Experimental verification of these band gaps is found in the diffuse reflectance spectra of *RE*AgZn$P_2$, as well as the lack of a sharp cutoff near the Fermi edge in the valence band spectra of *RE*CuZn$As_2$. XPS core-line spectra support the simple charge-balanced formulation $RE^{3+}M^{1+}Zn^{2+}(Pn^{3-})_2$, with the only possible source of unpaired electrons provided by the $RE^{3+}$ species accounting for the paramagnetic behaviour of these compounds.

## 5.5 References


1. Hoffmann, R.; Zheng, C. *J. Phys. Chem*. **1985**, *89*, 4175–4181.
2. Zheng, C.; Hoffmann, R. *J. Solid State Chem.* **1988**, *72*, 58–71.
3. Johrendt, D.; Felser, C.; Jepsen, O.; Andersen, O. K.; Mewis, A.; Rouxel, J. *J. Solid State Chem*. **1997**, *130*, 254–265.
4. Rotter, M.; Pangerl, M.; Tegel, M.; Johrendt, D. *Angew. Chem. Int. Ed.* **2008**, *47*, 7949–7952.
5. Johrendt, D.; Pöttgen, R. *Physica C* **2009**, *469*, 332–339.
6. Mandrus, D.; Sefat, A. S.; McGuire, M. A.; Sales, B. C. *Chem. Mater.* **2010**, *22*, 715–723.
7. Klüfers, P.; Mewis, A. *Z. Kristallogr*. **1984;** *169*, 135–147.
8. Zheng, C.; Hoffmann, R.; Nesper, R.; von Schnering, H. -G. *J. Am. Chem. Soc*. **1986**, *108*, 1876–1884.
9. Burdett, J. K.; Miller, G. J. *Chem. Mater.* **1990**, *2*, 12–26.
10. Kranenberg, C.; Johrendt, D.; Mewis, A. *Z. Anorg. Allg. Chem.* **1999**, *625*, 1787–1793.
11. Kranenberg, C.; Johrendt, D.; Mewis, A. *Solid State Sci*. **2002**, *4*, 261–265.
12. Wartenberg, F.; Kranenberg, C.; Pocha, R.; Johrendt, D.; Mewis, A.; Hoffmann, R. -D.; Mosel, B. D.; Pöttgen, R. *Z. Naturforsch. B: J. Chem. Sci.* **2002**, *57*, 1270–1276.
13. Alemany, P.; Llunell, M.; Canadell, E. *J. Comput. Chem.* **2008** *29*, 2144–2153.

14. Gascoin, F.; Ottensmann, S.; Stark, D.; Haïle, S. M.; Snyder, G. J. *Adv. Funct. Mater.* **2005** *15*, 1860–1864.

15. Kauzlarich, S. M.; Condron, C. L.; Wassei, J.K.; Ikeda, T.; Snyder, G. J.; *J. Solid State Chem.* **2009**, *182*, 240–245.

16. Wang, X .-J.; Tang, M. -B.; Chen, H. -H.; Yang, X. -X., Zhao, J. -T.; Burkhardt, U.; Grin, Yu. *Appl. Phys. Lett.* **2009**, *94*, 092106-1–092106-3.

17. Zhang, H.; Baitinger, M.; Tang, M. -B.; Man, Z. -Y.; Chen, H. -H.; Yang, X. -X.; Liu, Y.; Chen, L.; Grin, Yu.; Zhao, J .-T. *Dalton Trans.* **2010**, *39*, 1101–1104.

18. Flage-Larsen, E.; Diplas, S.; Prytz, Ø.; Toberer, E. S.; May, A. F. *Phys. Rev. B* **2010**, *81*, 205204-1–205204-7.

19. Guo, K.; Cao, Q. -G.; Feng, X. -J.; Tang, M. -B.; Chen, H. -H.; Guo, X.; Chen, L.; Grin, Yu.; Zhao, J. -T. *Eur. J. Inorg. Chem.* **2011**, 4043–4048.

20. May, A. F.; McGuire, M. A.; Singh, D. J.; Ma, J.; Delaire, O.; Huq, A.; Cai, W.; Wang, H. *Phys. Rev. B* **2012**, *85*, 035202-1–035202-10.

21. Ponnambalam, V.; Lindsey, S.; Xie, W.; Thompson, D.; Drymiotis, F.; Tritt, T. M. *J. Phys. D: Appl. Phys.* **2011**, *44*, 155406-1–155406-6.

22. Ponnambalam, V.; Morelli, D. T. *J. Electron. Mater*. **2013**,*42*, 1307-1312..

23. Kauzlarich, S. M.; Brown, S. R.; Snyder, G. J. *Dalton Trans.* **2007**, 2099–2107.

24. Snyder, G. J.; Toberer, E. S. *Nature Mater.* **2008**, *7*, 105–114.

25. Toberer, E. S.; May, A. F.; Snyder, G. J. *Chem. Mater.* **2010**, *22*, 624–634.

26. Mewis, A. *Z. Naturforsch. B: Anorg. Chem.*, *Org. Chem.* **1980**, *35*, 939–941.

27. Klüfers, P.; Mewis, A.; Schuster, H. -U. *Z. Kristallogr.* **1979**, *149*, 211–225.

28. Klüfers, P.; Neumann, H.; Mewis, A.; Schuster, H. -U. *Z. Naturforsch. B: Anorg. Chem., Org. Chem.* **1980**, *35*, 1317–1318.

29. Zwiener, G.; Neumann, H.; Schuster, H.-U. *Z. Naturforsch. B: Anorg. Chem., Org. Chem.* **1981**, *36*, 1195–1197.

30. Mahan, A.; Mewis, A. *Z. Naturforsch. B: Anorg. Chem., Org. Chem.* **1983**, *38*, 1041–1045.

31. Tejedor, P.; Stacy, A. M. *J. Solid State Chem.* **1990**, *89*, 227–236.

32. Blanchard, P. E. R.; Stoyko, S. S.; Cavell, R. G.; Mar, A. *J. Solid State Chem.***2011**, *184*, 97–103.

33. Khatun, M.; Stoyko, S. S.; Mar, A. *Inorg. Chem.* **2012**, *52*, 3148–3158.

34. Sheldrick, G. M. SHELXTL, version 6.12, Bruker AXS Inc., Madison, WI, 2001.

35. Gelato, L. M.; E. Parthé, *J. Appl. Crystallogr*. **1987**, *20*, 139–143

36. Gladyshevskii, E. I.; Kripyakevich, P. I.; Bodak, O. I. *Ukr. Fiz. Zh.* **1967**, *12*, 447–452.

37. Tank, R.; Jepsen, O.; Burkhardt, A.; Andersen, O. K. *TB-LMTO-ASA Program*, version 4.7, Max Planck Institut für Festkörperforschung, Stuttgart, Germany, 1998.

38. Fairley, N. CasaXPS, version 2.3.9, Casa Software Ltd., Teighnmouth, Devon, UK, 2003, http://www.casaxps.com.

39. Pauling, L. *The Nature of the Chemical Bond, 3rd ed.*, Cornell University Press, Ithaca, NY, 1960.

40. Grosvenor, A. P.; Cavell, R. G.; Mar, A. *Struct. Bonding* **2009**, *133*, 41–92.

41. Grosvenor, A. P.; Cavell, R. G.; Mar, A., *Chem. Mater*. **2006**, *18*, 1650–1657.

42. Grosvenor, A. P.; Cavell, R. G.; Mar, A. *J. Solid State Chem.* **2010**, *183*, 1477–1483.

43. Crerar, S. J.; Mar, A.; Grosvenor, A. P. *J. Solid State Chem.* **2012**, *196*, 79–86.

44. Ikeda, T.; Okada, K.; Ogasawara, H.; Kotani, A. *J. Phys. Soc. Jpn*., **1990**, *59*, 622–630.

45. Vasquez, R. P. *Surf. Sci. Spectra* **1993**, *2*, 144–148.

46. Vasquez, R. P. *Surf. Sci. Spectra* **1993**, *2*, 149–154.

47. Vasquez, R. P. *Surf. Sci. Spectra* **1998**, *5*, 262–266.

48. Frost, D. C.; Ishitani, A.; McDowell, C. A. *Mol. Phys.* **1972**, *24*, 861–877.

49. Chawla, S. K.; Sankarraman, N.; Payer, J. H. *J. Electron Spectrosc. Relat. Phenom.* **1992**, *62*, 1–18.

50. Roberts, A.; Engelberg, D.; Liu, Y.; Thompson, G. E.; Alexander, M. R. *Surf. Interface Anal.* **2002**, *33*, 697–703.

51. Wagner, C. D.; Naumkin, A. V.; Kraut-Vass, A.; Allison, J. W.; Powell, C. J.; Rumble Jr., J. R. *NIST X-ray Photoelectron Spectroscopy Database*, version 3.5 (web version), National Institute of Standards and Technology, Gaithersburg, MD, 2003, http://srdata.nist.gov/xps.

52. Scofield, J. H. *J. Electron Spectrosc. Relat. Phenom.* **1976**, *8*, 129–137.

53. Yeh, J. J.; Lindau, I. *At. Data Nucl. Data Tables* **1985**, *32*, 1–155.

# Chapter 6

## Quaternary Rare-Earth Transition-Metal Phosphides Adopting $CaAl_2Si_2$-Type Structures: *RE*$MnCuP_2$ (*RE* = La–Nd, Sm, Gd–Dy) and *RE*$AgCdP_2$ (*RE* = La-Nd)

### 6.1 Introduction

Many ternary phases with a general formula $AB_2X_2$ ($A$ = alkali, alkaline-earth, or rare-earth metal; $B$ = transition metal or main-group metalloid; $X$ = group 13-16 element) commonly adopt either the $ThCr_2Si_2$-type or $CaAl_2Si_2$-type structure.[1-5] The tetragonal $ThCr_2Si_2$-type structures have gained much attention after the discovery of superconductivity in $BaFe_2As_2$.[6-8] It is noteworthy that the compounds of $CaAl_2Si_2$-type structure are also interesting because they were identified to be promising materials for thermoelectric applications. $AB_2X_2$ compounds are made of covalently bonded anionic layers of $[B_2X_2]$ framework that can offer high electronic mobility and the ionically bonded *RE* cations which inhibit phonon mobility. This condition is called an "electron-crystal-phonon-glass" criterion[9-11] and materials satisfying this condition can be good candidates for thermoelectric properties. The flexibility of atomic sites in $CaAl_2Si_2$-type structure helps to design new materials with small band gaps, which are desirable for thermoelectric applications. Introducing complexity in these system is a common approach by which the physical properties can be improved strategically. There are only a handful of quaternary phosphides known to date, $YbMnCuP_2$,[13] *RE*$CuZnP_2$ (*RE* = La-Nd, Sm, Gd-Lu, Sc, Y),[14-

[19] *RE*AgZn$P_2$ (*RE* = La-Nd, Sm, Gd-Dy)[20] which adopt $CaAl_2Si_2$-type structure. The thermoelectric figure of merit of $YbZn_2P_2$ (*ZT* ~ 0.1) was improved substantially on introducing complexity by substituting one of the Zn atoms with a Cu atom, i.e. YCuZn$P_2$ (*ZT* = 0.6).[12]

This chapter discusses two new series of phosphides: *RE*MnCu$P_2$ (*RE* = Y, La-Sm, Gd-Lu) and *RE*AgCd$P_2$ (*RE* = La-Nd). Their crystal structures have been examined using powder X-ray diffraction and the electronic structure has been evaluated using band structure calculations. Diffuse reflectance measurements were performed to evaluate the optical band gap and the magnetic measurements were studied on TbMnCu$P_2$ and *RE*AgCd$P_2$ (*RE* = La-Nd) samples.

## 6.2 Experimental

### 6.2.1 Synthesis

Starting materials were freshly filed *RE* pieces (99.9%, Hefa), Ag powder (99.9%, A.D. Mackay), Cd powder (99.95%, Alfa Aesar), Cu powder (99.9999% Cerac), Mn powder (99.6%, Alfa-Aesar), and P lumps (99.999%, Aldrich). Initial trials were made on *RE* elements La, Pr, Nd, Sm and Gd to observe the extent of this series. Stoichiometric mixtures of the elements on a 0.3-g scale were ground, pressed into pellets, and loaded into fused-silica tubes, which were evacuated and sealed. The tubes were heated at 800 ºC for 10 days and then cooled to room temperature over 1 day. The products were analyzed by powder X-ray diffraction (XRD), performed on an Inel powder diffractometer equipped with a curved position-sensitive detector (CPS 120) and a Cu $K\alpha_1$ radiation source operated at 40 kV and 20 mA. Based on the initial trials, rare-earth substitution was extended to all

trivalent members in the *RE*CuMnP$_2$ series *RE* (Y, La-Sm, Gd-Lu), but it was limited to early trivalent members in *RE*AgCdP$_2$ (La-Nd). Phase-pure samples were made by multiple grinding and heating using the same heating procedure. The powder patterns of quaternary phases of *RE*AgCdP$_2$ and *RE*MnCuP$_2$ are shown in **Figure 6-1**. The cell parameters were evaluated by refining the powder X-ray patterns using Unit Cell software (**Table 6-1)**.[22] The *RE*AgCdP$_2$ samples were nearly pure whereas the *RE*MnCuP$_2$ samples contained small amounts of binary phosphides *RE*P. The Tb sample was made nearly phase pure under the described synthetic conditions and has been used for magnetic measurement. (**Figure 6-2**)

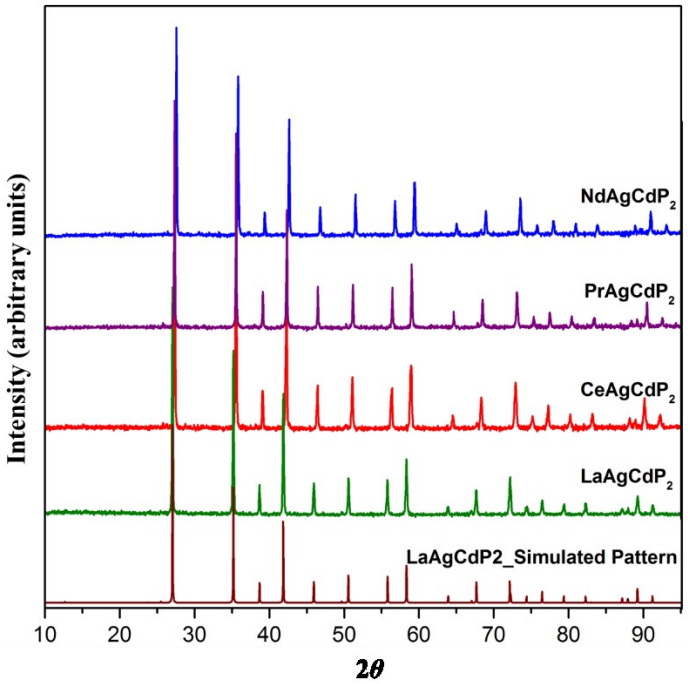


**Figure 6-1.** Experimental powder patterns of *RE*AgCdP$_2$ (top) with the simulated patterns of LaAgCdP$_2$ (bottom).

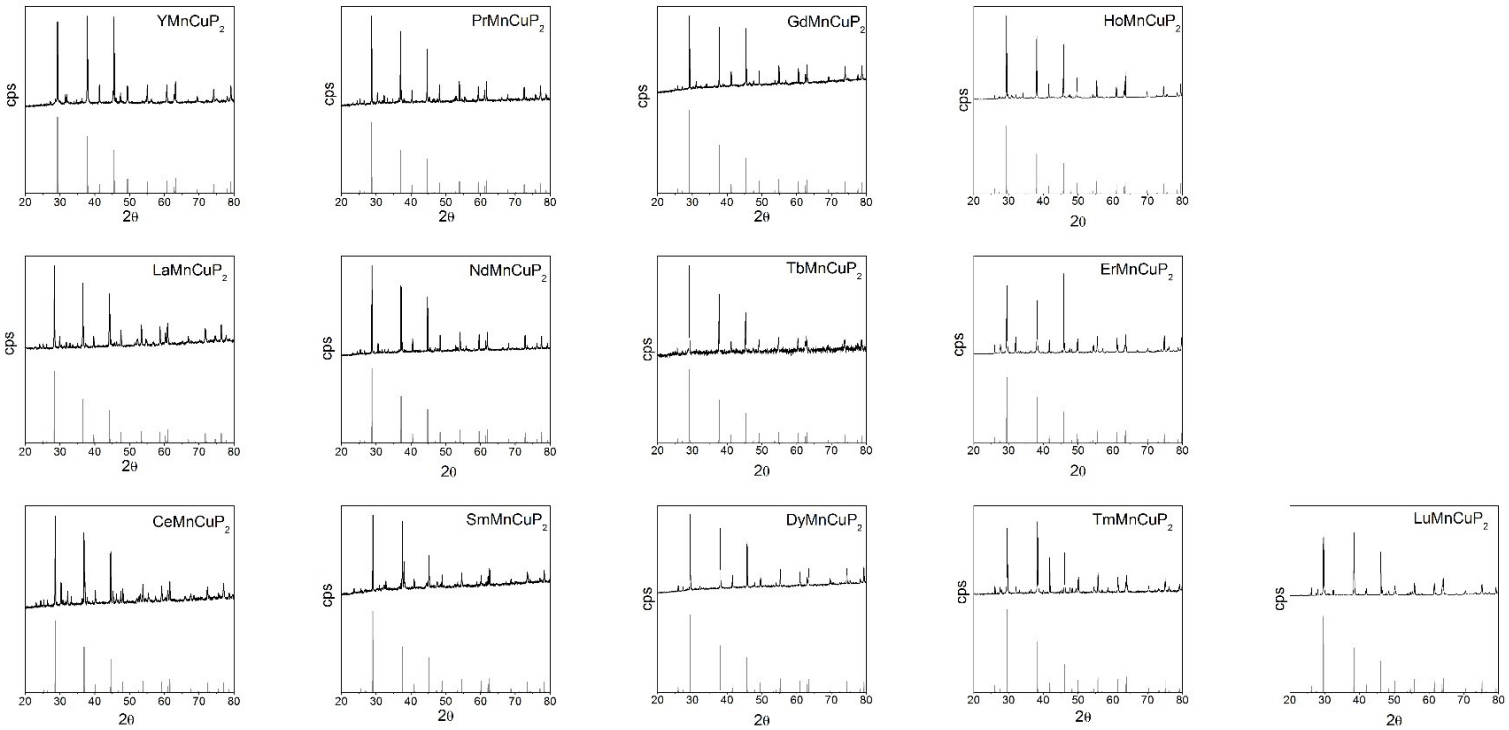


**Figure 6-2.** Experimental powder patterns of each samples of *RE*MnCuP$_2$ with the correspomding simulated patterns.

**Table 6-1.** Cell parameters for *RE*$MnCuP_2$ and *RE*$AgCdP_2$

| Compound | *a* (Å) | *c* (Å) | *V* (Å$^3$) | Reference |
|---|---|---|---|---|
| $YMnCuP_2$ | 3.9791(4) | 6.5464(9) | 89.77(2) | This work |
| $LaMnCuP_2$ | 4.0928(5) | 6.809(1) | 98.78(2) | This work |
| $CeMnCuP_2$ | 4.0620(4) | 6.7348(8) | 96.24(2) | This work |
| $PrMnCuP_2$ | 4.0542(4) | 6.7112(8) | 95.53(2) | This work |
| $NdMnCuP_2$ | 4.0425(3) | 6.6827(6) | 94.58(1) | This work |
| $SmMnCuP_2$ | 4.0118(6) | 6.613(2) | 92.18(3) | This work |
| $GdMnCuP_2$ | 3.9912(5) | 6.578(1) | 90.75(2) | This work |
| $TbMnCuP_2$ | 3.9821(6) | 6.554(1) | 90.00(2) | This work |
| $DyMnCuP_2$ | 3.9686(6) | 6.528(1) | 89.04(3) | This work |
| $HoMnCuP_2$ | 3.9621(6) | 6.514(1) | 88.56(3) | This work |
| $ErMnCuP_2$ | 3.9520(6) | 6.494(1) | 87.84(2) | This work |
| $TmMnCuP_2$ | 3.9407(6) | 6.469(1) | 87.00(3) | This work |
| $YbMnCuP_2$ | 3.949(1) | 6.484(1) | 87.54(5) | [13] |
| $LuMnCuP_2$ | 3.9325(8) | 6.456(2) | 86.46(3) | This work |
| $LaAgCdP_2$ | 4.3014(1) | 6.9552(4) | 111.445(1) | This work |
| $CeAgCdP_2$ | 4.2773(3) | 6.9105(4) | 109.492(7) | This work |
| $PrAgCdP_2$ | 4.2608(1) | 6.8874(4) | 108.267(7) | This work |
| $NdAgCdP_2$ | 4.2445(1) | 6.8607(5) | 107.043(8) | This work |

The cell parameters are refined from powder XRD except for $YbMnCuP_2$

### 6.2.2 Structure Determination

The structure determination of the new phosphides was carried out using powder X-ray diffraction method. A theoretical model of the powder patterns was generated using the PowderCell software[21] and the initial atomic positions and cell parameters were taken from previously reported *REMM'Pn*$_2$ compounds. Theoretical patterns were modeled with a mixed occupancy of transition metals. The theoretical patterns of *RE*MnCuP$_2$ and *RE*AgCdP$_2$ were then compared with the experimental patterns and the cell parameters were refined using Unit Cell software.[22]

### 6.2.3 Band Structure Calculation

Tight-binding linear muffin-tin orbital (TB-LMTO) band structure calculations were performed within the local density and atomic-spheres approximation with the use of the Stuttgart TB-LMTO program.[33] To examine the effects of substituting the rare-earth-metal or transition-metal components in *REMM'*P$_2$ (*M* = Cu, Ag; *M'* = Mn, Zn), a series of three compounds LaMnCuP$_2$, YMnCuP$_2$, and LaAgCdP$_2$ was considered. The mixed occupancy of the transition-metal site was modeled by a hypothetical superstructure in which *M* atoms alternate with *M'* atoms in an ordered distribution within separate sites in space group *P*3*m*1 (No. 156): *RE* in 1*a* (0, 0, 0); *M* in 1*b* (1/3, 2/3, ~0.37); *M'* in 1*c* (2/3, 1/3, ~0.63); P1 in 1*b* (1/3, 2/3, ~0.75); P2 in 1*c* (2/3, 1/3, ~0.25). The basis sets included La 6s/6p/5d/4f, Y 5s/5p/4d/4f, Cu 4s/4p/3d, Mn 4s/4p/3d, Ag 5s/5p/4d/4f, Cd 5s/5p/4d/4f and P 3s/3p/3d orbitals. The La 6p, Y 4f, Ag 4f, Cd 4f, and P 3d orbitals were downfolded. Integrations in reciprocal space were carried out with an improved tetrahedron method over 248 irreducible *k* points within the first Brillouin zone.

### 6.2.4 Optical Diffuse Reflectance Study

A Varian Cary 5000 spectrometer, equipped with a Harrick Praying Mantis diffuse reflectance accessory, was used to collect the optical diffuse reflectance spectra of the samples over the ultraviolet, visible, and near-infrared spectral regions (UV-vis-NIR). Barium sulfate (Fisher, 99.92%) was used as a 100% reflectance standard and placed in a sample holder to a depth of 3 mm. After the background was collected the ground sample was placed on top of the barium sulfate standard and scanned at a rate of 600 nm/min. The absorption intensity peaks were normalized to the highest peak and the accurate band gaps were identified by fitting to the Urbach function.

### 6.2.5 Magnetic Measurements

Measurements of dc magnetic susceptibility were made on powders of $TbMnCuP_2$ and *RE*$AgCdP_2$ (*RE* = La-Nd) under an applied field of 0.5 T on a Quantum Design 9T-PPMS dc magnetometer / ac susceptometer. The data were collected between 2 K and 350 K for $TbMnCuP_2$, but 2K and 300 K for *RE*$AgCdP_2$ (*RE* = La-Nd). The magnetic susceptibility values were corrected for contributions from the holder and underlying sample core diamagnetism.

## 6.3 Results and Discussion

The new quaternary rare-earth and transition-metal-containing phosphides were expected to crystallize in $CaAl_2Si_2$-type structure (**Figure 6-3**). A Zintl formalism of $RE^{3+}M^{1+}M'^{2+}(P^{3-})_2$ can be applied for these series. The typical $CaAl_2Si_2$-type structure (space group $P\bar{3}m1$) of *REMM'*$P_2$ is built of edge-sharing transition-metal-centered tetrahedra in which transition metals are disordered in a single site and form an anionic

network with P, $[MM'P_2]_n$. These anionic layers are separated with intervening *RE* atoms. Substituting the early rare-earth metals with later rare-earth metals reduces the *c*/*a* ratio as a result of lanthanide contraction (**Figure 6-4**). The P atoms in the anionic layer are four-coordinated with transition metal atoms in an "umbrella" geometry, where three bonds are shorter and stronger as compared with the fourth one. This bonding feature is also confirmed by band structure calculations. Along the *c*-axis, the arrangement of atoms is a honeycomb-like network made of transition-metal and P atoms, the *RE* atoms are within the cavities of this network as shown in **Figure 6-3**. The transition-metal atoms are tetrahedrally coordinated with P atoms forming a slab made of edge-sharing tetrahedra and the *RE* atoms are octahedrally coordinated with P forming a slab made of face-sharing octahedra. These slabs repeat alternately along the *c*-axis.

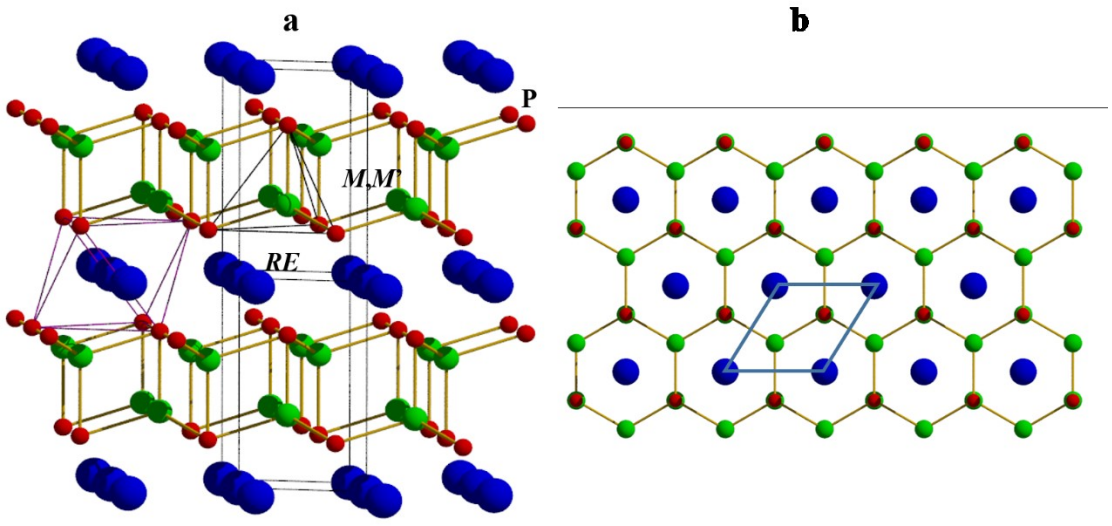


**Figure 6-3.** (a) Structure of $REMM'P_2$ ($M$ = Mn, Ag; $M'$ = Cu, Cd) built of $M$ and $M'$ centered tetrahedra separated by octahedrally coordinated *RE* atoms, (b) honeycomb-like network with *RE* atoms in the cavity.

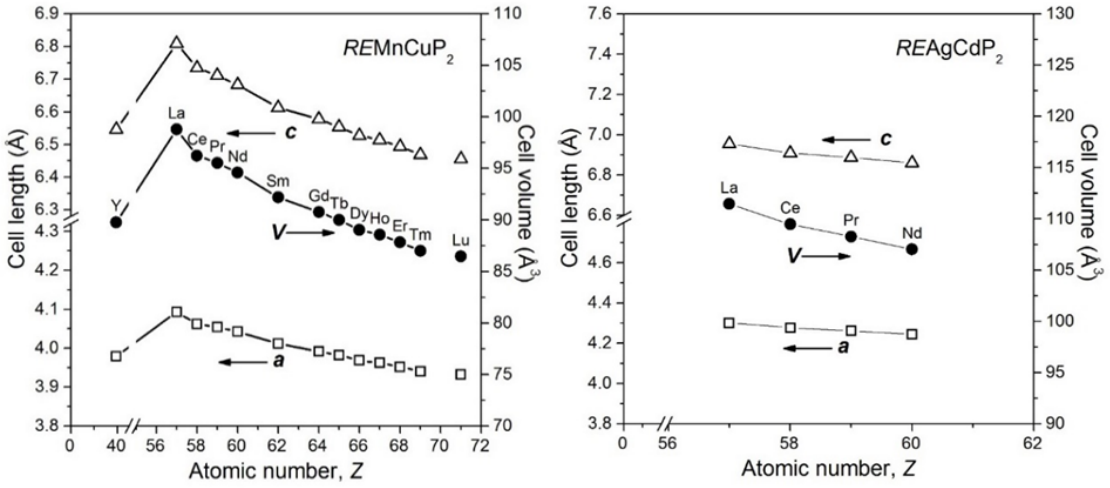


**Figure 6-4.** Cell parameters of *RE*$CuMnP_2$ and *RE*$AgCdP_2$.

Zintl phases are generally known for their semiconducting property. For understanding the bonding and electronic property of the series, theoretical calculations were performed on three different compounds: $LaMnCuP_2$, $YMnCuP_2$, and $LaAgCdP_2$. Two members from *RE*$CuMnP_2$ series were considered so that the contribution of both early and later rare-earth can be exmined. Superstructures were modeled for this purpose such that only heteroatomic Cu–Mn or Ag–Cd contacts are present within the [*MM*′$P_2$] slabs.

The band structure calculations show nearly empty states of *RE* (*RE* = La, Y) atoms in *RE*$MnCuP_2$(**Figure 6-5**). Cu 3d states are mostly filled in both cases but they are slightly deeper in $LaMnCuP_2$ (-5 to -2 eV) compared to $YCuMnP_2$ (-4 to -1 eV). The P states are mostly filled but the Mn levels are partially filled in both compounds. The Mn 3d and Cu 3d states overlap with the P 3p states in both calculations. The partially filled Mn 3d states are responsible for the metallic behaviour of *RE*$MnCuP_2$. The density of state calculations

on $LaAgCdP_2$ show that most of the levels are filled below the Fermi level leaving a bandgap of 0.5 eV. Both La and Cd states are nearly empty whereas both Ag and P states are mostly filled below the Fermi level. The Ag 3d states from -6 to -3 eV slightly overlap with the P 3p states -4 to 0 eV. P 3s states are filled far below the Fermi level (~10 eV) in *RE*$MnCuP_2$. Both Cd 3d and P 3s states are filled around -12 to -10 eV in $LaAgCdP_2$. Crystal orbital Hamilton population curves were plotted to evaluate the bonding interactions, which suggest that most of the stability of these compounds originate from the filled metal-phosphorus bonding levels. The bonding interactions are more optimized in $LaAgCdP_2$ by filling up to the Fermi level, above which they are antibonding within the conduction band. Bonding is not very well optimized in *RE*$MnCuP_2$ because there are some antibonding Mn–P levels below the Fermi level and few bonding Y–P and Cu–P levels above the Fermi level. Considerable mixing of transition-metal and phosphorus states leads to strong *M*–P bonding interactions for Mn–Cu (2.31 eV/bond), Cu–P (1.63 eV/bond) in $LaMnCuP_2$; Mn–Cu (2.57 eV/bond), Cu–P (1.74 eV/bond) in $YMnCuP_2$; and Ag–P (1.57 eV/bond), Cd–P (1.88 eV/bond) in $LaAgCdP_2$ (**Figure 6-5**). The metal–metal bonding among transition metals is relatively weak in all three cases with an -ICOHP value ~0.4 eV/bond in *RE*$MnCuP_2$ and 0.3 eV/bond in $LaAgCdP_2$. Even though most of the filled levels of rare-earth metals are above the Fermi level, there is a significant -ICOHP value for *RE*–P bonds such as 0.92 eV/bond in $LaMnCuP_2$, 1.23 eV/bond in $YMnCuP_2$, and 1.05 eV/bond in $LaAgCdP_2$ indicating some covalent character. The remaining ionic character of *RE*–P contributes to the stability of the structure and the weak *M–M* bonding also helps in the stability of [*MM*′$P_2$] slabs in $CaAl_2Si_2$-type structures.

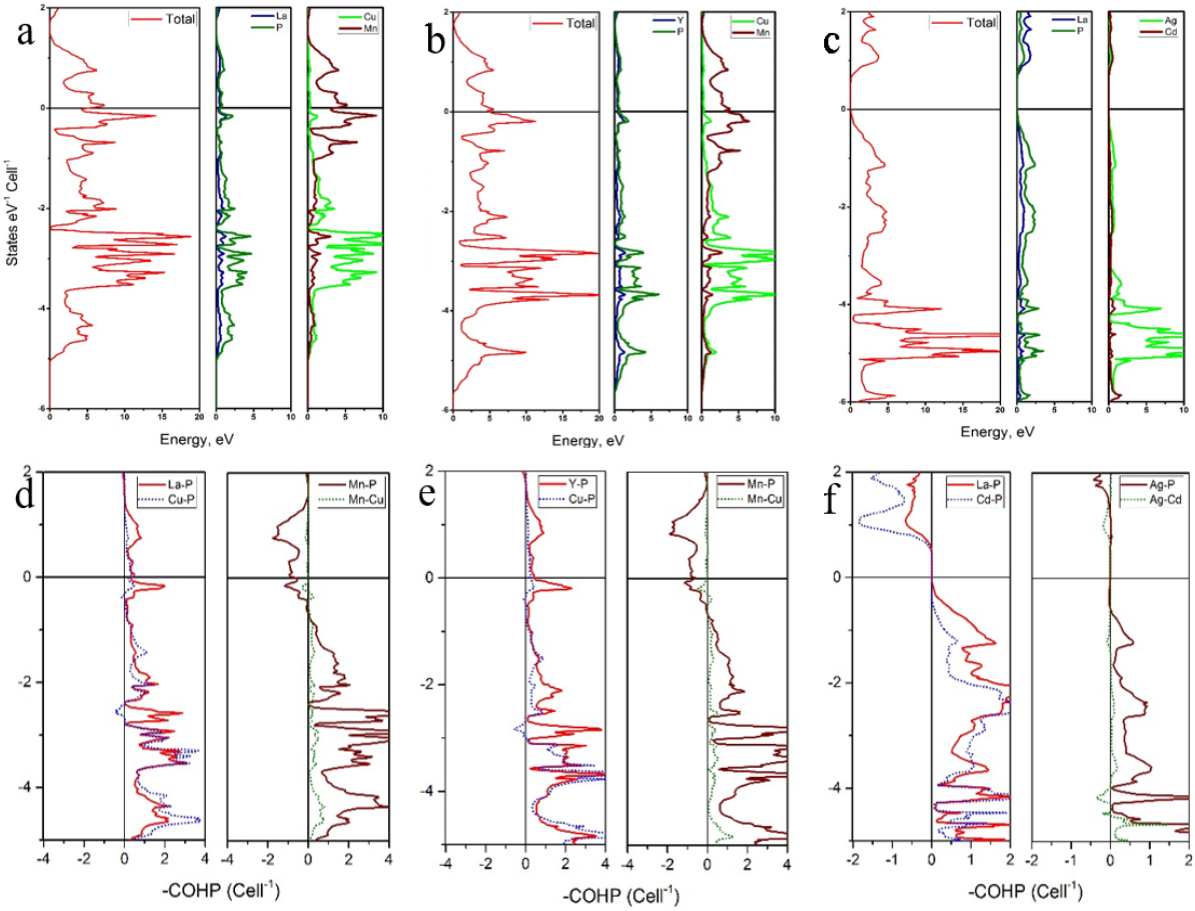


**Figure 6-5.** (a), (b), and (c) are the density of states of $LaMnCuP_2$, $YMnCuP_2$, and $LaAgCdP_2$ respectively; (d), (e), and (f) are the COHP curves of $LaMnCuP_2$, $YMnCuP_2$, and $LaAgCdP_2$ respectively.

From the band structure calculations of *RE*AgCdP$_2$ series, it is clear that they are small band gap semiconductors with an $E_g$ of ~0.5 eV. An optical band gap study on the powdered samples was performed using diffuse reflectance spectrometer. The raw percent reflectance (%*R*) data were converted to relative absorption ($\alpha_{KM}$) using a Kubelka-Munk function.[24] Further, the absorption coefficient is plotted by Urbach function to extract both the exact band gap and the type of band gap (direct or indirect band gap). An Urbach function can be expressed as $\alpha = A \bullet e^{(E-E_g)/E_u}$, where $A$ is a constant, $E$ is the photon energy in eV, $E_g$ is the bandgap energy and $E_u$ is the Urbach energy.[25] To accomplish this, the logarithm of absorption is plotted against photon energy and the Urbach tail appears as a linear region towards the bottom of the band edge. The absorption data were fit with the function, $\alpha = A \bullet (E-E_g)^2/E$ suggesting an indirect bandgap semiconductor.[25] The fitting of Urbach function provides a band gap og 0.76 eV for LaAgCdP$_2$ which decreases with rare-earth substitution to a value of 0.62 eV in NdAgCdP$_2$ (**Figure 6-6**). The values obtained from diffuse reflectance study are in better agreement with the values obtained from band structure calculations.

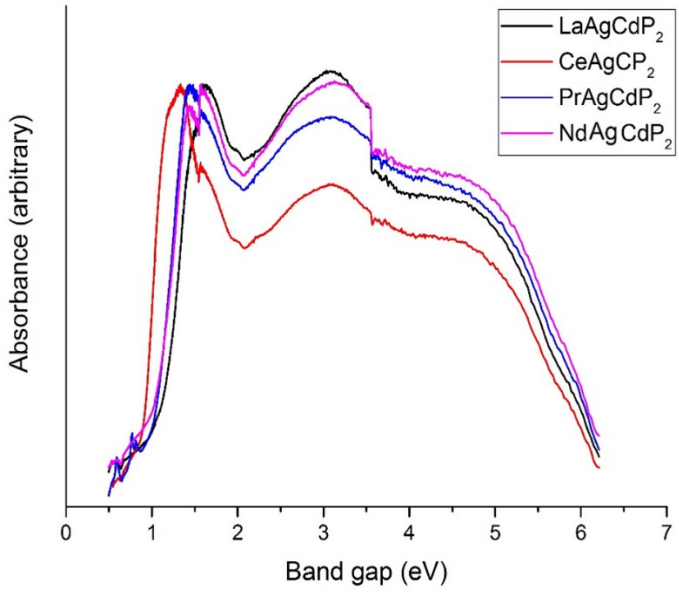


**Figure 6-6.** Normalized diffuse reflectance spectra of *RE*AgCdP$_2$.

Phase pure samples of *RE*AgCdP$_2$ permit the magnetic susceptibility study on all the members in this series (**Figure 6-7**). The effective magnetic moments were calculated by $\mu_{\text{eff}} = (8C)^{1/2}$ where $C$ is the Curie constant, which can be obtained by fitting the inverse of magnetic susceptibilities using Curie–Weiss law, $\chi = C/(T - \theta_{\text{P}})$, in the linear portion of the curve (typically 50-300 K). The magnetic data obtained from these fittings are summarized in **Table 6-2** and the effective magnetic moments are in close agreement with the theoretical free-ion values for $RE^{3+}$ species. The LaAgCdP$_2$ showed typical diamagnetic behaviour at higher temperatures and a small positive transition in magnetic susceptibility was observed at low temperatures, probably attributable to trace amounts of magnetic impurity (**Figure 6-9**). The other members in this series showed paramagnetic behaviour at higher temperatures with an antiferromagnetic transition at very low temperatures. The negative Weiss parameters in these samples suggest antiferromagnetic

interactions and the magnitude of these interactions decreases with smaller rare-earth as shown in **Table**.**6-2** A field-dependent study of two members in this series (transitions for $PrAgCdP_2$ at 10 K and $NdAgCdP_2$ at 12 K) was performed which suggest that these materials are simple antiferromagnets with no strong magnetization (**Figure 6-8**).

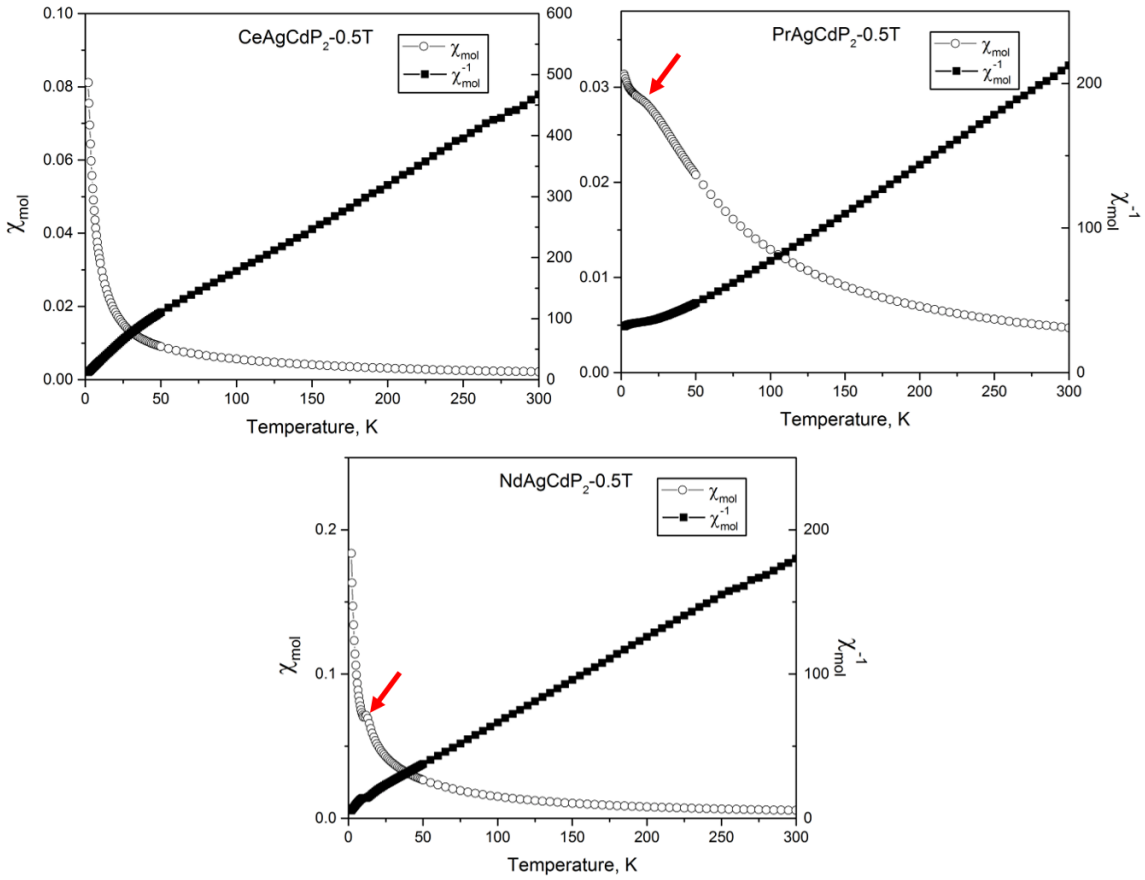


**Figure 6-7.** Molar susceptibility and inverse susceptibility of *RE*$AgCdP_2$ samples.

**Table 6-2** Magnetic data for *RE*AgCdP$_2$.

| Compound | $\theta_P$ (K) | $\mu_{\text{eff.meas.}}$ ($\mu_B$/f.u.) | $\mu_{\text{eff. theor.}}$ for $RE^{3+}$ ($\mu_B$) |
|---|---|---|---|
| CeAgCdP$_2$ | -49 (2) | 2.35 (1) | 2.54 |
| PrAgCdP$_2$ | -25 (1) | 3.53 (1) | 3.58 |
| NdAgCdP$_2$ | -15 (1) | 3.71 (1) | 3.62 |

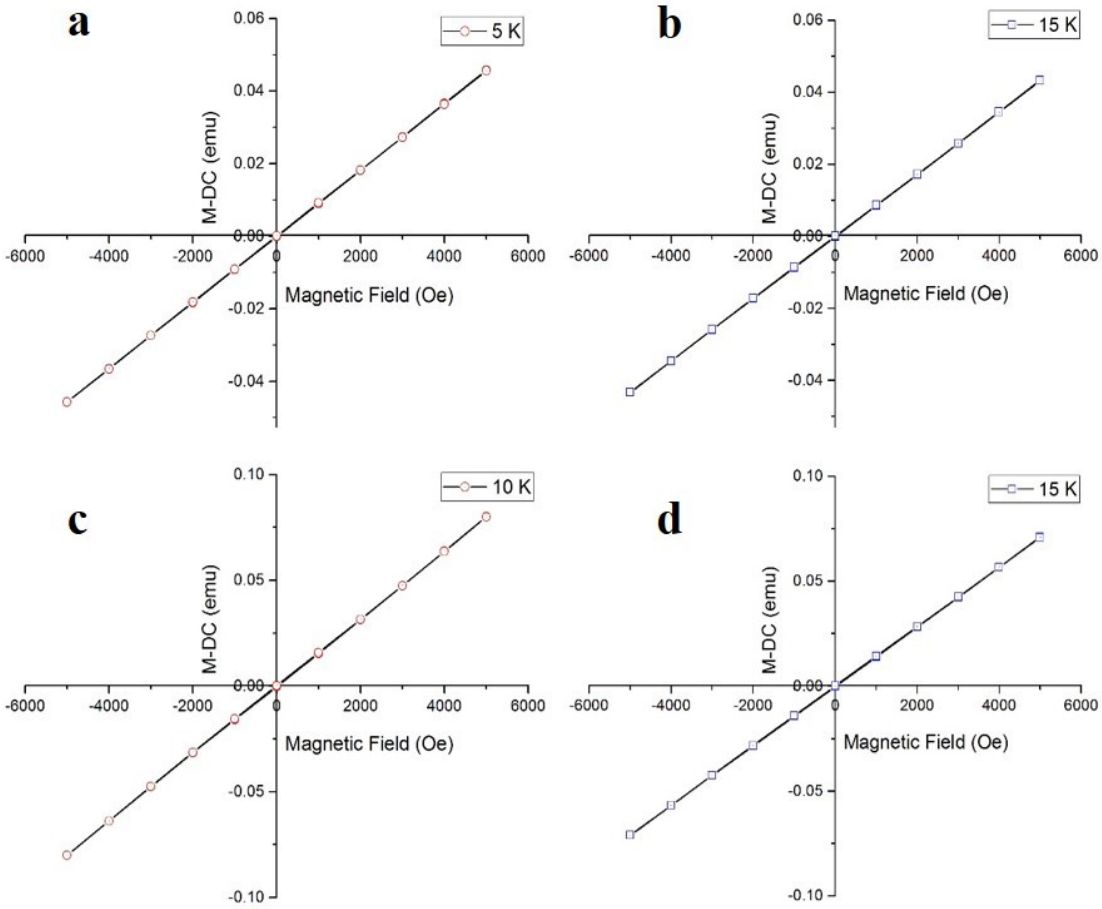


**Figure 6-8.** The magnetic behaviour of *RE*AgCdP$_2$ above and below the transition temperature, (**a** and **b**) PrAgCdP$_2$ (**c** and **d**) NdAgCdP$_2$.

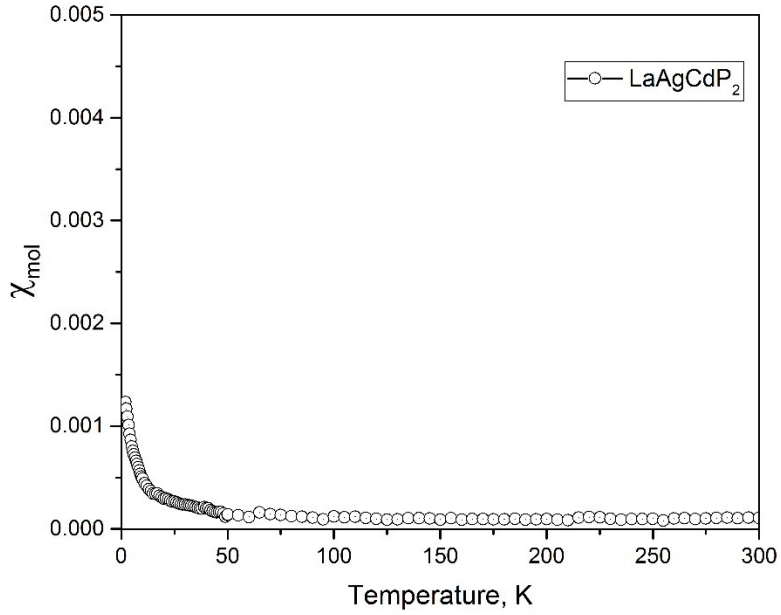


**Figure 6-9.** Diamagnetic behavior of $LaAgCdP_2$ and with small upturn in magnetic susceptibility due to impurity.

The magnetic measurements were limited to $TbMnCuP_2$ in the *RE*$MnCuP_2$ series because the other members were not phase-pure. The susceptibility as a function of temperature shows ferromagnetic transition ($T_C$) around 300 K and antiferromagnetic transition at very low temperature ($T_N$) of about 8 K **Figure 6-10**. The ferromagnetic transition slowly disappears at higher external magnetic fields (~3 T) **Figure 6-11**. Dependence of magnetization as a function of external magnetic field was measured above and below the transition temperature which shows a weak ferromagnetic behaviour with a small remanent magnetization **Figure 6-12**. The field-dependent study at low temperatures shows irreversibility of magnetic moments in this sample. A field-cooled study has to be carried out for interpreting the magnetic properties of these materials more accurately.

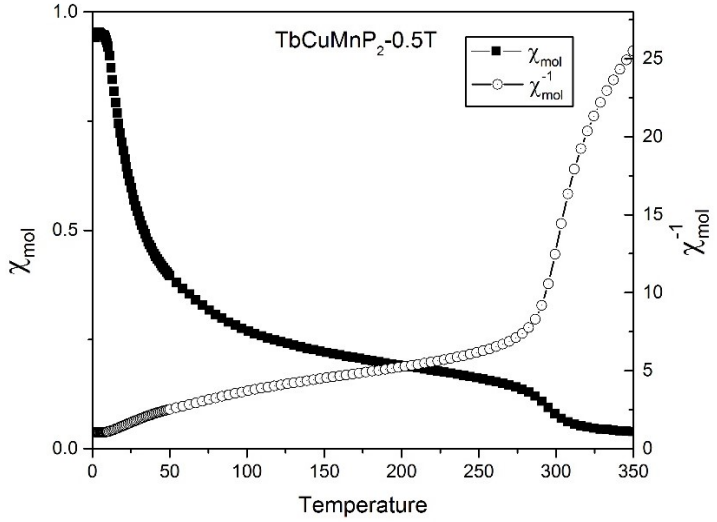


**Figure 6-10.** Molar susceptibility and inverse molar susceptibility of $TbMnCuP_2$

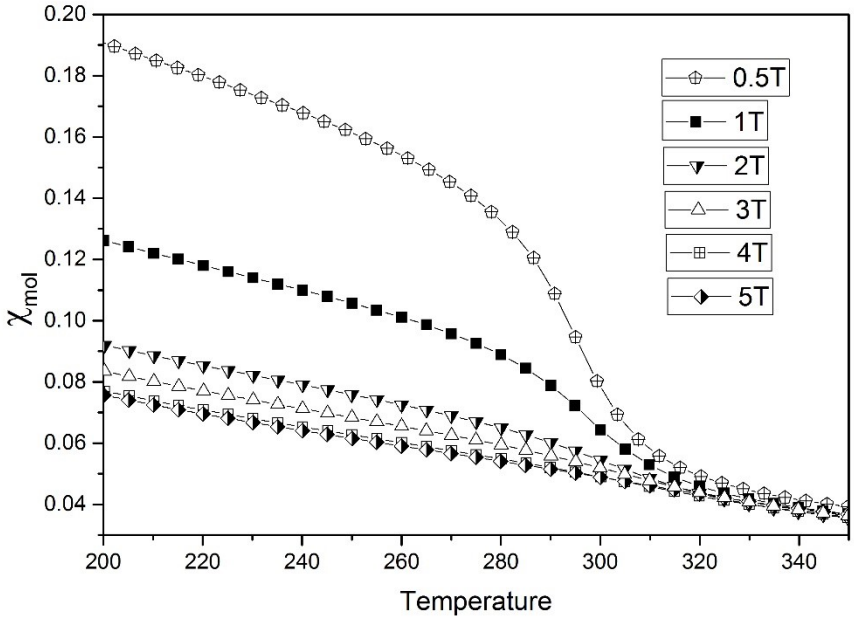


**Figure 6-11.** Disappearance of ferromagnetic transition with external field.

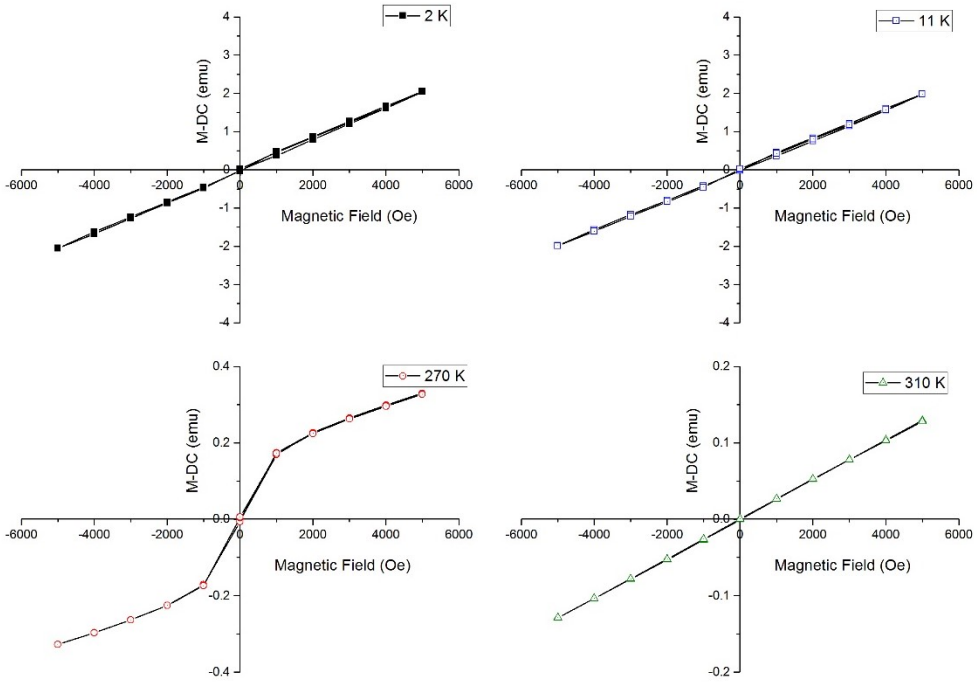


**Figure 6-12.** The field dependent study of $TbMnCuP_2$ at different temperatures.

## 6.4 Conclusion

The structure of two series of phosphides, *RE*$MnCuP_2$ and *RE*$AgCdP_2$, was identified using powder X-ray diffraction method. The substitution of smaller rare-earth gradually decreases the *c*/*a* ratio which brings the [*MM*′$P_2$] slabs closer. Band structure calculations suggest *RE*$MnCuP_2$ series are metallic whereas *RE*$AgCdP_2$ series are semiconducting. The metallic nature of *RE*$MnCuP_2$ is mostly because of the partially filled Mn states at the Fermi level. Substituting Mn with Zn, which provides filled states, shows semimetallic behaviour. The optical diffuse reflectance studies confirm that the band gaps of *RE*$AgCdP_2$ samples are comparable to the values obtained from band structure calculations. Magnetic measurements on *RE*$AgCdP_2$ show typical paramagnetic behaviour with a downturn in the susceptibility at very low temperature because of antiferromagnetic

ordering. The effective magnetic moment agrees better with the free-ion magnetic moment of $RE^{3+}$. $TbMnCuP_2$ shows ferromagnetic transition around room temperature but a detailed study has to be performed so that more in-depth knowledge on the magnetic behaviour can be obtained.

## 6.5 References


1. Hoffmann, R.; Zheng, C. *J. Phys. Chem*. **1985**, *89*, 4175–4181.
2. Jeitschko, W.; Glaum, R.; Boonk, L. *J. Solid State Chem.* **1987**, *69*, 93-100
3. Klüfers, P.; Mewis, A. *Z. Kristallogr*. **1984**, *169*, 135–147.
4. Kranenberg, C.; Johrendt, D.; Mewis, A. *Z. Anorg. Allg. Chem.* **1999**, *625*, 1787–1793.
5. Wartenberg, F.; Kranenberg, C.; Pocha, R.; Johrendt, D.; Mewis, A.; Hoffmann, R. -D.; Mosel, B.D.; Pöttgen, R. *Z. Naturforsch. B: J. Chem. Sci.* **2002**, *57*, 1270–1276.
6. Rotter, M.; Pangerl, M.; Tegel, M.; Johrendt, D. *Angew. Chem. Int. Ed.* **2008**, *47*, 7949–7952.
7. Johrendt, D.; Pöttgen, R. *Physica C* **2009**, *469*, 332–339.
8. Mandrus, D.; Sefat, A. S.; McGuire, M.A.; Sales, B. C. *Chem. Mater.* **2010**, *22*, 715–723.
9. Kauzlarich, S. M.; Brown, S. R.; Snyder, G. J. *Dalton Trans.* **2007**, 2099–2107.
10. Snyder, G. J.; Toberer, E. S. *Nature Mater.* **2008**, *7*, 105–114.
11. Toberer, E. S.; May, A. F.; Snyder, G. J. *Chem. Mater.* **2010**, *22*, 624–634.
12. Ponnambalam, V.; Lindsey, S.; Xie, W.; Thompson, D.; Drymiotis, F.; Tritt, T. T. *J. Phys. D: Appl. Phys.* **2011**, *44*, 155406.
13. Mewis, A. *Z. Naturforsch. B: Anorg. Chem.*, *Org. Chem.* **1980**, *35*, 939–941.
14. Klüfers, P.; Mewis, A.; Schuster, H. -U. *Z. Kristallogr.* **1979**, *149*, 211–225.
15. Klüfers, P.; Neumann, H.; Mewis, A.; Schuster, H. -U. *Z. Naturforsch. B: Anorg. Chem., Org. Chem.* **1980**, *35*, 1317–1318.
16. Zwiener, G.; Neumann, H.; Schuster, H. -U. *Z. Naturforsch. B: Anorg. Chem., Org. Chem.* **1981**, *36*, 1195–1197.

17. Mahan, A.; Mewis, A. *Z. Naturforsch. B: Anorg. Chem., Org. Chem.* **1983**, *38*, 1041–1045.

18. Tejedor, P.; Stacy, A. M. *J. Solid State Chem.* **1990**, *89*, 227–236.

19. Blanchard, P. E. R.; Stoyko, S. S.; Cavell, R. G.; Mar, A. *J. Solid State Chem.* **2011**, *184*, 97–103.

20. Stoyko, S. S.; Ramachandran, K. K.; Blanchard, P. E. R.; Rosmus, K. A.; Aitken, J. A.; Mar, A. *J. Solid State Chem.* **2015**, *54,* 860-866.

21. Kraus, W.; Nolze, G. *J. Appl. Cryst.* **1996**, *29*, 301-303.

22. Holland, T. J. B.; Redfern, S. A. T. *Mineral. Mag.* **1997**, *61*, 65-77.

23. Tank, R.; Jepsen, O.; Burkhardt, A.; Andersen, O. K. *TB-LMTO-ASA Program*, version 4.7, Max Planck Institut für Festkörperforschung, Stuttgart, Germany, 1998.

24. Kubelka, P.; Munk, F. *Z. Techn. Physik.* **1931**, *12*, 593.

25. Urbach, F. *Phys. Rev.* **1953**, *92*, 1324.

# Chapter 7

## 7.1 Conclusions

The primary goal of this thesis was achieved by synthesizing several series of new quaternary phosphides and arsenides, which are either metal-rich or pnicogen-rich. The new compounds were characterized by single-crystal and powder X-ray diffraction techniques. It is not obvious that the loaded nominal compositions resulted in expected products so that characterization techniques play a vital role in solid-state chemistry. The new products obtained in my research are listed below.

**Table 7-1.** Metal-rich and pnicogen-rich compounds.

| Compounds | Structure type | Metal-pnicogen ratio |
|---|---|---|
| $RE_2Mn_3Cu_9Pn_7$<br>(*RE* = La-Nd, Sm, Gd-Dy; *Pn* = P)<br>(*RE* = La-Nd; *Pn* = As) | $Zr_2Fe_{12}P_7$-type<br>$(RE^{3+})_2(Mn^{2+})_3(Cu^{1+})_9\,(Pn^{3-})_7$ | Metal-rich (2:1)<br>*Metallic* |
| $REMnCu_4P_3$<br>(*RE* = Gd-Dy) | $YCo_5P_3$-type<br>$RE^{3+}Mn^{2+}(Cu^{1+})_4(P^{3-})_3$ | Metal-rich (2:1)<br>*Metallic* |
| $REMnCuP_2$<br>(*RE* = Y, La-Nd, Sm, Gd-Dy) | $CaAl_2Si_2$-type<br>$RE^{3+}Mn^{2+}Cu^{1+}(P^{3-})_2$ | Metal-rich (3:2)<br>*Metallic* |
| $RECuZnAs_2$<br>(*RE* = Y, La-Nd, Sm, Gd-Lu) | $CaAl_2Si_2$-type<br>$RE^{3+}Cu^{1+}\ Zn^{2+}(As^{3-})_2$ | Metal-rich (3:2)<br>*Semi-metallic* |
| $REAgZnPn_2$<br>(*RE* = La-Nd, Sm, Gd-Dy; *Pn* = P, As) | $CaAl_2Si_2$-type<br>$RE^{3+}Ag^{1+}Zn^{2+}(Pn^{3-})_2$ | Metal-rich (3:2)<br>*Semiconducting* |
| $RECdP_2$<br>(*RE* = La-Nd) | $CaAl_2Si_2$-type<br>$RE^{3+}Ag^{1+}Cd^{2+}(P^{3+})_2$ | Metal-rich (3:2)<br>*Semiconducting* |
| $REAg_{1-x}Zn_yAs_2$<br>(*RE* = La-Nd, Sm, Gd-Dy) | $HfCuSi_2$-type<br>$(RE^{3+}(Ag^{1+})_{1-x}(Zn^{2+})_y$<br>$As1^{3+}As2^{1-\text{ to }1.5-})$ | $x > 0.5$, metal mono-arsenides,<br>$x < 0.5$, pnicogen-rich |

The compounds listed in the **Table 7-1** are charge balanced except for the $HfCuSi_2$-type compounds where excess electrons up to a maximum of 0.5 $e^-$ can be accommodated through occupation of weak As–As antibonding levels near the Fermi level. The studies reveal that the normal valence rules can be applied when the metal-nonmetal ratio is less than 2. In both series of metal-rich compounds, $RE_2Mn_3Cu_9Pn_7$ and $REMnCu_4P_3$, the VEC($X$) = 8 and no homoatomic bonds are expected according to the rule but the band structure calculations show the presence of strong *M–M* bonds. In the other series of metal-rich compounds which adopt the $CaAl_2Si_2$-type structure, where VEC($X$) = 8, the *M–M* bonds are relatively weak and the normal valence rules are valid. The $HfCuSi_2$-type compounds, where VEC($X$) varies from 7.25 (when the electron excess is 0.5) to 7 in a stoichiometric composition, have polyanionic networks and the normal valence rules are applicable. Since there are two crystallographically different As atoms, one is assigned as $As1^{3-}$ with no homoatomic bonds and $As2^{1-}$ with two-bonded networks in the stoichiometric structure. The two-bonded As2 is more distorted and forms a square planar network. It is also notable that the transition-metal sites are limited to species with $d^{10}$ configuration in HfCuSi-type structure.

The study was extended to the crystallographic site preferences in the $Zr_2Fe_{12}P_7$- and $YCo_5P_3$-type structures, which have two different coordination environments (CN4 and CN5) for Fe and Co. Detailed investigations of quaternary phases, $RE_2Mn_3Cu_9Pn_7$ and $REMnCu_4P_3$, provide insights into the relationship between site preferences and charges on the transition-metal atoms. The failure to make other compositions and the bond-valence-sum calculations suggested that the $Mn^{2+}$ prefers the CN5 and $Cu^{1+}$ prefers CN4

in both cases. This leads to a conclusion that the site preference depends on the charges of the atoms. It is also notable that our inability to prepare Ag-containing analogues suggests that both size and electronegativity are important factors. This study ensures the possibility of extending the investigations to higher members of $RE_{n(n-1)}M_{(n+1)(n+2)}Pn_{n(n+1)+1}$ with more coordination geometries (CN6 to CN3).

Rare-earth-containing transition-metal pnictides with $CaAl_2Si_2$-type structure were previously limited to $RE^{2+}M_2^{2+}Pn_2^{3-}$ (*RE* = Eu, Yb). They were extensively studied for their thermoelectric properties, mostly among antimonides. In this thesis, the flexibility of *M* positions has been studied among different transition metals with $d^5$-$d^{10}$ or $d^{10}$-$d^{10}$ combinations, resulting in new compounds $RE^{3+}M^{2+}M'^{1+}Pn_2^{3-}$. This opens up a new system for experimenting the structural flexibility and tuning the physical properties by interchanging *RE* and *M*/*M*' which was previously limited with Zn and Cd. Several series of quaternary compounds were made, as listed in **Table 7-1**.

The structural flexibility was then related to the physical properties of $CaAl_2Si_2$-type compounds. The comparison of the result obtained from these series suggests that $d^5$-$d^{10}$ combinations result in metallic behaviour whereas a band gap forms with $d^{10}$-$d^{10}$ combinations. *RE*$MnCuP_2$ is metallic in nature but *RE*$CuZnPn_2$ is semimetallic[1]; *RE*$AgMPn_2$ (*M* = Zn, Cd) becomes semiconducting as the bandgap. The studies also suggest that the band gap decreases by substituting P with As. There is a general trend of decrease in band gap by early rare-earth with later rare-earth metals. This gives a wide

range of tunability of band gap by many different ways. **Table 7-2** provides the trend of $E_g$ values in different *REMM'Pn*$_2$ (*Pn* = P, As).

**Table 7-2.** Trend in band gap of different *REMM'Pn*$_2$ (*Pn* = P, As).

| **Phosphides** | **Arsenides** |
|---|---|
| *Ln*MnCuP$_2$ (metallic)[a] | *Ln*MnCuAs$_2$ (Unknown) |
| *Ln*CuZnP$_2$ (Semimetallic)[a]<br>La → Later Rare-earth<br>$E_g$ decreases | *Ln*CuZnAs$_2$ (Metallic)[a] |
| *Ln*AgZnP$_2$ (Semiconducting)[a,b]<br>La → Later Rare-earth<br>$E_g$ decreases | *Ln*AgZnAs$_2$ (Metallic)[a] |
| *Ln*AgCdP$_2$ (Semiconducting)[a,b]<br>La → Later Rare-earth<br>$E_g$ decreases | *Ln*AgCdAs$_2$ (Unknown) |

[a] Theoretical Value, [b] Experimental Value

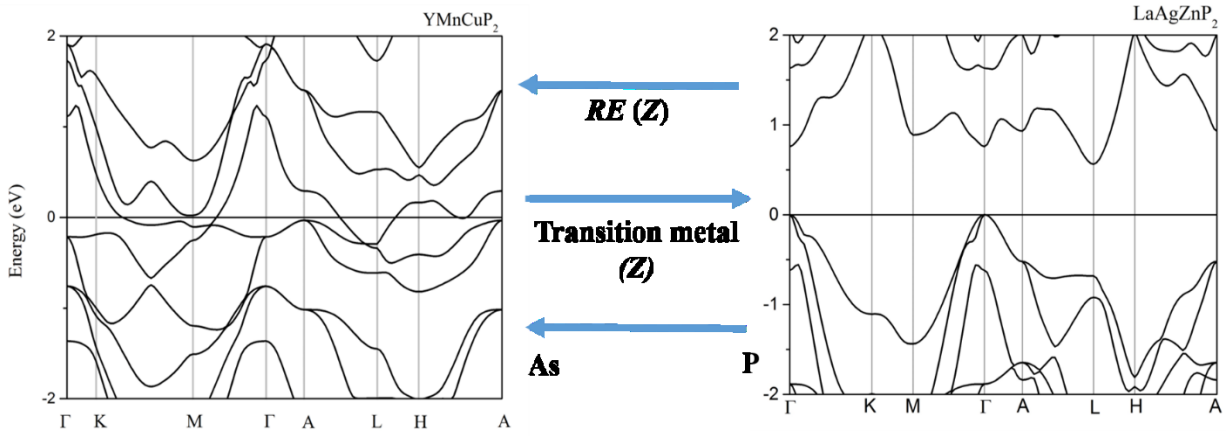


**Figure 7-1.** Strategic approach for tuning the band gap in quaternary phosphides and arsenides.

## 7.2 Future Work

Many binary and ternary phosphides and arsenides still remain to be discovered. Even the physical properties of many known phosphides and arsenides are not well studied either. There are nearly no ternary arsenides and phosphides reported that contain an early transition metal from groups 3 to 5 (**Table 1-1**). It will be a great opportunity to investigate new compounds and to evaluate the physical properties which may be good candidates for industrial applications. At the same time, it is also important to focus more on the materials that have been synthesized in my graduate studies and examine their properties more carefully. The continuation of my current work is discussed below in detail.

**$CaAl_2Si_2$-type compounds:**

$CaAl_2Si_2$-type compounds are good candidates for thermoelectric materials. In *REMM'*$Pn_2$ compounds, the ionically bonded *RE* atoms act as a phonon inhibitor and the anionic layer of $[MM'Pn_2]_n$ enhances the electrical conductivity. This satisfies the electron-crystal-phonon-class criterion, where thermal conductivity can be substantially reduced without any hindrance in electrical conductivity. The materials which have been discussed in this thesis satisfy the primary conditions for a good thermoelectric material, i.e., small band gap (<2 eV) and the electron-crystal-phonon-glass criterion. Further studies have to be done on these materials to experimentally verify the possibility of using them for thermoelectric applications.

Another interesting feature of $CaAl_2Si_2$-type structure is their ability to form homologous series. It has been reported among ternary arsenides by X. Lin *et al*[2] that

additional slabs of [*RE*As] can be inserted into the $REM_2As_2$ (or $RE_2M_4As_4$) compounds which can reduce the band gap with the addition of more layers. Some preliminary investigations are started already in *RE*MnCuP$_2$. This can be generalized into $RE_{2-y}M_2M'_2Pn_4 \cdot n(REPn)$.

**HfCuSi$_2$-type Compounds:**

The rare-earth containing quaternary compounds adopting HfCuSi$_2$-type structure are limited to $d^{10}$ transition elements in the anionic layer. There are studies done on ternary compounds of this structure type which suggest that the presence of *Pn–Pn* square nets can reduce the thermal conductivity but the main problem is their metallic behaviour. This is a good starting point for investigating new compounds of this structure type. The constituents can be changed in a systematic manner to tune the band gap without disrupting the low thermal conductivity. The tolerance of excess electron can substantially help in the electrical conductivity.

## 7.3 References


1. Blanchard, P. E. R.; Stoyko, S. S.; Cavell, R. G.; Mar, A. *J. Solid State Chem.* **2010**, *184*, 97-103.
2. Lin, X., Tabassum, D., Mar, A. *Dalton Trans.* **2015**, *44*, 20254-20264.

# Bibliography


1. West, A. R., *Solid State Chemistry and its Applications*, 2nd Ed., Wiley: United Kingdom, 2014.
2. Castillo-Ojeda, R.; Díaz-Reyes, J.; Galván-Arellano, M.; Peña-Sierra, R. *Advanced Material Research* **2014***, 976*, 25-29.
3. Hudl, M.; Campanini, D.; Caron, L.; Höglin, V.; Sahlberg, M.; Nordblad, P.; Rydh, A. *Phys. Rev. B* **2014**, *90***,** 144432 (1-5).
4. Saparov, B.; Mitchell, J.; Sefat, A. *Supercond. Sci. Technol.* **2012**, *25,* 084016 (1-10).
5. Spitzer, D. P.; Castellion, G. A.; Haacke, G. *J. Appl. Phys.* **1966**, *37*, 3795-3801.
6. Oyama; S. T.; Gott, T.; Zhao, H.; Lee, Y. K. *Catal. Today* **2009**, *143*, 94-107.
7. Oyama; S. T. *J. Catal* **2003**, *216*, 343-352.
8. Chen, J.; Zhou, S.; Ci, D.; Zhang, J.; Wang, R.; Zhang, *J. Ind. Eng. Chem. Res.* **2009**, *48*, 3812-3819.
9. Liu, X.; Chen, J.; Zhang, *J. Catal. Commun.* **2007**, *8*, 1905-1909.
10. Chen, J.; Han, M.; Zhao, S.; Pan, Z.; Zhang, Z. *Catal. Sci. Technol.* **2016**, DOI**:**10.1039/C5CY01751C.
11. Habas, S. E.; Baddour, F. G.; Ruddy, D. A.; Nash, C. P.; Wang, J.; Pan, M.; Hensley, J. E.; Schaidle, J. A. *Chem. Mater.* **2015**, *27*, 7580−7592.
12. Pfeiffer, H.; Tancret, F.; Brousse; T. *Mater. Chem. Phys.* **2005**, *92*, 534-539.
13. Stern, L.; Feng, L.; Song, F.; Hu, X.; *Energy Environ. Sci.* **2015**, *8*, 2347--2351.
14. Zhou, A.; Yang, B.; Wang, W.; Dai, X.; Zhao, M.; Xue, J; Han, M; Fan, C.; Li, Jingze *RSC Adv.* **2016**, *6*, 26800–26808.
15. Boyanov, S.; Bernardi, J.; Gillot, F.; Dupont, L.; Womes, M.; Tarascon, J. M.; Monconduit, L.; Doublet, M. L. *Chem. Mater.* **2006**, *18*, 3531-3538.
16. Tegus, O.; Brück, E.; Buschow, K. H. J.; de Boer, F. R. *Nature* **2002**, *415*, 150-152.
17. Ren, Z. -A.; Che, G. -C.; Dong, X. -L.; Yang, J.; Lu., W.; Yi., W.; Shen, X. -L.; Li, Z. -C.; Sun, L. -L.; Zhou, F. *Europhys. Lett.* **2008**, *83*, 17002.
18. Villars, P.; Cenzual, K. Pearson's Crystal Data - Crystal Structure Database for Inorganic Compounds, Release 2015/16, ASM international, Materials Park, Ohio, USA.
19. Jeitschko, W.; Glaum, R.; Boonk; L. *J. Solid State Chem*. **1987**, *69*; 93-100.
20. Guo, Q.; Pan, B. J.; Yu, J.; Ruan, B. B.; Chen, D. Y.; Wang, X. C.; Mu, Q. G.; Chen, G. F.; Ren, Z. A. *Sci. Bull.* **2016**, DOI 10.1007/s11434-016-1080-4.

21. Qi, Y.; Gao, Z.; Wang, L.; Wang, D.; Zhang, X.; Ma, Y. *New J. Phys.* **2008**, *10*, 123003 (1-6).

22. Gascoin, F.; Ottensmann, S.; Stark, D.; Haile, S. M.; Snyder, G. J. *Adv. Funct. Mater.* **2005**, *15*, 1860.

23. Yu, C.; Zhu T. J.; Zhang, S. N.; Zhao, X. B.; He, J.; Su, Z.; Tritt, T. M. *J. Appl. Phys.* **2008**, *104*, 013705.

24. Wang, X. J.; Tang, M. B.; Chen, H. H.; Yang, X. X.; Zhao, J. T.; Burkhardt, U.; Grin, Y.; *Appl. Phys. Lett*., **2009**, *94*, 092106.

25. Ponnambalam, V.; Lindsey, S.; Xie, W.; Thompson, D.; Drymiotis, F.; Tritt, T. T. *J. Phys. D: Appl. Phys.* **2011**, *44*, 155406.

26. Müller, U. *Inorganic Structural Chemistry*, 2nd ed., Wiley: Cheichester, 2007.

27. Kauzlarich, S. M., Ed. *Chemistry, Structure, and Bonding of Zintl Phases and Ions*, VCH Publishers: New York, 1996.

28. Rundqvist, S.; Jellinek, F. *Acta. Chem. Scand.* **1959**, *13*, 425-432.

29. Rundqvist, S. *Acta. Chem. Scand.* **1962**, *16*, 287-292.

30. Grosvenor, A. P.; Wik, S. D.; Cavell, R. G.; Mar, A. *Inorg. Chem.* **2005**, *44*, 8988-8998.

31. Hönle, W.; Von Schnering, H. G. *Z. Anorg. Allg. Chem.* **1979**, *34*, 194-206.

32. Iandelli, A.; Franceschi, E. A. **1973**, *30*, 211-216.

33. Bauer, G.; Zintl E. *Z. Phys. Chem.*, *Abt. B* **1937**, *37*, 323-352.

34. Bhella, S. S.; Shafi, S. P.; Trobec, F.; Bieringer, M.; Thangadurai, V. *Inorg. Chem.*, **2010**, *49*, 1699–1704.

35. Kraus, W., Nolze, G. *J. Appl. Cryst.***1996**, *29*, 301-303.

36. Holland, T. J. B.; Redfern, S. A. T. *Mineral. Mag.* **1997**, *61*, 65-77.

37. Diamond - Crystal and Molecular Structure Visualization Crystal Impact - Dr. H. Putz & Dr. K. Brandenburg GbR, Kreuzherrenstr. 102, 53227 Bonn, Germany <http://www.crystalimpact.com/diamond>.

38. Clegg, W. *Crystal Structure Determination*, Oxford University Press: Oxford, 1998.

39. Giacovazzo, C.; *Fundamentals of Crystallography*, 3rd Ed. Oxford University Press: Oxford, 1992.

40. Massa, W.; *Crystal Structure Determination*, 2nd Ed. Springer-Verlag: Berlin, 2004.

41. Sheldrick, G. M. SHELXTL. *Bruker AXS Inc.: Madison, WI* **2001***, 6.12*.

42. Gelato, L. M.; Parthé, E. *J. Appl. Crystallogr.* **1987***, 20*, 139-143.

43. Australian Microscopy and Microanalysis Research Facility 2014, accessed 17 June, 2016 <http://www.ammrf.org.au/myscope/sem/introduction/>

44. Kondo, J. Kondo Effect. *Progr. Theoret. Phys.* **1964***, 32*, 37.

45. Abramowitz, M.; Sutter, R. T.; Davidson, M. W., accessed 5 May 2016 <http://www.olympusmicro.com/primer/java/reflection/specular/>.

46. Kubelka, P.; Munk, F. *Z. Techn. Physik.* **1931***, 12*, 593.

47. Urbach, F. *Phys. Rev.* **1953***, 92*, 1324.

48. Yacobi, B. G. *Semiconductor Materials: An Introduction to Basic Principles.* Springer US: Boston, MA, 2003; pp 107-134.

49. Naumkin, A. V.; Kraut-Vass, A.; Gaarenstroom, S. W.; Powell, C. J. NIST X-ray Photoelectron Spectroscopy Database, accessed 5 May, 2016, <http://srdata.nist.gov/xps/>.

50. Dronkowski, R. *Computational Chemistry of Solid State Materials*, Wiley-VCH: Weinheim, 2005.

51. Hoffmann, R. *Angew. Chem. Int. Ed. Engl.* **1987***, 26*, 846-878.

52. Anderson, O. K. *Phys. Rev. B: Condens. Matter* **1975***, 12*, 3060-3083.

53. Castillo-Ojeda, R.; Díaz-Reyes, J.; Galván-Arellano, M.; Peña-Sierra, R. *Advanced Material Research* **2014***, 976*, 25-29.

54. Hudl, M.; Campanini, D.; Caron, L.; Höglin, V.; Sahlberg, M.; Nordblad, P.; Rydh, A. *Phys. Rev. B* **2014**, *90***,** 144432 (1-5).

55. Saparov, B.; Mitchell, J.; Sefat, A. *Supercond. Sci. Technol.* **2012**, *25,* 084016 (1-10).

56. Spitzer, D. P.; Castellion, G. A.; Haacke, G. *J. Appl. Phys.* **1966**, *37*, 3795-3801.

57. Oyama; S. T.; Gott, T.; Zhao, H.; Lee, Y. K. *Catal. Today* **2009**, *143*, 94-107.

58. Oyama; S. T. *J. Catal* **2003**, *216*, 343-352.

59. Chen, J.; Zhou, S.; Ci, D.; Zhang, J.; Wang, R.; Zhang, *J. Ind. Eng. Chem. Res.* **2009**, *48*, 3812-3819.

60. Liu, X.; Chen, J.; Zhang, *J. Catal. Commun.* **2007**, *8*, 1905-1909.

61. Chen, J.; Han, M.; Zhao, S.; Pan, Z.; Zhang, Z. *Catal. Sci. Technol.* **2016**, DOI**:**10.1039/C5CY01751C.

62. Habas, S. E.; Baddour, F. G.; Ruddy, D. A.; Nash, C. P.; Wang, J.; Pan, M.; Hensley, J. E.; Schaidle, J. A. *Chem. Mater.* **2015**, *27*, 7580−7592.

63. Pfeiffer, H.; Tancret, F.; Brousse; T. *Mater. Chem. Phys.* **2005**, *92*, 534-539.

64. Stern, L.; Feng, L.; Song, F.; Hu, X.; *Energy Environ. Sci.* **2015**, *8*, 2347--2351.

65. Zhou, A.; Yang, B.; Wang, W.; Dai, X.; Zhao, M.; Xue, J.; Han, M.; Fan, C.; Li, J. *RSC Adv.* **2016**, *6*, 26800–26808.

66. Boyanov, S.; Bernardi, J.; Gillot, F.; Dupont, L.; Womes, M.; Tarascon, J. M.; Monconduit, L.; Doublet, M. L. *Chem. Mater.* **2006**, *18*, 3531-3538.

67. Tegus, O.; Brück, E.; Buschow, K. H. J.; de Boer, F. R. *Nature* **2002**, *415*, 150-152.

68. Ren, Z. -A.; Che, G. -C.; Dong, X. -L.; Yang, J.; Lu., W.; Yi., W.; Shen, X. -L.; Li, Z. -C.; Sun, L. -L.; Zhou, F. *Europhys. Lett.* **2008**, *83*, 17002.

69. Jeitschko, W.; Glaum, R.; Boonk; L. *J. Solid State Chem*. **1987**, *69*; 93-100.

70. Guo, Q.; Pan, B. J.; Yu, J.; Ruan, B. B.; Chen, D. Y.; Wang, X. C.; Mu, Q. G.; Chen, G. F.; Ren, Z. A. *Sci. Bull.* **2016**, DOI 10.1007/s11434-016-1080-4.

71. Qi, Y.; Gao, Z.; Wang, L.; Wang, D.; Zhang, X.; Ma, Y. *New J. Phys.* **2008**, *10*, 123003 (1-6).

72. Gascoin, F.; Ottensmann, S.; Stark, D.; Haile, S. M.; Snyder, G. J. *Adv. Funct. Mater.* **2005**, *15*, 1860.

73. Yu, C.; Zhu T. J.; Zhang, S. N.; Zhao, X. B.; He, J.; Su, Z.; Tritt, T. M. *J. Appl. Phys.* **2008**, *104*, 013705.

74. Wang, X. J.; Tang, M. B.; Chen, H. H.; Yang, X. X.; Zhao, J. T.; Burkhardt, U.; Grin, Y. *Appl. Phys. Lett*. **2009**, *94*, 092106.

75. Ponnambalam, V.; Lindsey, S.; Xie, W.; Thompson, D.; Drymiotis, F.; Tritt, T. T. *J. Phys. D: Appl. Phys.* **2011**, *44*, 155406.

76. Rundqvist, S.; Jellinek, F. *Acta. Chem. Scand.* **1959**, *13*, 425-432.

77. Rundqvist, S. *Acta. Chem. Scand.* **1962**, *16*, 287-292.

78. Grosvenor, A. P.; Wik, S. D.; Cavell, R. G.; Mar, A. *Inorg. CHem.* **2005**, *44*, 8988-8998.

79. Hönle, W.; Von Schnering, H. G. *Z. Anorg. Allg. Chem.* **1979**, *34*, 194-206.

80. Iandelli, A.; Franceschi, E. A. **1973**, *30*, 211-216.

81. Bauer, G.; Zintl E. *Z. Phys. Chem.*, *Abt. B* **1937**, *37*, 323-352.

82. Kraus, W., Nolze, G. *J. Appl. Cryst.***1996**, *29*, 301-303.

83. Holland, T. J. B.; Redfern, S. A. T. *Mineral. Mag.* **1997**, *61*, 65-77.

84. Diamond - Crystal and Molecular Structure Visualization Crystal Impact - Dr. H. Putz & Dr. K. Brandenburg GbR, Kreuzherrenstr. 102, 53227 Bonn, Germany <http://www.crystalimpact.com/diamond>.

85. Clegg, W. *Crystal Structure Determination*, Oxford University Press: Oxford, 1998.

86. Giacovazzo, C. *Fundamentals of Crystallography*, 3rd Ed. Oxford University Press: Oxford, 1992.

87. Massa, W. *Crystal Structure Determination,* 2nd Ed. Springer-Verlag: Berlin, 2004.

88. Sheldrick, G. M. SHELXTL. *Bruker AXS Inc.: Madison, WI* **2001***, 6.12*.

89. Gelato, L. M.; Parthé, E. *J. Appl. Crystallogr.* **1987***, 20*, 139-143.

90. Australian Microscopy and Microanalysis Research Facility 2014, accessed 17 June, 2016 <http://www.ammrf.org.au/myscope/sem/introduction/>.

91. Kondo, J. Kondo Effect. *Progr. Theoret. Phys.* **1964***, 32*, 37.

92. Abramowitz, M.; Sutter, R. T.; Davidson, M. W., accessed 5 May 2016 <http://www.olympusmicro.com/primer/java/reflection/specular/>.

93. Kubelka, P.; Munk, F. *Z. Techn. Physik.* **1931***, 12*, 593.

94. Urbach, F. *Phys. Rev.* **1953***, 92*, 1324.

95. Yacobi, B. G. *Semiconductor Materials: An Introduction to Basic Principles*, Springer US: Boston, MA, 2003.

96. Naumkin, A. V.; Kraut-Vass, A.; Gaarenstroom, S. W.; Powell, C. J. NIST X-ray Photoelectron Spectroscopy Database, accessed 5 May, 2016, <http://srdata.nist.gov/xps/>.

97. Dronkowski, R. *Computational Chemistry of Solid State Materials*, Wiley-VCH: Weinheim: 2005.

98. Hoffmann, R. *Angew. Chem. Int. Ed. Engl.* **1987***, 26*, 846-878.

99. Anderson, O. K. *Phys. Rev. B: Condens. Matter* **1975***, 12*, 3060-3083.

100. Ackermann, J.; Wold, A. *J. Phys. Chem. Solids* **1977**, *38*, 1013-1016.

101. Ono, S.; Despault, G. J. G.; Calvert, L. D.; Taylor, J. B. *J. Less-Common Met.* **1970**, *22*, 51-59.

102. Wang, M.; Mar, A. *Acta Crystallogr. C* **2000**, *56*, 138-139.

103. Senko, M. E.; Dunn, H. M.; Weidenborner, J. E.; Cole, H. *Acta Crystallogr.***1959**, *12*, 76.

104. Jeitschko, W.; Moller, M. H. *Acta Crystallogr. B* **1979**, *35*, 573-579.

105. Trezbiatowski, W.; Lukaszewicz, K; Weglowski, S. *Acta Crystallogr.* **1957**, *10*, 792-793.

106. Furuseth, S.; Kjekshus, A. *Acta Crystallogr.* **1965**, *18*, 320-324.

107. Von Schnering, H. G.; Wichelhaus, W.; Wittmann, M.; Weber, H. P.; Peters, K. *Z. Kristallogr. - New Cryst. Struct.* **1998**, *213*, 460.

108. Chykhrij, S. I.; Kuz'ma, Y. B.; Oryshchyn, S. V. *Dopov. Akad. Nauk Ukr. RSR, Ser. B* **1989**, *3*, 60-62.

109. Martin, D. H. *Magnetism in Solids*, M. I. T. Press, Cambridge, 1967.

110. Kittel, C. *Introduction to Solid State Physics* 8th Ed, John Wiley & Sons, Hoboken, 2005.

111. Malinauskas, M.; Danilecius, P.; Juodkazis, S. *Opt. Express* **2011**, *19*, 5602-5610.

112. Schubert, E. F. *Light-Emitting Diodes* 2nd Ed., Cambridge University Press, Cambridge, 2006.

113. Pivan, J. -Y.; Guérin, R.; Sergent, M. *J. Solid State Chem.* **1987**, *68*, 11–21.

114. Jeitschko, W.; Pollmeier, P. G.; Meisen, U. *J. Alloys Compd.* **1993**, *196*, 105–109.

115. Jeitschko, W.; Braun, D. J.; Ashcraft, R. H.; Marchand, R. *J. Solid State Chem.* **1978**, *25*, 309–313.

116. Jeitschko, W.; Meisen, U.; Scholz, U. D. *J. Solid State Chem.* **1984**, *55*, 331–336.

117. Oryshchyn, S. V.; Zhak, O. V.; Budnyk, S. L.; Kuz'ma, Yu. B. *Russ. J. Inorg. Chem. (Engl. Transl.)* **2002**, *47*, 1411–1414; *Zh. Neorg. Khim.* **2002**, *47*, 1541–1544.

118. Jeitschko, W.; Jaberg, B. *Z. Anorg. Allg. Chem.* **1980**, *467*, 95–104.

119. Jeitschko, W.; Reinbold, E. J. *Z. Naturforsch. B: Anorg. Chem., Org. Chem.* **1985**, *40*, 900–905.

120. Budnyk, S.; Kuz'ma, Yu. B. *Pol. J. Chem.* **2002**, *76*, 1553–1558.

121. Pivan, J. Y.; Guérin, R.; Padiou, J.; Sergent, M. *J. Less-Common Met.* **1986**, *118*, 191–200.

122. Oryshchyn, S.; Babizhetsky, V.; Stoyko, S. S.; Kuz'ma, Yu. *Z. Kristallogr.–New Cryst. Struct.* **1999**, *214*, 428.

123. Braun, T. P.; DiSalvo, F. J. *J. Alloys Compd.* **2000**, *307*, 111–113.

124. Wurth, A.; Keimes, V.; Johrendt, D.; Mewis, A. *Z. Anorg. Allg. Chem.* **2001**, *627*, 2183–2190.

125. Stoyko, S. S.; Oryshchyn, S. V. *Coll. Abs. 9th Int. Conf. Crystal Chem. Intermet. Compd. (Lviv)* **2005**, *58*.

126. Jeitschko, W.; Jaberg, B. *J. Less-Common Met.* **1981**, *79*, 311–314.

127. Babizhets'ky, V.; Le Sénéchal, C.; Bauer, J.; Députier, S.; Guérin, R. *J. Alloys Compd.* **1999**, *287*, 174–180.

128. Babizhetskyy, V.; Guérin, R.; Simon, A. *Z. Naturforsch., B: J. Chem. Sci.* **2006**, *61*, 733–740.

129. Zelinska, M.; Zhak, O.; Oryshchyn, S.; Polianska, T.; Pivan, J. -Y. *Z. Naturforsch., B: J. Chem. Sci.* **2007**, *62*, 1143–1152.

130. Probst, H.; Mewis, A. *Z. Anorg. Allg. Chem.* **1991**, *597*, 173–182.

131. Stępień-Damm, H.; Kaczorowski, D.; Wochowski, K. *J. Alloys Compd.* **2001**, *315*, L4–L6.

132. Jeitschko, W.; Meisen, U.; Albering, J. *Dalton Trans.* **2010**, *39*, 6067–6073.

133. Pivan, J. Y.; Guérin, R.; Sergent, M. *J. Less-Common Met.* **1985**, *107*, 249–258.

134. Reehuis, M; Jeitschko, W. *J. Phys. Chem. Solids* **1989**, *50*, 563–569.

135. El Ghadraoui, E. H.; Pivan, J. Y.; Peña, O.; Guérin, R.; Bonville, P. *Physica B* **1990**, *163*, 185–187.

136. Zeppenfeld, K.; Jeitschko, W. *J. Phys. Chem. Solids* **1993**, *54*, 1527–1531.

137. Reehuis, M.; Ouladdiaf, B.; Jeitschko, W.; Vomhof, T.; Zimmer, B.; Ressouche, E. *J. Alloys Compd.* **1997**, *261*, 1–11.

138. Ebel, T.; Albering, J. H.; Jeitschko, W. *J. Alloys Compd.* **1998**, *266*, 71–76.

139. Babizhetskyy, V.; Isnard, O.; Hiebl, K. *Solid State Commun.* **2007**, *142*, 80–84.

140. Jeitschko, W.; Meisen, U.; Reinbold, E. J. *Z. Anorg. Allg. Chem.* **2012**, *638*, 770–778.

141. Budnyk, S.; Prots, Yu.; Schmidt, M.; Schnelle, W.; Kuz'ma, Yu.; Grin, Yu. *Z. Anorg. Allg. Chem.* **2004**, *630*, 1062–1067.

142. Lorenz, P.; Jung, W. *Z. Anorg. Allg. Chem.* **2009**, *635*, 920–925.

143. Dhahri, E. *J. Phys.: Condens. Matter* **1996**, *8*, 4351–4360.

144. Ganglberger, E. *Monatsh. Chem.* **1968**, *99*, 557–565.

145. Gladyshevskii, E. I.; Grin, Yu. N. *Kristallografiya* **1981**, *26*, 1204–1214.

146. Madar, R.; Ghetta, V.; Dhahri, E.; Chaudouet, P.; Senateur, J. P. *J. Solid State Chem.* **1987**, *66*, 73–85.

147. Prins, R.; Bussell, M. E. *Catal. Lett.* **2012**, *142*, 1413–1436.

148. Maple, M. B.; Hamlin, J. J.; Zocco, D. A.; Janoschek, M.; Baumbach, R. E.; White, B. D.; Fisher, I. R.; Chu, J. -H. *EPJ Web Conf.* **2012**, *23*, 00012-1–00012-8.

149. Stoyko, S. S.; Ramachandran, K. K.; Mullen, C. S.; Mar, A. *Inorg. Chem.* **2013**, *52*, 1040–1046.

150. El Ghadraoui, E. H.; Pivan, J. -Y.; Guérin, R. *J. Solid State Chem.* **1989**, *78*, 262–270.

151. Gelato, L. M.; Parthé, E. *J. Appl. Crystallogr.* **1987**, *20*, 139–143.

152. Meisen, U.; Jeitschko, W. *J. Less-Common Met.* **1984**, *102*, 127–134.

153. Tank, R.; Jepsen, O.; Burkhardt, A.; Andersen, O. K. *TB-LMTO-ASA Program*, version 4.7; Max Planck Institut für Festkörperforschung: Stuttgart, Germany, 1998.

154. Jakubowski-Ripke, U.; Jeitschko, W. *J. Less-Common Met.* **1988**, *136*, 261–270.

155. Jeitschko, W.; Brink, R.; Pollmeier, P. G. *Z. Naturforsch., B: J. Chem. Sci.* **1993**, *48*, 52–57.

156. Albering, J. H.; Jeitschko, W. *J. Solid State Chem.* **1995**, *117*, 80–87.

157. Thompson, C. M.; Kovnir, K.; Zhou, H.; Shatruk, M. *Z. Anorg. Allg. Chem.* **2011**, *637*, 2013–2017.

158. Venturini, G.; Malaman, B. *J. Alloys Compd.* **1997**, *261*, 19–25.

159. Li, B.; Corbett, J. D. *Inorg. Chem.* **2007**, *46*, 2237–2242.

160. Hoffmann, R. -D.; Pöttgen, R. *Z. Anorg. Allg. Chem.* **1999**, *625*, 994–1000.

161. Zhao, J. T.; Chabot, B.; Parthé, E. *Acta Crystallogr., Sect. C* **1987**, *43*, 1458–1461.

162. Brese, N. E.; O'Keeffe, M. *Acta Crystallogr., Sect. B* **1991**, *47*, 192–197.

163. Pauling, L. *The Nature of the Chemical Bond*, 3rd ed., Cornell University Press: Ithaca, NY, 1960.

164. Johrendt, D.; Pöttgen, R. *Physica C* **2009**, *469*, 332–339.

165. Pöttgen, R.; Johrendt, D. *Z. Naturforsch., B: J. Chem. Sci.* **2008**, *63*, 1135–1148.

166. Pitcher, M. J.; Parker, D. R.; Adamson, P.; Herkelrath, S. J. C.; Boothroyd, A. T.; Ibberson, R. M.; Brunelli, M.; Clarke, S. J. *Chem. Commun.* **2008**, 5918–5920.

167. Kawamata, T.; Iida, T.; Suzuki, K.; Satomi, E.; Kobayashi, Y.; Itoh, M.; Sato, M. *J. Phys. Soc. Jpn.* **2011**, *80*, 073710-1–0737010-3.

168. Katayama, N.; Kudo, K.; Onari, S.; Mizukami, T.; Sugawara, K.; Sugiyama, Y.; Kitahama, Y.; Iba, K.; Fujimura, K.; Nishimoto, N.; Nohara, M.; Sawa, H. *J. Phys. Soc. Jpn.* **2013**, *82*, 123702-1–123702-4.

169. Yakita, H.; Ogino, H.; Okada, T.; Yamamoto, A.; Kishio, K.; Tohei, T.; Ikuhara, Y.; Gotoh, Y.; Fujihisa, H.; Kataoka, K.; Eisaki, H.; Shimoyama, J. *J. Am. Chem. Soc.* **2014**, *136*, 846–849.

170. Sala, A.; Yakita, H.; Ogino, H.; Okada, T.; Yamamoto, A.; Kishio, K.; Ishida, S.; Iyo, A.; Eisaki, H.; M. Fujioka, Y. Takano, M. Putti, J. Shimoyama, *Appl. Phys. Express* **2014**, *7*, 073102-1–073102-4.

171. Kudo, K.; Kitahama, Y.; Fujimura, K.; Mizukami, T.; Ota, H.; Nohara, M. *J. Phys. Soc. Jpn.* **2014** *83* 093705-1–093705-4.

172. Kuz'ma, Yu.; Chykhrij, S. in: K. A. Gschneidner, Jr., L. Eyring (Eds.), *Handbook on the Physics and Chemistry of Rare Earths*, vol. 23, Elsevier, Amsterdam, **1996**, pp. 285–434.

173. O. L. Sologub, P. S. Salamakha, in: K. A. Gschneidner, Jr., J. -C. G. Bünzli, V. K. Pecharsky (Eds.), *Handbook on the Physics and Chemistry of Rare Earths*, vol. 33, Elsevier, Amsterdam, 2003, pp. 35–146.

174. Mar, A. in: K. A. Gschneidner, Jr., J. -C.G. Bünzli, V. K. Pecharsky (Eds.), *Handbook on the Physics and Chemistry of Rare Earths*, vol. 36, Elsevier, Amsterdam, 2006, pp. 1–82.

175. Brylak, M.; Möller, M. H.; Jeitschko, W. *J. Solid State Chem.* **1995**, *115*, 305–308.

176. Jemetio Feudjio, J. -P.; Doert, Th.; Böttcher, P.; *Z. Kristallogr.–New Cryst. Struct.* **2002**, *217*, 455–457.

177. Demchyna, R. O.; Kuz'ma, Yu. B.; Babizhetsky, V. S. *J. Alloys Compd.* **2001**, *315*, 158–163.

178. Eschen, M.; Jeitschko, W. *Z. Naturforsch., B: J. Chem. Sci.* **2003**, *58* 399–409.

179. Demchyna, R.; Jemetio, J. P. F.; Prots, Yu.; Doert, Th.; Akselrud, L. G.; Schnelle, W.; Kuz'ma, Yu.; Grin, Yu. *Z. Anorg. Allg. Chem.* **2004**, *630*, 635–641.

180. Nientiedt, A. T.; Jeitschko, W. *J. Solid State Chem.* **1999**, 142, 266–272.

181. Stoyko, S. S.; Mar, A. *J. Solid State Chem.* **2011**,*184*, 2360–2367.

182. Wang, M.; McDonald, R.; Mar, A. *J. Solid State Chem.* **1999**, *147*, 140–145.

183. Jemetio, J. -P.; Doert, Th.; Rademacher, O.; Böttcher, P. *J. Alloys Compd.* **2002**, 338, 93–98.

184. Mozharivskyj, Y.; Pecharsky, A. O.; Bud'ko, S.; Franzen, H. F. *Z. Anorg. Allg. Chem.* **2002**, *628,* 1619–1630.

185. Mozharivskyj, Y.; Franzen, H. F. *J. Phys. Chem. B* **2002**, *106*, 9528–9535.

186. Rutzinger, D.; Doert, Th.; Ruck, M. *Acta Crystallogr., Sect. B: Struct. Sci.* **2009**, 65, 519–526.

187. Rutzinger, D.; Bartsch, C.; Doert, Th., Ruck, M. *Acta Crystallogr., Sect. B: Struct. Sci.* **2009**, *65*, 527–534.

188. Rutzinger, D.; Bartsch, C.; Doerr, M.; Rosner, H.; Neu, V.; Doert, Th.; Ruck, M. *J. Solid State Chem.* **2010**, *183*, 510–520.

189. Tremel, W.; Hoffmann, R. *J. Am. Chem. Soc.* **1987**, *109,* 124–140.

190. Papoian, G.A.; Hoffmann, R. *Angew. Chem. Int. Ed.* **2000**, *39*, 2408–2448.

191. Cordier, G.; Schäfer, H.; Woll, P. *Z. Naturforsch. B: Anorg. Chem., Org. Chem.* **1985**, *40*, 1097–1099.

192. Sologub, O.; Hiebl, K.; Rogl, P.; Bodak, O. *J. Alloys Compd.* **1985**, *227*, 40–43.

193. Wollesen, P.; Jeitschko, W.; Brylak, M.; Dietrich, L. *J. Alloys Compd.* **1996**, *245*, L5–L8.

194. Flandorfer, H.; Sologub, O.; Godart, C.; Hiebl, K.; Leithe-Jasper, A.; Rogl, P.; Noël, H. *Solid State Commun.* **1996**, *97*, 561–565.

195. Tkachuk, A.V.; Zelinska, O.Ya.; Mar, A. *J. Solid State Chem.* **2006**, *179*, 1506–1512.

196. Zelinska, O.Ya.; Mar, A. *J. Solid State Chem.* **2006**, *179*, 3776–3783.

197. Tabassum, D., Lin, X.; Mar, A. *J. Alloys Compd.* **2015**, *636*, 187–190.

198. Lin, X.; Mar, A. *Inorg. Chem.* **2013**, *52*, 7261–7270.

199. Stoyko, S. S.; Ramachandran, K. K.; Blanchard, P. E. R.; Rosmus, K. A.; Aitken, J. A.; Mar, A. *J. Solid State Chem.* **2014**, *213*, 275–286.

200. Ramachandran, K. K.; Stoyko, S. S.; Mar, A. unpublished results.

201. Cordier, G.; Eisenmann, B.; Schäfer, H.; *Z. Anorg. Allg. Chem.* **1976**, *426*, 205–214.

202. Andrukhiv, L. S.; Lysenko, L. A.; Yarmolyuk, Ya. P.; Gladyshevskii, E. I.; *Dopov. Akad. Nauk Ukr. RSR, Ser. A: Fiz.-Tekh. Mat. Nauki* 1975, *7*, 645–648.

203. Gelato, L. M.; Parthé, E. *J. Appl. Crystallogr.* **1987**, *20*, 139–143.

204. Brechtel, E.; Cordier, G.; Schäfer, H.; *Z. Naturforsch., B: Anorg. Chem., Org. Chem.* **1979**, *34*, 251–255.

205. Rutzinger, D. Ph.D. thesis, Technische Universität Dresden, 2009.

206. Sengupta, K.; Rayaprol, S.; Sampathkumaran, E. V.; Doert, Th.; Jemetio, J. P. F. *Physica B* **2004**, *348*, 465–474.

207. Szlawska, M.; Kaczorowski, D. *J. Alloys Compd*. **2008**, *451*, 464–466.

208. Mukherjee, K.; Sampathkumaran, E. V.; Rutzinger, D.; Doert, Th.; Ruck, M. *J. Phys: Condens. Matter* **2009**, *21*, 506004-1–506004-8.

209. Doert, Th.; Schneidewind, A.; Hölzel, M.; Stockert, O.; Rutzinger, D.; Ruck, M. *J. Magn. Magn. Mater*. **2012**, *324*, 1157–1164.

210. Hoffmann, R.; Zheng, C. *J. Phys. Chem*. **1985**, *89*, 4175–4181.

211. Zheng, C.; Hoffmann, R. *J. Solid State Chem.* **1988**, *72*, 58–71.

212. Johrendt, D.; Felser, C.; Jepsen, O.; Andersen, O. K.; Mewis, A.; Rouxel, J. *J. Solid State Chem*. **1997**, *130*, 254–265.

213. Rotter, M.; Pangerl, M.; Tegel, M.; Johrendt, D. *Angew. Chem. Int. Ed.* **2008**, *47*, 7949–7952.

214. Mandrus, D.; Sefat, A. S.; McGuire, M. A.; Sales, B. C. *Chem. Mater.* **2010**, *22*, 715–723.

215. Klüfers, P.; Mewis, A. *Z. Kristallogr*. **1984**, *169*, 135–147.

216. Zheng, C.; Hoffmann, R.; Nesper, R.; von Schnering, H. -G. *J. Am. Chem. Soc*. **1986**, *108*, 1876–1884.

217. Burdett, J. K.; Miller, G. J. *Chem. Mater.* **1990**, *2*, 12–26.

218. Kranenberg, C.; Johrendt, D.; Mewis, A. *Z. Anorg. Allg. Chem.* **1999**, *625*, 1787–1793.

219. Kranenberg, C.; Johrendt, D.; Mewis, A. *Solid State Sci*. **2002**, *4*, 261–265.

220. Wartenberg, F.; Kranenberg, C.; Pocha, R.; Johrendt, D.; Mewis, A.; Hoffmann, R.-D.; Mosel, B.D.; Pöttgen, R. *Z. Naturforsch. B: J. Chem. Sci.* **2002**, *57*, 1270–1276.

221. Alemany, P.; Llunell, M.; Canadell, E. *J. Comput. Chem.* **2008**, *29*, 2144–2153.

222. Gascoin, F.; Ottensmann, S.; Stark, D.; Haïle, S.M.; Snyder, G.J. *Adv. Funct. Mater.* **2005**, *15*, 1860–1864.

223. Kauzlarich, S. M.; Condron, C. L.; Wassei, J. K.; Ikeda, T.; Snyder, G. J. *J. Solid State Chem.* **2009**, *182*, 240–245.

224. Wang, X. -J.; Tang, M. -B.; Chen, H. -H.; Yang, X. -X., Zhao, J. -T.; Burkhardt, U.; Grin, Yu. *Appl. Phys. Lett.* **2009**, *94*, 092106-1–092106-3.

225. Zhang, H.; Baitinger, M.; Tang, M.-B.; Man, Z. -Y.; Chen, H. -H.; Yang, X. -X.; Liu, Y.; Chen, L.; Grin, Yu.; Zhao, J. -T. *Dalton Trans.* **2010**, *39*, 1101–1104.

226. Flage-Larsen, E.; Diplas, S.; Prytz, Ø.; Toberer, E. S.; May, A. F. *Phys. Rev. B* **2010**, *81*, 205204-1–205204-7.

227. Guo, K.; Cao, Q. -G.; Feng, X. -J.; Tang, M.-B.; Chen, H. -H.; Guo, X.; Chen, L.; Grin, Yu.; Zhao, J. -T. *Eur. J. Inorg. Chem.* **2011**, 4043–4048.

228. May, A. F.; McGuire, M. A.; Singh, D. J.; Ma, J.; Delaire, O.; Huq, A.; Cai, W.; Wang, H. *Phys. Rev. B* **2012**, *85*, 035202-1–035202-10.

229. Ponnambalam, V.; Morelli, D. T. *J. Electron. Mater*. **2013**, *42*, 1307-1312.

230. Kauzlarich, S. M.; Brown, S. R.; Snyder, G. J. *Dalton Trans.* **2007**, 2099–2107.

231. Snyder, G. J.; Toberer, E. S. *Nature Mater.* **2008**, *7*, 105–114.

232. Toberer, E. S.; May, A. F.; Snyder, G.J. *Chem. Mater.* **2010**, *22*, 624–634.

233. Mewis, A. *Z. Naturforsch. B: Anorg. Chem.*, *Org. Chem.* **1980**, *35*, 939–941.

234. Klüfers, P.; Mewis, A.; Schuster, H. -U. *Z. Kristallogr.* **1979**, *149*, 211–225.

235. Klüfers, P.; Neumann, H.; Mewis, A.; Schuster, H. -U. *Z. Naturforsch. B: Anorg. Chem., Org. Chem.* **1980**, *35*, 1317–1318.

236. Zwiener, G.; Neumann, H.; Schuster, H. -U. *Z. Naturforsch. B: Anorg. Chem., Org. Chem.* **1981**, *36*, 1195–1197.

237. Mahan, A.; Mewis, A. *Z. Naturforsch. B: Anorg. Chem., Org. Chem.* **1983**, *38*, 1041–1045.

238. Tejedor, P.; Stacy, A. M. *J. Solid State Chem.* **1990**, *89*, 227–236.

239. Blanchard, P. E. R.; Stoyko, S. S.; Cavell, R. G.; Mar, A. *J. Solid State Chem.* **2011**, *184*, 97–103.

240. Khatun, M.; Stoyko, S. S.; Mar, A. *Inorg. Chem.* **2012**, *52*, 3148–3158.

241. Gelato, L. M.; Parthé, E. *J. Appl. Crystallogr*. **1987**, *20*, 139–143.

242. Gladyshevskii, E. I.; Kripyakevich, P. I.; Bodak, O. I. *Ukr. Fiz. Zh.* **1967**, *12*, 447–452.

243. Fairley, N. CasaXPS, version 2.3.9, Casa Software Ltd., Teighnmouth, Devon, UK, 2003, http://www.casaxps.com.

244. Grosvenor, A. P.; Cavell, R. G.; Mar, A. *Struct. Bonding* **2009**, *133*, 41–92.

245. Grosvenor, A. P.; Cavell, R. G.; Mar, A., *Chem. Mater*. **2006**, *18*, 1650–1657.

246. Grosvenor, A. P.; Cavell, R. G.; Mar, A. *J. Solid State Chem.* **2010**, *183*, 1477–1483.

247. Crerar, S. J.; Mar, A.; Grosvenor, A. P. *J. Solid State Chem.* **2012**, *196*, 79–86.

248. Ikeda, T.; Okada, K.; Ogasawara, H.; Kotani, A. *J. Phys. Soc. Jpn*., **1990**, *59*, 622–630.

249. Vasquez, R. P. *Surf. Sci. Spectra* **1993**, *2*, 144–148.

250. Vasquez, R. P. *Surf. Sci. Spectra* **1993**, *2*, 149–154.

251. Vasquez, R. P. *Surf. Sci. Spectra* **1998**, *5*, 262–266.

252. Frost, D. C.; Ishitani, A.; McDowell, C. A. *Mol. Phys.* **1972**, *24*, 861–877.

253. Chawla, S. K.; Sankarraman, N.; Payer, J. H. *J. Electron Spectrosc. Relat. Phenom.* **1992**, *62*, 1–18.

254. Roberts, A.; Engelberg, D.; Liu, Y.; Thompson, G. E.; Alexander, M. R. *Surf. Interface Anal.* **2002**, *33*, 697–703.

255. Wagner, C. D.; Naumkin, A. V.; Kraut-Vass, A.; Allison, J. W.; Powell, C. J.; Rumble Jr., J. R. *NIST X-ray Photoelectron Spectroscopy Database*, version 3.5 (web

version), National Institute of Standards and Technology, Gaithersburg, MD, 2003, http://srdata.nist.gov/xps.

256. Scofield, J. H. *J. Electron Spectrosc. Relat. Phenom.* **1976**, *8*, 129–137.

257. Yeh, J. J.; Lindau, I. *At. Data Nucl. Data Tables* **1985**, *32*, 1–155.

258. Rotter, M.; Pangerl, M.; Tegel, M.; Johrendt, D. *Angew. Chem. Int. Ed.* **2008**, *47*, 7949–7952.

259. Mandrus, D.; Sefat, A. S.; McGuire, M. A.; Sales, B. C. *Chem. Mater.* **2010**, *22*, 715–723.

260. Snyder, G. J.; Toberer, E. S. *Nature Mater.* **2008**, *7*, 105–114.

261. Toberer, E. S.; May, A. F.; Snyder, G. J. *Chem. Mater.* **2010**, *22*, 624–634.

262. Zwiener, G.; Neumann, H.; Schuster, H. -U. *Z. Naturforsch. B: Anorg. Chem., Org. Chem.* **1981**, *36*, 1195–1197.

263. Lin, X., Tabassum, D., Mar, A. *Dalton Trans.* **2015**, *44*, 20254-20264.